Advances in Differential Equations and Control Processes

ACADEMIC
ACADEMIC PUBLISHING PTE LTD

P-ISSN: 0974-3243
E-ISSN: 3048-734X
Volume 32 Issue 1, 2025

https://ojs.acad-pub.com/index.php/ADECP

ISSN 0974-3243
01
9 770974 324327

1

Editorial Team

Editor-in-Chief

Advisory Editor

Editorial Board Members

Volume 32 Issue 1 • 2025

Advances in Differential Equations and Control Processes

Editor-in-Chief

Prof. Ji-Huan He

Soochow University, China

ACADEMIC
ACADEMIC PUBLISHING PTE LTD

2025 | Volume 32 | Issue 1

Advances in Differential Equations and Control Processes

https://ojs.acad-pub.com/index.php/ADECP

Contents

Articles

1 **Generalized fixed-point theorem for strict almost ϕ-contractions with binary relations in b-metric spaces and its application to fractional differential equations**
Jiaojiao Wu, Fei He, Shu-fang Li

14 **Mathematical modelling and controllability analysis of fractional order coal mill pulverizer model**
Ghanshyam Malviya, Jaita Sharma, Vishant Shah, Gargi Trivedi

27 **Rolling optimization control method for hydro-photovoltaic-storage microgrid based on stochastic chance constraints**
Qianjin Gui, Wenfa Xu, Xiaoyang Li, Lirong Luo, Haifeng Ye, Zhengfeng Wang

48 **Performance evaluation of post-processed kinematic precise point positioning solution for environmental applications**
Ahmed Al Shouny

63 **Learning of a certain homogeneous reducible differential equation by means of ChatGpt in engineering students during the second semester of 2024 in Antofagasta-Chile**
Jorge Olivares, Byron Droguett, Pablo Martin

71 **Numerical solution of a 3D mathematical model for the progression of tumor angiogenic factor in a tissue**
Melike Keleş Duman, Serdal Pamuk

92 **Herd immunity in a coronavirus disease 2019 epidemic model with consideration of vaccination and quarantine interventions**
Moh Hasan, Faizal Rifky Fahreza

Editorials

117 **Transforming frontiers: The next decade of differential equations and control processes**
Ji-Huan He

122 **Differential equations: a bibliometric analysis**
João Paulo Davim

124 **Differential equation-driven intelligent control: Integrating AI, Quantum computing, and adaptive strategies for next-generation industrial automation**
Yue Cheng, Cheng-Li Luo, Chen Zhong, Hong Lin, Dragan Marinkovic, Ji-Huan He

Advances in Differential Equations and Control Processes 2025, 32(1), 2510.
https://doi.org/10.59400/adecp2510

Article

Generalized fixed-point theorem for strict almost ϕ-contractions with binary relations in b-metric spaces and its application to fractional differential equations

Jiaojiao Wu[1,2], Fei He[1,*], Shu-fang Li[2]

[1] School of Mathematical Sciences, Inner Mongolia University, Hohhot 010021, China

[2] School of Statistics and Mathematics, Inner Mongolia University of Financial and Economic, Hohhot 010070, China

*** Corresponding author:** Fei He, hefei@imu.edu.cn

CITATION

Wu J, He F, Li S. Generalized fixed-point theorem for strict almost ϕ-contractions with binary relations in b-metric spaces and its application to fractional differential equations. Advances in Differential Equations and Control Processes. 2025; 32(1): 2510. https://doi.org/10.59400/adecp2510

ARTICLE INFO

Received: 4 January 2025
Accepted: 24 January 2025
Available online: 14 February 2025

Abstract: The present study is centered around establishing a generalized fixed-point theorem for strict almost ϕ-contractions in b-metric spaces in the context of binary relations. Through the introduction of an innovative lemma, we offer distinct proof methodologies that diverge from the conventional ones in metric spaces. The achieved outcomes not only fortify but also broaden the domain of prior fixed-point theorems in the pertinent literature. Moreover, as a practical exemplification, the existence and uniqueness of solutions to fractional differential equations are illustrated convincingly, thereby connecting the theoretical and applied dimensions of the research.

Keywords: fixed point; strict almost ϕ-contractions; binary relations; b-metric spaces; fractional differential equations

MSC Classification: 47H10; 54H25

1. Introduction

Fixed-point theory has been a fundamental and crucial part of mathematics, and its influence has spread across numerous fields. The traditional contraction mappings and their associated fixed-point theorems, such as the well-known Banach contraction principle in metric spaces, have been the focus of intense research and continuous evolution. These theorems have proven to be extremely valuable in establishing the existence and uniqueness of solutions (abbreviated as EUS) for a wide range of mathematical problems.

In 1998, Czerwik [1] presented the concept of b-metric space with $b \geq 1$, which serves as a significant generalization of metric spaces, and established fixed-point theorems. Numerous fixed-point results within b-metric spaces have been investigated by various authors, as noted in references such as [2–4] and others. Analyzing mappings and their fixed-points within such spaces requires a reconsideration and expansion of conventional methods. Recently, a vital aspect of research in fixed-point theory has been centered on achieving results in relational metric spaces. The structure of relational metric space was initiated by Alam and Imdad [5]. As of now, usual contractions remain stronger than relational contractions. In 2008, Babu et al. [6] introduced a strict almost contraction fixed-point theorem. In 2023, Alharbi and Khan [7] introduced a new type of strict almost ϕ-contractions under binary relations in metric spaces, and derived the corresponding fixed-point theorem. By integrating binary relations into the study of almost ϕ-contractions in b-metric spaces, we can synthesize

and enhance multiple aspects of existing theories.

In the domain of fractional calculus, the necessity of ascertaining the EUS to fractional differential equations has been a major impetus for the application of fixed point theory. Fractional differential equations frequently depict complex physical and engineering phenomena that cannot be precisely modeled using traditional integer-order differential equations. For instance, in the research on anomalous diffusion in concrete [8, 9], fractional calculus offers a more precise framework for capturing non-Fickian behavior. In engineering, the utilization of fractional order derivatives in models of viscoelastic materials enables a more accurate representation of the material's memory and hereditary characteristics [10].

Ahmad et al. made remarkable achievements in the examination of Riemann-Liouville fractional integro-differential equations under fractional nonlocal multi-point and strip boundary conditions within the weighted space [11]. By employing the tools of fixed point theory, they managed to convert the initial and boundary value problems into fixed point problems, thus determining EUS. This work clearly illustrates the potency and adaptability of fixed point theory in the context of fractional differential equations.

Furthermore, the application of fixed point theory in fractional calculus extends beyond just proving existence and uniqueness. It acts as a basis for the development of numerical methods. Once the theoretical groundwork of existence and uniqueness is established, iterative algorithms based on fixed point iterations can be designed to approximate the solutions. This is of vital significance in practical computations and simulations, as it permits the quantitative analysis of systems modeled by fractional differential equations. Martin's work on the application of the variational iteration method in the context of fractional calculus for the dynamic analysis of viscoelastic beams [12] is an excellent example of this. His exploration of the stability aspects of this approach further emphasizes the importance of fixed point theory in fractional calculus.

In this study, we center our attention on devising a fixed-point theorem related to strict almost ϕ-contractions within the framework of b-metric spaces and under binary relations. By introducing an innovative lemma, we provide alternative proofs that differ from the traditional ones in metric spaces. The outcomes attained here not only reinforce but also widen the scope of existing fixed-point theorems in the relevant literature. Additionally, as an illustrative application, we convincingly exhibit EUS to fractional differential equations. Through this research, we strive to make a contribution to the continuously growing body of knowledge in fixed-point theory and its applications, especially in the area of fractional differential equations.

2. Preliminaries

Throughout the paper, let $\mathbb{Z}^+$ and $\mathbb{R}^+$ denote sets of positive integer numbers and nonnegative real numbers respectively.

Definition 1. *Let $\mathcal{M}$ be a nonempty set, $b \geq 1$ and $\mathcal{D} : \mathcal{M} \times \mathcal{M} \to [0, \infty)$ a function satisfying for any $\tilde{x}, \tilde{y}, \tilde{z} \in \mathcal{M}$* [1]*,*

1) $\mathcal{D}(\tilde{x}, \tilde{y}) = 0 \iff \tilde{x} = \tilde{y}$;

2) $\mathcal{D}(\tilde{x},\tilde{y}) = \mathcal{D}(\tilde{y},\tilde{x})$;

3) $\mathcal{D}(\tilde{x},\tilde{y}) \leq b[\mathcal{D}(\tilde{x},\tilde{z}) + \mathcal{D}(\tilde{z},\tilde{y})]$.

Then $\mathcal{D}$ is called a b-metric on $\mathcal{M}$ and the pair $(\mathcal{M},\mathcal{D},b)$ is a b-metric space.

Next, we will begin by noting that a subset of $\mathcal{M}\times\mathcal{M}$ is defined as a binary relation on the set $\mathcal{M}$. For $\tilde{x},\tilde{y}\in\mathcal{M}$, let $\tilde{x}\mathcal{R}\tilde{y}$ denote "$(\tilde{x},\tilde{y})\in\mathcal{R}$" and $\tilde{x}\hat{\mathcal{R}}\tilde{y}$ denote "$\tilde{x}\mathcal{R}\tilde{y}$ or $\tilde{y}\mathcal{R}\tilde{x}$".

Definition 2. *A pair $\tilde{x},\tilde{y}\in\mathcal{M}$ is $\mathcal{R}$-comparative if $\tilde{x}\hat{\mathcal{R}}\tilde{y}$* [5].

This is an important definition regarding the set $\mathcal{M}$ and the relation $\mathcal{R}$. It clearly identifies pairs of elements in $\mathcal{M}$ that have a specific relationship through $\mathcal{R}$. By defining when a pair $\tilde{x},\tilde{y}$ is $\mathcal{R}$-comparative and using the notation $\tilde{x}\hat{\mathcal{R}}\tilde{y}$, the discussion of their relative positions within $\mathcal{M}$ becomes simpler. This concept will likely be foundational for further results and investigations involving $\mathcal{R}$ on $\mathcal{M}$.

Definition 3. *The inverse of relation $\mathcal{R}$ is defined as: $\mathcal{R}^{-1} := \{(\tilde{x},\tilde{y})\in\mathcal{M}\times\mathcal{M} : \tilde{y}\mathcal{R}\tilde{x}\}$. Additionally, $\mathcal{R}^s := \mathcal{R}^{-1}\cup\mathcal{R}$ defines a symmetric relation on $\mathcal{M}$, which is commonly known as the symmetric closure of $\mathcal{R}$.*

The introduction of the inverse relation $\mathcal{R}^{-1}$ provides a way to reverse the direction of the relationship. It allows us to consider pairs in $\mathcal{M}\times\mathcal{M}$ where the order of elements is swapped compared to those in $\mathcal{R}$ [13].

Remark 1. *The symmetric $\mathcal{R}^s$ is also significant. $\tilde{x}\mathcal{R}^s\tilde{y} \iff \tilde{x}\hat{\mathcal{R}}\tilde{y}$ (see* [10]*). By taking the union of $\mathcal{R}$ and its inverse, we obtain a new relation that is symmetric. Symmetric relations often have useful properties and can simplify the analysis of the structure and behavior of elements within the set $\mathcal{M}$ with respect to the original relation $\mathcal{R}$.*

Definition 4. *For a subset $\mathcal{A}\subseteq\mathcal{M}$, the set*

$$\mathcal{R}\big|_{\mathcal{A}} := \mathcal{R}\cap(\mathcal{A}\times\mathcal{A})$$

is referred to as the restriction of $\mathcal{R}$ to $\mathcal{A}$, and it constitutes a relation on $\mathcal{A}$ [7].

Definition 5. *$\mathcal{R}$ is T-closed, if $(T\tilde{x})\mathcal{R}(T\tilde{y}), \forall\tilde{x},\tilde{y}\in\mathcal{M}$ satisfying $\tilde{x}\mathcal{R}\tilde{y}$* [5].

In other words, if two elements have a specific relationship, applying the transformation T to both should result in the same relationship between their images.

Definition 6. *The sequence $\{\tilde{x}_n\}\subset\mathcal{M}$ is $\mathcal{R}$-preserving, if $\tilde{x}_n\mathcal{R}\tilde{x}_{n+1}$, $\forall n\in\mathbb{N}$* [5].

Specifically, this indicates that for every natural number n, the relationship $\tilde{x}_n\mathcal{R}\tilde{x}_{n+1}$ is valid. Roughly speaking, each element in the sequence is connected to the following element through the relation $\mathcal{R}$.

Definition 7. *The $(\mathcal{M},\mathcal{D},b)$ is called $\mathcal{R}$-complete, if each $\mathcal{R}$-preserving Cauchy sequence in $\mathcal{M}$ converges.*

In simpler terms, it means that if you have a sequence of elements that gets arbitrarily close to each other while also maintaining a specific relationship, then there is a point in the structure where this sequence will settle down or converge.

Definition 8. *The subset $\mathcal{A}\subseteq\mathcal{M}$ is $\mathcal{R}$-directed, if for every $\tilde{x}\mathcal{R}\tilde{y}$, $\exists\tilde{z}\in\mathcal{M}$ verifying $\tilde{x}\mathcal{R}\tilde{z}$ and $\tilde{z}\mathcal{R}\tilde{y}$* [14].

Definition 9. *The mapping T is $\mathcal{R}$-continuous at $\tilde{x}\in\mathcal{M}$, if for each $\mathcal{R}$-preserving*

sequence $\{\tilde{x}_n\} \subseteq \mathcal{M}$ *with* $\lim_{n\to\infty} \mathcal{D}(\tilde{x}_n, \tilde{x}) = 0$, *verifying*

$$\lim_{n\to\infty} \mathcal{D}(T\tilde{x}_n, T\tilde{x}) = 0$$

A mapping that is continuous with respect to $\mathcal{R}$ *at every point is referred to as* $\mathcal{R}$*-continuous.*

Definition 10. $\mathcal{R}$ *is termed as* $\mathcal{D}$*-self-closed, if every* $\mathcal{R}$*-preserving* $\{\tilde{x}_n\} \subseteq \mathcal{M}$ *verifying* $\lim_{n\to\infty} \mathcal{D}(\tilde{x}_n, \tilde{x}) = 0$, *has a subsequence* $\{\tilde{x}_{n_k}\}$ *satisfying* $\tilde{x}_{n_k} \hat{\mathcal{R}} \tilde{x}$, *where* $\tilde{x} \in \mathcal{M}$.

Next, we will introduce the main theorems obtained by previous scholars, which also serve as a corollary to our main results.

For the family of all mappings from $\mathbb{R}^+$ to $\mathbb{R}^+$ as follows:

$$\Phi = \left\{ \phi : \phi^{-1}(\{0\}) = \{0\}, \phi(r) < r \text{ and } \limsup_{q\to r} \phi(q) < r, \forall r > 0 \right\}$$

Theorem 1. *Let* $(\mathcal{M}, \mathcal{D})$ *be a metric space,* $\mathcal{R}$ *a relation on* $\mathcal{M}$ *and* $T : \mathcal{M} \to \mathcal{M}$ *a mapping* ([7], Theorem 4). *The conditions are as follows:*

(i) $(\mathcal{M}, \mathcal{D})$ *is* $\mathcal{R}$*-complete;*

(ii) $\exists x_0 \in \mathcal{M}$ *satisfying* $x_0 \mathcal{R} (Tx_0)$ *and* T*-closed;*

(iii) $\mathcal{R}$ *is locally* T*-transitive;*

(iv) $\mathcal{R}$ *is* $\mathcal{D}$*-self-closed, or* T *is* $\mathcal{R}$*-continuous;*

(v) *there exists* $\phi \in \Phi$ *and* $L \geq 0$ *verifying*

$$\mathcal{D}(T\tilde{x}, T\tilde{y}) \leq \phi(\mathcal{D}(\tilde{x}, \tilde{y})) + L \min\{\mathcal{D}(\tilde{x}, T\tilde{x}), \mathcal{D}(\tilde{x}, T\tilde{y}), \mathcal{D}(\tilde{y}, T\tilde{y}), \mathcal{D}(\tilde{y}, T\tilde{x})\} \quad (1)$$

for all $x, y \in \mathcal{M}$ *with* $x\mathcal{R}y$;

(vi) $T(\mathcal{M})$ *is* $\mathcal{R}$*-directed.*

Then, if conditions $(i) - (v)$ *are satisfied,* T *admits a fixed-point. Additionally, if condition* (vi) *is also satisfied, then* T *admits a unique fixed-point.*

Remark 2. *In fact, Equation* (1) *is a strict almost* ϕ*-contraction.*

Following Jleli et al. [15], let Ω represent the collection of all functions $\omega : [0, \infty)^4 \to [0, \infty)$ that are continuous and satisfy the condition that $\omega(q_1, q_2, q_3, q_4) = 0$ if and only if $q_1 q_2 q_3 q_4 = 0$.

For example, the following functions [15] belong to Ω:

(1) $\omega(q1, q2, q3, q4) = L \min\{q_1, q_2, q_3, q_4\}$;

(2) $\omega(q1, q2, q3, q4) = e^{q_1 q_2 q_3 q_4} - 1$;

(3) $\omega(q1, q2, q3, q4) = q_1 q_2 q_3 q_4$;

(4) $\omega(q1, q2, q3, q4) = \ln(1 + q_1 q_2 q_3 q_4)$.

In light of the above, this paper extends conclusion to b-metric spaces, replaces L with ω, and presents results on the existence and uniqueness of fixed-points for strict almost ϕ-contractions under binary relations in b-metric spaces.

We state the following theorem, which establishes the equivalence of certain conditions related to the transformation T and the distances between elements in the structure $\mathcal{M}$.

Theorem 2. *For each* $\phi \in \Phi$ *and* $\omega \in \Omega$, *the following conditions are equivalent:*

(1) $\mathcal{D}(T\tilde{x}, T\tilde{y}) \leq \phi(\mathcal{D}(\tilde{x}, \tilde{y})) + \omega\left(\mathcal{D}(\tilde{x}, T\tilde{x}), \mathcal{D}(\tilde{x}, T\tilde{y}), \mathcal{D}(\tilde{y}, T\tilde{y}), \mathcal{D}(\tilde{y}, T\tilde{x})\right),$
$\forall \tilde{x}, \tilde{y} \in \mathcal{M}$ *with* $\tilde{x}\mathcal{R}\tilde{y}$;

(2) $\mathcal{D}(T\tilde{x}, T\tilde{y}) \leq \phi(\mathcal{D}(\tilde{x}, \tilde{y})) + \omega\left(\mathcal{D}(\tilde{x}, T\tilde{x}), \mathcal{D}(\tilde{x}, T\tilde{y}), \mathcal{D}(\tilde{y}, T\tilde{y}), \mathcal{D}(\tilde{y}, T\tilde{x})\right),$
$\forall \tilde{x}, \tilde{y} \in \mathcal{M}$ *with* $\tilde{x}\hat{\mathcal{R}}\tilde{y}$.

Proof. The conclusion $(2) \Rightarrow (1)$ is obviously valid. Conversely, let (1) holds. Suppose that $\tilde{x}, \tilde{y} \in \mathcal{M}$ with $\tilde{x}\hat{\mathcal{R}}\tilde{y}$. Then, in case $\tilde{x}\mathcal{R}\tilde{y}$, $(1) \Rightarrow (2)$. Otherwise, $\tilde{y}\mathcal{R}\tilde{x}$, one has

$$\begin{aligned}\mathcal{D}(T\tilde{x}, T\tilde{y}) &= \mathcal{D}(T\tilde{y}, T\tilde{x}) \\ &\leq \phi(\mathcal{D}(\tilde{y}, \tilde{x})) + \omega\left(\mathcal{D}(\tilde{y}, T\tilde{y}), \mathcal{D}(\tilde{y}, T\tilde{x}), \mathcal{D}(\tilde{x}, T\tilde{x}), \mathcal{D}(\tilde{x}, T\tilde{y})\right), \\ &= \phi(\mathcal{D}(\tilde{x}, \tilde{y})) + \omega\left(\mathcal{D}(\tilde{x}, T\tilde{x}), \mathcal{D}(\tilde{x}, T\tilde{y}), \mathcal{D}(\tilde{y}, T\tilde{y}), \mathcal{D}(\tilde{y}, T\tilde{x})\right).\end{aligned}$$

It follows that $(1) \Rightarrow (2)$. □

3. Main result

Converting the fixed-point theorem from metric spaces to b-metric spaces is quite a challenging endeavor. Through the introduction of an innovative lemma, we offer distinct proof methodologies that diverge from the conventional ones in metric spaces. The following lemma is new and useful, and will be used for proving our theorems.

Lemma 1. *Let* $(\mathcal{M}, \mathcal{D}, b)$ *be a* b-MS *with* $1 \leq b$. *Let* $[\alpha, \beta]$ *be a closed interval with* $0 < \alpha < \beta \leq \epsilon$. *Suppose that* $T : \mathcal{M} \to \mathcal{M}$ *satisfies:*

$$\mathcal{D}(T\tilde{x}, T\tilde{y}) \leq \phi(\mathcal{D}(\tilde{x}, \tilde{y})),\ \forall \tilde{x}, \tilde{y} \in \mathcal{M} \tag{2}$$

where $\phi \in \Phi$. *then*

(*i*) $\inf_{\alpha \leq r \leq \beta}[r - \phi(r)] > 0$;

(*ii*) $\forall \tilde{x}, \tilde{y} \in \mathcal{M}$ *verifying* $\mathcal{D}(\tilde{x}, \tilde{y}) < \beta$, $\exists n_0 \in \mathbb{N}^+$ *such that* $\mathcal{D}(T^{n_0}\tilde{x}, T^{n_0}\tilde{y}) < \alpha$.

Proof. (*i*) Suppose not, then we have $\inf_{\alpha \leq r \leq \beta}[r - \phi(r)] = 0$. Moreover, there exists a sequence $\{r_k\} \subset [\alpha, \beta]$ such that $r_k - \phi(r_k) \to 0$ as $k \to \infty$. Since $\{r_k\}$ is bounded, we may assumed that $\{r_k\}$ converges to $r_0 \in [\alpha, \beta]$. We obtain $\lim_{k\to\infty} \phi(r_k) = \lim_{k\to\infty} r_k - [r_k - \phi(r_k)] = r_0$. By hypothesis of ϕ, we have

$$r_0 = \lim_{k\to\infty} \phi(r_k) \leq \limsup_{r\to r_0} \phi(r) < r_0$$

which is a contradiction.

(*ii*) By means of (*i*), for each $r \in [\alpha, \beta]$, we denote

$$\sigma = \inf_{\alpha \leq r \leq \beta}[r - \phi(r)] > 0 \tag{3}$$

$\forall \tilde{x}, \tilde{y} \in \mathcal{M}$ with $\mathcal{D}(\tilde{x}, \tilde{y}) < \beta$, from Equation (3) it follows that

$$\mathcal{D}(T\tilde{x}, T\tilde{y}) \leq \phi(\mathcal{D}(\tilde{x}, \tilde{y})) \leq \mathcal{D}(\tilde{x}, \tilde{y}) - \sigma < \beta - \sigma \tag{4}$$

If $\mathcal{D}(T\tilde{x}, T\tilde{y}) < \alpha$, then we take $n_0 = 1$. If $\mathcal{D}(T\tilde{x}, T\tilde{y}) \in [\alpha, \beta)$, then by Equation

(4) we have

$$\mathcal{D}(T^2\tilde{x}, T^2\tilde{y}) \leq \phi(\mathcal{D}(T\tilde{x}, T\tilde{y})) \leq \mathcal{D}(T\tilde{x}, T\tilde{y}) - \sigma < \beta - 2\sigma \tag{5}$$

Continuing this process, for $i \in \mathbb{N}$, if $\mathcal{D}(T^i\tilde{x}, T^i\tilde{y}) < \alpha$, then we take $n_0 = i$. If $\mathcal{D}(T^i\tilde{x}, T^i\tilde{y}) \in [\alpha, \beta)$, we have $\mathcal{D}(T^{i+1}\tilde{x}, T^{i+1}\tilde{y}) < \beta - (i+1)\sigma$. Therefore, $\exists n_0 \in \mathbb{Z}^+$ such that $\mathcal{D}(T^{n_0}\tilde{x}, T^{n_0}\tilde{y}) < \alpha$ for all $\tilde{x}, \tilde{y} \in \mathcal{M}$ where $\mathcal{D}(\tilde{x}, \tilde{y}) < \beta$. □

We first characterized the degree of non-linear contraction from the perspective of the decreasing amounts of contraction over local intervals. Our lemma describes the lower bound of the degree of contraction, ensuring that the sequence of points generated by the contraction mapping is indeed a Cauchy sequence. This leads us to the following technical lemma, which is the core of the fixed-point proof.

Conclusion (i) is a property of the function ϕ, derived from the nature of pure functions. Conclusion (ii) is an extension of Conclusion (i). Specifically, if the distance between two points is less than β, then after applying the operator T to these two points and iterating the function ϕ a certain number of times, the distance can be made less than α. This is because each iteration has a minimum decrease, and the amount of decrease in each step is greater than or equal to this minimum decrease. Therefore, after a sufficient number of iterations, the distance will indeed be less than α.

At this point, one proposes the following fact.

Theorem 3. *Let $(\mathcal{M}, \mathcal{D}, b)$ be a b-metric space with $1 \leq b$, $\mathcal{R}$ a relation on $\mathcal{M}$ and $T : \mathcal{M} \to \mathcal{M}$ a mapping. The conditions are as follows:*

(i) *$(\mathcal{M}, \mathcal{D}, b)$ is $\mathcal{R}$-complete;*

(ii) *$\exists \tilde{x}_0 \in \mathcal{M}$ verifying $\tilde{x}_0 \mathcal{R} (T\tilde{x}_0)$, and $\mathcal{R}$ is T-closed;*

(iii) *$\mathcal{R}$ is $\mathcal{D}$-self-closed or T is $\mathcal{R}$-continuous;*

(iv) *$\exists \phi \in \Phi$ and $\omega \in \Omega$ verifying;*

$$\mathcal{D}(T\tilde{x}, T\tilde{y}) \leq \phi(\mathcal{D}(\tilde{x}, \tilde{y})) + \omega\left(\mathcal{D}(\tilde{x}, T\tilde{x}), \mathcal{D}(\tilde{x}, T\tilde{y}), \mathcal{D}(\tilde{y}, T\tilde{y}), \mathcal{D}(\tilde{y}, T\tilde{x})\right) \tag{6}$$

$\forall \tilde{x}, \tilde{y} \in \mathcal{M}$ with $\tilde{x} \mathcal{R} \tilde{y}$;

(v) *$\mathcal{R}\big|_{T(\mathcal{M})}$ remains complete or $T(\mathcal{M})$ is $\mathcal{R}$-directed.*

Then, if conditions $(i) - (iv)$ are satisfied, T admits a fixed-point. Additionally, if condition (v) is also satisfied, then T admits a unique fixed-point.

Proof. By (ii), we take $\tilde{x}_0 \in \mathcal{M}$ satisfying $\tilde{x}_0 \mathcal{R} (T\tilde{x}_0)$. We define the sequence $\{\tilde{x}_n\}_{n=0}^{\infty} \subseteq \mathcal{M}$ as $\tilde{x}_n = T\tilde{x}_{n-1} = T^n\tilde{x}_0$, where $n \in \mathbb{N}$.

We will show the outcome in several steps:

1) We claim that $\{\tilde{x}_n\}$ is $\mathcal{R}$-preserving.

By (ii), we have $(T^n\tilde{x}_0)\mathcal{R}(T^{n+1}\tilde{x}_0)$, hence, $\tilde{x}_n \mathcal{R} \tilde{x}_{n+1}$, $\forall n \in \mathbb{N}_0$.

2) We claim that $\lim_{n\to\infty} \mathcal{D}(\tilde{x}_n, \tilde{x}_{n-1}) = 0$

Since $\phi \in \Phi$, we have $\phi(r) \leq r$, $\forall r \in \mathbb{R}^+$. Suppose that $v_n = \mathcal{D}(\tilde{x}_n, \tilde{x}_{n-1})$. By

$\mathcal{R}$-preserving and Equation (6), we have

$$\begin{aligned} v_{n+1} &= \mathcal{D}(T\tilde{x}_n, T\tilde{x}_{n-1}) \\ &\leq \phi(\mathcal{D}(\tilde{x}_n, \tilde{x}_{n-1})) + \omega\left(\mathcal{D}(\tilde{x}_n, \tilde{x}_{n+1}), \mathcal{D}(\tilde{x}_{n-1}, \tilde{x}_n), 0, \mathcal{D}(\tilde{x}_{n-1}, \tilde{x}_{n+1})\right) \\ &= \phi(v_n) \\ &\leq v_n \end{aligned}$$

Moreover, $\{v_n\}$ is nonnegative and decreasing. Therefore,

$$\lim_{n\to\infty} v_n = v \geq 0$$

In fact, if $v > 0$, then,

$$v = \lim_{n\to\infty} v_{n+1} \leq \liminf_{n\to\infty} \phi(v_n) \leq \limsup_{q\to v} \phi(q) < v$$

this is contradictory. As a result, $\lim_{n\to\infty} v_n = 0$.

3) We claim that $\{\tilde{x}_n\} \subset \mathcal{M}$ is a Cauchy sequence.

For closed interval $[\frac{1}{2b}, 1]$, Lemma 1 implies that for any $\tilde{x}, \tilde{y} \in \mathcal{M}$ with $\mathcal{D}(\tilde{x}, \tilde{y}) < 1$, there exists $k \in \mathbb{Z}^+$ such that $\mathcal{D}(T^k\tilde{x}, T^k\tilde{y}) < \frac{1}{2b}$. Notice that $\lim_{n\to\infty} \mathcal{D}(\tilde{x}_n, \tilde{x}_{n-1}) = 0$. Thus there exists $N \in \mathbb{N}$, such that

$$\mathcal{D}(\tilde{x}_N, \tilde{x}_{N+1}), \mathcal{D}(\tilde{x}_N, \tilde{x}_{N+2}), \ldots, \mathcal{D}(\tilde{x}_N, \tilde{x}_{N+k})$$

are not greater than $\frac{1}{2b}$. Hence, for any natural number $m > N$, if $m \leq N + k$, we obtain $\mathcal{D}(\tilde{x}_N, \tilde{x}_m) \leq \frac{1}{2b} < 1$; if $m = N + k + 1$, by $\mathcal{D}(\tilde{x}_N, \tilde{x}_{N+1}) < 1$ and Lemma 1, we have $\mathcal{D}(\tilde{x}_{N+k}, \tilde{x}_{N+k+1}) < \frac{1}{2b}$. Moreover,

$$\mathcal{D}(\tilde{x}_N, \tilde{x}_m) \leq b[\mathcal{D}(\tilde{x}_N, \tilde{x}_{N+k}) + \mathcal{D}(\tilde{x}_{N+k}, \tilde{x}_{N+k+1})] < b[\frac{1}{2b} + \frac{1}{2b}] = 1$$

By induction, for any $m > N$, we have $\mathcal{D}(\tilde{x}_N, \tilde{x}_m) < 1$. Let $M := \sup_{m,n\in\mathbb{N}} \mathcal{D}(\tilde{x}_n, \tilde{x}_m)$.

Now, we show that $\{\tilde{x}_n\} \subset \mathcal{M}$ is a Cauchy sequence. For any $\epsilon > 0$, according to Lemma 1, there is $k \in \mathbb{Z}^+$ such that $\mathcal{D}(\tilde{x}, \tilde{y}) \leq M$ and $\mathcal{D}(T^k\tilde{x}, T^k\tilde{y}) < \epsilon$, $\forall \tilde{x}, \tilde{y} \in \mathcal{M}$. Furthermore, for any $m, n \in \mathbb{N}$ with $m > n \geq k$, due to $\mathcal{D}(\tilde{x}_{n-k}, \tilde{x}_{m-k}) \leq M$, by Lemma 1, we have that $\mathcal{D}(\tilde{x}_n, \tilde{x}_m) < \epsilon$. Thus $\{\tilde{x}_n\}$ is a Cauchy sequence.

Since $\{\tilde{x}_n\}$ is a $\mathcal{R}$-preserving Cauchy sequence, hence by (i), $\exists \tilde{x}^* \in \mathcal{M}$ verifying $\lim_{n\to\infty} \mathcal{D}(\tilde{x}_n, \tilde{x}^*) = 0$.

4) We claim that the above $\tilde{x}^*$ is the fixed-point of T

If $\mathcal{R}$ is $\mathcal{D}$-self-closed, then we take a subsequence $\{\tilde{x}_{n_k}\} \subset \{\tilde{x}_n\}$ verifying $\tilde{x}_{n_k} \hat{\mathcal{R}} \tilde{x}^*$, $\forall k \in \mathbb{N}$. From the hypotheses on ϕ Equation (6), Proposition 2 and $\tilde{x}_{n_k} \hat{\mathcal{R}} \tilde{x}^*$, we obtain

$$\begin{aligned}
&\mathcal{D}(\tilde{x}_{n_{k+1}}, T\tilde{x}^*) \\
&= \mathcal{D}(T\tilde{x}_{n_k}, T\tilde{x}^*) \\
&\leq \phi(\mathcal{D}(\tilde{x}_{n_k}, \tilde{x}^*)) + \omega\left(\mathcal{D}(\tilde{x}_{n_k}, \tilde{x}_{n_{k+1}}), \mathcal{D}(\tilde{x}_{n_k}, T\tilde{x}^*), \mathcal{D}(\tilde{x}^*, T\tilde{x}^*), \mathcal{D}(\tilde{x}^*, \tilde{x}_{n_{k+1}})\right) \\
&\leq \mathcal{D}(\tilde{x}_{n_k}, \tilde{x}^*) + \omega\left(\mathcal{D}(\tilde{x}_{n_k}, \tilde{x}_{n_{k+1}}), \mathcal{D}(\tilde{x}_{n_k}, T\tilde{x}^*), \mathcal{D}(\tilde{x}^*, T\tilde{x}^*), \mathcal{D}(\tilde{x}^*, \tilde{x}_{n_{k+1}})\right).
\end{aligned}$$

Computing the limit of the above and by $\mathcal{D}(\tilde{x}_{n_k}, \tilde{x}^*) \to 0$ as $n \to \infty$, we derive $\mathcal{D}(\tilde{x}_{n_{k+1}}, T\tilde{x}^*) \to 0$ as $n \to \infty$, therefore, it can be concluded that $T\tilde{x}^* = \tilde{x}^*$.

If T is $\mathcal{R}$-continuous, since $\{\tilde{x}_n\}$ is $\mathcal{R}$-preserving verifying $\lim_{n\to\infty} \mathcal{D}(\tilde{x}_n, \tilde{x}^*) = 0$, then $\lim_{n\to\infty} \mathcal{D}(T\tilde{x}_n, T\tilde{x}^*) = 0$. This shows that $\lim_{n\to\infty} \mathcal{D}(\tilde{x}_{n+1}, T\tilde{x}^*) = 0$. Hence, we have $T\tilde{x}^* = \tilde{x}^*$.

5) We claim that T has a unique fixed point $\tilde{x}^* \in \mathcal{M}$.

If $\tilde{y}^* \in \mathcal{M}$ with $T\tilde{y}^* = \tilde{y}^*$ and $\tilde{x}^* \neq \tilde{y}^*$, then $\mathcal{D}(\tilde{x}^*, \tilde{y}^*) > 0$. As $\tilde{x}^*, \tilde{y}^* \in T(\mathcal{M})$, the following will be discussed in two cases:

Case 1: If $\mathcal{R}\big|_{T(\mathcal{M})}$ remains complete, then we get $\tilde{x}^*\hat{\mathcal{R}}\tilde{y}^*$. Using Equation (6) and Proposition 2, one obtains

$$\begin{aligned}
\mathcal{D}(\tilde{x}^*, \tilde{y}^*) &= \mathcal{D}(T\tilde{x}^*, T\tilde{y}^*) \\
&\leq \phi(\mathcal{D}(\tilde{x}^*, \tilde{y}^*)) + \omega\left(0, \mathcal{D}(\tilde{x}^*, T\tilde{y}^*), 0, \mathcal{D}(\tilde{y}^*, T\tilde{x}^*)\right) \\
&< \mathcal{D}(\tilde{x}^*, \tilde{y}^*).
\end{aligned}$$

This is contradictory. Hence, $\tilde{x}^* = \tilde{y}^*$.

Case 2: If $T(\mathcal{M})$ is $\mathcal{R}$-directed, then $\exists \tilde{z} \in \mathcal{M}$ satisfying $\tilde{x}^*\mathcal{R}\tilde{z}$ and $\tilde{y}^*\mathcal{R}\tilde{z}$.

Denote $u_n = \mathcal{D}(\tilde{x}^*, T^n\tilde{z})$, using $\mathcal{R}$ is T-closed, $\phi(r) \leq r$ and Equation (6), one obtains

$$\begin{aligned}
&\mathcal{D}(\tilde{x}^*, T^n\tilde{z}) \\
&= \mathcal{D}(T\tilde{x}^*, T(T^{n-1}\tilde{z})) \\
&\leq \phi(\mathcal{D}(\tilde{x}^*, T^{n-1}\tilde{z})) + \omega\left(0, \mathcal{D}(\tilde{x}^*, T^n\tilde{z}), \mathcal{D}(T^{n-1}\tilde{z}, T^n\tilde{z}), \mathcal{D}(T^{n-1}\tilde{z}, T\tilde{x}^*)\right) \\
&\leq \mathcal{D}(\tilde{x}^*, T^{n-1}\tilde{z})
\end{aligned}$$

So, $u_n \leq u_{n-1}$. Moreover, $\{u_n\}$ is a non-increasing and nonnegative sequence; and hence

$$\lim_{n\to\infty} u_n = u \geq 0$$

Indeed, if $u > 0$, then,

$$u = \lim_{n\to\infty} u_{n+1} \leq \liminf_{n\to\infty} \phi(u_n) \leq \limsup_{q\to u} \phi(q) < u$$

this is contradictory. Hence, $\lim_{n\to\infty} u_n = \mathcal{D}(\tilde{x}^*, T^n\tilde{z}) = 0$.

Similarly, one can find $\mathcal{D}(\tilde{y}^*, T^n\tilde{z}) = 0$.

$$\mathcal{D}(\tilde{x}^*, \tilde{y}^*) \leq b\mathcal{D}(\tilde{x}^*, T^n\tilde{z}) + b\mathcal{D}(\tilde{y}^*, T^n\tilde{z}) \to 0, \ \ as \ \ n \to \infty$$

Hence, $\tilde{x}^* = \tilde{y}^*$. □

Remark 3. *Theorem 3 is set in a b-metric space, which generalizes the concept of a metric space by allowing for a broader range of distance functions. Additionally, the conditions on the binary relation are weaker because the universal relation (which involves no restrictions) is a special case of a relation. The compression condition is also comparatively relaxed.*

Building on our findings, we will derive several well-known fixed point theorems by reviewing recent research. It is well known that b-metric space is a generalization of metric space. Using Theorem 3, we can obtain the fixed point theorem result of Alharbi and Khan ([7], Thorem 4) in metric space.

Under the restriction $\mathcal{R} = \mathcal{M} \times \mathcal{M}$, the universal relation, Theorem 3 deduces the following fixed point theorem.

Corollary 1. *Let $(\mathcal{M}, \mathcal{D}, b)$ be a complete b-*MS *with $b \geq 1$. Suppose that $T : \mathcal{M} \to \mathcal{M}$ is a mapping such that*

$$d(T\tilde{x}, T\tilde{y}) \leq \phi(d(\tilde{x}, \tilde{y})), \ for\ all\ \tilde{x}, \tilde{y} \in \mathcal{M} \tag{7}$$

where $\phi \in \Phi$. Then T possesses a unique fixed point in $\mathcal{M}$.

Remark 4. *Note that the conclusion is up to date in b-MS.*

Corollary 2. *Let $(\mathcal{M}, \mathcal{D})$ be a complete metric space* [16]. *Suppose that $T : \mathcal{M} \to \mathcal{M}$ is a mapping such that*

$$d(T\tilde{x}, T\tilde{y}) \leq \phi(d(\tilde{x}, \tilde{y})), \ for\ all\ \tilde{x}, \tilde{y} \in \mathcal{M} \tag{8}$$

where $\phi \in \Phi$. Then T possesses a unique fixed point.

4. Applications to fractional differential equation

Fractional differential equations play a crucial role in various fields, they provide a more comprehensive and refined framework for understanding and analyzing complex dynamic systems that cannot be adequately described by integer-order models. There are many definitions on fractional derivatives, the two-scale fractal derivative [17–19] is based on the idea of the two-scale fractal geometry. In the study of porous media or rough surfaces, this derivative can better capture the behavior where the properties change with different scales.

The fractional derivative in the Ji-Huan He sense offers an alternative approach to fractional calculus. They have unique properties and algorithms for handling fractional-order differentials and integrals. These derivatives have been applied in areas such as signal processing and control theory [20–22].

In general, fractional derivatives allow for a more accurate description of systems with memory, non-local effects, and anomalous diffusion. They can model processes where the rate of change is not simply proportional to the first-order derivative. For instance, in viscoelastic materials, the stress-strain relationship often exhibits fractional-order behavior. Different types of fractional derivatives provide various tools for scientists and engineers to analyze and understand the underlying dynamics of complex systems, enabling more accurate predictions and better designs in many

disciplines including physics, biology, and engineering.

Now, we shall discuss the subsequent fractional differential equation

$$ {}^{c}D^{\alpha}_{0+}\tilde{x}(s) = g(s, \tilde{x}(s)), s \in [0,1] \tag{9}$$

where

$$ \tilde{x}(0) + {}^{c}D^{\beta}_{0+}\tilde{x}(0) = 0, \;\; \tilde{x}(1) + {}^{c}D^{\beta}_{0+}\tilde{x}(1) = 0 \tag{10}$$

${}^{c}D^{\alpha}_{0+}$ is the Caputo fractional derivative (see [23]), $1 < \alpha \leq 2$ and $0 < \beta \leq 1$ are real number and $g : [0,1] \times [0,\infty) \to [0,\infty)$ is a continuous function.

Let $\mathcal{M} := C[0,1]$ be the set of all real continuous functions on a closed interval I, and define $\mathcal{D} : \mathcal{M} \times \mathcal{M} \to \mathbb{R}$:

$$ \mathcal{D}(\tilde{x}, \tilde{y}) = \begin{cases} \frac{1}{7} \max\limits_{s\in[0,1]} |\tilde{x}(s) - \tilde{y}(s)|, & \tilde{x}(s)\tilde{y}(s) \equiv 0, \forall s \in [0,1] \\ \max\limits_{s\in[0,1]} |\tilde{x}(s) - \tilde{y}(s)|, & \text{other} \end{cases} \tag{11}$$

where $\tilde{x}, \tilde{y} \in \mathcal{M}$.

Let $\mathcal{R}$ be a relation on $\mathcal{M}$ as

$$ \tilde{x}\mathcal{R}\tilde{y} \iff \tilde{x}(s) \geq \tilde{y}(s), \;\; \forall \tilde{x}, \tilde{y} \in \mathcal{M}, \forall s \in [0,1]$$

It can be easily proved that $(\mathcal{M}, \mathcal{D}, b)$ is $\mathcal{R}$-complete with the coefficient $b = 7$ and $\mathcal{R}$ is $\mathcal{D}$-self-closed.

For simplicity, we consider the case where $\beta = 1$.

Notice that $\tilde{x} \in \mathcal{M}$ is the solution of Equation (9) $\iff$ $\tilde{x}$ solves the following integral equation,

$$\begin{aligned} \tilde{x}(s) =& \frac{1}{\Gamma(\alpha)} \int_0^1 (1-v)^{\alpha-1}(1-s)g(v, \tilde{x}(v))dv \\ &+ \frac{1}{\Gamma(\alpha-1)} \int_0^1 (1-v)^{\alpha-2}(1-s)g(v, \tilde{x}(v))dv \\ &+ \frac{1}{\Gamma(\alpha)} \int_0^s (s-v)^{\alpha-1} g(v, \tilde{x}(v))dv \end{aligned}$$

Theorem 4. *Consider problem Equation* (9) *with* $g : [0,1] \times [0,\infty) \to [0,\infty)$ *continuous and assume the conditions:*

(*i*) *For any* $\tilde{x}, \tilde{y} \in \mathcal{M}$ *verifying* $\tilde{x}\mathcal{R}\tilde{y}$*, satisfies*

$$ 0 \leq g(s, \tilde{x}(s)) - g(s, \tilde{y}(s)) \leq \frac{1}{4}\phi\left(\tilde{x}(s) - \tilde{y}(s)\right) \tag{12}$$

where $\phi \in \Phi$ *is nondecreasing;*

(*ii*)

$$ \sup_{s\in(0,1)} \frac{1}{4} \left| \frac{1-s}{\Gamma(\alpha+1)} + \frac{1-s}{\Gamma(\alpha)} + \frac{s^{\alpha}}{\Gamma(\alpha+1)} \right| := \theta < 1$$

(*iii*) $\exists \lambda \in \mathcal{M}$ *satisfying*

$$\begin{aligned}\lambda(s) \geq & \frac{1}{\Gamma(\alpha)} \int_0^1 (1-v)^{\alpha-1}(1-s)g(v,\lambda(v))dv \\ & + \frac{1}{\Gamma(\alpha-1)} \int_0^1 (1-v)^{\alpha-2}(1-s)g(v,\lambda(v))dv \\ & + \frac{1}{\Gamma(\alpha)} \int_0^s (s-v)^{\alpha-1} g(v,\lambda(v))dv\end{aligned}$$

hold. Then there exists a unique solution for Equation (9)*.*

Proof. The integral operator $T : \mathcal{M} \to \mathcal{M}$ defined by

$$\begin{aligned}(T\tilde{x})(s) = & \frac{1}{\Gamma(\alpha)} \int_0^1 (1-v)^{\alpha-1}(1-s)g(v,\tilde{x}(v))dv \\ & + \frac{1}{\Gamma(\alpha-1)} \int_0^1 (1-v)^{\alpha-2}(1-s)g(v,\tilde{x}(v))dv \\ & + \frac{1}{\Gamma(\alpha)} \int_0^s (s-v)^{\alpha-1} g(v,\tilde{x}(v))dv.\end{aligned}$$

With the help of Equation (12) it can be verified that $\mathcal{R}$ is T-closed.

Let $\tilde{x}, \tilde{y} \in \mathcal{M}$ verifying $\tilde{x}\mathcal{R}\tilde{y}$ consider

$$\begin{aligned}|T\tilde{x}(s) - T\tilde{y}(s)| = & \frac{1}{\Gamma(\alpha)} \int_0^1 (1-v)^{\alpha-1}(1-s)\left[g(v,\tilde{x}(v)) - g(v,\tilde{y}(v))\right]dv \\ & + \frac{1}{\Gamma(\alpha-1)} \int_0^1 (1-v)^{\alpha-2}(1-s)\left[g(v,\tilde{x}(v)) - g(v,\tilde{y}(v))\right]dv \\ & + \frac{1}{\Gamma(\alpha)} \int_0^s (s-v)^{\alpha-1}\left[g(v,\tilde{x}(v)) - g(v,\tilde{y}(v))\right]dv \\ \leq & \frac{1}{4}\phi\left(\tilde{x}(s) - \tilde{y}(s)\right)\left[\frac{1}{\Gamma(\alpha)} \int_0^1 (1-v)^{\alpha-1}(1-s)dv\right. \\ & + \frac{1}{\Gamma(\alpha-1)} \int_0^1 (1-v)^{\alpha-2}(1-s)dv \\ & \left. + \frac{1}{\Gamma(\alpha)} \int_0^s (s-v)^{\alpha-1}dv\right] \\ = & \frac{1}{4}\phi\left(\tilde{x}(s) - \tilde{y}(s)\right)\left[\frac{1-s}{\Gamma(\alpha+1)} + \frac{s^\alpha}{\Gamma(\alpha+1)} + \frac{1-s}{\Gamma(\alpha)}\right]\end{aligned}$$

Hence, we have

$$\begin{aligned}\mathcal{D}(T\tilde{x}(s), T\tilde{y}(s)) &\leq \phi(\mathcal{D}(\tilde{x}(s), \tilde{y}(s))) \sup_{s\in(0,1)} \frac{1}{4}\left|\frac{1-s}{\Gamma(\alpha+1)} + \frac{1-s}{\Gamma(\alpha)} + \frac{s^\alpha}{\Gamma(\alpha+1)}\right| \\ &\leq \phi\left(\mathcal{D}(\tilde{x}(s), \tilde{y}(s))\right)\end{aligned}$$

For any $\tilde{x}^*, \tilde{y}^* \in T(\mathcal{M})$, take $\tilde{z} := \min\{T\tilde{x}^*, T\tilde{y}^*\}$ implying thereby $T\tilde{x}^* \geq \tilde{z}$ and $T\tilde{y}^* \geq \tilde{z}$. This show that $T(\mathcal{M})$ is $\mathcal{R}$-directed.

From Theorem 3, we see that the Equation (9) possesses a unique solution. □

5. Conclusions

In this paper, we explored the strict almost ϕ-contraction fixed-point theorem in b-metric space with binary relations. The conditions (i)–(iv) of Theorem 3 ensure the existence of fixed-points, while condition (v) guarantees their uniqueness. Utilizing our results, we derive several corollaries applicable. Obviously, this study enhances our understanding of fixed points in b-metric spaces.

In many viscoelastic materials, the diffusion behavior may exhibit non-local and memory-dependent characteristics, necessitating a more nuanced approach, such as fractional differential equations. By incorporating the binary relation $\mathcal{R}$ as part of the proposed fixed-point theorem, we can model interactions and dependencies more flexibly, capturing how the historical states of the material directly influence the diffusion process in conjunction with its current state. This capability enables us to more accurately identify stable states or solutions, which is crucial for understanding how materials respond under various stress conditions. Moreover, we convincingly demonstrate EUS for fractional differential equations.

In the following, we will focus on the case where the boundary condition parameter $\beta \neq 1$ in Equation (10) of the research examples.

Author contributions: Writing—original draft preparation, JW and SL; writing—review and editing, FH; funding acquisition, FH. All authors have read and agreed to the published version of the manuscript.

Funding: This research was funded by the National Natural Science Foundation of China (12061050) and the Natural Science Foundation of Inner Mongolia (2020MS01004).

Acknowledgments: The authors wish to express their hearty thanks to the anonymous referees for their valuable suggestions and comments.

Conflict of interest: The authors declare no conflict of interest.

References

1. Czerwik S. Nonlinear set-valued contraction mappings in b-metric spaces. Atti Sem. Math. Fis. Univ. Modena. 1998; 46: 263–276.
2. Amini-Harandi A. Fixed point theory for quasi-contraction maps in b-metric spaces. Fixed Point Theory. 2014; 15: 351–358.
3. Dung NV, Hang VTL. On relaxations of contraction constants and Caristi's theorem in b-metric spaces. J. Fixed Point Theory Appl. 2016; 18: 267–284.
4. Saleem N, Vujaković J, Baloch WU, et al. Coincidence point results for multivalued Suzuki type mappings using θ-contraction in b-metric spaces. Mathematics. 2019; 7(11): 1017. doi:10.3390/math7111017
5. Alam A, Imdad M. Relation-theoretic contraction principle. J. Fixed Point Theory Appl. 2015; 17: 693–702.
6. Babu GVR, Sandhya ML, Kameshwari MVR. A note on a fixed point theorem of Berinde on weak contractions. Carpathian J. Math. 2008; 24: 8–12.
7. Alharbi AF, Khan FA. Almost boyd-wong type contractions under binary relations with applications to boundary value problems. Axioms. 2023; 12: 896. doi:10.3390/axioms12090896
8. He CH, Liu HW, Liu C. A fractal-based approach to the mechanical properties of recycled aggregate concretes. Facta Universitatis, Series: Mechanical Engineering. 2024; 22(2): 329–342.

9. He CH, Liu C, Fractal dimensions of a porous concrete and its effect on the concrete's strength. Facta Universitatis Series: Mechanical Engineering. 2023; 21 (1): 137–150.
10. Palacios-Pineda LM, Elías-Zúñiga A, Perales-Martnez IA, et al. The fractal rheology of magnetorheological elastomers described through the modified zener model and the cole-cole plot. Fractals. 2024; 32(5). doi: 10.1142/S0218348X24500877
11. Ahmad B, Alghamdi B, Agarwal RP, et al. Riemann-Liouville fractional integro-differential equations with fractional nonlocal multi-point boundary conditions. Fractals. 2022; 30(1). doi:10.1142/S0218348X22400023
12. Martin O. Stability approach to the fractional variational iteration method used for the dynamic analysis of viscoelastic beams. Journal of Computational and Applied Mathematics. 2019; 346: 261–267.
13. Lipschutz S. Schaum's Outlines of Theory and Problems of Set Theory and Related Topics. McGraw-Hill Publishing; 1964.
14. Samet B, Turinici M. Fixed point theorems on a metric space endowed with an arbitrary binary relation and applications. Commun. Math. Anal. 2012; 13: 82–97.
15. Jleli M, Rajić VC, Samet B, et al. Fixed point theorems on ordered metric spaces and applications to nonlinear elastic beam equations. J. Fixed Point Theory Appl. 2012; 12: 175–192. doi:10.1007/s11784-012-0081-4
16. Boyd DW, Wong JS. On nonlinear contractions. Proc. Am. Math. Soc. 1969; 20: 458–464.
17. Wang Y, Gepreel KA, Yang YJ. Variational principles for fractal boussinesq-like $b(m, n)$ equation. Fractals. 2023; 31(7). doi:10.1142/S0218348X23500639
18. Wang Y, Hou W, Gepreel K, et al. A fractal-fractional tsunami model considering near-shore fractal boundary. Fractals. 2024; 32(2). doi:10.1142/S0218348X24500403
19. Fang JH, Nadeem M, Islam A, et al. Modified residual power series approach for the computational results of Newell-Whitehead-Segel model with fractal derivatives. Alexandria Engineering Journal. 2023; 77: 503–512. doi:10.1016/j.aej.2023.06.094
20. Sayevand K. On a flexible extended homotopy perturbation method and its applications in applied chemistry. Journal of Mathematical Chemistry. 2020; 58 (6): 1291–1305
21. Wang Y, An JY. Amplitude-frequency relationship to a fractional Duffing oscillator arising in microphysics and tsunami motion. Journal of Low Frequency Noise Vibration and Active Control. 2019; 38(3–4): 1008–1012.
22. Sayevand K, Rostami M. Fractional optimal control problems: optimality conditions and numerical solution. IMA Journal of Mathematical Control and Information. 2018; 35(1): 123–148.
23. Kilbas AA, Marzan SA. Nonlinear differential equations with the Caputo fractional derivative in the space of continuously differentiable functions. Differ. Equations. 2005; 41: 84–89.

Advances in Differential Equations and Control Processe 2025, 32(1), 2075.
https://doi.org/10.59400/adecp2075

Article

Mathematical modelling and controllability analysis of fractional order coal mill pulverizer model

Ghanshyam Malviya[1,2], Jaita Sharma[1], Vishant Shah[3], Gargi Trivedi[1,*]

[1] Department of Applied Mathematics, Faculty of Technology and Engineering, The Maharja Sayajirao University of Baroda, Vadodara 390002, India

[2] Institute of Sciences, Humanities and Liberal Studies, Indus University, Ahmedabad 382115, India

[3] Applied Science and Humanities, School of Engineering, P P Savani University, Dhamdod 394125, India

*** Corresponding author:** Gargi Trivedi, gargi1488@gmail.com

CITATION

Malviya G, Sharma J, Shah V, Trivedi G. Mathematical modelling and controllability analysis of fractional order coal mill pulverizer model. Advances in Differential Equations and Control Processes. 2025; 32(1): 2075. https://doi.org/10.59400/adecp2075

ARTICLE INFO

Received: 18 November 2024
Accepted: 23 January 2025
Available online: 4 March 2025

Abstract: This paper investigates the controllability of nonlinear dynamical systems and their applications, with a focus on fractional-order systems and coal mill models. A novel theorem is proposed, providing sufficient conditions for controllability, including constraints on the steering operator and nonlinear perturbation bounds. The theorem establishes the existence of a contraction mapping for the nonlinear operator, enabling effective control strategies for fractional systems. The methodology is demonstrated through rigorous proof and supported by an iterative algorithm for controller design. Additionally, the controllability of a coal mill system represented as a nonlinear differential system, is analyzed. The findings present new insights into the interplay of fractional dynamics and nonlinear systems, offering practical solutions for real-world control problems.

Keywords: fractional system; nonlinear systems; coal mill pulverizer model; pulverizer; coal mill; power plant; controllability analysis

AMS Classfication: 93B05; 34H05; 93C10; 93C15

1. Introduction

In recent decades, there has been a growing interest in integral equations and fractional differential and their importance in various scientific fields, including science and engineering [1–3]. The appeal of fractional calculus lies in its ability to effectively describe memory and hereditary properties of diverse materials and processes through fractional derivatives. Many real-world systems are better characterized by non-integer order dynamic models derived from fractional calculus, such as the Basset problem, the Bagley-Torvik equation, and various fluid dynamics models. Fractional dynamical systems have recently attracted significant interest in control system communities, even though fractional-order control problems have been studied since the 1960s. Extending traditional controllers or control schemes to non-integer orders introduces more tuning parameters and enhances flexibility in adjusting a control system's response time. As a result, fractional-order control systems have notably impacted practical applications across all areas of control theory [4–8]. Despite this, the study of fractional-order dynamical systems in the context of control theory has been limited due to a lack of suitable mathematical methods. However, several researchers have made successful attempts in this field [9–12]. Recently, Kaczorek [13] explored fractional control problems in SISO and MIMO systems, highlighting that fractional-order controllers

often exhibit superior performance compared to their integer-order counterparts [13,14] Consequently, research on fractional-order systems remains an active and expanding area world wide. A control system is composed of interconnected components designed to produce a desired response. Controllability, a key structural property of dynamical systems, signifies the ability to steer a system from any initial state to any final state using a set of permissible controls. Investigating the controllability of fractional dynamical systems is essential for various applied problems, as fractional order derivatives and integrals often yield more effective results in control theory than their integerorder counterparts. Despite its importance, recent contributions to the controllability of fractional dynamical systems have been relatively scarce [15].

The controllability of linear fractional dynamical systems was studied by Matignon and D'Andréa-Novel [16] , while Vinagre et al. [17] introduced key concepts for fractional-order systems. Bettayeb and Djennoune [18] examined controllability using rank conditions. Chen et al. [19] concentrated on robust controllability for uncertain fractional-order linear time-invariant systems formulated in state-space representation. Guermah et al. [20] discussed the controllability and observability of discrete-time fractional-order systems. Mozyrska and Torres [21, 22] derived results on controllability and introduced modified energy control approaches for fractional linear systems using Riemann-Liouville and Caputo derivatives. In recent studies, Balachandran et al. [23–27] analyzed the controllability of both linear and nonlinear fractional dynamical systems, providing sufficient conditions for controllability in systems with fractional orders $0 < \alpha \leq 1$ and $1 < \alpha \leq 2$. Govindraj and George [27] analyzed the controllability of semilinear systems through a functional analytic approach, assuming that the nonlinear term meets Lipschitzian and monotonicity conditions. This research underscores the controllability of semilinear fractional dynamical systems where the nonlinear term does not include a controller.

This manuscript examines the controllability conditions for a nonlinear Caputo fractional system described as follows:

$$\begin{aligned} {}^{c}D^{\alpha}_{t_0}x(t) &= \mathcal{A}x(t) + \mathcal{B}u(t) + \mathcal{F}(t, x(t), u(t)) \\ x(t_0) &= x_0 \end{aligned} \tag{1}$$

for $0 < \alpha \leq 1$. Here, $x(t)$, defined in the Hilbert space $\mathbb{X}$, represents the state vector for all $t \in [t_0, t_1]$, and $u(t) \in \mathbb{L}^2([t_0, t_1], \mathbb{U})$ denotes the control input of the system Equation (1). The operators $\mathcal{A}$ and $\mathcal{B}$ are linear. These controllability conditions are further applied to analyze the controllability of the coal mill pulverizer model, which is governed by a nonlinear system of the form Equation (1) as we emphasize the need for a fractional model to represent the Coal Mill Pulverizer system accurately. Traditional integer-order models fail to capture the inherent nonlinearities, time-varying dynamics, and memory effects present in the system. The fractional model, by its nature, can account for these complexities, offering a more accurate representation of the system's behavior. For instance, in the coal mill pulverization process, we observe that the dynamics of coal feed rate and pulverizer pressure exhibit non-integer-order dependencies that the fractional model captures effectively. This

capability is especially important for processes exhibiting long-term memory and time delays.

2. Preliminaries

This section presents fundamental concepts from fractional calculus, controllability of linear systems, and non-linear functional analysis, which form the foundation for this work.

Definition 1. *The Riemann-Liouville fractional integral operator of order $\nu > 0$ for a function $g \in L_1(\mathbb{R}_+)$ is expressed as :*

$$J_{a+}^{\nu} g(t) = \frac{1}{\Gamma(\nu)} \int_a^t (t-\tau)^{\nu-1} g(\tau)\, d\tau,$$

provided the integral on the right-hand side converges. Here, $\Gamma(\cdot)$ represents the gamma function [28].

Definition 2. *The Caputo fractional derivative of order $\nu > 0$, where $m-1 < \nu < m$ and $m \in \mathbb{N}$, is defined as :*

$${}^{c}D_{a+}^{\nu} g(t) = \frac{1}{\Gamma(m-\nu)} \int_a^t (t-\tau)^{m-\nu-1} \frac{d^m g(\tau)}{d\tau^m}\, d\tau$$

provided the integral exists, where $m = \lfloor \nu \rfloor + 1$. [28]

Definition 3. *The one-parameter and two-parameter Mittag-Leffler functions are defined, respectively, as:*

$$E_{\nu}(z) = \sum_{k=0}^{\infty} \frac{z^k}{\Gamma(\nu k + 1)}, \quad E_{\nu,\mu}(z) = \sum_{k=0}^{\infty} \frac{z^k}{\Gamma(\nu k + \mu)}$$

where $\nu, \mu > 0$ and $z \in \mathbb{C}$.

Definition 4. *Let $\mathcal{T}_{\alpha}(t)$ and $\mathcal{T}_{\alpha,\beta}(t)$, for $t \geq 0$, denote families of operators mapping $\mathbb{X}$ into itself* [28]. *These operators, generated by a linear operator $A : \mathbb{X} \to \mathbb{X}$, satisfy the following conditions :*

1) $\mathcal{T}_{\alpha}(0) = I$ *and* $\mathcal{T}_{\alpha,\beta}(0) = I$, *where I is the identity operator.*

2) $\mathcal{T}_{\alpha}(t)$ *satisfies the linear fractional equation* ${}^{c}D^{\alpha} x(t) = A(t)x(t)$ *in a Banach space $\mathbb{X}$.*

3) $\lim_{\mu \to 1} \mathcal{T}_{\alpha,\beta}(t) = \mathcal{T}_{\alpha}(t)$.

Now we will discuss the Controllability of Linear Systems as the controllability of a nonlinear system depends on the controllability of a corresponding linear system. Therefore, we have first discussed the controllability of the corresponding linear system

$$\begin{aligned} {}^{c}D_{t_0}^{\alpha} x(t) &= \mathcal{A}x(t) + \mathcal{B}u(t) \\ x(t_0) &= x_0 \end{aligned} \tag{2}$$

where x is the state vector and u is the controller of the system Equation (2).

The solution of the system Equation (2) is given by

$$x(t) = \mathcal{T}_\alpha(t-t_0)x_0 + \int_{t_0}^{t}(t-s)^{\alpha-1}\mathcal{T}_{\alpha,\alpha}(t-s)\mathcal{B}u(s)ds. \tag{3}$$

The linear system Equation (2) is controllable over the interval $[t_0, t_1]$ if there exists a controller $u(t)$ steers the initial state x_0 to desired final state x_1 at time t_1. This means the solution Equation (3) at time $t = t_1$ steers

$$x_1 = x(t_1) = \mathcal{T}_\alpha(t_1-t_0)x_0 + \int_{t_0}^{t_1}(t_1-s)^{\alpha-1}\mathcal{T}_{\alpha,\alpha}(t_1-s)\mathcal{B}u(s)ds$$

For discussion of controllability of the linear system Equation (2) define an operator $\mathcal{C} : \mathbb{L}^2([t_0, t_1], \mathbb{U}) \to \mathbb{X}$ by

$$\mathcal{C}u(t) = \int_{t_0}^{t_1}(t_1-s)^{\alpha-1}\mathcal{T}_{\alpha,\alpha}(t_1-s)\mathcal{B}u(s)ds \tag{4}$$

whose adjoint $\mathcal{C}^* : \mathbb{X} \to \mathbb{L}^2([t_0, t_1], \mathbb{U})$

$$\mathcal{C}^*\omega = (t_1-t)^{1-\alpha}\mathcal{B}^*\mathcal{T}_{\alpha,\alpha}(t_1-t)\omega \tag{5}$$

Finally defining the operator $\mathcal{W} : \mathbb{X} \to \mathbb{X}$ by

$$\mathcal{W}\omega = \int_{t_0}^{t_1}\mathcal{T}_{\alpha,\alpha}(t_1-s)\mathcal{B}\mathcal{B}^*\mathcal{T}^*_{\alpha,\alpha}(t_1-s)\omega ds \tag{6}$$

forgoing theorem gives a characterization for the controllability of linear system over $[t_0, t_1]$ Equation (2).

Theorem 1. *The following statements are equivalent* [27]*:*

1) The system Equation (2) *is controllable.*

2) $Range(\mathcal{C}) = \mathbb{X}$.

3) There exist $\gamma > 0$ *such that* $||\mathcal{C}^*\omega||^2 \geq \gamma^2||\omega||^2$ *for all* $\omega \in \mathbb{X}$.

4) There exist $\gamma > 0$ *such that* $< \mathcal{W}\omega, \omega > \geq \gamma^2||\omega||^2$ *for all* $\omega \in \mathbb{X}$.

5) $Kernel(\mathcal{C}^*) = \{0\}$ *and* $Range(\mathcal{C}^*)$ *is closed.*

A controller that steers given initial state x_0 *to desired final state* x_1 *is given by*

$$u(t) = (t_1-t)^{1-\alpha}\mathcal{B}^*\mathcal{T}^*_{\alpha,\alpha}(t_1-t)\mathcal{W}^{-1}\left[x_1 - \mathcal{T}_{\alpha,\alpha}(t_1-t_0)x_0\right]$$

Corollary 1. *If the system Equation* (2) *is controllable on* $[t_0, t_1]$ *then, there exists steering operator* $\mathcal{S} : \mathbb{X} \to L^2([t_0, t_1], \mathbb{U})$ *define by* $\mathcal{S}\omega = \mathcal{C}^*\mathcal{W}^{-1}\omega$ *is the right inverse of* $\mathcal{C}$ [27]. *This means* $\mathcal{C} \circ \mathcal{S} = I$.

3. Controllability of nonlinear system

This section discusses the controllability of the Caputo fractional nonlinear system. The system governed by

$$\begin{aligned} {}^cD_{\alpha,t_0}x(t) &= \mathcal{A}x(t) + \mathcal{B}u(t) + \mathcal{F}(t, x(t), u(t)) \\ x(t_0) &= x_0 \end{aligned} \tag{7}$$

where $0 < \alpha \leq 1$, $x(t)$ represents the state, and $u(t)$ denotes the controller of the system described by Equation (7). models a Caputo fractional nonlinear system where $0 < \alpha \leq 1$ is the fractional order. In this context, $x(t)$ represents the state vector, capturing the system's dynamic states, while $u(t)$ denotes the control input applied to influence the system's behavior. The system matrix $\mathcal{A}$ encapsulates the inherent dynamics, such as damping or stiffness effects, and the control matrix $\mathcal{B}$ describes how the control inputs impact the system's states. The term $\mathcal{F}(t, x(t), u(t))$ accounts for nonlinearities, including effects such as friction or saturation, which depend on the system state and control. The use of the Caputo fractional derivative ${}^{c}D_{\alpha,t_0}$ introduces memory effects, meaning that the current state depends not only on the present dynamics but also on the entire past behavior. Equation (8) provides the mild solution of Equation (8), derived using fractional calculus principles. The solution is expressed as Assuming the nonlinear function $\mathcal{F}$ is sufficiently well-behaved so that the system Equation (7) admits a unique mild solution:

$$x(t) = \mathcal{T}_\alpha(t - t_0)x_0 + \int_{t_0}^{t} (t - s)^{\alpha-1}\mathcal{T}_{\alpha,\alpha}(t - s)\left[\mathcal{B}u(s) + \mathcal{F}(s, x(s), u(s))\right] ds \quad (8)$$

for all fixed u.

The system described by Equation (7) is considered controllable over the interval $[t_0, t_1]$ if there exists a controller $u(t)$ that drives the initial state x_0 to the desired final state x_1 at time t_1. This means

$$x_1 = x(t_1) = \mathcal{T}_\alpha(t-t_0)x_0 + \int_{t_0}^{t_1} (t_1-s)^{\alpha-1}\mathcal{T}_{\alpha,\alpha}(t_1-s)\left[\mathcal{B}u(s) + \mathcal{F}(s, x(s), u(s))\right] ds$$

The above equation represents the fractional-order system's free-response operator. The first term, $\mathcal{T}_\alpha(t - t_0)x_0$, captures the free evolution of the state starting from the initial condition x_0, while the integral term incorporates the effects of the control input $u(t)$ and the nonlinearities $\mathcal{F}(t, x(t), u(t))$. The kernel $(t - s)^{\alpha-1}$ reflects the memory characteristic inherent in fractional-order systems.

To analyze the controllability of a nonlinear system, we define the operator $\mathcal{G} : \mathbb{L}^2([t_0, t_1], \mathbb{U}) \to \mathbb{X}$ by

$$\begin{aligned} \mathcal{G}u &= \int_{t_0}^{t_1} (t_1 - s)^{\alpha-1}\mathcal{T}_{\alpha,\alpha}(t_1 - s)\left[\mathcal{B}u(s) + \mathcal{F}(s, x(s), u(s))\right] ds \\ &= \mathcal{C}u + \int_{t_0}^{t_1} (t_1 - s)^{\alpha-1}\mathcal{T}_{\alpha,\alpha}(t_1 - s)\mathcal{F}(s, x(s), u(s))ds \end{aligned} \quad (9)$$

then operator determines whether the system is controllable by mapping the input space to the state space, with controllability achieved if and only if $\mathcal{G}$ is onto. The nonlinear term $\mathcal{F}(t, x(t), u(t))$ must satisfy certain regularity conditions, such as Lipschitz continuity, to ensure the existence and uniqueness of the mild solution, which is necessary for practical implementation of control strategies.

Assuming controllability of the corresponding linear system, define the operator $\bar{\mathcal{G}} : \mathbb{X} \to \mathbb{X}$ by

$$\begin{aligned}\bar{\mathcal{G}}\omega = \mathcal{G}\circ\mathcal{S}\omega &= \mathcal{C}\circ\mathcal{S}\omega + \int_{t_0}^{t_1}(t_1-s)^{\alpha-1}\mathcal{T}_{\alpha,\alpha}(t_1-s)\mathcal{F}(s,x_\omega(s),\mathcal{S}\omega(s))ds \\ &= \omega + \mathcal{H}\omega = (\mathcal{I}+\mathcal{H})\omega\end{aligned} \tag{10}$$

where $\mathcal{I}$ is the identity operator Equation(7).

Theorem 2. *The system Equation* (7) *is controllable if the operator $\bar{\mathcal{G}}$ is non-singular, and the controller that steers the initial state to the desired final state x_1 at time t_1 is given by*

$$u(t) = \mathcal{C}^*\mathcal{W}^{-1}\bar{\mathcal{G}}^{-1}\left[x_1 - \mathcal{T}_\alpha(t_1-t_0)x_0\right]$$

Proof. Since the operator $\bar{\mathcal{G}}$ is non-singular, substituting the controller into the Equation (8), the state of the system at $t = t_1$ becomes:

$$\begin{aligned}x(t_1) &= \mathcal{T}_\alpha(t-t_0)x_0 + \mathcal{G}u \\ &= \mathcal{T}_\alpha(t-t_0)x_0 + (\mathcal{I}+\mathcal{H})(\mathcal{C}\mathcal{C}^*)\mathcal{W}^{-1}(\mathcal{I}+\mathcal{H})^{-1}\left[x_1 - \mathcal{T}_\alpha(t_1-t_0)x_0\right] \\ &= x_1\end{aligned}$$

Hence, the system is controllable over the interval $[t_0, t_1]$. □

Therefore, the controllability of system Equation (7) reduces to the invertibility of the operator $\bar{\mathcal{G}}$. The following theorem derives the conditions under which the operator $\bar{\mathcal{G}}$ is non-singular.

Theorem 3. *If the operator $\mathcal{H}^{(n)}$ is a contraction for some $n \geq 1$, then $\bar{\mathcal{G}}$ is non-singular.*

Proof. If $\mathcal{H}^{(n)}$ is a contraction for some $n \geq 1$, then by the Banach fixed point theorem, the operator equation $\omega = -\mathcal{H}\omega$ has a unique solution. This implies that the equation $(\mathcal{I}+\mathcal{H})\omega = 0$ has a unique trivial solution. Hence, the operator $\bar{\mathcal{G}}$ is non-singular. □

The next theorem discusses the controllability of the nonlinear system Equation (7).

Theorem 4. *If*

1) The corresponding linear system is controllable.

2) There exist constants f_1 and f_2 such that

$$||\mathcal{F}(t,x_1,u_1) - \mathcal{F}(t,x_2,u_2)|| \leq f_1||x_1-x_2|| + f_2||u_1-u_2||$$

for all $x, u \in \mathbb{B}_{r_0}(x_0,u_0)$ for some $r_0 > 0$ where

$$u_0(t) = (t_1-t)^{1-\alpha}\mathcal{B}^*\mathcal{T}^*_{\alpha,\alpha}(t_1-t)\mathcal{W}^{-1}\left[x_1 - \mathcal{T}_{\alpha,\alpha}(t_1-t_0)x_0\right]$$

then the nonlinear system Equation (7) *is controllable over $[t_0,t_1]$ and the controller which drives the system Equation* (7) *to desired final state x_1 at $t = t_1$ is given by*

$$u(t) = \mathcal{C}^*\mathcal{W}^{-1}\bar{\mathcal{G}}^{-1}\left[x_1 - \mathcal{T}_\alpha(t_1-t_0)x_0\right]$$

Proof. To prove the system is controllable, it is sufficient to prove that the operator $\mathcal{H}^{(n)}$

is a contraction for some $n \geq 1$. Therefore, for $x_1, x_2, u_1, u_2 \in \mathbb{B}(x_0, u_0)$, consider

$$||\mathcal{H}^{(n)}x_1 - \mathcal{H}^{(n)}x_2|| \leq \int_{t_0}^{t_1} (t_1 - s)^{\alpha-1} ||\mathcal{T}_{\alpha,\alpha}|| \, ||\mathcal{H}^{(n-1)}x_1 - \mathcal{H}^{(n-1)}x_2|| \, ds$$

$$\leq M^2(f_1 + f_2 S) \int_{t_0}^{t_1} \int_{t_0}^{t_1} (t_1 - s)^{\alpha-1}(t_1 - s_1) ||\mathcal{H}^{(n-2)}x_1 - \mathcal{H}^{(n-2)}x_2|| \, ds_1 \, ds$$

$$\leq M^3(f_1 + f_2 S)^2 \int_{t_0}^{t_1} \int_{t_0}^{t_1} (t_1 - s)^{\alpha-1}(s - s_1)(s_1 - s_2)^{\alpha-1} ||\mathcal{H}^{(n-3)}x_1 - \mathcal{H}^{(n-3)}x_2|| \, ds_2 \, ds_1 \, ds$$

and continuing this process gives

$$||\mathcal{H}^{(n)}x_1 - \mathcal{H}^{(n)}x_2|| \leq M^n(f_1 + f_2 S)^{(n)} \int_{t_0}^{t_1} (t_1 - t_0)^{n(\alpha-1)} \frac{(t_1 - s)^{n-1}}{(n-1)!} \, ds \, ||x_1 - x_2||$$

$$\leq \frac{M^n(f_1 + f_2 S)^{(n)}(t_1 - t_0)^{n\alpha}}{n!} ||x_1 - x_2||$$

where S is a bound for the steering operator $\mathcal{S}$ and is finite as the corresponding linear system is controllable.

Since

$$\frac{M^n(f_1 + f_2 S)^{(n)}(t_1 - t_0)^{n\alpha}}{n!} \to 0 \quad \text{as} \quad n \to \infty$$

there exists an n such that the operator $\mathcal{H}$ is a contraction. Hence, the system Equation (7) is controllable, and the controller $u(t)$ which drives the system Equation (7) to the desired final state x_1 is given by

$$u(t) = \mathcal{C}^* \mathcal{W}^{-1} \bar{\mathcal{G}}^{-1} \left[x_1 - \mathcal{T}_\alpha(t_1 - t_0) x_0 \right]$$

This completes the proof. □

The algorithm to find the controller and the state is given by

$$\begin{aligned}
u^{(n)}(t) &= \mathcal{C}^* \mathcal{W}^{-1} (\mathcal{I} + \mathcal{H})^{-1} \left[x_1 - \mathcal{T}_\alpha(t_1 - t_0) x_0 \right] \\
x^{(n+1)}(t) &= \mathcal{T}_\alpha(t - t_0) x_0 + \int_{t_0}^{t} (t - s)^{\alpha-1} \mathcal{T}_{\alpha,\alpha}(t - s) \left[\mathcal{B} u^{(n)}(s) + \mathcal{F}(s, x^{(n)}(s), u^{(n)}(s)) \right] ds \\
\mathcal{H}^{(n)} x_1^{(n)} &= \int_{t_0}^{t_1} (t_1 - s)^{\alpha-1} \mathcal{T}_{\alpha,\alpha}(t_1 - s) \mathcal{F}(s, x^{(n-1)}(s), \mathcal{S} x^{(n-1)}(s)) \, ds
\end{aligned} \tag{11}$$

where

$$u_0(t) = (t_1 - t)^{1-\alpha} \mathcal{B}^* \mathcal{T}_{\alpha,\alpha}^*(t_1 - t) \mathcal{W}^{-1} \left[x_1 - \mathcal{T}_{\alpha,\alpha}(t_1 - t_0) x_0 \right]$$

4. Modelling and controllability analysis of the coal mill system

This section provides an overview of the coal mill process and its modeling and Controllability Analysis. A simplified schematic of a roll mill is shown in **Figure 1**. In the system, raw coal is transported via conveyor belts and fed into the mill, where rollers crush it on a grinding table. Fine coal particles are carried upward by primary air introduced from the mill's base, which directs them toward the classifier section. The classifier selectively allows the smallest particles to exit the mill while larger

particles are returned to the grinding table for further processing. Rotary classifiers, when employed, enable adjustment of coal output by modifying the rotational speed, allowing larger particles to pass if needed.The general flow of coal particles within the mill is illustrated in **Figure 1**. The mathematical model developed for this system primarily captures the nominal grinding process [29]. However, it is also robust enough to represent the dynamic behavior during start-up and shutdown operations. The key aspect of the model is the circulation of coal particles within the mill, as depicted in the layout.

As illustrated in **Figure 1**, the circulation of coal particles forms a fundamental aspect of the model.

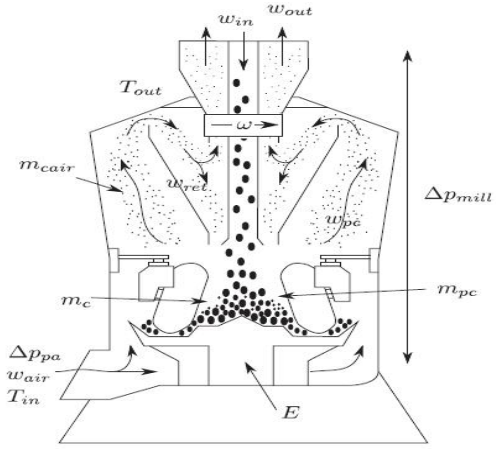

Figure 1. Flow of coal particles in a roll wheel mill [30].

To develop the mathematical model, the following parameters and variables are defined [29], as illustrated in **Figure 2:**

- $m_c(t)$: Mass of raw coal awaiting pulverization.
- $m_{pc}(t)$: Mass of pulverized coal present on the grinding table.
- $m_{cair}(t)$: Mass of coal particles transported pneumatically within the mill.
- $w_{in}/w_c(t)$: Mass flow rate of raw coal entering the mill.
- $w_{ret}(t)$: Mass flow rate of particles rejected by the classifier and returned for further grinding.
- w_{pc}: Mass flow rate of coal picked up from the table by primary air.
- w_{out}: Mass flow rate of pulverized coal exiting the mill.
- w_{air}: Mass flow rate of primary air.
- ω: Rotational speed of the classifier.

Using the principle of continuity, the rate of change of mass of coal (m_c) to be pulverized is equal to the mass flow of raw coal (w_c/w_{in}) and the return flow of the particles rejected by the classifier (w_{ret}) and the grinding rate which is proportional to the mass of raw coal at the grinding table (m_c).

$$\frac{d}{dt}m_c(t) = w_c(t) + w_{ret}(t) - \theta_1 m_c(t) \tag{12}$$

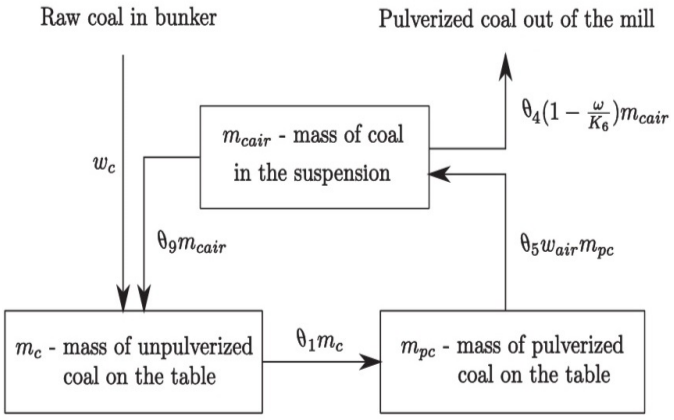

Figure 2. Schematic representation of coal particle flow dynamics in a mill [30].

The rate of change of pulverized coal (m_{pc}) at the table is equal to the amount of grinded raw coal(m_c) minus the amount of coal picked up by the primary air from the table (w_{pc})

$$\frac{d}{dt}m_{pc}(t) = \theta_1 m_c(t) - w_{pc}(t) \tag{13}$$

The mass flow of the coal particles collected from the grinding table by primary air (w_{pc}) minus the fuel out of the mill (w_{out}) and the return flow of the rejected particles to the table (w_{ret}) are equal to the rate of change in the mass of the particles in the pneumatic transport up (m_{cair}) in the mill

$$\frac{d}{dt}m_{cair}(t) = w_{pc}(t) - w_{out}(t) - w_{ret}(t) \tag{14}$$

The primary air mass flow $(wair)$ and the mass of pulverised coal on the table (mpc) are proportional to the mass flow of pulverized particles picked up by the primary air (w_{pc}) to be transferred towards the classifier.

$$\frac{d}{dt}w_{pc}(t) = \theta_5 w_{air}(t) m_{pc}(t) \tag{15}$$

The mass flow of pulverized coal out of the mill $(wout)$ is proportional to the mass of coal lifted off the table $(mcair)$ and is influenced by the classifier speed $omega$.

$$w_{out}(t) = \theta_4 m_{cair}(t)(1 - \frac{\omega(t)}{\theta_6}) \tag{16}$$

where $0 < \omega(t) < \theta_6.\theta_6$

The mass of coal in the pneumatic transport m_{cair} is equal to the mass flow of coal returning to the grinding table proportional to

$$w_{ret}(t) = \theta_9 m_{cair}(t) \tag{17}$$

Niemczyk et al. [30] proposed a mathematical model for the coal mill pulverizer problem, described by a nonlinear system of differential Equations (12)–(14) can be written as:

$$\begin{aligned}
\frac{d}{dt}m_c(t) &= w_c(t) + \theta_9 m_{cair}(t) - \theta_1 m_c(t) \\
\frac{d}{dt}m_{pc}(t) &= \theta_1 m_c(t) - \theta_5 w_{air}(t) m_{pc}(t) \\
\frac{d}{dt}m_{cair}(t) &= \theta_5 w_{cair}(t) m_{pc}(t) - \theta_4 m_{cair}(t)\left(1 - \frac{\omega(t)}{\theta_6}\right) - \theta_9 m_{cair}(t)
\end{aligned} \tag{18}$$

where the variables represent the mass of coal to be pulverized $m_c(t)$, the mass of pulverized coal on the table $m_{pc}(t)$, and the mass of particles in pneumatic transport $m_{cair}(t)$, while $w_c(t)$ and $w_{air}(t)$ are the respective mass flows, and $\omega(t)$ denotes the classifier speed.

Let us define the system states as $x_1(t) = m_c(t)$, $x_2(t) = m_{pc}(t)$, and $x_3(t) = m_{cair}(t)$, while the control inputs are $u_1(t) = w_c(t)$, $u_2(t) = w_{air}(t)$, and $u_3(t) = \omega(t)$. With this, the model in Equation (18) becomes:

$$\begin{aligned}
\dot{x}_1 &= -\theta_1 x_1 + \theta_9 x_3 + u_1 \\
\dot{x}_2 &= \theta_1 x_1 - \theta_5 u_2 x_2 \\
\dot{x}_3 &= -(\theta_4 + \theta_9) x_3 + \theta_5 u_2 x_2
\end{aligned} \tag{19}$$

where the constants θ_1, θ_4, θ_5, θ_6, and θ_9 are known system parameters.

The coal mill pulverizer system exhibits highly nonlinear behaviors, time-varying dynamics, and long-term memory effects, making its control and modeling particularly challenging. Traditional integer-order models often fail to accurately capture these complexities due to their inability to represent the system's hereditary and memory-dependent properties. Fractional-order models, on the other hand, inherently incorporate memory effects and fractional dynamics, offering a more precise representation of such systems. For example, the grinding process in a pulverizer involves not only instantaneous changes in the coal flow but also long-term effects of grinding and accumulation, which are naturally modeled by fractional derivatives. This study, therefore, leverages fractional-order modeling to better characterize the coal mill's dynamics, providing a foundation for more effective control strategies. In the context of coal mill systems, fractional calculus provides significant advantages over traditional integer-order models by accurately capturing the inherent complexities of the process. Coal pulverization involves non-linearities, time-varying dynamics, and considerable memory effects due to delays in grinding and material transport. While integer-order models can approximate some dynamics, they often fail to address the long-term dependencies and intricate transient behaviors observed in real-world systems. Therefore, we now propose a fractional-order version of the system in Equation (19), given by:

$$\begin{aligned}
{}^cD^\alpha x_1 &= -\theta_1 x_1 + \theta_9 x_3 + u_1 \\
{}^cD^\alpha x_2 &= \theta_1 x_1 - \theta_5 u_2 x_2 \\
{}^cD^\alpha x_3 &= -(\theta_4 + \theta_9) x_3 + \theta_5 u_2 x_2 + \theta_4 x_3 \frac{u_3}{\theta_6}
\end{aligned} \tag{20}$$

Next, we focus on the controllability analysis of the fractional system in Equation

(20), assuming a constant control input $u_2 = 0.02$. This leads to the simplified system:

$$\begin{aligned} {}^cD^\alpha x_1 &= -\theta_1 x_1 + \theta_9 x_3 + u_1 \\ {}^cD^\alpha x_2 &= \theta_1 x_1 - 0.02\theta_5 x_2 \\ {}^cD^\alpha x_3 &= 0.02\theta_5 x_2 - (\theta_4 + \theta_9) x_3 + \theta_4 x_3 \frac{u_3}{\theta_6} \end{aligned} \tag{21}$$

This can be expressed in a more compact form as:

$${}^cD^\alpha x(t) = \mathcal{A}x(t) + \mathcal{B}u(t) + \mathcal{F}(t, x(t), u(t)) \tag{22}$$

where $x = \begin{bmatrix} x_1 \\ x_2 \\ x_3 \end{bmatrix}$ represents the state vector and $u = \begin{bmatrix} u_1 & u_2 & u_3 \end{bmatrix}$ is the control input. The system matrices $\mathcal{A}$, $\mathcal{B}$, and the nonlinear term $\mathcal{F}(t, x(t), u(t))$ are given by:

$$\mathcal{A} = \begin{bmatrix} -\theta_1 & 0 & \theta_9 \\ \theta_1 & -0.02\theta_5 & 0 \\ 0 & -0.02\theta_5 & -(\theta_4 + \theta_9) \end{bmatrix}, \mathcal{B} = \begin{bmatrix} 1 \\ 0 \\ 0 \end{bmatrix}, \mathcal{F}(t, x(t), u(t)) = \begin{bmatrix} 0 \\ 0 \\ \frac{\theta_4}{\theta_6} x_3 u_3 \end{bmatrix}$$

Since the rank of the controllability matrix $P = [B : AB : A^2B]$ is 3 therefore the controllability Gramian of the linearized system is non-singular, the system is controllable in the linear case. Moreover, the nonlinear term $\mathcal{F}(t, x(t), u(t))$ satisfies a Lipschitz condition, with constants $f_1 = \frac{\theta_4}{\theta_6}|u_3^0|$ and $f_2 = \frac{\theta_4}{\theta_6}|x_3^0|$, ensuring that:

$$||\mathcal{F}(t, x(t), u(t)) - \mathcal{F}(t, y(t), v(t))|| \leq f_1||x - y|| + f_2||u - v||$$

By the controllability theorem, this implies that the system is controllable over a finite time interval. The transition from traditional integer-order models to fractional-order systems provides enhanced controllability insights for the coal mill pulverizer system. By accounting for memory and hereditary effects, fractional dynamics enable the model to capture gradual changes and interdependencies that would otherwise be overlooked in integer-order approaches. For instance, the system's response to varying coal loads and grinding pressures is significantly influenced by past operational states, which are naturally incorporated through fractional derivatives.

5. Conclusion and future direction

This study presents a comprehensive analysis of the controllability of nonlinear dynamical systems, with a focus on fractional-order systems and coal mill models. A theorem establishing sufficient conditions for controllability was rigorously derived, demonstrating the role of contraction mappings in ensuring system control. The proposed iterative algorithm offers a practical framework for designing controllers capable of driving nonlinear systems to desired states. Furthermore, the application to the coal mill system highlights the adaptability of the methodology to real-world industrial processes. The results emphasize the significance of fractional dynamics in advancing the understanding and control of complex systems, laying a foundation

for further research and development in this field. Looking ahead, future research will extend this methodology to more complex systems and incorporate additional control strategies. The application of fractional dynamics to other industrial processes and emerging technologies, such as robotics and autonomous systems, will also be explored. Moreover, future work will focus on refining the iterative algorithm to enhance computational efficiency and robustness, particularly for large-scale systems.

Author contributions: Conceptualization, GM and JS; methodology, GM; software, GT; validation, VS, JS and GM; formal analysis, VS, GM and GT; investigation, JS; resources, JS; data curation, VS; writing—original draft preparation, GM and GT; writing—review and editing, GT; visualization, JS; supervision, JS; project administration,JS. All authors have read and agreed to the published version of the manuscript.

Conflict of interest: The authors declare no conflict of interest.

References

1. Torvik PJ, Bagley RL. On the appearance of the fractional derivative in the behavior of real materials. Journal of Applied Mechanics; 1984; 51(2): 294–298.
2. Magin R. Fractional Calculus in Bioengineering. Begell House Publishing; 2006.
3. Trivedi G, Shah V, Sharma J, Sanghvi R. On the solution of non-instantaneous impulsive Hilfer fractional integro-differential evolution system. Mathematica Applicanda. 2023; 51(1): 3–20.
4. Bao X, Ma W, Li X. Controllability of fractional complex networks. Fractal and Fractional. 2024; 8(1): 43.
5. Ahsan M, Saeed M. Mehmood A, et al. The study of HIV diagnosis using complex fuzzy hypersoft mapping and proposing appropriate treatment, Fractal and Fractional. IEEE Access. 2021; 9: 104405–104417.
6. Shah V, Sharma J, Samei ME, Trivedi G. The trajectory controllability of second-order semilinear systems using a functional analytic approach. Journal of Computational and Engineering Mathematics. 2024; 11(4): 22–32.
7. Parastesh F, Aram Z, Namazi H, et al. A simple chaotic model for development of HIV virus. Scientia Iranica. 2021; 28(3): 1643–1652.
8. Ma W, Bao X, Ma C. Controllability of higher-order networks. Physica A: Statistical Mechanics and its Applications. 2024; 653: 130180.
9. Axtell M, Bise ME. Fractional calculus applications in control systems. In: Proceedings of the IEEE 1990 National Aerospace and Electronics Conference; 21–25 May 1990; New York, NY, USA.
10. Bagley RL, Calico RA. Fractional order state equations for the control of viscoelastically damped structure. Journal of Guidance, Control and Dynamics. 1991; 14(2): 304–311.
11. Monje CA, Chen YQ, Vinagre BM, et al. Fractional-order Systems and Controls: Fundamentals and Applications. Springer Publishing; 2010.
12. Petr´aˆs I. Control of fractional order Chua's system. Journal of Electrical Engineering. 2002; 53(7–8): 219–222.
13. Kaczorek T. Selected Problems of Fractional Systems Theory. Springer-Verlag Berlin and Heidelberg GmbH and Co. K; 2011.
14. Klamka J. Controllability of dynamical systems. Bulletin of the Polish Academy of Sciences Technical Sciences. 1993; 61(2): 283–310.
15. He CH, Liu HW, Liu C. A fractal-based approach to the mechanical properties of recycled aggregate concretes. Facta Universitatis, Series: Mechanical Engineering. 2024; 22(2): 329–342.
16. Matignon D, d'Andr´ea-Novel B. Some results on controllability and observability of finite dimensional fractional differential systems. In: Proceedings of the IAMCS, IEEE Conference on Systems, Man and Cybernetics Lille; 9–12 July 1996; (Paris), France.
17. Vinagre BM, Monje CA, Calderon AJ. Fractional order systems and fractional order control actions, Lecture 3 of the IEEE CDCO2 TW 2: Fractional Calculus Applications in Automatic Control and Robotics, Las Vegas, 2002.

18. Bettayeb M, Djennoune S. New results on the controllability and observability of fractional dynamical systems. Journal of Vibration and Control. 2008; 14: 1531–1541.
19. Chen Y, Ahn HS, Xue D. Robust controllability of interval fractional order linear time invariant systems. Signal Processing. 2006; 86(10): 2794–2802.
20. Guermah S, Djennoune S, Bettayeb M. Controllability and observability of linear discrete-time fractional-order systems. International Journal of Applied Mathematics and Computer. 2008; 18(2): 213–222.
21. Mozyrska D, Torres DFM. Minimal modified energy control for fractional linear control systems with the Caputo derivative. Carpathian Journal of Mathematics. 2010; 26: 210–221.
22. Mozyrska D, Torres DFM. Modified optimal energy and initial memory of fractional continuous-time linear systems. Signal Processing. 2011; 91(3): 379–385.
23. Balachandran K, Park JY, Trujillo JJ. Controllability of nonlinear fractional dynamical systems. Nonlinear Analysis. 2012; 75(4): 1919–1926.
24. Balachandran K, Kokila J, Trujillo JJ. Relative controllability of fractional dynamical systems with multiple delays in control. Computer and Mathematics with Applications. 2012; 64(10): 3037–3045.
25. Balachandran K, Govindaraj V, Rodriguez-Germ´a L, Trujillo JJ. Controllability of nonlinear higher order fractional dynamical systems. Nonlinear Dynamics. 2013; 71(4): 605–612.
26. Balachandran K, Govindaraj V, Rodriguez-Germ´a L, Trujillo JJ. Controllability results for nonlinear fractional-order dynamical systems. Journal of Optimization Theory and Applications. 2013; 156(1): 33–44.
27. Govindaraj V, George RK. Controllability of Fractional Dynamical Systems using Functional Analytics Approach. Mathematical Control and Related Fields. 2017; 7(4): 537–562.
28. Shah V, Sharma J, George RK. Existence and uniqueness of classical and mild solutions of fractional Cauchy problem with impulses. Malaya J. Mat. 2023; 11(1): 66–79.
29. Sharma J, Malviya G, Shah V. Controllability Analysis of Coal Mill Pulverizer Model. Communications on Applied Nonlinear Analysis. 2025; 32(2s): 580–591.
30. Niemczyk P, Bendtson JD, Andersen P. Derivation and validation of a coal mill model for control. Control Engineering Practice. 2012; 20(5): 519–530.

Advances in Differential Equations and Control Processes 2025, 32(1), 2799.
https://doi.org/10.59400/adecp2799

Article

Rolling optimization control method for hydro-photovoltaic-storage microgrid based on stochastic chance constraints

Qianjin Gui[1,*], Wenfa Xu[1], Xiaoyang Li[1], Lirong Luo[1], Haifeng Ye[2], Zhengfeng Wang[2]

[1] State Grid Anhui Electric Power Co., Ltd. Anqing Power Supply Company, Anqing 246000, China
[2] State Grid Anhui Electric Power Co., Ltd., Hefei 230000, China
*** Corresponding author:** Qianjin Gui, qianjin_gui@126.com

CITATION

Gui Q, Xu W, Li X, et al. Rolling optimization control method for hydro-photovoltaic-storage microgrid based on stochastic chance constraints. Advances in Differential Equations and Control Processes. 2025; 32(1): 2799. https://doi.org/10.59400/adecp2799

ARTICLE INFO

Received: 18 February 2025
Accepted: 3 March 2025
Available online: 11 March 2025

Abstract: Hydro-photovoltaic-storage (HPS) microgrid has gradually become an important measure to optimize the energy structure and ensure the reliability of regional power supply. However, due to the strong randomness and spatiotemporal correlations of hydropower and photovoltaic (PV) output, traditional deterministic optimization methods are difficult to support the accurate regulation and reliable operation of microgrid with a high proportion of renewable energy integration. On this basis, a rolling optimization control method for HPS microgrid based on stochastic chance constraints is proposed. A novel multivariate scenario reduction method considering hydro-PV correlations is presented to characterize the uncertainty of renewable energy output, and a day-ahead stochastic optimal scheduling model based on chance-constrained programming is constructed. Combined with stochastic model predictive control strategies, the day-ahead scheduling plan can be adjusted at multiple time scales, both intraday power compensation and real-time adjustments, to suppress the intraday power fluctuations induced by day-ahead scenario errors and reduce the influence of the uncertainty of hydro-PV power output on microgrid operation. Experimental results show that compared with the traditional deterministic scheduling method, the proposed method can effectively improve the stability and economy of HPS microgrid operation under complex uncertain conditions.

Keywords: hydro-photovoltaic-storage microgrid; stochastic optimal scheduling; correlated uncertainties; multivariate scenario reduction; model predictive control

1. Introduction

In recent years, driven by the construction of new power systems with renewable energy as the main component, the proportion of renewable energy integrated into the grid has gradually increased, significantly alleviating the energy crisis. The hydro-photovoltaic-storage (HPS) microgrid is a new multi-energy complementary power generation system that combines hydropower, photovoltaic (PV) power generation, and energy storage technology, which is an effective way to promote renewable energy consumption, improve energy utilization efficiency, and reduce energy costs [1,2]. However, the strong randomness in hydropower and PV output severely restricts the operational reliability of the microgrid and its support to the regional distribution network. Therefore, optimizing the operation of HPS microgrids under uncertain conditions is crucial for enhancing the power supply reliability and the overall economic benefits of the system.

Compared to the traditional deterministic optimization scheduling methods based on point forecasts, microgrid stochastic optimization scheduling represents the statistical distribution characteristics of renewable sources and loads through a series

of discrete scenarios. It can flexibly address the adverse effects of source-load uncertainty on microgrid scheduling while avoiding the risks brought by the single deterministic decisions as much as possible [3–6]. In Rezaee Jordehi et al. [7], a tri-level stochastic operational planning framework based on renewable energy scenarios was developed for isolated microgrids with hydrogen refueling station integrated energy hubs. In Azizivahed et al. [8], scenario-based stochastic programming was used to handle the uncertainty of wind-solar output in reconfigurable multi-microgrids, and both technical and economic aspects of the microgrid system were improved significantly. To increase the robustness of system operation, Seyedeh-Barhagh et al. [9] and Shaillan et al. [10] proposed the risk-aware stochastic optimal energy management models for the microgrids with PV and wind generation. In Hu and Li [11], a transfer learning-based scenario generation method was adopted to characterize the uncertainty of multiple wind energy sources for the stochastic optimal scheduling of a microgrid with newly built wind farms. Wu et al. [12] presented an improved spectral clustering method for scenario reduction of renewable energy in the stochastic optimal dispatching of the electricity-hydrogen-gas-heat integrated energy system. In Abunima et al. [13], a two-stage stochastic optimization algorithm considering the potential future PV profile in a probability density function form was proposed, which can decrease the operation cost compared to the conventional optimization method considering the worst-case scenarios. Li et al. [14] addressed the uncertainty of wind-solar output in microgrids by constructing a stochastic optimal scheduling model to minimize operating costs and, combined with Conditional Value-at-Risk (CVaR), avoided most risk losses with minimal cost. Jani et al. [15], a two-stage optimization model was established for the stochastic day-ahead and real-time energy management of networked microgrids considering the integration of renewable sources. Moreover, multi-stage stochastic optimization models considering the uncertainty of PV output were proposed to enhance the security of the power supply of microgrids in Aaslid et al. [16] and Kizito et al. [17].

Although the scenario-based stochastic scheduling method is widely used for uncertainty modeling of renewable energy to improve the accuracy of decision results and achieve reliable microgrid operations in uncertain environments, it requires generating a great number of scenarios for decision-making. The number of scenarios increases exponentially with the increase of the scheduling stage, greatly increasing the time costs and solving difficulty. In this aspect, Heitsch and Römisch [18] developed the famous probability distance-based scenario reduction methods, namely fast forward selection (FFS) and simultaneous backward reduction (SBR), which have been adopted to improve the solving efficiency of various practical scheduling problems [19–21]. In Beltran et al. [22], a multistage scenario reduction method based on quadratic process distance was presented for solving the stochastic medium-term hydrothermal scheduling problem. Zhan et al. [23] presented an improved Kantorovich distance-based forward selection method to shorten the time consumption of scenario reduction. Considering the correlations between the renewable energy sources, Hu and Li [24], Hu and Li [25] developed the comprehensive optimal scenario reduction model to minimize the partial correlation loss and maximize the probabilistic similarity degree after the reduction operation. However, existing scenario reduction methods cannot simultaneously preserve the

spatial and temporal correlations of renewable sources, which will have a significant impact on the decision-making reliability and accuracy for HPS microgrid scheduling.

Considering the impact of source-load uncertainty on the stable operation of microgrids, model predictive control (MPC), which adjusts the original plan through rolling optimization and feedback correction, has been widely applied in microgrid optimization scheduling. Zhang et al. [26], Bazmohammadi et al. [27] considered the randomness of loads and the uncertainty of wind-solar output, combining MPC with scenario analysis methods, and proposed an optimization scheduling strategy for microgrids based on stochastic MPC. Jiao et al. [28] adopted robust stochastic MPC with different granularity models to handle source-load uncertainty and established a two-stage optimal scheduling framework for microgrids, improving computational efficiency and economic performance. Lin et al. [29], Wei et al. [30] developed the scenario-based stochastic model predictive control approach for microgrid operation under uncertainties to balance the computational efficiency, robustness and economy of the scheduling results. However, although extensive studies have been conducted on the optimal scheduling of microgrids under uncertain conditions, there are relatively few studies that simultaneously consider the uncertainty of hydropower and PV output, especially the spatial and temporal correlations between hydro-PV power output. Moreover, the existing studies on the optimization scheduling of HPS microgrids only focused on the day-ahead scheduling stage, without considering the impact of scenario errors on the scheduling results. In the actual scheduling process, the real-time changes in hydro-solar power output and user loads will affect the stability and economic operation of HPS microgrids, which still requires further research.

In light of the above, the main contributions of this paper are summarized as follows:

(1) A multi-timescale rolling optimization control method for an HPS microgrid based on stochastic model predictive control is proposed. In the day-ahead scheduling stage, a stochastic optimal scheduling model for the HPS microgrid based on chance-constrained programming is constructed to obtain a reference scheduling plan. Based on a stochastic model predictive control strategy, a closed-loop scheduling is conducted through rolling optimization and feedback correction across multiple time scales, including intraday power compensation optimization and real-time power adjustments. Experimental results indicate that the proposed method can not only minimize the power fluctuations caused by day-ahead scenario errors but also effectively suppress the impact of hydro-PV power uncertainty on the stable and economic operation of the HPS microgrid.

(2) To improve the solving efficiency of HPS microgrid scheduling models, a multivariate scenario reduction method considering the correlations between hydro-PV output is proposed. It aims to maximize the probability similarity of the original scenario sets and the preserved scenario set, and minimize the temporal and spatial correlation loss of hydro-PV output scenarios before and after scenario reduction. A comprehensive optimal scenario reduction model is constructed, and the overall process of iterative scenario reduction is provided based on the optimal redistribution rule. The simulation results show that the proposed method can preserve the statistical

characteristics of the reduced scenario to the greatest extent possible, and effectively improve the decision reliability and accuracy of HPS microgrid scheduling.

The rest of this paper is organized as follows: In Section 2, a multi-time scale optimal scheduling model for the HPS microgrid is proposed, and the stochastic MPC strategy involved in the rolling optimization process is also presented. The multivariate scenario reduction method considering spatiotemporal correlations among sources is developed in Section 3. The experimental results are discussed in Section 4. Finally, the conclusions are drawn in Section 5.

2. Multi-time scale optimal scheduling method for HPS microgrid

2.1. Description of HPS microgrid system

The structure of the grid-connected HPS microgrid in this study is shown in **Figure 1**. The entire system consists of a small hydropower station, distributed photovoltaic (PV) generation units, a hybrid energy storage system, and user loads. Given the high randomness and volatility of hydropower and PV output, the hybrid energy storage system includes two components: Batteries and supercapacitors. The batteries are served as energy-type storage devices, which can store a large amount of electrical energy and are suitable for power response with slow changes. On the other hand, the supercapacitors are power-type storage devices, which are capable of rapid charging and discharging, to provide a fast response to power fluctuations. Both batteries and supercapacitors leverage the complementary advantages of power variation.

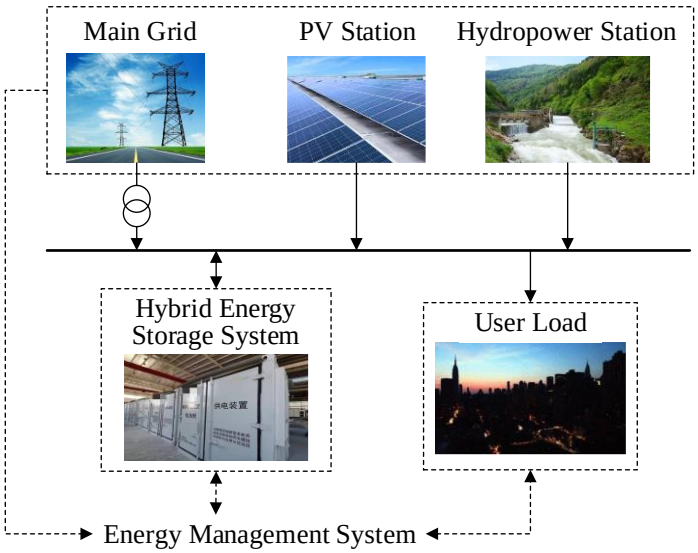

Figure 1. Structure of the HPS microgrid.

In the grid-connected mode of the HPS microgrid, if there is still surplus hydro-PV power output after meeting the load at a certain moment, the excess power will be stored in the battery. If the hydro-PV power output is insufficient to meet the load demand, it is necessary to consider purchasing electricity from the external network. If the hydro-PV output meets the load demand and the battery for energy storage is fully charged, the remaining power can be sent into the main grid. Based on the above,

the optimal scheduling problem of the HPS microgrid is grounded in the uncertain representative scenarios of PV power output, hydropower output, and load demand to reasonably arrange the charging and discharging power of the hybrid energy storage system as well as the interaction power between the HPS microgrid and the external grid.

2.2. Day-ahead stochastic chance-constrained programming model

The energy-optimal scheduling model for the HPS microgrid aims to minimize the total operating costs, which include the total operation and maintenance costs of the system C_{om}, battery depreciation and degradation costs C_{B}, and the energy interaction cost between the microgrid and the main grid C_{G}. Considering the randomness and correlation of the hydropower and PV power outputs within the microgrid, the spatiotemporal correlated scenarios for hydro-PV power outputs are generated by using the scenario generation and reduction methods introduced in Section 3. This method enables the characterization of the uncertainty in hydro-PV power output, and the day-ahead optimization scheduling model is constructed as a chance-constrained programming, with the objective function as follows:

$$\min_{P_{\text{B}},P_{\text{G}}} C_{\text{total}} = \sum_{t=1}^{T}(C_{\text{om}} + C_{\text{B}} + C_{\text{G}}) \tag{1}$$

where C_{total} is the total operating cost of the HPS microgrid system, and can be calculated as follows:

$$C_{\text{om}} = \sum_{s=1}^{S} \rho_{\text{s}} [C_{\text{PV}} P_{\text{PV}}^{s}(t)\Delta t + C_{\text{HE}} P_{\text{HE}}^{s}(t)\Delta t] + C_{\text{CN}} P_{\text{B}}(t)\Delta t \tag{2}$$

$$C_{\text{B}} = [k_s(1-\eta_{\text{Bc}})P_{\text{Bc}}(t)\Delta t] + [k_s(1-\eta_{\text{Bd}})P_{\text{Bd}}(t)\Delta t] \tag{3}$$

$$C_{\text{G}} = \begin{cases} C_{\text{p}}(t)P_{\text{G}}(t)\Delta t, & P_{\text{G}}(t) \geqslant 0 \\ C_{\text{s}}(t)P_{\text{G}}(t)\Delta t, & P_{\text{G}}(t) < 0 \end{cases} \tag{4}$$

here, ρ_{s} is the occurring probability corresponding to scenario s. S is the total number of scenarios. T is the number of scheduling periods. C_{PV} is the maintenance cost per unit of photovoltaic power. $P_{\text{PV}}^{s}(t)$ is the photovoltaic generation power at time t under scenario s; C_{HE} is the maintenance cost per unit of hydro power; $P_{\text{HE}}^{s}(t)$ is the output power of small hydropower station at time t under scenario s; C_{CN} is the maintenance cost per unit of battery charging and discharging power; $P_{\text{B}}(t)$ is the charging and discharging power of the battery at time t; k_{s} is the coefficient of battery depreciation and degradation cost; η_{Bc} and η_{Bd} are the charging and discharging efficiencies of the battery, respectively; $P_{\text{Bc}}(t)$ and $P_{\text{Bd}}(t)$ are the charging and discharging power of the battery, respectively; $C_{\text{p}}(t)$ and $C_{\text{s}}(t)$ are the purchasing and selling electricity prices at time t for HPS microgrid system; $P_{\text{G}}(t)$ is the

interaction power between the HPS microgrid system and the main power grid at time t.

The established day-ahead stochastic optimization of the HPS microgrid needs to satisfy the following constraints:

(1) Power balance constraint

$$\Pr\{P_{\mathrm{G}}(t)-P_{\mathrm{B}}(t)+P_{s}^{\mathrm{PV}}(t)+P_{s}^{\mathrm{HE}}(t)\geqslant P_{\mathrm{L}}(t)\}\geqslant \vartheta \tag{5}$$

where $\Pr\{\cdot\}$ represents the occurring probability of the event; $P_{\mathrm{L}}(t)$ denotes the user load at time t; ϑ is the confidence level of the chance constraint. Stochastic chance constraint programming adopts the principle that the final decision is allowed to fail to satisfy the constraint to a certain extent (i.e., the constraint of unfavorable cases is not satisfied), while ensuring that the probability of the constraint being valid is not less than a certain confidence level. The chance-constrained programming does not meet the constraint conditions and does not incur any penalty. There is no need to introduce compensation, but the constraint conditions are established with a certain probability, thus reducing the conservatism of constraints and better realizing decision-making under uncertain conditions.

(2) Upper and lower limit constraint of battery power

$$P_{\mathrm{B,max}}^{\mathrm{d}}\leqslant P_{\mathrm{B}}(t)\leqslant P_{\mathrm{B,max}}^{\mathrm{c}} \tag{6}$$

where $P_{\mathrm{B,max}}^{\mathrm{d}}$ and $P_{\mathrm{B,max}}^{\mathrm{c}}$ are the maximum discharging power and maximum charging power of the battery, respectively.

(3) State of charge constraint of battery

$$S_{\mathrm{B}}^{\min}\leqslant \frac{E_{\mathrm{B}}(t)}{E_{\mathrm{BA}}(t)}\leqslant S_{\mathrm{B}}^{\max} \tag{7}$$

where $S_{\mathrm{B}}^{\min}$ and $S_{\mathrm{B}}^{\max}$ are the lower and upper limits of the battery state of charge, respectively. $E_{\mathrm{BA}}(t)$ is the actual capacity of the battery at time t. $E_{\mathrm{B}}(t)$ denotes the energy storage of the battery at time t, and can be calculated as:

$$E_{\mathrm{B}}(t)=\begin{cases} E_{\mathrm{B}}(t-1)-P_{\mathrm{B}}(t)\Delta t\eta_{\mathrm{Bc}}, & P_{\mathrm{B}}(t)>0 \\ E_{\mathrm{B}}(t-1)-\dfrac{P_{\mathrm{B}}(t)\Delta t}{\eta_{\mathrm{Bd}}}, & P_{\mathrm{B}}(t)\leqslant 0 \end{cases} \tag{8}$$

(4) Purchasing and selling power constraint

$$P_{\mathrm{G,min}}\leqslant P_{\mathrm{G}}(t)\leqslant P_{\mathrm{G,max}} \tag{9}$$

where $P_{\mathrm{G,min}}$ and $P_{\mathrm{G,max}}$ are the lower and upper limits of the interaction power between the HPS microgrid system and the main grid, respectively.

2.3. Intraday power compensation model

Considering the impact of potential scenario errors in hydro-PV outputs during the day-ahead scheduling stage, the intraday rolling optimization of the HPS microgrid

firstly assesses whether the day-ahead scheduling strategy can track the output within 4 h based on ultra-short-term forecast values. If the day-ahead strategy cannot effectively track the output, a deterministic intraday power compensation model is constructed with the objective of minimizing power adjustment costs. The objective function is calculated as:

$$\min_{P_{\mathrm{B}},P_{\mathrm{G}},P_{\mathrm{sc}}} C_{\mathrm{in}} = \sum_{t=1}^{T_{\mathrm{in}}} [\lambda_{\mathrm{B}} \Delta P_{\mathrm{B}}(t) + \lambda_{\mathrm{G}} \Delta P_{\mathrm{G}}(t) + C_{\mathrm{sc}}(t)] \tag{10}$$

where C_{in} denotes the intraday power adjustment cost of the HPS system. λ_{B} and λ_{G} are the cost coefficients for the battery power adjustment and interaction power adjustment with the main grid, respectively. $\Delta P_{\mathrm{B}}(t)$ and $\Delta P_{\mathrm{G}}(t)$ denote adjustment amounts for the battery power and the interaction power with the main grid at time t, respectively. $C_{\mathrm{sc}}(t)$ is the depreciation and degradation costs of supercapacitor at time t, which is calculated as [31]:

$$C_{\mathrm{sc}} = \frac{R_{\mathrm{sc}} \Delta t}{T_{\mathrm{sc}}} \tag{11}$$

where T_{sc} is the overall lifespan of the supercapacitor. R_{sc} denotes the replacement cost of the supercapacitor. In addition to satisfying the above constraints Equations (6)–(9), the intraday optimization of the HPS microgrid system should also satisfy the following constraints:

(1) Power balance constraint

$$P_{\mathrm{L}}(t) = P_{\mathrm{PV}}(t) + P_{\mathrm{HE}}(t) + P_{\mathrm{G}}(t) - P_{\mathrm{B}}(t) - P_{\mathrm{sc}}(t) \tag{12}$$

where $P_{\mathrm{PV}}(t)$ and $P_{\mathrm{HE}}(t)$ are the ultra-short-term forecast values of PV power generation and hydropower generation at time t, respectively. $P_{\mathrm{sc}}(t)$ denotes the charging or discharging power of the supercapacitor at time t.

(2) Upper and lower limit constraint of supercapacitor power

$$P_{\mathrm{sc,max}}^{\mathrm{d}} \leqslant P_{\mathrm{sc}}(t) \leqslant P_{\mathrm{sc,max}}^{\mathrm{c}} \tag{13}$$

where $P_{\mathrm{sc,max}}^{\mathrm{d}}$ and $P_{\mathrm{sc,max}}^{\mathrm{c}}$ are the maximum discharging power and maximum charging power of supercapacitor, respectively.

(3) State of charge constraint of supercapacitor

$$S_{\mathrm{sc}}^{\min} \leqslant \frac{E_{\mathrm{sc}}(t)}{E_{\mathrm{sc,r}}(t)} \leqslant S_{\mathrm{sc}}^{\max} \tag{14}$$

where $S_{\mathrm{sc}}^{\min}$ and $S_{\mathrm{sc}}^{\max}$ are the lower and upper limits of the supercapacitor state of charge, respectively. $E_{\mathrm{sc,r}}(t)$ is the actual capacity of the supercapacitor at time t. $E_{\mathrm{sc}}(t)$ denotes the energy storage of the supercapacitor at time t, and can be calculated as:

$$E_{\mathrm{sc}}(t)=\begin{cases} E_{\mathrm{sc}}(t-1)-P_{\mathrm{sc}}(t)\Delta t\eta_{\mathrm{scc}}, & P_{\mathrm{sc}}(t)>0 \\ E_{\mathrm{sc}}(t-1)-\dfrac{P_{\mathrm{sc}}(t)\Delta t}{\eta_{\mathrm{scd}}}, & P_{\mathrm{sc}}(t)\leqslant 0 \end{cases} \tag{15}$$

where η_{scc} and η_{scd} are the charging and discharging efficiencies of the supercapacitor, respectively.

2.4. Real-time optimization scheduling

In the real-time optimization scheduling of the hydro-photovoltaic-storage microgrid, the current measured photovoltaic power, hydropower, and state of charge of the energy storage system are used to determine whether the current energy storage operation strategy can track the reported power of the hydro-photovoltaic-storage system. If it cannot track, efforts are made to minimize the difference between the combined output of the hydro-photovoltaic-storage system and the target output within the operating constraints of the energy storage system. The specific process is illustrated in **Figure 2**.

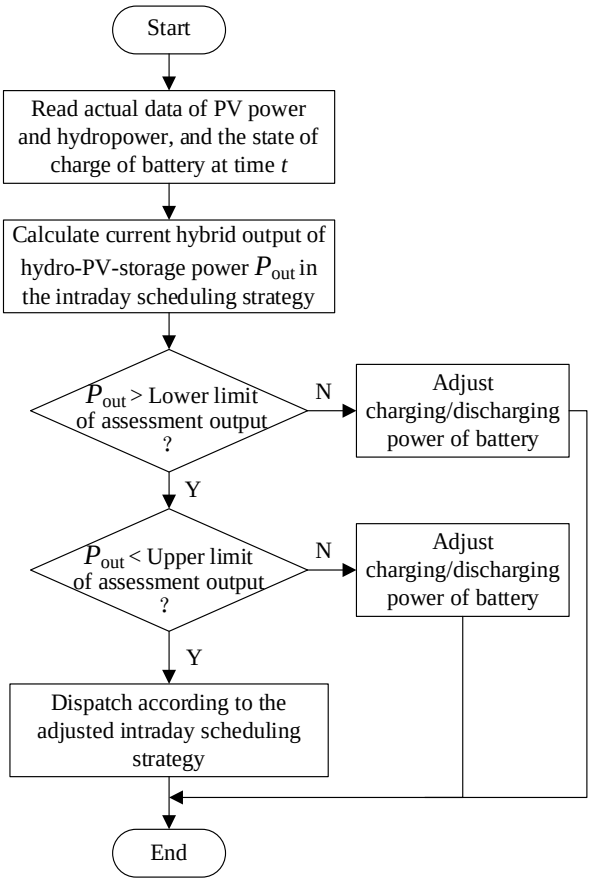

Figure 2. Real-time scheduling process of HPS microgrid.

Firstly, the actual data of PV power $P_t^{\mathrm{PV,real}}$ and hydropower $P_t^{\mathrm{HE,real}}$ at the current time t are input into the real-time scheduling process, as well as the state of charge of battery SOC_t^{real}. The battery's maximum charging power $P_t^{B,\mathrm{ch,max}}$ and the maximum

discharging power $P_t^{B,\mathrm{dis,max}}$ at current time t are calculated based on SOC_t^{real}. The combined power output of hydro-PV-storage can be calculated based on $P_t^{\mathrm{PV,real}}$, $P_t^{\mathrm{HE,real}}$ and the obtained intraday rolling optimization strategy. If the current combined output P_{out} is less than the lower limit of assessment output, it indicates that the hydro-PV-storage output is low and the discharging power of the battery is necessary to be increased. If the current combined output P_{out} exceeds the upper limit of assessment output, it indicates that the hydro-PV-storage output is high, and the charging power of the energy storage system needs to be increased. If the current combined output P_{out} falls within the range of assessment output, the obtained optimization strategy can be conducted in the real-time scheduling process.

2.5. Multi-timescale rolling optimization based on MPC

MPC is a model-based closed-loop optimization control strategy, and the core idea is rolling optimization in a finite time domain. Considering that the scenario errors of hydropower and PV power output decrease with the shortening of the time scale, the optimization scheduling of HPS microgrids is divided into three stages: 1) Day-ahead stochastic optimization; 2) intraday power compensation optimization; and 3) real-time rolling correction. A multi-time scale rolling optimization scheduling framework for HPS microgrids is established, as shown in **Figure 3**.

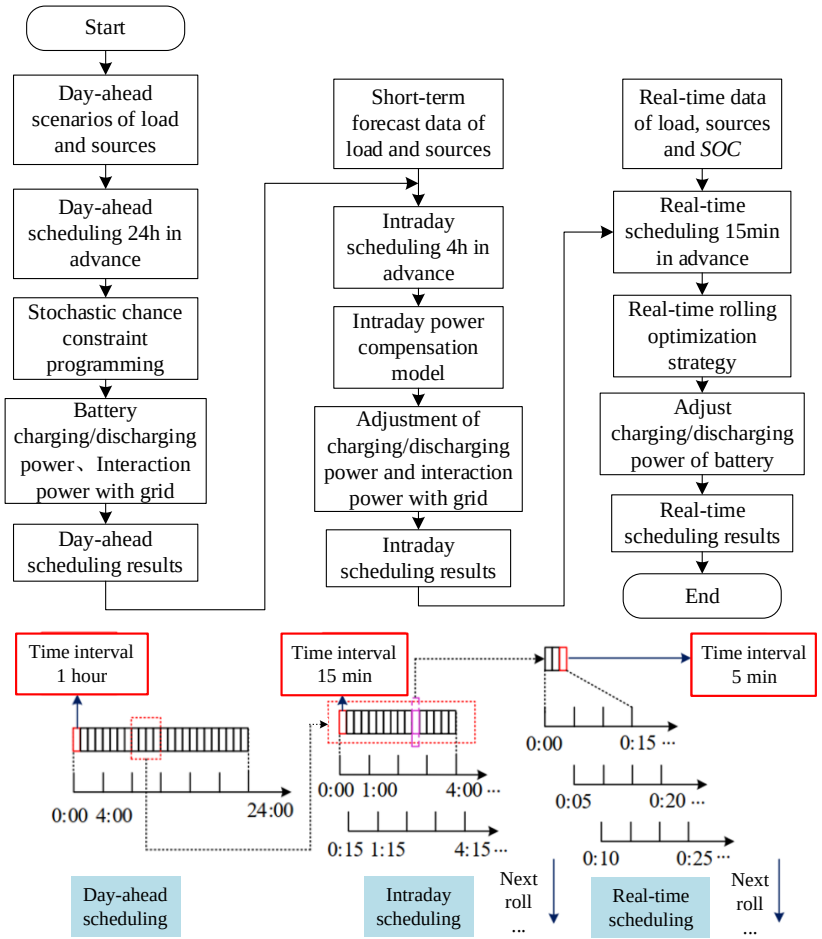

Figure 3. Multi-time scale rolling optimization framework for HPS microgrid.

In the day-ahead stochastic scheduling stage, a scheduling plan is developed 24 h in advance based on the typical scenario set of hydro-PV power with a time interval of 1h. With the lowest total operating cost of the system as the optimization goal, the charging and discharging power of the battery and the interactive power with the main grid are optimized for scheduling, and the scheduling plan for each hour of the next day is formulated. Then, the plan is released in advance as a definite value so that the operation state of each piece of equipment in the HPS microgrid is regulated according to the reference plan in the day-ahead scheduling stage.

In the intraday power compensation scheduling stage, in order to eliminate the deviation between the day-ahead reference plan and the actual intraday scheduling plan caused by scenario errors as far as possible, the intraday scheduling plan is updated every 15 min. Each rolling optimization inputs the ultra-short-term forecasting information of load, PV and hydropower outputs over the subsequent time periods. The revised 4-hour scheduling plan is optimized using MPC, with the objective of minimizing the power adjustment costs, resulting in an adjusted plan for the charging/discharging power of supercapacitors and interaction power with the main grid for the corresponding time period. Only the revised plan for the next time period is issued at this time interval. When the next scheduling cycle arrives, the above process is repeated to determine the intraday scheduling plan, which is then used as deterministic inputs in the real-time scheduling stage.

In the real-time scheduling stage, the scheduling plan is updated every 5 min based on the real-time information of renewable sources and load. After each rolling optimization, the scheduling plan is optimized for the next 15 min to correct the deviation between the previous intraday scheduling plan and the real-time conditions, modifying the charging and discharging power and interaction power. Through the MPC-based rolling optimization and feedback correction, the impact of uncertain hydropower and photovoltaic outputs on the reliable and stable operation of the microgrid is mitigated.

3. Representative scenario generation and reduction method

3.1. Scenario generation for correlated hydro-PV power

In this study, due to the non-normal probabilistic distribution for hydropower and PV power output, as well as the spatial and temporal correlations between renewable sources, the original distribution space should firstly be mapped to an independent standard normal distribution space to obtain discrete samples [32]. Afterwards, Cholesky decomposition and inverse transformation can be used to generate multivariate scenarios with specific correlations [33]. Suppose that $\mu_i\ (i=1,\cdots,m)$ denotes the m random variables, such as hydropower and PV power output, corresponding to various units; Λ_μ is the correlation matrix of the random variables. The specific scenario generation process can be summarized as follows:

1) Transform Λ_μ into the standardized correlation matrix Λ_v using the numerical search algorithm in Qin et al. [33]. Here, $v_i\ (i=1,\cdots,m)$ is consistently following a standard normal distribution;

2) Produce several n-dimensional samples whose elements follow a standard normal distribution and are independent of each other for each vector *V*;
3) Adopt Cholesky decomposition to factorize Λ_υ as $\Lambda_\upsilon = \Sigma\upsilon\Sigma_\upsilon^\top$ and obtain the correlated samples following normal distribution based on $\upsilon = \Sigma_\upsilon V$. Here, the elements in *V* are consistent with the correlations in Λ_υ;
4) Suppose that $F_{\mu_i}^{-1}$ is the inverse function and $\Phi(\upsilon_i)$ denotes the corresponding non-normal cumulative distribution of υ_i, the correlated scenarios of μ_i can be generated from the resultant υ_i in Step (3) based on the inverse transformation $\mu_i = F_{\mu_i}^{-1}[\Phi(\upsilon_i)]$ $(i = 1, \cdots, m)$.

3.2. Multivariate scenario reduction considering hydro-PV correlations

Due to the fact that the computational complexity of solving the stochastic programming model largely depends on the number of scenarios being studied, it is necessary to use scenario reduction methods to eliminate possible redundancies in the generated scenarios, thereby improving the efficiency of problem solving, especially in the large-scale systems. Unlike traditional probability distance-based scenario reduction techniques, this paper proposes an optimization-based scenario reduction model to determine the most representative scenario from the original scenario set. The goal is to maximize the sum of probability similarities between the original and reduced sets in the statistical space while minimizing the sum of correlation loss in both spatial and temporal scales after scenario reduction. The corresponding mathematical description is constructed as follows:

$$\begin{aligned} &\max_{I_{\tilde{\tau}}, \tilde{S}_{\tilde{\tau}}} \sum_{\tilde{\tau} \in \tilde{\Omega}_1} \sum_{\tau \in I_{\tilde{\tau}}} \left[Sim(s_\tau, \tilde{s}_{\tilde{\tau}}) - \beta corrloss_{S,T}(s_\tau, \tilde{s}_{\tilde{\tau}}) \right] \\ &\text{s.t.} \bigcup_{s_\tau, \tilde{s}_{\tilde{\tau}}} I_{\tilde{\tau}} = \Omega_1, \\ &\quad \sum_{\tau \in \Omega_1} p_\tau = 1, \\ &\quad I_{\tilde{\tau}} \cap I_{\tilde{\tau}'} = \varnothing, \ \forall \tilde{\tau} \neq \tilde{\tau}', \ \tilde{\tau}, \tilde{\tau}' \in \tilde{\Omega}_1 \end{aligned} \tag{16}$$

where Ω_1 denotes the original scenario set with the size of N_1. Ω_1 consists of the original scenario s_τ with the corresponding occurring probability p_τ. τ is the scenario node in Ω_1, and the correlation matrices in the spatial and temporal scales are $\Lambda_{\mu,\,space}$ and $\Lambda_{\mu,time}$, respectively. $\tilde{\Omega}_1$ is the reduced scenario set with the size of $\tilde{N}_1$. $\tilde{\Omega}_1$ consists of the preserved scenario $\tilde{s}_{\tilde{\tau}}$ corresponding to the occurring probability $\tilde{p}_{\tilde{\tau}}$. $\tilde{\tau}$ is the scenario node in $\tilde{\Omega}_1$. For $\tilde{\Omega}_1$, the correlation matrices in the spatial and temporal scales are $\tilde{\Lambda}_{\mu,\,space}$ and $\tilde{\Lambda}_{\mu,time}$, respectively. $I_{\tilde{\tau}}$ is the clustering subset divided by τ. The node $\tilde{\tau}$ can then be adopted to substitute the original nodes in $I_{\tilde{\tau}}$. Moreover, $Sim(\cdot)$ in Equation (16) denotes the probability similarity function, which is presented in Hu and Li [24] and used to measure the similarity degree of the reduced scenarios and the original scenarios, which can be calculated as follows:

$$Sim(s_i, s_j) = \frac{1}{n}\left[\sum_{k=1}^{n}\left(1 - \frac{p_i p_j}{p_i + p_j}\frac{|s_i^k - s_j^k|}{\left|\max\limits_{1\leqslant l\leqslant n}\{s_l^k\} - \min\limits_{1\leqslant l\leqslant n}\{s_l^k\}\right| + \varepsilon}\right)\right] \quad (17)$$

where k $(k=1, \cdots, n)$ corresponds to the *k*-th random variable in the scenario vector s_i (corresponding to the occurring probability p_i) and s_j (corresponding to the occurring probability p_j) of the n-dimensional scenario set with the size of N_1. ε is a very small constant that prevents molecules of fractions from being divided by 0. The larger the value of *Sim*, the greater the probability of similarity between the reduced scenarios and the original scenarios in the overall probability space.

Furthermore, $corrloss_{S,T}(\cdot)$ in Equation (16) denotes the correlation loss in both spatial and temporal scales between the preserved scenario set and the initial scenario set. It can be calculated as the sum of squares of the upper triangular elements in the spatial and temporal correlation deviation matrices $\Delta\Lambda_{spatial}$ and $\Delta\Lambda_{temporal}$, which are based on the calculation of Pearson correlation coefficients. In previous studies [24], it is known that the correlation between multiple random variables can nontrivially change the structure of the feasible region in MSVP so that the obtained programming results will be affected under different correlation levels. It is crucial to capture the correlation between random variables and introduce the correlations into the programming model reasonably, because even accurate solving and analyzing methods cannot compensate for the inaccurate scenario input. Therefore, the proposed metric of correlation loss in this paper is crucial, which can reflect the change of correlation before and after scenario reduction. From the perspective of approximating the solution results of MSVP before scenario reduction, it is meaningful to retain the correlation of the original scenario set (i.e., correlation loss is as small as possible), which has also been shown in the simulation analysis in the paper. Therefore, correlation loss is a good metric to characterize the multi-stochastic variable case.

Suppose the spatial dimension of hydro-PV generation units is *S*, the temporal dimension of hydro-PV power output to be considered is *T*, the calculation formula of total correlation loss can be calculated as follows:

$$\Delta\Lambda_{spatial} = \Lambda_{spatial} - \tilde{\Lambda}_{spatial} = \begin{bmatrix} 0 & \Delta\rho_{12} & \cdots & \Delta\rho_{1S} \\ \Delta\rho_{21} & 0 & \cdots & \Delta\rho_{2S} \\ \vdots & \vdots & \ddots & \vdots \\ \Delta\rho_{S1} & \Delta\rho_{S2} & \cdots & 0 \end{bmatrix} = (\Delta\rho_{ij})_{S\times S},\ (i,j=1, \cdots, S) \quad (18)$$

$$\Delta\Lambda_{temporal} = \Lambda_{temporal} - \tilde{\Lambda}_{temporal} = \begin{bmatrix} 0 & \Delta\hat{\rho}_{12} & \cdots & \Delta\hat{\rho}_{1T} \\ \Delta\hat{\rho}_{21} & 0 & \cdots & \Delta\hat{\rho}_{2T} \\ \vdots & \vdots & \ddots & \vdots \\ \Delta\hat{\rho}_{T1} & \Delta\hat{\rho}_{T2} & \cdots & 0 \end{bmatrix} = (\Delta\hat{\rho}_{ij})_{T\times T},\ (i,j=1, \cdots, T) \quad (19)$$

$$corrloss_{S,T}(s, \tilde{s}) = \sum_{i=1}^{S-1}\sum_{j=i+1}^{S}(\Delta\rho_{ij})^2 + \sum_{i=1}^{T-1}\sum_{j=i+1}^{T}(\Delta\hat{\rho}_{ij})^2 \quad (20)$$

here, $\Lambda_{spatial}$ and $\Lambda_{temporal}$ are the spatial and temporal correlation matrices of the original scenario set, respectively. $\tilde{\Lambda}_{spatial}$ and $\tilde{\Lambda}_{temporal}$ are the spatial and temporal correlation matrices of the reduced scenario set, respectively. ρ_{ij} is the spatial Pearson correlation coefficient of various renewable energy sources, and $\hat{\rho}_{ij}$ is the autocorrelation coefficient in the temporal scale of each unit. The value of $corrloss_{S,T}(s,\tilde{s})$ represents the deviation degree of spatial and temporal correlations between the preserved scenarios s in $\tilde{\Omega}_1$ and the original scenarios $\tilde{s}$ in Ω_1. The smaller the value of $corrloss_{S,T}(s,\tilde{s})$ is, the better the original correlation properties are to be preserved in $\tilde{\Omega}_1$ after the reduction operation.

β in Equation (16) denotes the correlation weight. A smaller β can select the preserved scenarios with high probability similarity but relatively large spatiotemporal correlation loss after reduction, while a larger β can ensure a high degree of correlation preservation in the original scenarios but low probability similarity. Therefore, by adjusting the value of β reasonably, an appropriate balance can be achieved between the two objectives in the scenario reduction process. In general, β takes the value of 0.5 to make a balance of the two goals. Then, the representative scenarios can be produced by conducting the following reduction operations:

1) Calculate the probability similarity matrix $SIM_{N_1\times N_1}$. Each element $SIM(i,j)$ in the matrix corresponds to the probability similarity $Sim(s_i,s_j)$ of the original scenarios s_i and s_j by Equation (17);
2) Compute the spatiotemporal correlation loss after reducing the scenarios s_i and s_j by Equations (18)–(20), and then the correlation loss matrix $CorrLoss_{N_1\times N_1}$ can be obtained by $CorrLoss(i,j)=corrloss(s_{(s_i,s_j)},\tilde{s})$. The preserved scenarios $\tilde{s}$ without s_i and s_j is in reference to the original scenarios $s_{(s_i,s_j)}$;
3) Normalize the elements in $SIM_{N_1\times N_1}$ and $CorrLoss_{N_1\times N_1}$ based on Equations (21) and (22), and obtain matrices $SIM'_{N_1\times N_1}$ and $CorrLoss'_{N_1\times N_1}$;

$$SIM'(i,j)=\frac{Sim(s_i,s_j)-SIM_{\min}}{SIM_{\max}-SIM_{\min}} \tag{21}$$

$$CorrLoss'(i,j)=\frac{corrloss(s_i,s_j)-CorrLoss_{\min}}{CorrLoss_{\max}-CorrLoss_{\min}} \tag{22}$$

4) Construct the comprehensive objective matrix $SIMCorr_{N_1\times N_1}$ by $SimCorr(i,j)=SIM'(i,j)-\beta CorrLoss'(i,j)$;
5) Find the optimal scenario pair (s_i,s_j) to be reduced corresponding to the maximum value in $SIMCorr_{N_1\times N_1}$;
6) As illustrated in **Figure 4**, merge the two optimal scenarios s_i (with probability p_i) and s_j (with probability p_j) into a new scenario s_{new} (with probability p_{new}) based on the optimal redistribution rule as follows [24]:

$$s_{new} = \frac{p_i s_i + p_j s_j}{p_i + p_j} \tag{23}$$

$$p_{new} = p_i + p_j \tag{24}$$

7) Replace the selected scenario pair (s_i, s_j) to s_{new} and the preserved scenario set $\tilde{\Omega}_1$ is refined. The size of $\tilde{\Omega}_1$ is then be decreased by one;
8) Conduct the iterative reduction on the scenario set and go back to Step (1) until the size of $\tilde{\Omega}_1$ is equal to the prespecified value $\tilde{N}_1$.

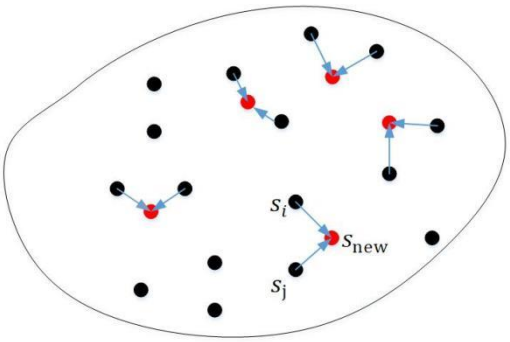

Figure 4. Illustration of optimal redistribution rule for scenario reduction.

The solution process of model (16) is similar to the process of solving scenarios with minimized Kantorovich distance in fast forward selection and simultaneous backward reduction in Heitsch and Römisch [18]. It is a recursive process. As the scale of the scenario set increases, especially for thousands of scenarios, the complexity of solving the reduction model will be greatly increased. The advantages and significance of the proposed method are more focused on the fact that the solution results by our method can achieve a closer accuracy to the solution results obtained in the original scenario set under the same degree of reduction (cutting down the same number of scenarios) compared with other methods.

4. Results and analysis

In this section, the basic data description and parameter settings for the HPS microgrid scheduling are firstly provided. Then, the performance of representative scenarios obtained by the proposed spatiotemporal scenario reduction method is compared with several typical methods. Finally, the HPS microgrid scheduling results of the constructed multi-time scale optimization model are analyzed in detail.

4.1. Data description and parameter settings

In the case study, the HPS microgrid system consists of two photovoltaic generator units, a small hydropower generator unit, a battery energy storage device, a supercapacitor energy storage device, and user loads. In grid-connected mode, the HPS microgrid can interact with the main grid for energy exchange, selling or purchasing electrical energy. The total capacity of the battery energy storage device is 200 kWh, with a rated charging and discharging power of 20 kW, and maximum and

minimum state of charge (SOC) values of 0.9 and 0.1, respectively. The charging/discharging efficiency is 82%, and the unit energy degradation cost for the battery is 6000 ¥/kWh. The supercapacitor energy storage device has a total capacity of 150 kWh, a rated charge and discharge power of 10 kW, and maximum and minimum SOC values of 0 and 1, respectively. The charging/discharging efficiency is 92%, and the unit energy degradation cost for the supercapacitor is 36,000 ¥/kWh. The upper and lower limits of the interaction power between the HPS microgrid system and the main grid are ±300 kW. During peak hours 8:00–16:00 and 18:00–22:00, the purchase and sale prices of electricity are 1.322 ¥/kWh and 0.661 ¥/kWh, respectively. During off-peak hours 6:00–8:00 and 16:00–18:00, the purchase and sale prices are 0.832 ¥/kWh and 0.416 ¥/kWh, respectively. During the valley period 22:00–6:00, the purchase and sale prices are 0.369 ¥/kWh and 0.185 ¥/kWh, respectively. The confidence level for the day-ahead stochastic chance constraint ϑ is set to 0.8.

The proposed optimal scheduling model for the HPS microgrid based on stochastic chance constraints is constructed using MATLAB and solved using the Genetic Algorithm toolbox and CPLEX solver. All experiments are implemented on a DELL PC equipped with an Intel Core i7-6700 CPU(3.4GHz) and 8GB of RAM.

4.2. Evaluation of scenario reduction results

During the day-ahead stochastic scheduling stage of HPS microgrid, based on historical data of hydropower, PV power output and user load, 50 representative scenarios with spatial and temporal correlations are produced through the initially generated scenario set with the size of 1000 and the proposed scenario reduction method. The time-series scenario of the net load power for the HPS microgrid is calculated and shown in **Figure 5**.

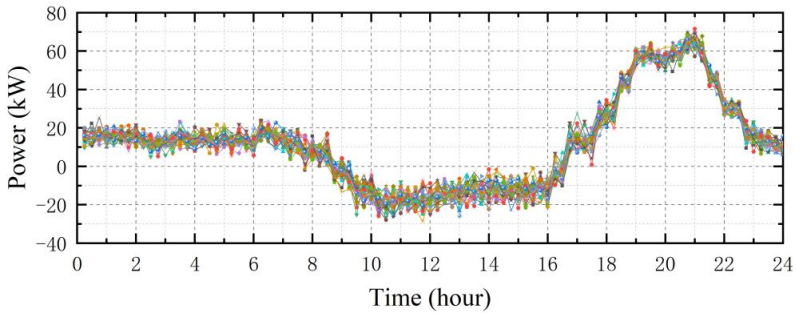

Figure 5. Representative scenarios of daily net load of HPS microgrid.

In order to evaluate the performance of the proposed scenario reduction method, the statistical deviations (e.g., mean, standard deviation, median, skewness and kurtosis) between the reduced scenario set and the original scenario set by our method are compared with the results of other typical reduction methods, including FFS [18], SBR [18], and Sim&Corrloss [24]. Different from the Sim&Corrloss method, the proposed method reasonably takes both spatial and temporal correlations into account in the calculation of the correlation loss function, thereby preserving the specific correlation characteristics of original scenarios in the reduction process. As the degree of scenario reduction increases, the physical characteristics of the reduced scenario set will inevitably deviate from the original scenario set. From the comparative statistical

deviation results in **Table 1**, compared with other methods, the proposed method can always achieve the smallest deviation between the reduced scenario set and the original scenario set for various statistical indicators. It can indicate that the introduction of a spatiotemporal correlation loss term in the comprehensive reduction model can effectively preserve the essential characteristics of the scenarios, thus having more advantages in preserving the statistical features of the scenario input space for solving the HPS microgrid stochastic scheduling model.

Table 1. Statistical deviation results of the reduced scenarios under different methods.

Statistics	FFS [18]	SBR [18]	Sim&Corrloss [24]	The proposed method
Mean	0.538	0.349	0.265	0.224
St. dev	0.240	0.187	0.159	0.086
Median	0.916	0.705	0.433	0.271
Skewness	0.393	0.352	0.314	0.280
Kurtosis	0.759	0.643	0.372	0.311

Moreover, the comparative results of the decision deviation degrees in the reduced scenarios under different methods are listed in **Table 2**. The decision deviation degree (i.e., the battery power and the interaction power with the main grid) obtained by using the proposed method is the lowest among the four methods. It indicates that compared with other scenario reduction methods, using a probability similarity function and comprehensive spatial-temporal correlation loss for scenario fusion can better ensure that the decision output is correct and effective as much as possible. On this basis, the deviation degree of the objective function value (i.e., total scheduling cost) obtained by the proposed method is the closest to the actual objective value before reduction among these methods, indicating that preserving the correlation between hydro-PV power outputs in the reduced scenario can greatly improve the approximation effect of the objective function value of the decision output space. It is necessary to consider both temporal and spatial correlation characteristics in the scenario reduction process. Therefore, the comprehensive scenario reduction method proposed in this paper is effective and can make the decision results for HPS microgrid scheduling more accurate and reliable.

Table 2. Decision deviation degrees of the reduced scenarios under different methods.

Decisions	FFS [18] (%)	SBR [18] (%)	Sim&Corrloss [24] (%)	The proposed method (%)
P_{B}	12.584	10.197	4.263	3.170
P_{G}	11.526	9.905	5.814	3.452
C_{total}	9.242	8.481	4.153	2.637

4.3. Comparative analysis of microgrid scheduling

To verify the effectiveness of the proposed optimal scheduling method for the HPS microgrid, the stochastic optimization method considering the uncertainty of

sources and load using chance constraints is compared with the deterministic optimization method based on the point prediction of source and load in Ju et al. [34]. The comparative results of the interactive power with the main grid, the battery charging/discharging power and the total scheduling results under different methods are shown in **Figures 6–8**, respectively.

As shown in **Figures 6** and **7**, the blue dashed line represents the power results after the day-ahead and intraday optimization scheduling, while the red solid line represents the scheduling results after real-time rolling optimization adjustments. It can be observed that the proposed method can achieve smaller power adjustments during real-time rolling optimization. During more scheduling periods, the real-time power adjustment amounts of the proposed method are nearly negligible. It indicates that using stochastic chance constraints to address the uncertainty of hydro-PV output can effectively enhance the robustness of day-ahead scheduling results. As for the deterministic scheduling method in Ju et al. [34], the total power mismatch for the HPS microgrid scheduling over 24 h before real-time power adjustment is 154.587 kWh. In contrast, the corresponding power mismatch amount using the proposed method is 91.813 kWh. It demonstrates that during the day-ahead stochastic optimal scheduling stage, using representative scenarios to characterize the uncertainty of hydro-PV output and adopting stochastic chance constraints in the scheduling model can significantly improve the ability of the microgrid system to deal with real-time variations of uncertain factors, thereby ensuring the stability and safety of the HPS microgrid system in the actual operation.

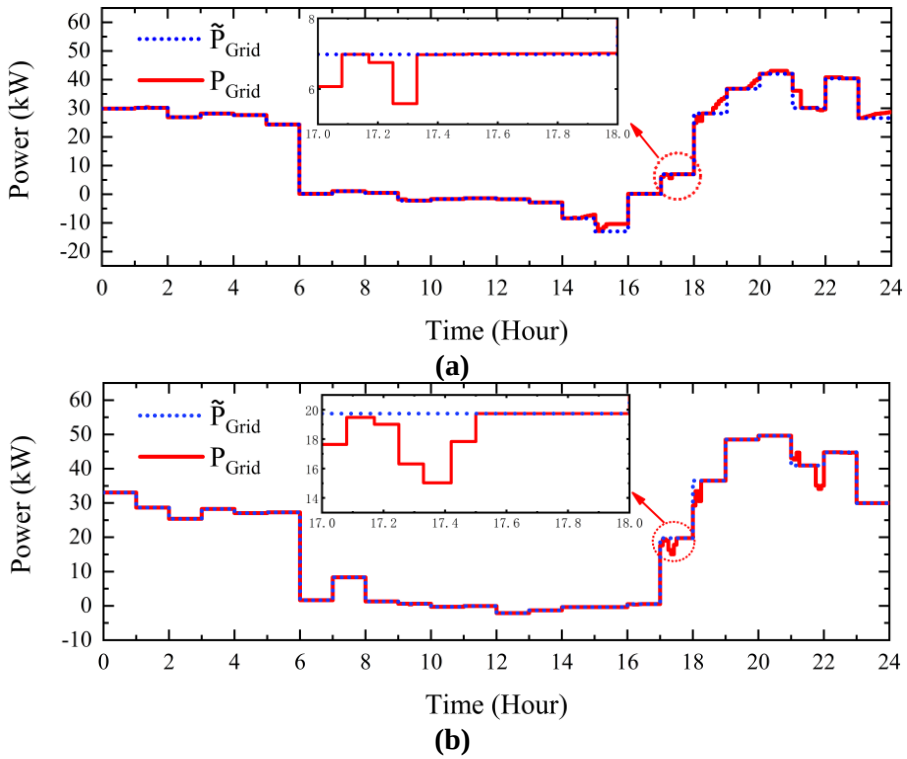

Figure 6. Comparison results of interactive power with the main grid under different methods: **(a)** Deterministic optimization method [34]; **(b)** the proposed stochastic method.

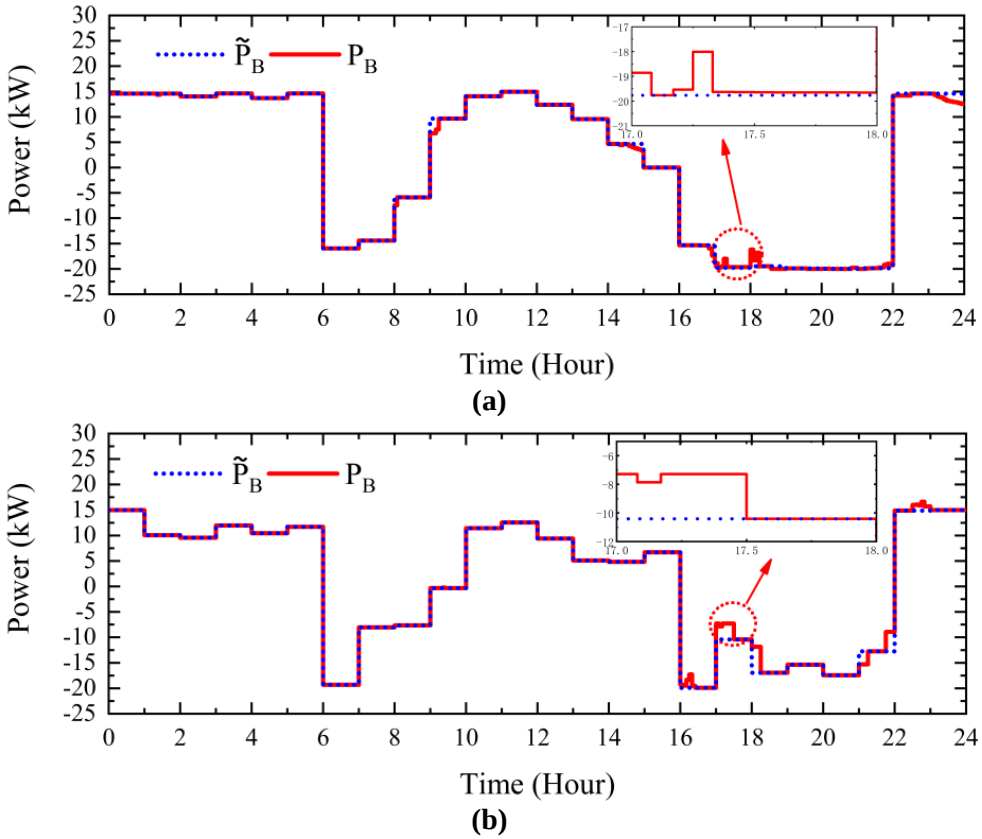

Figure 7. Comparison results of battery charging/discharging power under different methods: **(a)** Deterministic optimization method [34]; **(b)** the proposed stochastic method.

Figure 8a,b show the multi-time scale optimal scheduling results for the HPS microgrid using the deterministic method in Ju et al. [34] and the proposed method, respectively. **Table 3** lists the comparative results of the operating costs in the day-ahead and intraday stages, as well as the real-time scheduling stage, for different methods. It can be seen that the scheduling results for the charging and discharging power of the battery are influenced by electricity prices. During the low-price periods, the battery energy storage system prioritizes charging, whereas in high-price periods, the battery acts as the main power supply device and prioritizes discharging, taking advantage of the price differential to ensure the economic operation of the microgrid. Additionally, the proposed method fully considers the uncertainty of hydro-PV output as well as load. Compared to the deterministic scheduling method in Ju et al. [34], more power was purchased from the main grid during the day-ahead and intraday scheduling stages in the proposed method to ensure the feasibility of the scheduling results under various uncertain scenarios. This resulted in fewer power adjustments during the real-time scheduling stage, effectively reducing the power adjustment costs and minimizing the power fluctuations caused by scenario errors. Compared with the traditional deterministic scheduling method, the compensation power of our method can be significantly reduced by 62.774 kWh, and our power compensation cost can be significantly reduced by 144.916¥, which indicates that the proposed stochastic optimization method can effectively ensure the economy and reliability of microgrid

scheduling under uncertain conditions. Therefore, the proposed stochastic scheduling method significantly mitigates the impact of the uncertainty of hydro-PV output on the stability and economic operation of the microgrid, thereby enhancing the stability and efficiency of the HPS system under complex uncertain conditions.

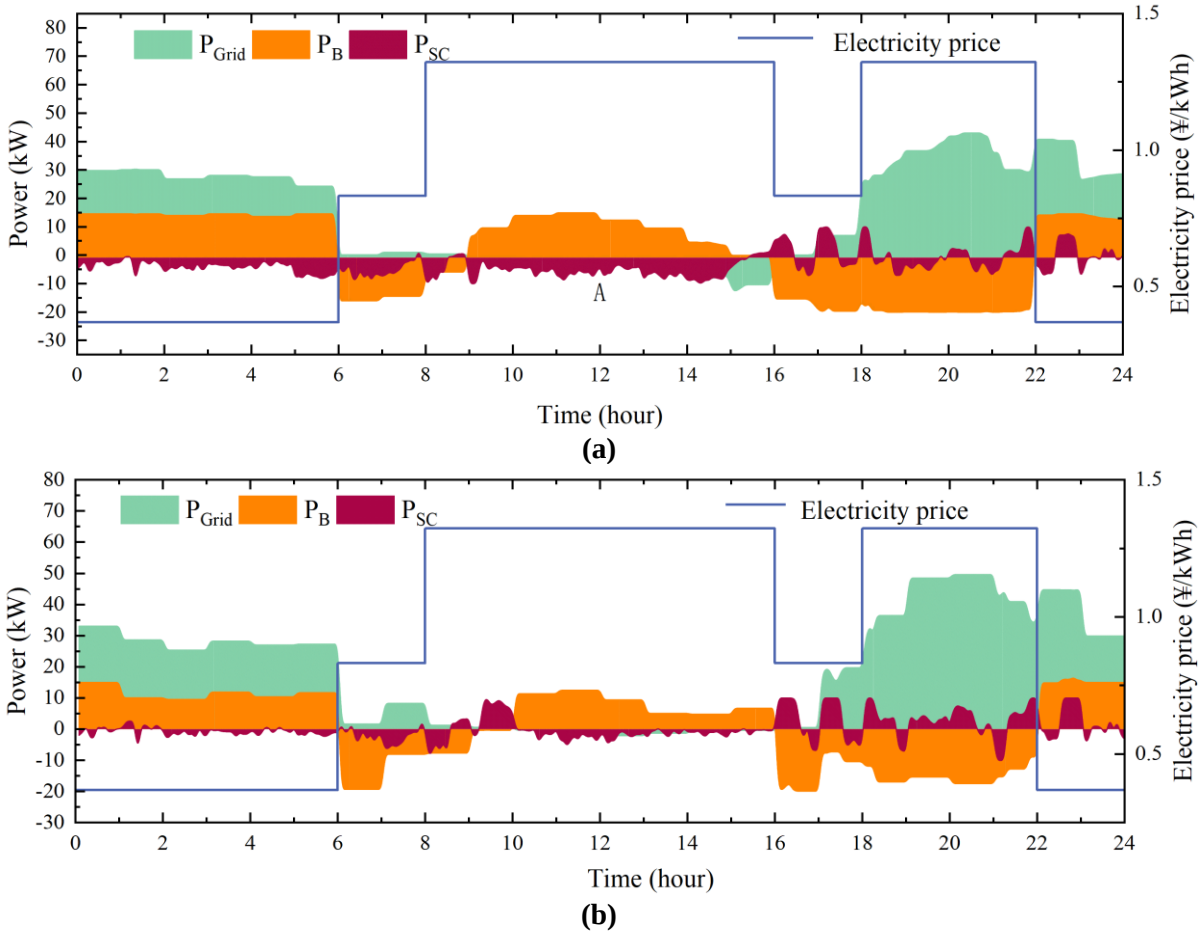

Figure 8. Comparison results of total scheduling results for HPS microgrid under different methods: **(a)** Deterministic optimization method [34]; **(b)** the proposed stochastic method.

Table 3. Comparison of operation costs of HPS microgrid under different methods.

Methods	Day-ahead & Intraday (¥)	Real-time (¥)	Total costs (¥)
Deterministic method [34]	291.674	380.501	672.175
The proposed method	357.935	169.324	527.259

5. Conclusions

To mitigate the adverse impacts of the uncertainty of hydro-PV output on the actual operation of microgrid systems, this paper proposes a rolling optimization control method for HPS microgrids based on stochastic chance constraints. By using a novel multivariate scenario reduction method to obtain the representative scenarios for hydro-PV output, a day-ahead stochastic optimization scheduling model and an intraday power compensation model are established, respectively. Then, the real-time power adjustment strategies are presented. Stochastic model predictive control is employed for multi-time-scale rolling optimization and feedback correction, aiming to

minimize the operating costs of the HPS microgrid. Experimental results of HPS microgrid scheduling indicate that compared to the traditional deterministic optimization methods, the proposed method can better deal with the uncertainty of hydro-PV output to achieve lower power compensation and operation costs. Through scenario-based stochastic optimization, multi-time-scale rolling optimization and feedback correction, it effectively suppresses the power fluctuations of various units caused by source-load uncertainty, thereby significantly improving the stability and economic efficiency of microgrid operations.

Author contributions: Conceptualization, QG and WX; methodology, QG; software, XL; validation, XL, LL and HY; formal analysis, ZW; investigation, QG; resources, XL; data curation, XL; writing—original draft preparation, QG; writing—review and editing, QG; visualization, WX; supervision, QG; project administration, QG; funding acquisition, QG. All authors have read and agreed to the published version of the manuscript.

Conflict of interest: The authors declare no conflict of interest.

References

1. Olatunde O, Hassan MY, Abdullah MP, et al. Hybrid photovoltaic/small-hydropower microgrid in smart distribution network with grid isolated electric vehicle charging system. Journal of Energy Storage. 2020; 31: 101673. doi: 10.1016/j.est.2020.101673
2. Guan Y, Vasquez JC, Guerrero JM, et al. Frequency Stability of Hierarchically Controlled Hybrid Photovoltaic-Battery-Hydropower Microgrids. IEEE Transactions on Industry Applications. 2015; 51(6): 4729–4742. doi: 10.1109/tia.2015.2458954
3. Bagheri F, Dagdougui H, Gendreau M. Stochastic optimization and scenario generation for peak load shaving in Smart District microgrid: Sizing and operation. Energy and Buildings. 2022; 275: 112426. doi: 10.1016/j.enbuild.2022.112426
4. Deng J, Li H, Hu J, et al. A new wind speed scenario generation method based on spatiotemporal dependency structure. Renewable Energy. 2021; 163: 1951–1962. doi: 10.1016/j.renene.2020.10.132
5. Zhu X, Yu Z, Liu X. Security constrained unit commitment with extreme wind scenarios. Journal of Modern Power Systems and Clean Energy. 2020; 8(3): 464–472. doi: 10.35833/mpce.2018.000797
6. Ma H, Zhang W, Wang A. A two-phase robust comprehensive optimal scheduling strategy for regional distribution network based on multiple scenarios. Frontiers in Energy Research. 2024; 12. doi: 10.3389/fenrg.2024.1496302
7. Rezaee Jordehi A, Mansouri SA, Tostado-Véliz M, et al. A tri-level stochastic model for operational planning of microgrids with hydrogen refuelling station-integrated energy hubs. International Journal of Hydrogen Energy. 2024; 96: 1131–1145. doi: 10.1016/j.ijhydene.2024.11.401
8. Azizivahed A, Gholami K, Arefi A, et al. Stochastic scheduling of energy sharing in reconfigurable multi-microgrid systems in the presence of vehicle-to-grid technology. Electric Power Systems Research. 2024; 231: 110285. doi: 10.1016/j.epsr.2024.110285
9. Seyedeh-Barhagh S, Abapour M, Mohammadi-Ivatloo B, et al. Optimal scheduling of a microgrid based on renewable resources and demand response program using stochastic and IGDT-based approach. Journal of Energy Storage. 2024; 86: 111306. doi: 10.1016/j.est.2024.111306
10. Shaillan HM, Tohidi S, Hagh MT, et al. Risk-aware two-stage stochastic short-term planning of a hybrid multi-microgrid integrated with an all-in-one vehicle station and end-user cooperation. Journal of Energy Storage. 2024; 78: 110083. doi: 10.1016/j.est.2023.110083
11. Hu J, Li H. A transfer learning-based scenario generation method for stochastic optimal scheduling of microgrid with newly-built wind farm. Renewable Energy. 2022; 185: 1139–1151. doi: 10.1016/j.renene.2021.12.110

12. Wang Z, Hu J, Liu B. Stochastic optimal dispatching strategy of electricity-hydrogen-gas-heat integrated energy system based on improved spectral clustering method. International Journal of Electrical Power & Energy Systems. 2021; 126: 106495. doi: 10.1016/j.ijepes.2020.106495
13. Abunima H, Park WH, Glick MB, et al. Two-Stage stochastic optimization for operating a Renewable-Based Microgrid. Applied Energy. 2022; 325: 119848. doi: 10.1016/j.apenergy.2022.119848
14. Li K, Yang F, Wang L, et al. A scenario-based two-stage stochastic optimization approach for multi-energy microgrids. Applied Energy. 2022; 322: 119388. doi: 10.1016/j.apenergy.2022.119388
15. Jani A, Karimi H, Jadid S. Two-layer stochastic day-ahead and real-time energy management of networked microgrids considering integration of renewable energy resources. Applied Energy. 2022; 323: 119630. doi: 10.1016/j.apenergy.2022.119630
16. Aaslid P, Korpås M, Belsnes MM, et al. Stochastic operation of energy constrained microgrids considering battery degradation. Electric Power Systems Research. 2022; 212: 108462. doi: 10.1016/j.epsr.2022.108462
17. Kizito R, Liu Z, Li X, et al. Multi-stage stochastic optimization of islanded utility-microgrids design after natural disasters. Operations Research Perspectives. 2022; 9: 100235. doi: 10.1016/j.orp.2022.100235
18. Heitsch H, Römisch W. Scenario reduction algorithms in stochastic programming. Computational Optimization and Applications. 2003; 24: 187–206.
19. Xu J, Yi X, Sun Y, et al. Stochastic Optimal Scheduling Based on Scenario Analysis for Wind Farms. IEEE Transactions on Sustainable Energy. 2017; 8(4): 1548–1559. doi: 10.1109/tste.2017.2694882
20. Pandzic H, Dvorkin Y, Qiu T, et al. Toward Cost-Efficient and Reliable Unit Commitment Under Uncertainty. IEEE Transactions on Power Systems. 2016; 31(2): 970–982. doi: 10.1109/tpwrs.2015.2434848
21. Park S, Xu Q, Hobbs BF. Comparing scenario reduction methods for stochastic transmission planning. IET Generation, Transmission & Distribution. 2019; 13(7): 1005–1013. doi: 10.1049/iet-gtd.2018.6362
22. Beltran F, de Oliveira W, Finardi EC. Application of Scenario Tree Reduction Via Quadratic Process to Medium-Term Hydrothermal Scheduling Problem. IEEE Transactions on Power Systems. 2017; 32(6): 4351–4361. doi: 10.1109/tpwrs.2017.2658444
23. Zhan J, Chung CY, Zare A. A fast solution method for stochastic transmission expansion planning. IEEE Transactions on Power Systems. 2017; 32(6): 4684–4695. doi: 10.1109/tpwrs.2017.2665695
24. Hu J, Li H. A new clustering approach for scenario reduction in multi-stochastic variable programming. IEEE Transactions on Power Systems. 2019; 34(5): 3813–3825. doi: 10.1109/tpwrs.2019.2901545
25. Hu J, Li H, Liu Z. Scenario reduction based on correlation sensitivity and its application in microgrid optimization. International Transactions on Electrical Energy Systems. 2021; 31(3). doi: 10.1002/2050-7038.12747
26. Zhang Y, Meng F, Wang R, et al. Uncertainty-resistant stochastic MPC approach for optimal operation of CHP microgrid. Energy. 2019; 179: 1265–1278. doi: 10.1016/j.energy.2019.04.151
27. Bazmohammadi N, Tahsiri A, Anvari-Moghaddam A, et al. Stochastic predictive control of multi-microgrid systems. IEEE Transactions on Industry Applications. 2019; 55(5): 5311–5319. doi: 10.1109/tia.2019.2918051
28. Jiao F, Zou Y, Zhang X, et al. Online optimal dispatch based on combined robust and stochastic model predictive control for a microgrid including EV charging station. Energy. 2022; 247: 123220. doi: 10.1016/j.energy.2022.123220
29. Lin Y, Li L, Zhang J, et al. A scenario-based stochastic model predictive control approach for microgrid operation at an Australian cotton farm under uncertainties. International Journal of Electrical Power & Energy Systems. 2024; 159: 110025. doi: 10.1016/j.ijepes.2024.110025
30. Wei S, Gao X, Zhang Y, et al. An improved stochastic model predictive control operation strategy of integrated energy system based on a single-layer multi-timescale framework. Energy. 2021; 235: 121320. doi: 10.1016/j.energy.2021.121320
31. Hu J, Yan P, Tan G. A two-layer optimal scheduling method for microgrids based on adaptive stochastic model predictive control. Measurement Science and Technology. 2025; 36(2): 026208. doi: 10.1088/1361-6501/ada39b
32. Hu J, Yan P, Tan G. Spatiotemporal dependence modeling of wind speeds via adaptive-selected mixture pair copulas for scenario-based applications. Renewable Energy. 2025; 244: 122650. doi: 10.1016/j.renene.2025.122650
33. Qin Z, Li W, Xiong X. Incorporating multiple correlations among wind speeds, photovoltaic powers and bus loads in composite system reliability evaluation. Applied Energy. 2013; 110: 285–294. doi: 10.1016/j.apenergy.2013.04.045
34. Ju C, Wang P, Goel L, Xu Y. A two-layer energy management system for microgrids with hybrid energy storage considering degradation costs. IEEE Transactions on Smart Grid. 2018; 9(6): 6047–6057. doi: 10.1109/tsg.2017.2703126

Advances in Differential Equations and Control Processes 2025, 32(1), 2807.
https://doi.org/10.59400/adecp2807

Article

Performance evaluation of post-processed kinematic precise point positioning solution for environmental applications

Ahmed Al Shouny

Department of Geomatics, King Abdulaziz University, Jeddah 21589, Saudi Arabia; ametaowa@kau.edu.sa

CITATION

Al Shouny A. Performance evaluation of post-processed kinematic precise point positioning solution for environmental applications. Advances in Differential Equations and Control Processes. 2025; 32(1): 2807. https://doi.org/10.59400/adecp2807

ARTICLE INFO

Received: 18 February 2025
Accepted: 7 March 2025
Available online: 13 March 2025

Abstract: Precise Point Positioning (PPP) is a modern satellite-based technique known for its simplicity, efficiency, and cost-effectiveness, eliminating the need for a reference or base station. This study evaluates the accuracy of Precise Point Positioning (PPP) solutions for both static and kinematic observations using the CSRS-PPP service. To ensure a fair comparison, PPP-derived results were assessed against relative positioning techniques. Field measurements, including static and kinematic data, were collected across a 39 km² study area in northern Egypt to generate topographic contour maps. The findings indicate that PPP is a viable alternative for static positioning, achieving a 2D horizontal accuracy of ±2.54 cm, though vertical accuracy is lower at 11.3 cm. In kinematic mode, horizontal accuracy is ±5 cm, while vertical accuracy decreases to 18.4 cm. While the achieved 2D accuracy meets the needs of most environmental applications, the lower height precision may not be suitable for tasks requiring high vertical accuracy.

Keywords: post-processed kinematic PPP; CSRS-PPP; relative positioning; static measurements

1. Introduction

Differential GNSS (DGNSS) using carrier phase observations has become widely used across various fields, offering centimeter-level accuracy in both static and kinematic modes. However, it requires at least two GNSS receivers—one as a base and one as a rover—operating simultaneously. For high-accuracy applications like geodesy, static and rapid static methods are preferred, achieving millimeter-level precision [1] but requiring extended measurement and processing time which could limit its applications [2,3]. Kinematic methods, while slightly less accurate, are widely used in several applications such as land surveying, mapping, construction, border, aircraft positioning, mining, agriculture, and marine works [4]. Initially, Post-Processed Kinematic (PPK) was the only available solution for kinematic GPS data, but Real-Time Kinematic (RTK) was later introduced, providing instant corrections through continuous radio communication. RTK has since become a crucial tool due to its speed, accuracy, and cost-effectiveness.

Both static and kinematic relative positioning techniques have limitations that restrict their use in various applications and regions. The requirement of at least two receivers for simultaneous measurement increases fieldwork complexity and time. A major challenge is the scarcity of reference points, especially in remote and coastal areas [5]. Static mode requires lengthy installation and post-processing, making it impractical for some applications. RTK is limited by a maximum base-rover separation of 20 km [6], which affects ambiguity resolution for centimeter-level

accuracy. Additionally, RTK connections are prone to signal interruptions due to physical obstructions, interference, or environmental conditions.

Over several years, researchers and scientists perform many studies to develop new techniques and approaches to overcome the above-mentioned limitations of relative positioning methods. These approaches include Continuously Operating Reference Station (CORS), the Virtual Reference Station (VRS) [7], and Precise Point Positioning (PPP). PPP has been considered one of the most popular positioning approaches in recent years. The development of the PPP technique was a result of the precise GPS clock and orbit products provided by the International Global Navigation Satellite System (GNSS) service (IGS) organization. PPP can process observations collected by single or dual-frequency receivers using both static and kinematic methods [8]. Thanks to IGS products, PPP can achieve cm-level accuracy without the need for using reference stations [9]. So PPP is considered easier and less expensive than relative positioning techniques, and therefore it has become the most widely used approach for several scientific and practical fields.

The obtained accuracies of the PPP solution for static and kinematic methods in various applications have been investigated in several studies [10–15]. They have concluded that PPP for static mode can achieve mm to cm level accuracy in positions. However, in kinematic mode, PPP can achieve centimeters to a few decimeters in positions [5,12,16–18]. According to numerous research investigations, it was concluded that PPP vertical error is about twice the value of the PPP horizontal errors [5,19,20]. The different available services and software of PPP were assessed and compared in several studies. The Canadian Spatial Reference System Precise Point Positioning (CSRS-PPP) service concluded as the most accurate PPP service [11,12,21–23].

This study evaluates PPP accuracy for both static and kinematic measurements using the CSRS-PPP service and compares the results with relative positioning techniques. The adaptation of the PPP kinematic mode in environmental applications is examined to assess its obtained accuracy in horizontal and vertical components. The study area covering approximately 39 km^2 is placed alongside the Mediterranean Sea coast in the northern region of Egypt. The choice of this coastal area is because of its significance in continuous construction and development projects that led to the permanent need for coastal protection strategies and works to fight erosion caused by global warming. Additionally, the area's unique geographical and climatic conditions, such as high humidity, temperature variations, and potential ionospheric disturbances, may influence GNSS positioning accuracy. Another key factor in selecting this coastal region is due to the severe shortage of reference points in most of the coastal areas. This paper is organized as follows. First, a brief discussion of relative positioning and PPP techniques and their mathematical models is presented. Second, the study area and field measurements are discussed. Next, the results are presented, compared, and analyzed. Finally, the conclusions of the paper were introduced.

2. Relative positioning and PPP techniques

Relative positioning methods, also known as differential positioning techniques, are considered the most accurate techniques for the estimation of positions in both

horizontal and vertical components. Static and rapid static are used for geodetic and surveying applications that require the highest accuracy. However, they need a long time of observations and also a post-processing stage. For long baselines, only the static method is applicable for observations. Kinematic methods include both PPK and RTK. RTK provides positions instantaneously by receiving corrections from the base units via radio connection. Unlike static methods, RTK does not require post-processing, and its achieved accuracy is less than static accuracy, but it can achieve an acceptable accuracy up to cm-level accuracy [24]. PPK can provide more accuracy than RTK as a result of the post-processing stage that removes data blunders and errors [4]. PPK can provide us with cm-accuracy after solving ambiguity [1]. PPK, unlike RTK, can't provide positions in real time. PPK needs less occupation time than static and rapid static methods. However, it requires initialization time at the beginning of the observing process and after losing the satellite signals. This initialization process is essential for solving ambiguity. The PPK method consists of two primary modes. The first is the continuous mode, where the rover remains in motion, making it ideal for applications such as railway surveys and GPS-controlled photogrammetry. The second mode, which we employed in this study, is the stop-and-go mode. In this approach, the rover briefly pauses at each unknown point for less than two minutes. Compared to the continuous mode, stop-and-go surveying offers higher accuracy and is better suited for contour and detail surveys. This is because data can be averaged over the collection period at each site, reducing uncertainty and improving positional accuracy by minimizing errors when the receiver remains stationary at designated points [4]. The estimation of positions by relative positioning using the double differencing principle in phase measurements is calculated by equation [25]:

$$\nabla\Delta\phi_t = \nabla\Delta r_{(t,t-\tau)} + \nabla\Delta ds_{(t-\tau)} - \nabla\Delta d_{iono} + \nabla\Delta d_{tropo} + \nabla\Delta\lambda N + \nabla\Delta\varepsilon(\phi) \quad (1)$$

where: $\nabla\Delta$ is the double difference operator at the time of receiving data (t), ϕ is the phase measurement, τ is the travel time from satellite to receiver, $t-\tau$ is the satellite time, $r_{(t,t-\tau)}$ refers to the true geometric range, ds is the orbital prediction error, d_{iono} and d_{tropo} are the ionospheric and tropospheric errors, respectively, λ is the wavelength, N is the integer phase ambiguity, and ε denotes the noise component. The tropospheric delay is the sum of the wet and hydrostatic parts.

Due to the extensive use of GNSS in a variety of applications and fields, it was necessary for researchers and organizations to develop new strategies and techniques. The main concern of these strategies is to be simpler, cost-effective, widely popular, and to achieve an acceptable accuracy compared with traditional relative positioning techniques. One of these modes developed strategies is PPP techniques. PPP was first introduced and discussed by [9]. It was first developed for static works only but later, with the availability of precise real-time satellite orbit and clock products provided by the IGS organization. It was adopted in kinematic applications [16]. PPP is considered the most popular used GNSS technique in scientific research and several applications. PPP is also known as Single Point Positioning (SPP), as it used only one receiver without the need for reference point occupation, as shown in **Figure 1**. Not only is PPP simple and cost-effective with global coverage, but it also achieves an acceptable accuracy in static and kinematic modes. PPP solutions can be obtained using either

web-based online services or different software/web-based online services such as MAGIC-GNSS, Automatic Precise Positioning Service (APPS), Trimble CenterPoint (RTX), GNSS Analysis and Positioning Software (GAPS), and CSRS-PPP. Regarding software, they are divided into two categories: Scientific software (GipsyX, GAMIT, GLAB, and the most popular one) and commercial software (GRAF-NAV) [26].

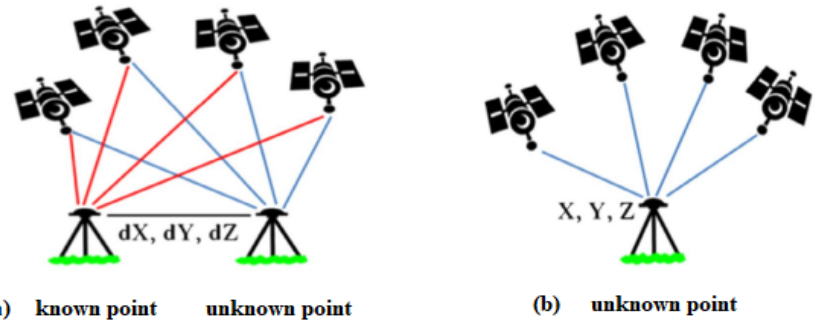

Figure 1. Schematic depicting **(a)** relative positioning; and **(b)** point positioning.

In this study, CSRS-PPP online service is considered the globally used popular PPP service [27]. It can process both static and kinematic data with no charge, and this service provides registered users with a PDF file containing results and graphical information of the processing solution. Full explanation and details of the CSRS-PPP service were introduced by [28–30]. It should be noted that one of the most important parts of the PPP technique is the solution type of initial phase ambiguities, which can be fixed or float. A few online services are fixing the ambiguities, also called PPP with Ambiguity Resolution (PPP-AR) PPP-AR solutions, while most of them solve ambiguities as a float. CSRS-PPP has provided solutions as PPP-Float until October 20th, 2020. After this date, the CSRS-PPP system upgraded to CSRSPPP-Ambiguity Resolution (PPP-AR), and solutions were produced by fixing the GPS ambiguities based on the decoupled clock model (DCM) for the data collected after January 1st, 2018 [31]. Our field measurements were collected before 2018, so they were processed using CSRS-PPP solutions.

The mathematical modeling equation of PPP of pseudo range and carrier phase observations is shown in Equations (2) and (3) [32]:

$$l_p = \rho + c(dt - dT) + M\ ztd + \varepsilon_p \tag{2}$$

$$l_\phi = \rho + c(dt - dT) + M\ ztd + N\lambda + \varepsilon_\phi \tag{3}$$

where:

l_P (Pseudo-range observation): Is the ionosphere-free combination of the L1 and L2 pseudo ranges (2.54P1–1.54P2);

l_ϕ (Carrier phase observation): Is the ionosphere-free combination of L1 and L2 carrier phases (2.54ϕ1–1.54ϕ2);

ρ (Geometric range): Is the geometrical range computed as a function of satellite and station coordinates;

c (Speed of light): Is the constant speed at which electromagnetic signals travel in a vacuum (~299,792,458 m/s);

dt (Receiver clock bias): Is the station clock offset from GPS time;
dT (Satellite clock bias): Is the satellite clock offset from GPS time;
M (Mapping function): Is a function to map tropospheric from slant to zenith;
ZTD (Zenith Tropospheric Delay): is the tropospheric zenith total delay due to the neutral atmosphere, wavelength, and ionosphere-free combination. The tropospheric delay is the sum of the wet and hydrostatic parts.
λ (Carrier wavelength): Is the carrier or carrier combination, wavelength;
N (Integer ambiguity): Is the unknown number of full carrier phase cycles between the satellite and receiver, critical for high-precision positioning;
εP Measurement noise and unmodeled errors in pseudo-range observation (m);
εP Measurement noise and unmodeled errors in carrier phase observation (m).

3. Material and results

3.1. Study area and measurements

The selected area of this research is placed alongside the Mediterranean Sea coast zone located in the northern region of Egypt, as shown in **Figure 2**. The area is confined between Al Burullus city at a longitude of 30°57′51″ and Rosetta city at E30°23′18″ with about 60 km of longitudinal length and an average of 0.5 km perpendicular to the coastal line. It covers an approximate area of 39 km^2. The selection of this region is due to the increasing necessity for development activities to prevent shorelines from erosion induced by global warming. So, a topographic map with high accuracy was required by ECPA for determining the best locations of protection works along the area continuously. This map was produced by the Survey Research Institute [33]. Static and kinematic GPS observations, in addition to leveling measurements, were collected and discussed by [4]. A brief discussion about these measurements is presented in the following sections.

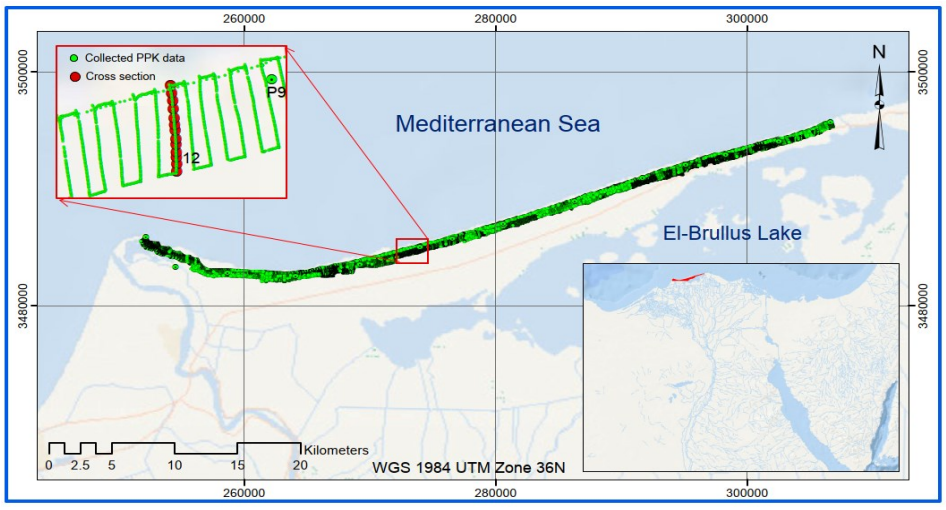

Figure 2. The study area with a part of kinematic measurements.

3.1.1. Static GPS observations

As a result of the scarcity of reference points throughout many coastal regions, it was important to establish a new permanent reference point to cover all the study area

for current and future required measurements. Fourteen control points were installed across the study area, as shown in **Figure 3**, with an approximate spacing of 5 km. This distance was determined based on the terrain characteristics to ensure optimal positioning accuracy. The chosen separation was specifically selected to account for geoid undulation variations within the study area, as the collected measurements were intended to develop a methodology for generating topographic contour maps using the post-processed kinematic differential GPS technique (PPK-GPS) [4]. To achieve the required accuracy, the selected spacing was carefully considered; however, it may vary depending on specific surveying requirements and the terrain conditions of the investigated area. To ensure sustainability of these points for future works, a cub-shaped concrete structure with upper dimensions of 40 × 40 cm and lower dimensions of 50 × 50 cm was built with a total height of 1 m divided into equal parts over and underground as shown in **Figure 4**. A metal cap with a 10 cm steel rod fixed above the concrete for the observation process.

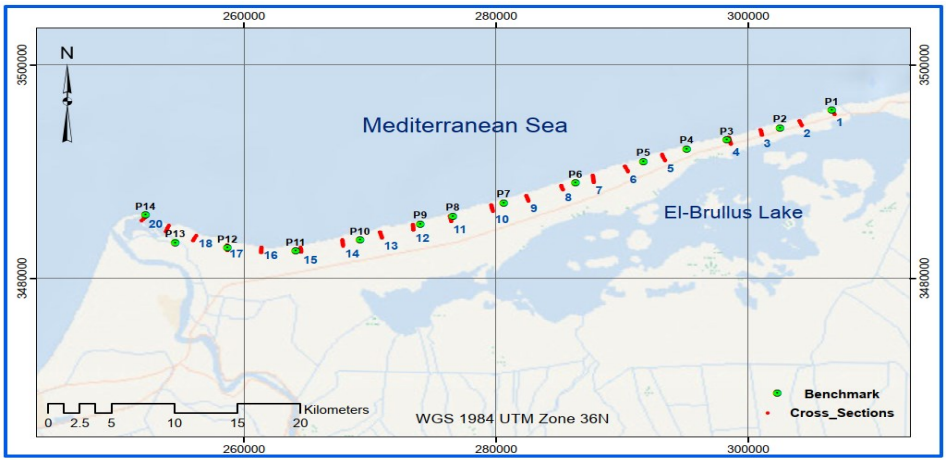

Figure 3. Location of control stations and check cross sections along the study area.

To calculate the accurate 3-D coordinates of these established 14 control points, static GPS observations were performed with occupation times ranging from 2 to 3 hours. They were linked with the nearest two first-order triangulation points of the Egyptian Surveying Authority (ESA) to be solved as an over-constrained network [34]. Observations were collected using 4 dual-frequency 5700 Trimble receivers and processed using Trimble Business Center Software (TBC). The precise ephemeris was used to enhance the accuracy of the estimated coordinates. The required horizontal and vertical precisions of ± (2 cm + 1 ppm) and (± 5 cm + 1 ppm) were achieved for all points. The network was adjusted relative to the International Terrestrial Reference Frame (ITRF) system at 2014 epochs according to the measurement date.

To address GPS measurement challenges related to signal interference and multipath effects, various strategies can be implemented. Utilizing high-quality GNSS receivers, interference-resistant antennas, and avoiding electronic interference sources helps reduce signal disruptions. In our coastal study area, multipath effects were negligible due to the open-sky environment. Furthermore, to achieve optimal accuracy and minimize errors, appropriate observation timing, the use of PPK observation methods (stop and go mode), and post-processing techniques were applied.

Figure 4. Two photos of the established control stations.

3.1.2. Kinematic measurements

To create an accurate topographic map for the study area using GPS observations, the Post-Processed Kinematic (PPK) method and Stop and Go mode were adopted for collecting data. During kinematic observations, one receiver occupied the nearest reference station as a base, and 2 other receivers were used as rovers. The area was divided into parallel cross-sections perpendicular to the seacoast line with 100 m separated distances between each cross-section, as shown in **Figure 2**. The cross-sections varied in length between 0.4 and 0.6 km. The average space between observed points using stop and go modes is 10 m. All data were then processed using TBC software to estimate the accurate 3-D coordinates. The cross-sections point average accuracy was (1.2 cm) and (2.4 cm) for HZ and VL positions, respectively. Twenty of these cross-sections with a spacing of approximately 3 km, as shown in **Figure 3,** were selected to be compared with their solution results obtained using CSRS-PPP service. The main purpose of these twenty cross-sections during measurements is to be observed using PPK modes and also leveling methods to fairly judge the achieved precision of producing topographic maps using PPP methods as discussed by [4].

3.1.3. PPP static and kinematic results

The main objective of this study is to evaluate the CSRS-PPP service accuracy for static and kinematic measurements. So, after solving these measurements using relative positioning techniques and estimating the final processed accurate 3-D coordinates using TBC software. Static and kinematic raw data observations were uploaded to the CSRS-PPP online website [29] for solutions. The website accepts only Receiver Independent Exchange format (RINEX) for static and kinematic data. Users must manually upload RINEX files, and large datasets may take longer to process, making them less convenient for high-frequency or large-scale GNSS campaigns. Users can't upload any other format, and they have to convert their observation files format into RINEX format for uploading, where any errors in formatting can lead to processing failures without clear troubleshooting guidance. Users are able to upload multiple RINEX files in a single (zip) or (tar) archive. An error email from the service may be received due to various reasons, such as duplicated data blocks in the submitted RINEX observation file at one or more epochs, and they must be corrected by

resubmitting the file for processing. Also, an insufficient number of epochs and observed satellites may cause failure in processing the file.

The reference system for the software is based on ITRF 2014 (epoch 2014 according to measurement date); the obtained coordinates have Cartesian XYZ format and Ellipsoidal and UTM (Universal Transverse Mercator) system zone 36 [29]. A PDF report was received via user email after about 2 min of uploading data. The PDF report is about five pages, including solution results, final coordinates, and several plots showing ambiguity status, tracked satellite, and pseudo-range and carrier phase residuals. We should conclude that the received PDF report from the CSRS-PPP service has several limitations, including a lack of in-depth error analysis, such as multipath effects, atmospheric delays, and satellite geometry limitations. It provides general accuracy estimates but lacks detailed statistical analyses or confidence intervals for positioning errors. After receiving CSRS-PPP solutions, their estimated results for both static and kinematic measurements were compared with results that were obtained using the relative positioning solution. **Figure 5** displays a flowchart of the study methodology.

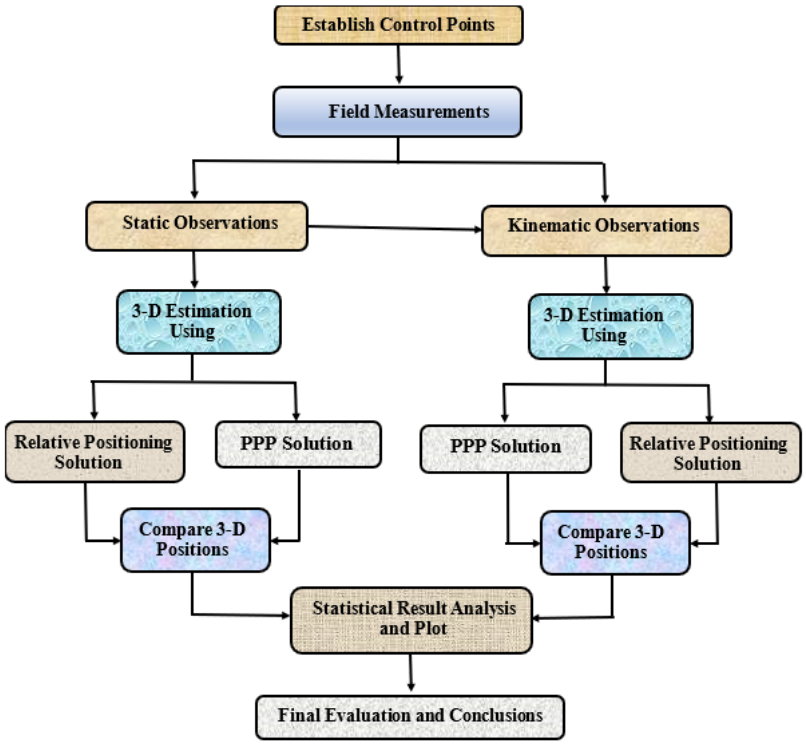

Figure 5. Flowchart of the study methodology.

3.2. Results

3.2.1. Static results

Table 1 shows the differences between coordinates obtained from static PPP and relative positioning solutions for the 14 control points, and **Table 2** represents the summary of statistics, maximum, minimum, RMS, median, and NMAD for these differences. **Figure 6** shows the violin plots of results. The computed values of Normalized Median Absolute Deviation (NMAD) and violin plots were used to

acquire a better understanding of differences, detect outliers, and emphasize data peaks. As seen from the results, the difference of 2D position reaches 2.1 cm and 2.5 cm as a maximum value with RMSE values of 1.2 cm and 1.4 cm for both East and North, respectively. While the height component differences range between −5.9 and 11.3 cm with an RMSE value of 9.1 cm.

Table 1. Differences between static CSRS-PPP and relative positioning solutions of control stations.

point ID	ΔN	ΔE	ΔH
P1	0.018	−0.017	0.081
P2	−0.004	0.007	0.1
P3	0.008	−0.017	0.059
P4	−0.007	0.010	0.108
P5	0.000	−0.005	0.074
P6	−0.001	−0.014	0.083
P7	−0.020	0.011	0.094
P8	0.025	0.008	0.078
P9	−0.005	0.011	0.113
P10	−0.009	0.013	0.085
P11	0.020	0.021	0.096
P12	0.016	−0.006	0.089
P13	0.004	0.012	0.104
P14	−0.016	−0.002	0.099

Table 2. Differences in statistics between static CSRS-PPP and relative positioning solutions of control stations.

	Min	Max	RMSE	Median	NMAD
ΔE	−0.017	0.021	0.012	0.007	0.012
ΔN	−0.02	0.025	0.014	−0.001	0.010
ΔH	−0.113	−0.059	0.091	−0.091	0.011

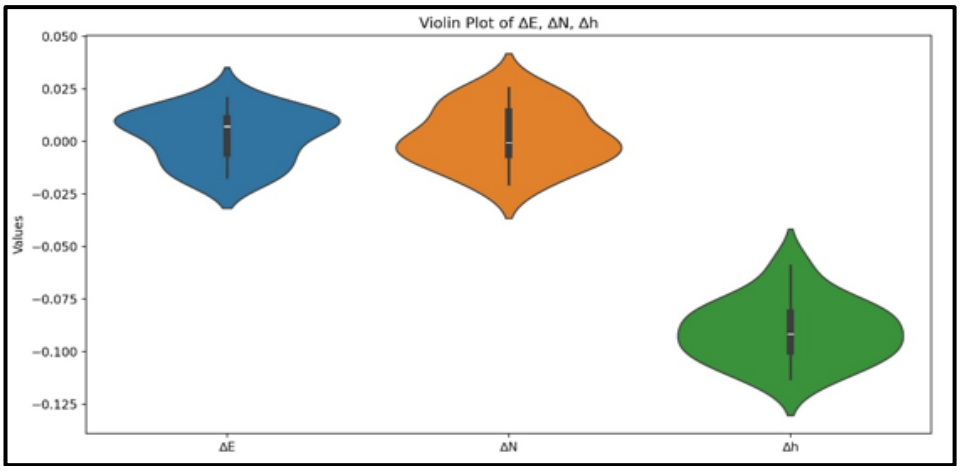

Figure 6. Violin plots of the difference of the static CSRS-PPP solution.

3.2.2. Kinematic results

As mentioned before, the twenty cross-sections of kinematic observations were solved using both CSRS-PPP and relative positioning. The average horizontal and vertical GPS positioning uncertainties for each cross-section point are provided in **Table 3**.

Table 3. The average HZ and VL precision for the 20 check cross-sections.

Sec	HZ. Precision (m)	VL. Precision (m)	Sec	HZ. Precision (m)	VL. Precision (m)
1	0.012	0.022	11	0.014	0.031
2	0.011	0.017	12	0.012	0.022
3	0.011	0.018	13	0.010	0.014
4	0.015	0.029	14	0.010	0.019
5	0.012	0.022	15	0.014	0.024
6	0.014	0.023	16	0.010	0.019
7	0.014	0.029	17	0.014	0.023
8	0.013	0.028	18	0.011	0.020
9	0.015	0.037	19	0.011	0.017
10	0.015	0.032	20	0.014	0.020

Table 4 shows the statistics summary of the differences between two solution results for 2D position and height components and **Figure 7a,b** represents graphically the absolute differences for 2D position and height components respectively. **Figure 8** shows the median values of ΔE, ΔN, and Δh for all cross sections.

Table 4. Statistics values for kinematic measurement differences of the twenty cross-sections.

Min Max Median RMSE	**SEC.1**	**SEC.2**	**SEC.3**	**SEC.4**	**SEC.5**	**SEC.6**	**SEC.7**	**SEC.8**	**SEC.9**	**SEC.10**
ΔN	−0.035 0.030 −0.003 0.021	−0.038 0.014 −0.017 0.021	−0.046 0.007 −0.022 0.026	−0.036 0.020 −0.019 0.022	−0.036 0.000 −0.020 0.024	−0.028 0.012 −0.017 0.019	−0.029 0.001 −0.017 0.017	−0.014 0.004 −0.006 0.007	−0.030 −0.010 −0.022 0.023	−0.020 0.005 −0.005 0.010
ΔE	−0.044 0.014 −0.006 0.022	−0.049 0.026 −0.006 0.018	−0.011 0.030 0.005 0.012	−0.040 0.008 −0.015 0.021	−0.031 0.000 −0.016 0.019	−0.049 −0.022 −0.034 0.034	−0.047 −0.021 −0.037 0.037	−0.048 −0.030 −0.036 0.037	−0.041 −0.011 −0.032 0.031	−0.050 −0.034 −0.043 0.043
Δh	−0.125 −0.046 −0.096 0.094	−0.184 −0.092 −0.122 0.133	−0.141 −0.065 −0.102 0.104	−0.096 −0.045 −0.073 0.070	−0.106 −0.036 −0.071 0.073	−0.142 −0.084 −0.112 0.114	−0.121 −0.093 −0.108 0.106	−0.109 −0.079 −0.099 0.098	−0.141 −0.067 −0.102 0.107	−0.168 −0.102 −0.124 0.130
Min Max Median RMSE	**SEC.11**	**SEC.12**	**SEC.13**	**SEC.14**	**SEC.15**	**SEC.16**	**SEC.17**	**SEC.18**	**SEC.19**	**SEC.20**
ΔN	−0.050 0.012 −0.016 0.026	−0.036 −0.003 −0.019 0.021	−0.045 0.044 −0.004 0.023	−0.042 0.041 −0.011 0.026	−0.040 0.032 −0.018 0.028	−0.042 0.032 −0.030 0.029	−0.030 0.039 −0.009 0.021	−0.047 0.043 −0.012 0.028	−0.037 0.021 −0.009 0.018	−0.043 0.005 −0.020 0.025

Table 4. (*Continued*).

Min Max Median RMSE	SEC.11	SEC.12	SEC.13	SEC.14	SEC.15	SEC.16	SEC.17	SEC.18	SEC.19	SEC.20
ΔE	−0.032 0.007 −0.016 0.017	−0.037 −0.003 −0.021 0.021	−0.044 0.038 −0.018 0.026	−0.047 0.034 −0.021 0.028	−0.037 0.036 −0.006 0.024	−0.034 0.030 0.010 0.020	−0.041 0.047 −0.016 0.029	−0.036 0.030 −0.003 0.022	−0.036 −0.002 −0.015 0.021	−0.030 0.037 −0.015 0.021
Δh	−0.128 −0.095 −0.110 0.112	−0.173 −0.115 −0.143 0.146	−0.129 −0.082 −0.097 0.103	−0.128 −0.051 −0.089 0.098	−0.173 −0.072 −0.108 0.124	−0.138 −0.067 −0.118 0.115	−0.162 −0.074 −0.110 0.116	−0.150 −0.070 −0.111 0.113	−0.135 −0.071 −0.097 0.105	−0.151 −0.067 −0.113 0.113

We can notice from the table a considerable variation in Δh cross-sections, indicating that height difference is more variable than ΔE and ΔN. As shown in the figure, the 2D position differences have a maximum value of 5 cm or better with an average median of 3.5 cm and RMSE of 3.4 cm for all cross-section points. While differences of height components fall within the range between values of 3.6 cm and 18.4 cm with an RMSE value of 10.9 cm.

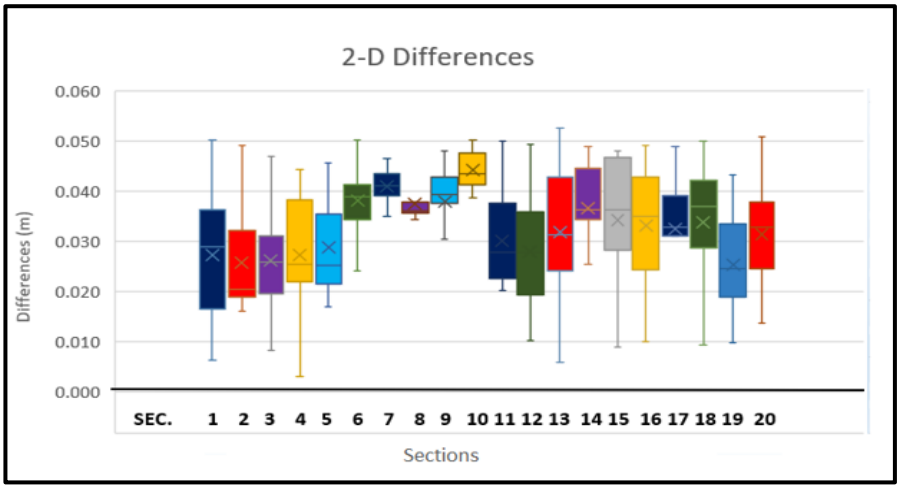

(a) Box plot for all cross-sections of height component.

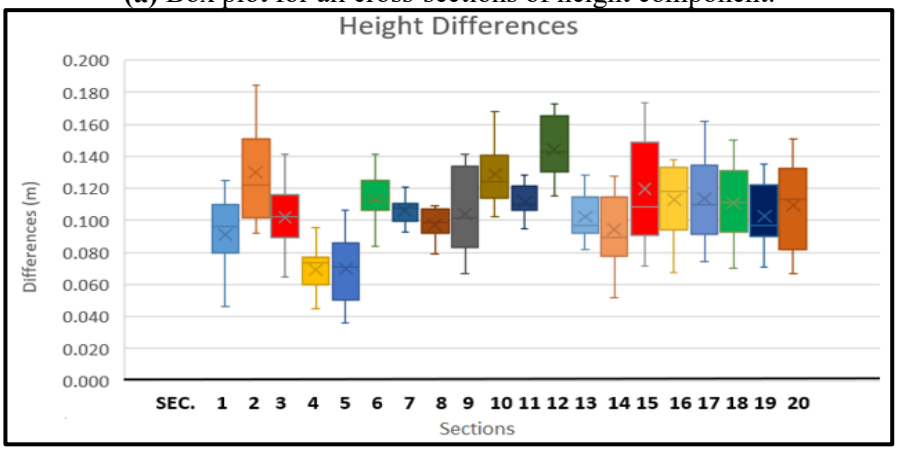

(b) Box plot for all cross-sections of 2D positions.

Figure 7. Box plots for all cross-sections of both 2D and height components.

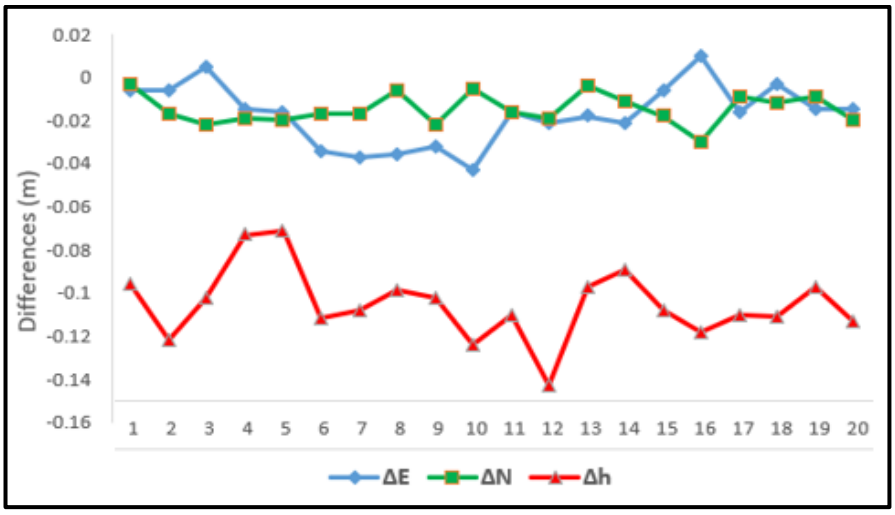

Figure 8. Median values for all cross sections.

4. Discussion

The main objective of this research is to evaluate the estimated accuracy of PPP solutions for post-processed kinematic observations using the CSRS-PPP service. The use of the PPP technique spread rapidly in many fields and applications as a result of its simplicity, cost-effectiveness, and acceptable accuracy. Field static and kinematic observations were collected and solved using both relative positioning and PPP techniques, and their results were compared to fairly evaluate the obtained accuracy. According to the obtained results, the outfinding proved that PPP service is an efficient method in static mode, especially for horizontal positioning, where the differences were less than 2.54 cm. However, PPP achieves a lower accuracy for the height component with a height difference of up to 11.3 cm. For kinematic mode, the achieved horizontal accuracy was judged satisfactory with a higher discrepancy of 4.7 cm. But in the height component accuracy, it was not satisfied because the differences reached up to 18.4 cm, and these values may not be suited for a variety of applications that require the highest accuracy.

Vertical accuracy in PPP is generally lower than horizontal accuracy due to various limitations in GNSS positioning and error modeling. Factors such as poor satellite geometry due to fewer observed satellites, tropospheric and ionospheric delays, and multipath effects, particularly in urban areas, degraded vertical accuracy. Additionally, long convergence times and inaccuracies in atmospheric corrections and satellite orbit data further reduce accuracy and precision. In our measurements, good satellite geometry with sufficient available satellites and an open-sky environment with minimal multipath were achieved. However, the primary causes of larger elevation errors are ionospheric delays, satellite orbital errors, and atmospheric modeling limitations. The accuracy achieved by the kinematic PPP solution can be suitable for various applications requiring movement-based measurements, practically in open areas. However, its reliability decreases in urban environments and forested regions. Additionally, it isn't suitable for applications that demand immediate results.

5. Conclusion

The extensive improvement of modern technology had a significant impact on all fields and led to the development of new approaches. Several new positioning techniques and methods were developed in surveying and geodesy fields. The main concern in the developed techniques is to decrease the fieldwork and minimize the cost and time of works. However, these modern techniques should achieve a suitable accuracy. One of the most popular modern positioning techniques is PPP, or single point positioning, with no need for reference or base stations. In this study we evaluate the accuracy of the CSRS-PPP solution in both static and kinematic modes using field measurements. Solutions derived from CSRS-PPP were compared with those estimated from relative positioning techniques.

Based on the results, the CSRS-PPP technique could be used for the solution of static measurements as an alternative method to the relative positioning technique. PPP achieves a suitable accuracy, especially in horizontal positions, for several applications and fields, and about 11.3 cm height level accuracy is obtained by the CSRS-PPP solution. For the kinematic mode, CSRS-PPP provides us with an accuracy of ± 5 cm for 2D positions and approximately 18.4 cm or better for height components. The achieved 2D position accuracy is considered acceptable for most moving measurement environmental applications. However, height accuracy may not be suitable for many applications. It should be noted that PPP may not be suitable for several applications that require immediate results. PPP accuracy is affected by multipath errors and atmospheric conditions, making it less reliable in urban areas, forests, and coastal regions with frequent signal interference. Unlike RTK, which can resolve integer ambiguities quickly using local base stations, PPP often relies on float solutions (PPP-Float) or slower ambiguity resolution techniques (PPP-AR), affecting rapid positioning needs.

Further work is required for improving the accuracy of height components via kinematic PPP to fulfill other applications that require higher accuracy and should be investigated. This improvement of PPP-derived heights may be achieved by integrating with ground station corrections, multi-frequency PPP, INS (Inertial Navigation Systems) integration, advanced tropospheric models, and the use of machine learning for error modeling. Various PPP services that offer kinematic solutions should be examined and compared with the results of this study. Additionally, modern PPP algorithms, such as PPP-AR and PPP-Float, should be analyzed and discussed. Additionally, the impact of the region's diverse geographical environment and climatic conditions on measurement accuracy should be thoroughly examined.

Funding: This research work was funded by Institutional Fund Projects under grant No. (IFPIP-1238-137-1443).

Acknowledgment: The authors gratefully acknowledge technical and financial support provided by the Ministry of Education and King Abdulaziz University, DSR, Jeddah, Saudi Arabia.

Data availability: The data used in this study were obtained from the corresponding author upon reasonable request.

Conflict of interest: The author declares no conflict of interest.

References

1. ElShouny AF. The combined adjustment of terrestrial and satellite control network [Master's thesis]. Minoufiya University; 2008.
2. Xu G. GPS: Theory, Algorithms and Applications, 2nd ed. Springer; 2007. ISBN 978-3-642-09181-0.
3. Leick A. GPS Satellite Surveying. Wiley; 1990.
4. El Shouny A, Nagy Y, Magdy H. Evaluating the performance of using PPK-GPS technique in producing topographic contour map. Marine Geodesy. 2017; 40(4): 224–238.
5. Liu R, Guo B, Zhang A, Yimwadsana B. Research on GPS precise point positioning algorithm with a Sea Surface Height Constraint. Ocean Engineering. 2020; 197: 106826.
6. El-Mowafy A. Precise real-time positioning using Network RTK. Global Navigation Satellite Systems: Signal, Theory and Applications. 2012; 7: 161–188.
7. Wanninger L. Virtual Reference Stations (VRS). GPS Solution. 2003: 7: 143–144.
8. Dardanelli G, Maltese A, Pipitone C, et al. NRK, PPP or static, that is, the question. Testing different positioning solutions for GNSS survey. Remote Sensing. 2021; 13(7): 1406.
9. Zumberge JF, Heflin MB, Jefferson DC, et al. Precise point positioning for the efficient and robust analysis of GPS data from large networks. Journal of Geophysical Research. 1997; 102(B3): 5005–5017.
10. Dawidowicz K, Krzan G. Coordinate estimation accuracy of static Precise Point Positioning using online PPP service: A case study. Acta Geodaetica et Geophysica. 2014; 49: 37–55.
11. El-Mowafy A. Analysis of Web-Based GNSS Post-Processing Services for Static and Kinematic Positioning Using Short Data Spans. Survey Review. 2011; 43: 535–549.
12. Gandolfi S, Tavasci L, Poluzzi L. Study on GPS–PPP Precision for Short Observation Sessions. GPS Solut. 2017; 21: 887–896.
13. Ge Y, Cao X, Lyu D, et al. An investigation of PPP time transfer via BDS-3 PPP-B2b service. GPS Solutions. 2023; 27(2): 61.
14. Guo Q. Precision comparison and analysis of four online free PPP services in static positioning and tropospheric delay estimation. GPS Solutions. 2015; 19(4): 537–544.
15. Martín Furones ÁE, Anquela Julián AB, Berné Valero JL, Sanmartin M. Kinematic GNSS-PPP results from various software packages and raw data configurations. Scientific Research and Essays. 2012; 7(3): 419–431.
16. Anquela AB, Martín A, Berné JL, Padín J. Gps and Glonass Static and Kinematic PPP Results. J. Surv. Eng. 2013; 139: 47–58.
17. Abdallah A, Schwieger V. Kinematic Precise Point Positioning (PPP) Solution for Hydrographic Applications. In: Proceedings of the FIG Working Week May 2015 from the Wisdom of the Ages to the Challenges of the Modern World; Sofia, Bulgaria; 17–21 May 2015.
18. Alkan RM, Ozulu İM, Ilci V. Precise Point Positioning (PPP) technique versus network-RTK GNSS. FIG Working Week. 2016; 2016: 1–10.
19. DeSanto JB, Chadwell CD, Sandwell DT. Kinematic post-processing of ship navigation data using precise point positioning. Journal of Navigation. 2019; 72(3): 795–804.
20. Yang FX, Zhao L, Li L, et al. Performance evaluation of kinematic BDS/GNSS real-time precise point positioning for maritime positioning. Journal of Navigation. 2019; 72(1): 34–52.
21. ElShouny A, Miky Y. Accuracy assessment of relative and precise point-positioning online GPS processing services. Journal of Applied Geodesy. 2019: 13(3): 215–227.
22. Bulbul S, Bilgen B, Inal C. The performance assessment of Precise Point Positioning (PPP) under various observation conditions. Measurement. 2021; 171: 108780.
23. Mendez Astudillo J, Lau L, Tang YT, Moore T. Analyzing the Zenith Tropospheric Delay Estimates in online precise point Positioning (PPP) Services and PPP Software Packages. Sensors. 2018; 18: 580. doi: 10.3390/s18020580

24. Heo Y, Li B, Lim S, Rizos C. Development of a network real-time kinematic processing platform. In: Proceedings of the 22nd International Technical Meeting of Satellite Division of the Institute of Navigation (ION GNSS 2009); Savannah, GA, USA; 22–25 September 2009.
25. Lachapelle G, Cannon ME, Lu G. High Precision GPS Navigation with Emphasis on Carrier Phase Ambiguity Resolution. Marine Geodesy. 1992; 15: 253–269.
26. Al Shouny A, Kamel A, Miky Y. Kinematic precise point positioning heights enhancement using static measurements and Voronoi's corrector surface. International Journal of Digital Earth. 2024; 17(1): 2327843.
27. Alkan RM, Saka MH, Ozulu İM, İlçi V. Kinematic precise point positioning using GPS and GLONASS measurements in marine environments. Measurement. 2017; 109: 36–43.
28. Mireault Y, Tétreault P, Lahaye F, et al. Online Precise Point Positioning: A New, Timely Service from Natural Resources Canada. GPS World. 2008; 19(9): 59–64.
29. Natural Resources Canada. Precise Point Positioning. Available online: http://www.nrcan.gc.ca/earth-sciences/geomatics/geodetic-referencesystems/tools-applications/10925#ppp (accessed on 2 December 2022).
30. Tétreault P, Kouba J, Héroux P, Legree P. CSRS-PPP: An internet service for GPS user access to the Canadian spatial reference frame. Geomatica. 2005; 5 (1): 17–28.
31. Mutlu B, Erol S, Alkan RM. The performance analysis of the post-mission web-based static and kinematic PPP-AR service. Rudarsko-Geološko-Naftni Zbornik. 2023; 38(4): 103–116.
32. Heroux P, Kouba J. GPS precise point positioning using IGS orbit products. Phys. Chem. Earth. 2001; 26: 573–578
33. Survey Research Institute (SRI) Technical Report. The technical report of the survey work performed for the area between Rosetta and El-Brullus as part of the project adaptation of the Nile Delta to climatic changes and sea water rise. NWRC; 2014.
34. Sobeih MF, Doma MI, El Shoney AF. Mixture-Order Design of GPS Networks Based on Genetic algorithms. ERJ Engineering Research Journal. 2010; 33(4): 431–439.

Advances in Differential Equations and Control Processes 2025, 32(1), 2259.
https://doi.org/10.59400/adecp2259

Article

Learning of a certain homogeneous reducible differential equation by means of ChatGpt in engineering students during the second semester of 2024 in Antofagasta-Chile

Jorge Olivares[1,*], **Byron Droguett**[2], **Pablo Martin**[2]

[1] Department of Mathematics, University of Antofagasta, Antofagasta 1240000, Chile

[2] Department of Physics, University of Antofagasta, Antofagasta 1240000, Chile

*** Corresponding author:** Jorge Olivares, jorge.olivares@uantof.cl

CITATION

Olivares J, Droguett B, Martin P. Learning of a certain homogeneous reducible differential equation by means of ChatGpt in engineering students during the second semester of 2024 in Antofagasta-Chile. Advances in Differential Equations and Control Processes. 2025; 32(1): 2259. https://doi.org/10.59400/adecp2259

ARTICLE INFO

Received: 10 December 2024
Accepted: 6 February 2025
Available online: 17 March 2025

Abstract: The main objective of this research work was to investigate the learning of a certain homogeneous reducible differential equation by means of ChatGpt in engineering students, during the second semester of 2024 in Antofagasta-Chile. This research followed a qualitative case study approach. Four students of the differential equations course were chosen. Personalized interviews of three questions, related to the general objective and two specific ones, were established after solving a certain exercise, through ChatGpt collaboration. It was found that the opinions expressed about the use of this artificial intelligence are very positive and valuable, evidencing what was stated by several authors. Finally, it can be concluded that the perception of ChatGpt enriches the mathematical confidence in the development of computers, which generates security in learning.

Keywords: case study; qualitative; artificial intelligence; learning strategies; differential equations

1. Introduction

Research on learning the homogeneous reducible differential equation $y' = 2 - y/x$ using ChatGPT among engineering students, particularly at the University of Antofagasta in Chile, stems from the need to explore innovative educational methodologies that integrate advanced technological tools into the teaching-learning process. In an era where digital technologies play an increasingly prominent role in education, it is essential to investigate how platforms like ChatGPT can enhance the understanding of complex mathematical concepts and improve the overall learning experience. This study focuses on identifying both the positive aspects that students perceive when using this tool and the difficulties and limitations they face, which will allow us to obtain a comprehensive view of its effectiveness in learning homogeneous reducible differential equations. The qualitative case study approach selected for this research is particularly appropriate as it allows a deep and contextualized exploration of the experiences perceived by the students. Through interviews and a problem to solve, this approach offers a rich understanding of the phenomenon studied, which can contribute to the improvement of educational practices along with the birth of new strategies, as stated by [1–8]. In [9], research on the teaching of differential equations highlights that this is an active field with a growing number of articles published over the last decade. However, much remains to be done to address the challenges associated with teaching and learning differential equations through the use of artificial intelligence in the various educational institutions where this subject is taught.

Lastly, the use of teaching strategies, along with information and communication technologies (ICT) such as ChatGPT, can strengthen teacher-student relationships and contribute to the creation of environments conducive to knowledge and learning [10].

2. Methodology and materials

The present research is a qualitative case study in which 4 students, out of a total of 12, were selected by the principal investigator from an engineering differential equations course during the second semester of 2024. The study investigates the role of ChatGPT in the learning process for solving a homogeneous reducible differential equation.

2.1. Objectives

2.1.1. General objective

To investigate the learning process of the homogeneous reducible differential equation

$$\frac{dy}{dx} = 2 - \frac{y}{x}$$

using ChatGPT among engineering students during the second semester of 2024 in Antofagasta, Chile.

2.1.2. Specific objectives

1) To identify the positive aspects perceived by engineering students when using ChatGPT to learn the homogeneous reducible differential equation.
2) To explore the difficulties and limitations experienced by engineering students in using ChatGPT to solve the homogeneous reducible differential equation.

2.2. Methodology

The study was divided into the following phases:

2.2.1. Phase 1: Initial resolution

The teacher and 12 students were in a classroom equipped with internet access and computers. The teacher divided the students into 3 groups of 4 and sent them the exercise

$$\frac{dy}{dx} = 2 - \frac{y}{x}$$

via email. Students were instructed to solve the problem without using AI or other technological tools, and without consulting the teacher. This phase lasted 30 min.

2.2.2. Phase 2: Interaction with ChatGPT

The teacher provided a link to ChatGPT: https://chatgpt.com/share/6715a21e-4388-800f-976b-d507a06a8e37.

Students were asked to use ChatGPT individually, and as groups to solve the exercise, and to provide feedback on the answers generated by the AI. This phase lasted 30 min.

2.2.3. Phase 3: Sharing results

Each student shared their resolution of the exercise via email with their classmates and the teacher. This phase lasted 5 min.

2.2.4. Phase 4: Interviews

The teacher selected 4 students and conducted individual interviews, posing the following questions:

1) How would you describe your experience using ChatGPT to learn the differential equation $\frac{dy}{dx} = 2 - \frac{y}{x}$?
2) What specific aspects of ChatGPT did you find most beneficial in learning the differential equation $\frac{dy}{dx} = 2 - \frac{y}{x}$?
3) What were the main difficulties or limitations you faced in using ChatGPT to solve the differential equation $\frac{dy}{dx} = 2 - \frac{y}{x}$?

This phase lasted 25 min. At the end of the session, the teacher thanked all participants for their collaboration.

2.3. Answers given by students to the exercise

2.3.1. Answers given by first student

Figure 1 and the answers of the first student to the three interview questions were as follows:

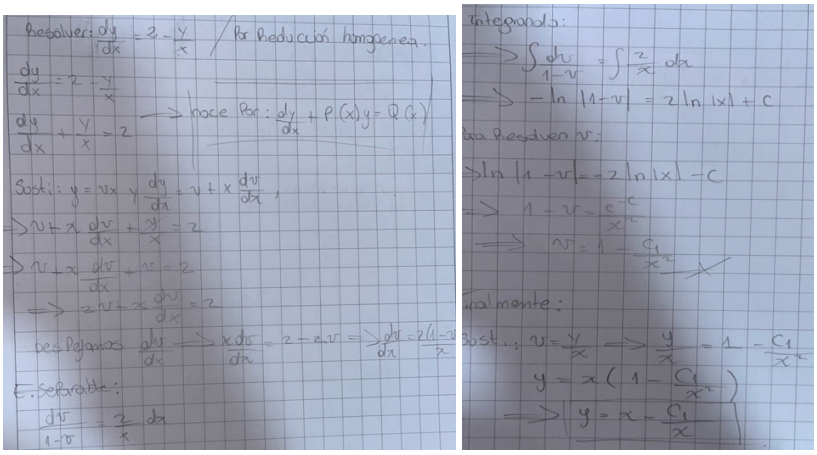

(**a**) (**b**)

Figure 1. Responses provided by first student. (**b**) is the continuation of the response in (**a**).

Response 1: My experience with this AI, in general, is always satisfactory because I found a very good tool for study, and everything is very easy to understand.

Response 2: The most specific aspects are the fast delivery of information and the ability to focus on exactly what you want to study. No matter how difficult the subject may seem, with this Artificial Intelligence, everything becomes easier.

Response 3: The main limitation is that the Artificial Intelligence is not free, which restricts the study time. Additionally, you have to be very specific in the instructions; otherwise, it may not provide the correct resolution or result.

2.3.2. Answers given by second student

Figure 2 and the second Student answers to the three interview questions were as follows:

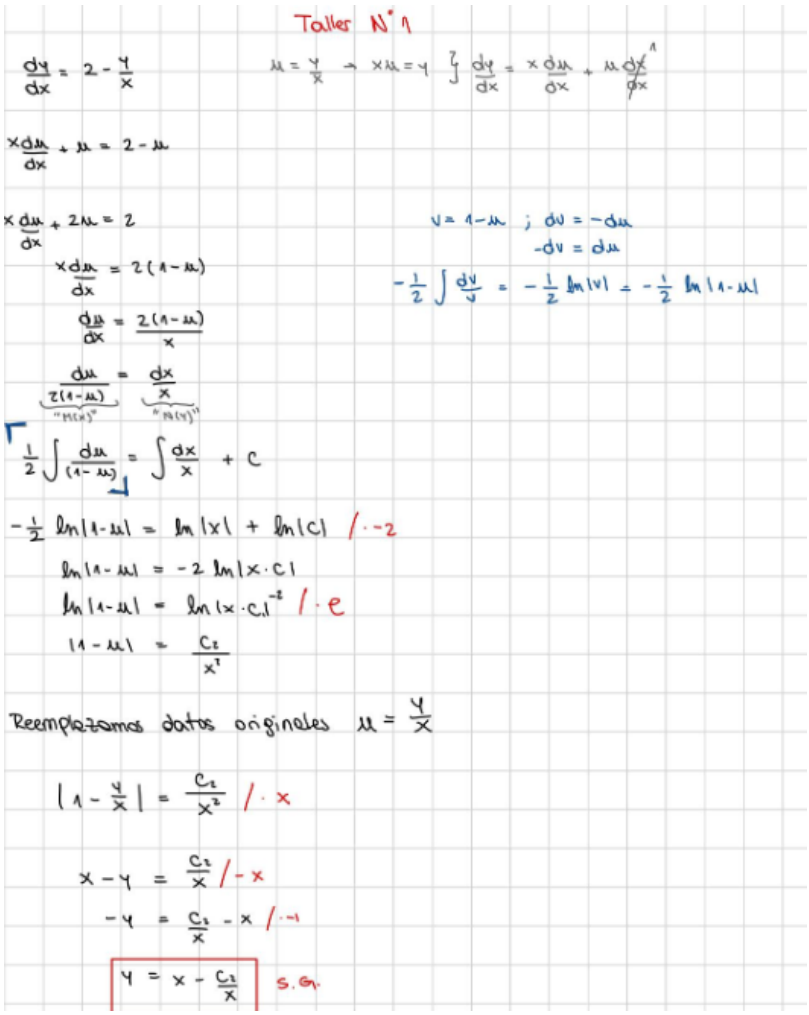

Figure 2. Responses provided by second student.

Response 1: This process was faster for me, because the steps were easier to visualize, and more aligned with my own approach.

Response 2: The most useful aspect was that the ChatGPT could explain concepts directly and clearly without skipping difficult steps, making them easy to understand on the first attempt.

Response 3: I did not find any difficulty in understanding each step, as it was very similar to my approach. However, ChatGPT skipped some steps that I had already understood.

2.3.3. Answers given by third student

Figure 3 and the third Student answers to the three interview questions were as follows:

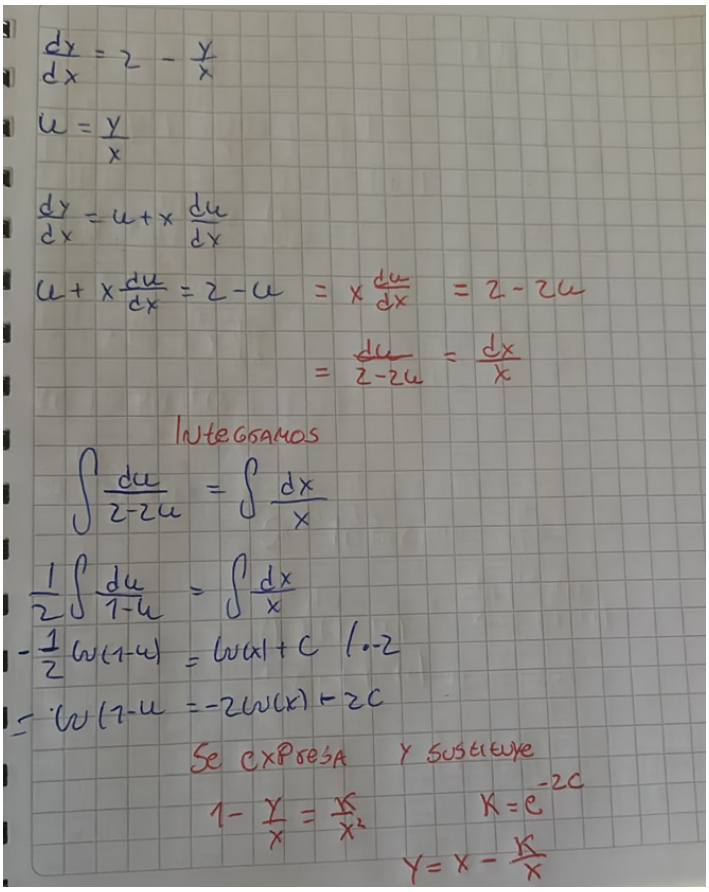

Figure 3. Responses provided by third student.

Response 1: It was really effective for studying because I could use ChatGPT's explanations as references when solving exercises.

Response 2: It simplified the process by breaking down the steps, allowing me to integrate them more easily without overcomplicating the process.

Response 3: ChatGPT can make mistakes, so it is not a good idea to rely 100%.

2.3.4. Answers given by student 4

Figure 4 and the fourth Student answers to the three interview questions were as follows:

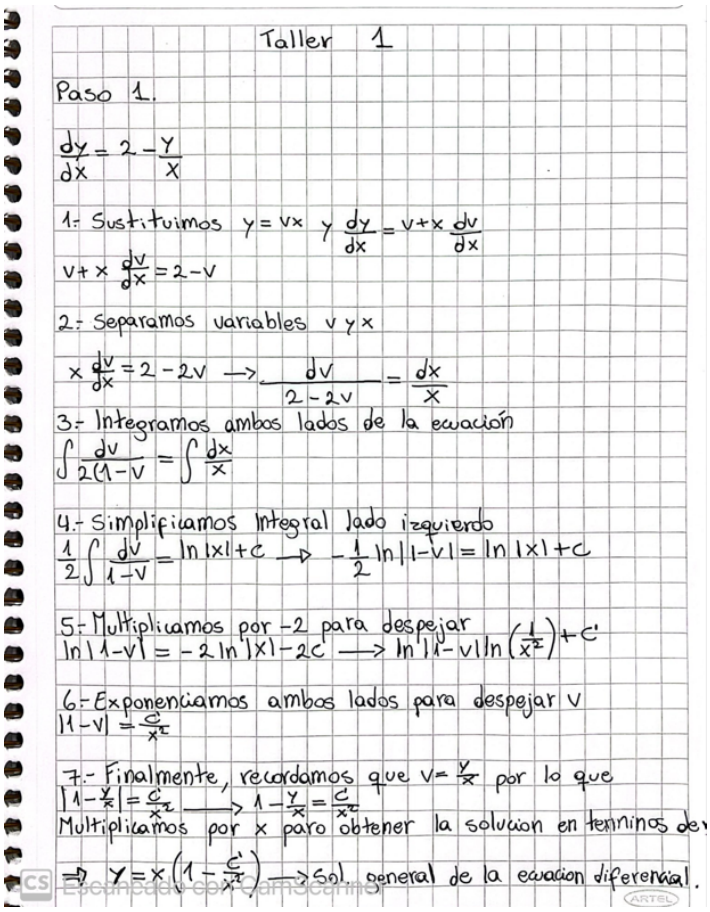

Figure 4. Responses provided by fourth student.

Response 1: My experience was good because it helped me significantly in solving the exercise.

Response 2: The most beneficial aspect was the clear, step-by-step explanations.

Response 3: I did not encounter any difficulties or limitations.

3. Discussion

The three interview questions were derived from the study of objectives. Based on the responses to question 1 and references [1,2], there is consensus on the importance of adapting educational strategies, such as to one employed in this research, to create positive educational experiences, and foster a blended, guided learning process involving both the teacher and ChatGPT.

Similarly, considering the answers to questions 2 and 3, along with reference [3], it becomes evident that conducting qualitative studies of this nature is essential. Such studies help establish clear expectations and to provide guidance on the integration of artificial intelligence tools like ChatGPT in mathematics learning processes [4], particularly in the context of differential equations.

4. Conclusions

4.1. Conclusion to question 1

The responses of the four students reflect a positive perception of using ChatGPT in learning differential equations. They found that the AI facilitated their understanding by providing clear and straightforward explanations of the steps. Additionally, they

noted that the tool made the learning process faster and more visually accessible, allowing them to derive useful references for their exercises.

4.2. Conclusion to question 2

In general, students appreciated the speed and accessibility of the information provided, as well as the clarity and simplicity of the explanations. They valued that ChatGPT did not omit challenging steps and affirmed the usefulness of the step-by-step, organized approach in the explanations.

4.3. Conclusion to question 3

Some students highlighted the need to provide very specific instructions and pointed out the limitation of access due to the tool not being free. Others mentioned that ChatGPT can occasionally make errors, which required them to confirm its output with additional sources. However, some students reported no significant difficulties, noting that the tool was straightforward and comprehensible.

5. Summary

In summary, the use of ChatGPT was enthusiastically received by students for their learning process. This indicates the need to continue exploring and rethinking traditional learning methods in light of advancements like ChatGPT, as suggested by references [5,6].

Furthermore, this research raises important questions for readers about conducting new studies that combine artificial intelligence with other software tools. It invites exploration of the educational and research activities that can be undertaken, as proposed in references [7,8].

Author contributions: Conceptualization, JO, BD and PM; methodology, JO, BD and PM; software, JO, BD and PM.; validation, JO, BD and PM; formal analysis, JO, BD and PM; resources, JO, BD and PM; data curation, JO, BD and PM; writing—original draft preparation, JO, BD and PM; writing—review and editing, JO, BD and PM; visualization, JO, BD and PM ; supervision, JO, BD and PM; project administration, JO, BD and PM; funding acquisition, JO, BD and PM. All authors have read and agreed to the published version of the manuscript.

Acknowledgments: This work was funded by Research Management Directorate at the University of Antofagasta-Chile. We thank the University of Antofagasta, especially the Teaching Innovation Management Area via the University Teaching Investigation Support Program (PAIDU) to which the University Teaching Investigation Core belongs (NIDU 2-001-22) called “Geogebra Applets for teaching Mathematics”, whose members are responsible for the investigation which led to the present publication. Thank you for your support, accompaniment and formative program intended to promote investigation in Teaching and elevating the academic indicators of this institution.

Conflict of interest: The authors declare no conflict of interest.

References

1. Sánchez-Ruiz LM, Moll-López S, Nuñez-Pérez A, et al. ChatGPT Challenges Blended Learning Methodologies in Engineering Education: A Case Study in Mathematics. Applied Sciences. 2023; 13(10): 6039.
2. Farahani MS, Ghasmi G. Artificial Intelligence in Education: A Comprehensive Study. Forum for Education Studies. 2024; 2(3): 1379.
3. Wardat Y, Tashtoush MA, AlAli R, Jarrah AM. ChatGPT: A Revolutionary Tool for Teaching and Learning Mathematics. Eurasia Journal of Mathematics, Science and Technology Education. 2023; 19(7): em2286.
4. Ávila MU, Crespo LF, Moya M, et al. Using GPT chat as a literacy strategy in digital teacher competence in mathematics education (Spanish). In: Proceedings of the 19th National Congress on Technology in Education and Education in Technology-TE&ET; 13–14 June 2024; Morón, Venezuela.
5. Galli MG, Kanobel MC. ChatGPT in Higher Education: exploring its potential and limitations (Spanish). Educación Superior y Sociedad (ESS). 2023; 35(2): 174–195.
6. Berrones Yaulema LP, Buenaño Barreno PN. ChatGPT in the Educational Environment (Spanish). Esprint Research. 2023; 2(2): 45–54.
7. Funes JO, Parada BD, de Julian PM, Villegas AB. Incorporation of GeoGebra Applets and ChatGPT to Strengthen the Learning of Exact Equations in Engineering Students. In: Mathematics and Computer Science: Contemporary Developments. Narosa Publishing House; 2024. pp. 133–143.
8. Funes JO, Valero Kari ER, Martin P. Description of Parameter Variation Learning with Artificial Intelligence and GeoGebra in Students of a Differential Equations Course. Journal of Physics: Conference Series. 2024; 2701: 012049.
9. Lozada E, Guerrero-Ortiz C, Coronel A, Medina R. Classroom methodologies for teaching and learning ordinary differential equations: A systemic literature review and bibliometric analysis. Mathematics. 2021; 9(7): 745.
10. Ojeda AD, Solano-Barliza AD, Alvarez D, Cárcamo EB. Analysis of the impact of ChatGPT artificial intelligence on teaching and learning processes in higher education (Spanish). Formación Universitaria. 2023; 16(6): 61–70.

Advances in Differential Equations and Control Processes 2025, 32(1), 2489.
https://doi.org/10.59400/adecp2489

Article

Numerical solution of a 3D mathematical model for the progression of tumor angiogenic factor in a tissue

Melike Keleş Duman, Serdal Pamuk*

Department of Mathematics, University of Kocaeli (Umuttepe Campus), Kocaeli 41001, Turkey
*** Corresponding author:** Serdal Pamuk, spamuk@kocaeli.edu.tr

CITATION

Duman MK, Pamuk S. Numerical solution of a 3D mathematical model for the progression of tumor angiogenic factor in a tissue. Advances in Differential Equations and Control Processes. 2025; 32(1): 2489.
https://doi.org/10.59400/adecp2489

ARTICLE INFO

Received: 31 December 2024
Accepted: 5 March 2025
Available online: 18 March 2025

Abstract: In this work, the movement of tumor angiogenic factor in a three-dimensional tissue is obtained by the Method of Lines. This method transforms a partial differential equation into a system of ordinary differential equations together with the initial and boundary conditions. The more the number of lines is increased, the more the accuracy of the method increases. This method results in very accurate numerical solutions for linear and non-linear problems in contrast with other existing methods. We present Matlab-generated figures, which are the movement of tumor angiogenic factor in porous medium and explain the biological importance of this progression. The computer codes are also provided.

Keywords: method of lines; porosity; tumor angiogenic factor; numerical solution; porous medium

1. Introduction

Angiogenesis is known as the formation of new capillaries from pre-existing vessels in a tissue. Tumor growth and metastasis depend on angiogenesis and lymphangiogenesis triggered by a chemical signal from tumor angiogenic factor (TAF), in a phase of rapid growth [1]. Over the last few years, some mathematical models have appeared in the literature to estimate and observe the behavior of the tumor growth process.

The Method of Lines (MOL) is a general way of converting a partial differential equation (PDE) to a system of ordinary differential equations (ODE) [2,3]. The partial derivatives concerning the space variables are discretized to get a system of ODE together with initial and boundary conditions. The choice of spatial discretization and the position of the spatial discretization points are important for the performance of the method [4]. One can find a general framework for a convergence analysis of this method to nonlinear problems in [5] where the readers may find out the 'distance' between the solution to the system of ODE and the solution to the given PDE. It is worth emphasizing a few words about the accuracy of the method: High-order spatial and temporal discretization improves accuracy but increases computational cost; also, explicit schemes require small time steps for stability, while implicit schemes avoid this but are more expensive. Sometimes, choosing the 'right' scheme depends on the structure of the problem.

The advantage of the MOL is that it has not only the simplicity of the explicit methods but also the stability advantage of the implicit ones [3,6]. MOL is popularly used in science and engineering fields [7–10]. Moreover, it has wide applicability to physical, chemical, and biological systems modeled by PDE.

The MOL is applied to various types of problems such as the fractional diffusion equation [11,12], parabolic integro-differential equations [13], two-dimensional sine-Gordon equation [14], elliptic partial differential equations which describe steady-state mass and energy transport in solids [15], parabolic partial differential equations [4,16] and hyperbolic partial differential equations with stiff nonlinear source terms [17]. Also, the Authors of [18] applied the MOL for 1D, 2D and 3D heat equations with Dirichlet, Neumann, Robin and periodic boundary conditions and obtained the convergence criteria for this method for all types of boundary conditions.

In [2] the Authors applied the MOL to get the numerical solution of a 1D model of TAF for the movement of endothelial cells in the capillary while in [19] they solved numerically the analogous 2D model in ExtraCellular Matrix (ECM), where they envisaged a capillary segment of length L microns located along the x-axis on the interval $[0, L]$ with a tumor located l microns above the y-axis as shown in **Figure 1**. After they scaled x by x/L and y by y/l they obtained a unit square $[0,1] \times [0,1]$, which we will be using 'this' matrix in our computations.

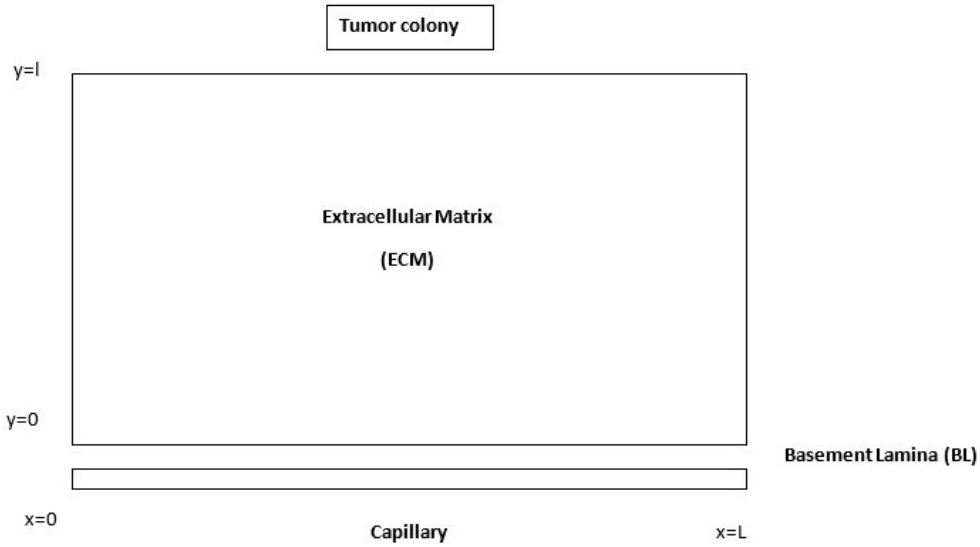

Figure 1. ExtraCellular Matrix (ECM).

Moving from 2D to 3D tumor modeling introduces several key novelties that significantly improve the realism and predictive power of the model. While 2D models are computationally efficient and useful for preliminary studies, 3D models capture the full spatial complexity of tumor growth, making them more biologically relevant [20–28]. In 2D models cells move only in a plane, ignoring migration in the z-axis while in 3D models cells migrate in all directions, better modeling metastasis, invasion, and ECM interactions. Therefore, the novelty in transitioning from 2D to 3D tumor modeling is that 3D tumor modeling brings us closer to real tumor behavior**,** allowing for personalized medicine, accurate treatment simulations, and better predictions for patient outcomes [18,29–34].

In light of this fact, we focus on the progression of TAF in 3D and study the following problem originally studied in [19] in 2D version:

$$u_t = \nabla.\big(D(x,y,z)\nabla(u^n)\big) + u_r(y,z,t), (x,y,z) \in \Omega, 0 < t \leq T \qquad (1)$$

$$u(x,y,z,0) = 0, (x,y,z) \in \Omega \tag{2}$$

$$u_x(0,y,z,t) - \alpha u(0,y,z,t) = 0, (y,z) \in \partial\Omega|_{x=0},\ 0 < t \leq T \tag{3}$$

$$u(1,y,z,t) = 0, (y,z) \in \partial\Omega|_{x=1},\ 0 < t \leq T \tag{4}$$

$$u_y(x,0,z,t) = 0, (x,z) \in \partial\Omega|_{y=0},\ 0 < t \leq T \tag{5}$$

$$u_y(x,1,z,t) = 0, (x,z) \in \partial\Omega|_{y=1},\ 0 < t \leq T \tag{6}$$

$$u_z(x,y,0,t) = 0, (x,y) \in \partial\Omega|_{z=0},\ 0 < t \leq T \tag{7}$$

$$u_z(x,y,1,t) = 0, (x,y) \in \partial\Omega|_{z=1},\ 0 < t \leq T \tag{8}$$

(One may find the derivation of Equation (1) in Appendix A) where $u = u(x,y,z,t)$ and $D(x,y,z)$ represent the TAF concentration and the TAF diffusion in a porous medium, respectively. Here, $\Omega \subset \boldsymbol{R}^3$ is an open bounded domain with a smooth boundary $\partial\Omega$ and α is a positive constant. As mentioned in [35], the diffusion process is a complex phenomenon that occurs in three dimensions. There, the Authors provide a nice analysis for their fractal diffusion equation model to obtain the relation between the diffusion coefficient and the two-scale fractality for the porosity. Therefore, one may call n in Equation (1) as the parameter associated with porosity. Also, $u_r(y,z,t)$ represents a source function for the TAF that is being supplied to the tissue throughout the domain.

$$u_r(y,z,t) = \begin{cases} v_0 \dfrac{\left(1 - e^{-\left(1-\frac{r}{\delta}\right)^2}\right)^m}{1 - e^{-1}}, & r \leq \delta \\ 0, & r > \delta \end{cases}$$

where $r = \sqrt{\left(y - \frac{1}{2}\right)^2 + \left(z - \frac{1}{2}\right)^2}$, $(0 \leq y, z \leq 1)$, the radius of a circle centered at the point $(1/2,1/2)$, and v_0, δ and m are some positive constants (see **Figure 2**). Our source function u_r is the type of a unimodal function (kind of a Gaussian Source Function). In tumor modeling it refers to a function that has a single peak, meaning the tumor growth rate initially increases in the ECM, reaches a maximum, and then declines. This function is particularly useful for capturing tumor growth dynamics influenced by resource limitations, immune response, or therapy effects**.** It is known that a unimodal function allows for the inclusion of both proliferation and apoptosis (cell death).

2. Method

We now apply MOL to our problem defined by Equations (1)–(8) by choosing as a block-shaped domain. The reason why we choose such a domain is that the treatment of boundary conditions in the finite difference approach (and by extension MOL) is crucial in determining the accuracy, stability and convergence of the solution. Even

small errors in how the boundary conditions are handled can lead to large inaccuracies in the solution, particularly when sharp gradients or fluxes are involved.

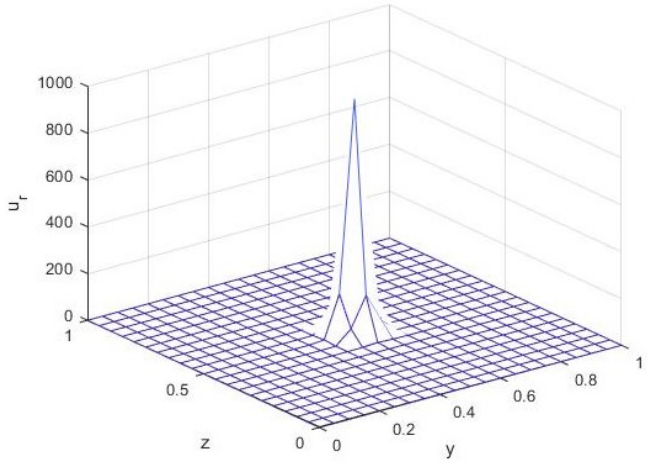

Figure 2. The source function $u_r(y, z, t)$.

While numerically solving our problem we may have sharp gradients (on the boundaries of the domain) especially for nonlinear cases. Therefore, we take $\Omega = [0,1] \times [0,1] \times [0,1]$ and envisage a uniform grid $W = \{(x_i, y_j, z_k, t)\colon x_i = (i-1)h_x, y_j = (j-1)h_y, z_k = (k-1)h_z, i = 1\colon M, j = 1\colon N, k = 1\colon K, h_x = 1/(M-1), h_y = 1/(N-1), h_z = 1/(K-1)\}$ on Ω (as sketched in **Figure 3**).

Since it is hard to find experimental data for $D(x, y, z)$ and n, we take them as positive constants (using literature values) for our numerical computations. We also suppose that the solution of Equation (1), $u(x, y, z, t)$ can be approximated by $u_{i,j,k} = u(x_i, y_j, z_k, t)$. We now discretize Equation (1) by central difference approximation to obtain the following difference scheme.

$$\frac{du_{i,j,k}}{dt} \sim D\left(\frac{u^n_{i+1,j,k} - 2u^n_{i,j,k} + u^n_{i-1,j,k}}{h_x^2} + \frac{u^n_{i,j+1,k} - 2u^n_{i,j,k} + u^n_{i,j-1,k}}{h_y^2} + \frac{u^n_{i,j,k+1} - 2u^n_{i,j,k} + u^n_{i,j,k-1}}{h_z^2}\right) + u_{r\,j,k} \quad (9)$$

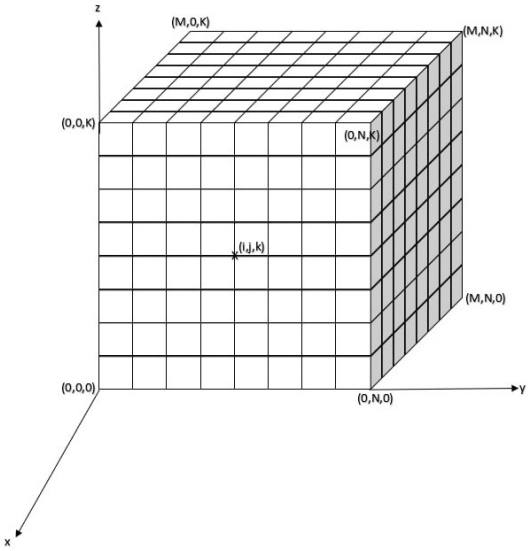

Figure 3. Geometry of the mesh points.

The initial and boundary conditions in Equations (2)–(8) become

$$u_{i,j,k} = 0, i = 1{:}M, j = 1{:}N, k = 1{:}K, t = 0 \tag{10}$$

$$\frac{\partial u_{1,j,k}}{\partial x} - \alpha u_{1,j,k} = 0, j = 1{:}N, k = 1{:}K, t > 0 \tag{11}$$

$$u_{M,j,k} = 0, j = 1{:}N, k = 1{:}K, t > 0 \tag{12}$$

$$\frac{\partial u_{i,1,k}}{\partial y} = \frac{\partial u_{i,N,k}}{\partial y} = 0, i = 1{:}M, k = 1{:}K, t > 0 \tag{13}$$

$$\frac{\partial u_{i,j,1}}{\partial z} = \frac{\partial u_{i,j,K}}{\partial z} = 0, i = 1{:}M, j = 1{:}N, t > 0 \tag{14}$$

Similarly, using the central difference approximations for the boundary conditions in Equations (11), (13) and (14), we get the following large system of ODE from Equation (9)

$$\frac{du_{1,1,1}}{dt} = \frac{2D}{h_x^2}u_{2,1,1}^n - 2D\left(\frac{1}{h_x^2} + \frac{1}{h_y^2} + \frac{1}{h_z^2} + \frac{\alpha}{h_x}\right)u_{1,1,1}^n + \frac{2D}{h_y^2}u_{1,2,1}^n + \frac{2D}{h_z^2}u_{1,1,2}^n + u_{r_{1,1}} \tag{15}$$

$$\frac{du_{M,1,1}}{dt} = \frac{D}{h_x^2}\left(u_{M-1,1,1}^n\right) - 2D\left(\frac{1}{h_x^2} + \frac{1}{h_y^2} + \frac{1}{h_z^2}\right)u_{M,1,1}^n + \frac{2D}{h_y^2}u_{M,2,1}^n + \frac{2D}{h_z^2}u_{M,1,2}^n + u_{r_{1,1}} \tag{16}$$

$$\frac{du_{1,N,1}}{dt} = \frac{2D}{h_x^2}u_{2,N,1}^n - 2D\left(\frac{1}{h_x^2} + \frac{1}{h_y^2} + \frac{1}{h_z^2} + \frac{\alpha}{h_x}\right)u_{1,N,1}^n + \frac{2D}{h_y^2}u_{1,N-1,1}^n + \frac{2D}{h_z^2}u_{1,N,2}^n + u_{r_{N,1}} \tag{17}$$

$$\frac{du_{1,1,K}}{dt} = \frac{2D}{h_x^2}u_{2,1,K}^n - 2D\left(\frac{1}{h_x^2} + \frac{1}{h_y^2} + \frac{1}{h_z^2} + \frac{\alpha}{h_x}\right)u_{1,1,K}^n + \frac{2D}{h_y^2}u_{1,2,K}^n + \frac{2D}{h_z^2}u_{1,1,K-1}^n + u_{r_{1,K}} \tag{18}$$

$$\frac{du_{1,N,K}}{dt} = \frac{2D}{h_x^2}u_{2,N,K}^n - 2D\left(\frac{1}{h_x^2} + \frac{1}{h_y^2} + \frac{1}{h_z^2} + \frac{\alpha}{h_x}\right)u_{1,N,K}^n + \frac{2D}{h_y^2}u_{1,N-1,K}^n + \frac{2D}{h_z^2}u_{1,N,K-1}^n + u_{r_{N,K}} \tag{19}$$

$$\frac{du_{M,1,K}}{dt} = \frac{D}{h_x^2}\left(u_{M-1,1,K}^n\right) - 2D\left(\frac{1}{h_x^2} + \frac{1}{h_y^2} + \frac{1}{h_z^2}\right)u_{M,1,K}^n + \frac{2D}{h_y^2}u_{M,2,K}^n + \frac{2D}{h_z^2}u_{M,1,K-1}^n + u_{r_{1,K}} \tag{20}$$

$$\frac{du_{M,N,1}}{dt} = \frac{D}{h_x^2}\left(u_{M-1,N,1}^n\right) - 2D\left(\frac{1}{h_x^2} + \frac{1}{h_y^2} + \frac{1}{h_z^2}\right)u_{M,N,1}^n + \frac{2D}{h_y^2}u_{M,N-1,1}^n + \frac{2D}{h_z^2}u_{M,N,2}^n + u_{r_{N,1}} \tag{21}$$

$$\frac{du_{M,N,K}}{dt} = \frac{D}{h_x^2}\left(u_{M-1,N,K}^n\right) - 2D\left(\frac{1}{h_x^2} + \frac{1}{h_y^2} + \frac{1}{h_z^2}\right)u_{M,N,K}^n + \frac{2D}{h_y^2}u_{M,N-1,K}^n + \frac{2D}{h_z^2}u_{M,N,K-1}^n + u_{r_{N,K}} \tag{22}$$

$$\frac{du_{i,1,1}}{dt} = \frac{D}{h_x^2}\left(u_{i+1,1,1}^n + u_{i-1,1,1}^n\right) - 2D\left(\frac{1}{h_x^2} + \frac{1}{h_y^2} + \frac{1}{h_z^2}\right)u_{i,1,1}^n + \frac{2D}{h_y^2}u_{i,2,1}^n + \frac{2D}{h_z^2}u_{i,1,2}^n + u_{r_{1,1}},\ \ i = 2{:}M-1 \tag{23}$$

$$\frac{du_{i,1,K}}{dt} = \frac{D}{h_x^2}\left(u_{i+1,1,K}^n + u_{i-1,1,K}^n\right) - 2D\left(\frac{1}{h_x^2} + \frac{1}{h_y^2} + \frac{1}{h_z^2}\right)u_{i,1,K}^n + \frac{2D}{h_y^2}u_{i,2,K}^n + \frac{2D}{h_z^2}u_{i,1,K-1}^n + u_{r_{1,K}},\ \ i = 2{:}M-1 \tag{24}$$

$$\frac{du_{i,N,1}}{dt}=\frac{D}{h_x^2}\left(u_{i+1,N,1}^n+u_{i-1,N,1}^n\right)-2D\left(\frac{1}{h_x^2}+\frac{1}{h_y^2}+\frac{1}{h_z^2}\right)u_{i,N,1}^n+\frac{2D}{h_y^2}u_{i,N-1,1}^n+\frac{2D}{h_z^2}u_{i,N,2}^n+u_{r_{N,1}},\ \ i=2:M-1 \tag{25}$$

$$\frac{du_{i,N,K}}{dt}=\frac{D}{h_x^2}\left(u_{i+1,N,K}^n+u_{i-1,N,K}^n\right)-2D\left(\frac{1}{h_x^2}+\frac{1}{h_y^2}+\frac{1}{h_z^2}\right)u_{i,N,K}^n+\frac{2D}{h_y^2}u_{i,N-1,K}^n+\frac{2D}{h_z^2}u_{i,N,K-1}^n+u_{r_{N,K}},\ \ i=2:M-1 \tag{26}$$

$$\frac{du_{1,j,1}}{dt}=\frac{2D}{h_x^2}u_{2,j,1}^n-2D\left(\frac{1}{h_x^2}+\frac{1}{h_y^2}+\frac{1}{h_z^2}+\frac{\alpha}{h_x}\right)u_{1,j,1}^n+\frac{D}{h_y^2}\left(u_{1,j+1,1}^n+u_{1,j-1,1}^n\right)+\frac{2D}{h_z^2}u_{1,j,2}^n+u_{r_{j,1}},\ j=2:N-1 \tag{27}$$

$$\frac{du_{1,j,K}}{dt}=\frac{2D}{h_x^2}u_{2,j,K}^n-2D\left(\frac{1}{h_x^2}+\frac{1}{h_y^2}+\frac{1}{h_z^2}+\frac{\alpha}{h_x}\right)u_{1,j,K}^n+\frac{D}{h_y^2}\left(u_{1,j+1,K}^n+u_{1,j-1,K}^n\right)+\frac{2D}{h_z^2}u_{1,j,K-1}^n+u_{r_{j,K}},j=2:N-1 \tag{28}$$

$$\frac{du_{M,j,1}}{dt}=\frac{D}{h_x^2}\left(u_{M-1,j,1}^n\right)-2D\left(\frac{1}{h_x^2}+\frac{1}{h_y^2}+\frac{1}{h_z^2}\right)u_{M,j,1}^n+\frac{2D}{h_z^2}u_{M,j,2}^n+\frac{D}{h_y^2}\left(u_{M,j+1,1}^n+u_{M,j-1,1}^n\right)+u_{r_{j,1}},\ \ j=2:N-1 \tag{29}$$

$$\frac{du_{M,j,K}}{dt}=\frac{D}{h_x^2}\left(u_{M-1,j,K}^n\right)-2D\left(\frac{1}{h_x^2}+\frac{1}{h_y^2}+\frac{1}{h_z^2}\right)u_{M,j,K}^n+\frac{2D}{h_z^2}u_{M,j,K-1}^n+\frac{D}{h_y^2}\left(u_{M,j+1,K}^n+u_{M,j-1,K}^n\right)+u_{r_{j,K}},\ j=2:N-1 \tag{30}$$

$$\frac{du_{1,1,k}}{dt}=\frac{2D}{h_x^2}u_{2,1,k}^n-2D\left(\frac{1}{h_x^2}+\frac{1}{h_y^2}+\frac{1}{h_z^2}+\frac{\alpha}{h_x}\right)u_{1,1,k}^n+\frac{2D}{h_y^2}u_{1,2,k}^n+\frac{D}{h_z^2}\left(u_{1,1,k+1}^n+u_{1,1,k-1}^n\right)+u_{r_{1,k}},k=2:K-1 \tag{31}$$

$$\frac{du_{M,1,k}}{dt}=\frac{D}{h_x^2}\left(u_{M-1,1,k}^n\right)-2D\left(\frac{1}{h_x^2}+\frac{1}{h_y^2}+\frac{1}{h_z^2}\right)u_{M,1,k}^n+\frac{2D}{h_y^2}u_{M,2,k}^n+\frac{D}{h_z^2}\left(u_{M,1,k+1}^n+u_{M,1,k-1}^n\right)+u_{r_{1,k}},\ \ k=2:K-1 \tag{32}$$

$$\frac{du_{1,N,k}}{dt}=\frac{2D}{h_x^2}u_{2,N,k}^n-2D\left(\frac{1}{h_x^2}+\frac{1}{h_y^2}+\frac{1}{h_z^2}+\frac{\alpha}{h_x}\right)u_{1,N,k}^n+\frac{2D}{h_y^2}u_{1,N-1,k}\frac{D}{h_z^2}+\left(u_{1,N,k+1}^n+u_{1,N,k-1}^n\right)+u_{r_{N,k}},\ \ k=2:K-1 \tag{33}$$

$$\frac{du_{M,N,k}}{dt}=\frac{D}{h_x^2}\left(u_{M-1,N,k}^n\right)-2D\left(\frac{1}{h_x^2}+\frac{1}{h_y^2}+\frac{1}{h_z^2}h_x\right)u_{M,N,k}^n+\frac{2D}{h_y^2}u_{M,N-1,k}\frac{D}{h_z^2}+\left(u_{M,N,k+1}^n+u_{M,N,k-1}^n\right)+u_{r_{N,k}},\ \ k=2:K-1 \tag{34}$$

$$\frac{du_{1,j,k}}{dt}=\frac{D}{h_y^2}\left(u_{1,j+1,k}^n+u_{1,j-1,k}^n\right)-2D\left(\frac{1}{h_x^2}+\frac{1}{h_y^2}+\frac{1}{h_z^2}+\frac{\alpha}{h_x}\right)u_{1,j,k}^n+\frac{D}{h_z^2}\left(u_{1,j,k+1}^n+u_{1,j,k-1}^n\right)+\frac{2D}{h_x^2}u_{2,j,k}^n+u_{r_{j,k}},\ j=2:N-1,k=2:K-1 \tag{35}$$

$$\frac{du_{M,j,k}}{dt} = \frac{D}{h_x^2}\left(u^n_{M-1,j,k}\right) - 2D\left(\frac{1}{h_x^2}+\frac{1}{h_y^2}+\frac{1}{h_z^2}\right)u^n_{M,j,k} + \frac{D}{h_y^2}\left(u^n_{M,j+1,k}+u^n_{M,j-1,k}\right) + \frac{D}{h_z^2}\left(u^n_{M,j,k+1}+u^n_{M,j,k-1}\right) + u_{r_{j,k}}, j = 2{:}N-1, k = 2{:}K-1 \tag{36}$$

$$\frac{du_{i,1,k}}{dt} = \frac{D}{h_x^2}\left(u^n_{i+1,1,k}+u^n_{i-1,1,k}\right) - 2D\left(\frac{1}{h_x^2}+\frac{1}{h_y^2}+\frac{1}{h_z^2}\right)u^n_{i,1,k} + \frac{2D}{h_y^2}u^n_{i,2,k} + \frac{D}{h_z^2}\left(u^n_{i,1,k+1}+u^n_{i,1,k-1}\right) + u_{r_{1,k}},\ i = 2{:}M-1, k = 2{:}K-1 \tag{37}$$

$$\frac{du_{i,N,k}}{dt} = \frac{D}{h_x^2}\left(u^n_{i+1,N,k}+u^n_{i-1,N,k}\right) - 2D\left(\frac{1}{h_x^2}+\frac{1}{h_y^2}+\frac{1}{h_z^2}\right)u^n_{i,N,k} + \frac{2D}{h_y^2}u^n_{i,N-1,k} + \frac{D}{h_z^2}\left(u^n_{i,N,k+1}+u^n_{i,N,k-1}\right) + u_{r_{N,k}},\ i = 2{:}M-1, k = 2{:}K-1 \tag{38}$$

$$\frac{du_{i,j,1}}{dt} = \frac{D}{h_x^2}\left(u^n_{i+1,j,1}+u^n_{i-1,j,1}\right) - 2D\left(\frac{1}{h_x^2}+\frac{1}{h_y^2}+\frac{1}{h_z^2}\right)u^n_{i,j,1} + \frac{D}{h_y^2}\left(u^n_{i,j+1,1}+u^n_{i,j-1,1}\right) + \frac{2D}{h_z^2}u^n_{i,j,2} + u_{r_{j,1}}, i = 2{:}M-1, j = 2{:}N-1, \tag{39}$$

$$\frac{du_{i,j,K}}{dt} = \frac{D}{h_x^2}\left(u^n_{i+1,j,K}+u^n_{i-1,j,K}\right) - 2D\left(\frac{1}{h_x^2}+\frac{1}{h_y^2}+\frac{1}{h_z^2}\right)u^n_{i,j,K} + \frac{2D}{h_z^2}u^n_{i,j,K-1} + \frac{D}{h_y^2}\left(u^n_{i,j+1,K}+u^n_{i,j-1,K}\right) + u_{r_{j,K}}, i = 2{:}M-1, j = 2{:}N-1 \tag{40}$$

To validate this system of ODE, since our 3D model is an extension of the 2D model by [19], we show below that our system reduces exactly to the system on page 893 of [19]. We do it by taking $k = 1$ (which corresponds to taking $z = 0$) in the uniform grid W defined above so that it becomes $W = \{(x_i, y_j, t): x_i = (i-1)h_x, y_j = (j-1)h_y, i = 1{:}M, j = 1{:}N, h_x = 1/(M-1), h_y = 1/(N-1)\}$ on the unit square $[0,1] \times [0,1]$. In this case $u(x,y,z,t)$ can be approximated by $u_{i,j,l}$ (or simply by $u_{i,j}$), and the system of ODE Equations (15)–(40) now reads

$$\frac{du_{1,1}}{dt} = \frac{2D}{h_x^2}u^n_{2,1} - 2D\left(\frac{1}{h_x^2}+\frac{1}{h_y^2}+\frac{\alpha}{h_x}\right)u^n_{1,1} + \frac{2D}{h_y^2}u^n_{1,2} + u_{r_1} \tag{41}$$

$$\frac{du_{M,1}}{dt} = \frac{D}{h_x^2}\left(u^n_{M-1,1}\right) - 2D\left(\frac{1}{h_x^2}+\frac{1}{h_y^2}\right)u^n_{M,1} + \frac{2D}{h_y^2}u^n_{M,2} + u_{r_1} \tag{42}$$

$$\frac{du_{1,N}}{dt} = \frac{2D}{h_x^2}u^n_{2,N} - 2D\left(\frac{1}{h_x^2}+\frac{1}{h_y^2}+\frac{\alpha}{h_x}\right)u^n_{1,N} + \frac{2D}{h_y^2}u^n_{1,N-1} + u_{r_N} \tag{43}$$

$$\frac{du_{M,N}}{dt} = \frac{D}{h_x^2}\left(u^n_{M-1,N}\right) - 2D\left(\frac{1}{h_x^2}+\frac{1}{h_y^2}\right)u^n_{M,N} + \frac{2D}{h_y^2}u^n_{M,N-1} + u_{r_N} \tag{44}$$

$$\frac{du_{i,1}}{dt} = \frac{D}{h_x^2}\left(u^n_{i+1,1}+u^n_{i-1,1}\right) - 2D\left(\frac{1}{h_x^2}+\frac{1}{h_y^2}\right)u^n_{i,1} + \frac{2D}{h_y^2}u^n_{i,2} + u_{r_1}, i = 2{:}M-1 \tag{45}$$

$$\frac{du_{i,N}}{dt} = \frac{D}{h_x^2}\left(u^n_{i+1,N}+u^n_{i-1,N}\right) - 2D\left(\frac{1}{h_x^2}+\frac{1}{h_y^2}\right)u^n_{i,N} + \frac{2D}{h_y^2}u^n_{i,N-1} + u_{r_N}, i = 2{:}M-1 \tag{46}$$

$$\frac{du_{1,j}}{dt} = \frac{2D}{h_x^2}u_{2,j}^n - 2D\left(\frac{1}{h_x^2} + \frac{1}{h_y^2} + \frac{\alpha}{h_x}\right)u_{1,j}^n + \frac{D}{h_y^2}\left(u_{1,j+1}^n + u_{1,j-1}^n\right) + u_{r_j}, j = 2{:}N-1 \quad (47)$$

$$\frac{du_{M,j}}{dt} = \frac{D}{h_x^2}\left(u_{M-1,j}^n\right) + \frac{D}{h_y^2}\left(u_{M,j+1}^n + u_{M,j-1}^n\right) - 2D\left(\frac{1}{h_x^2} + \frac{1}{h_y^2}\right)u_{M,j}^n + u_{r_j}, j = 2{:}N-1 \quad (48)$$

$$\frac{du_{i,j}}{dt} = \frac{D}{h_x^2}\left(u_{i+1,j}^n + u_{i-1,j}^n\right) - 2D\left(\frac{1}{h_x^2} + \frac{1}{h_y^2}\right)u_{i,j}^n + \frac{D}{h_y^2}\left(u_{i,j+1}^n + u_{i,j-1}^n\right) + u_{r_j}, i = 2{:}M-1, j = 2{:}N-1 \quad (49)$$

which is exactly the system of ODE on page 893 of [19].

3. Numerical experiments

In this section we obtain the numerical solution of the initial-boundary value problem given in Equations (1)–(8). We let $D = 0.0036, \alpha = 0.05, v_0 = 1000, m = 3, \delta = 0.15, M = 21, N = 21$ and $K = 21$ for numerical purposes. We take $n = 1$ for the linear case and take $n = 2$ for the non-linear case. We write the following computer code in Matlab in order to perform numerical solutions of the large ODE system appearing in Equations (15)–(40) together with the initial and boundary conditions given in Equations (10)–(14). The layout of the code is as follows.

First, we give the Matlab code that solves our system of ODE's, and name this code as 'fparabolic3dsolver.m'. Second, we present the code that generates the source function $u_r\ (y, z, t)$ whose name is 'bound.m'. Finally, the discretized ODE system (15)–(40) is coded in an m-file called 'fparabolic3d.m'. As seen in the code fparabolic3dsolver.m, we have obtained the numerical solution of our large system of ODE by using the ODE solver ODE45 built in Matlab. The contents of these m-files can be found in Appendix B (Algorithm 1).

3.1. A test problem on the accuracy of MOL

Since it is difficult to find an analytical solution to realistic PDE problems in science, the numerical solution is an approximation to the analytical solution, and one expects that it represents the analytical solution with good accuracy. The accuracy of the solution of our ODE system (obtained from the discretization of the given PDE) satisfies the user-specified error tolerances, which ensures the semi-analytical property inherent in this class of methods. Replacing the second spatial derivatives $\frac{\partial^2 u}{\partial x^2}, \frac{\partial^2 u}{\partial y^2}, \frac{\partial^2 u}{\partial z^2}$ by three-point central difference (with $O(h^2)$ accuracy) leads to a set of ODE defined on discrete lines of $x_i = (i-1)h_x, y_j = (j-1)h_y, z_k = (k-1)h_z, (i = 1{:}M, j = 1{:}N, k = 1{:}K)$ as appear in Equations (15)–(40). Note that the stability limit places an upper limit on Δt for a given D, $\Delta x, \Delta y$ and Δz; if one attempts to increase the accuracy of our ODE system by using a smaller $\Delta x, \Delta y$ and Δz (larger number of grid points in x, y and z by increasing M, N and K), a smaller value of Δt is required to keep the CFL number, $D\Delta t\left(\frac{1}{\Delta x^2} + \frac{1}{\Delta y^2} + \frac{1}{\Delta z^2}\right)$, below its critical value. We have used 'ode45', an ODE solver built in Matlab, to solve our system of ODE. This function implements a Runge-Kutta method with a variable time step for efficient computation. A 4th order Runge-Kutta solver uses 4 evaluations, so it can exactly integrate cubic

functions. A 5th order Runge-Kutta solver actually uses 6 terms, so it can be used for quartic and quintic functions. Since 'ode45' uses both 4th and 5th order methods to obtain error estimates in each step, these methods will have a growing error discrepancy when going from cubic to quartic functions and beyond. This is because the 4th order method will not be able to integrate functions of order higher than a cubic very accurately, and it will do progressively worse as the order increases. In order to obtain a higher accuracy for polynomials of order 4 and above, reduce the 'RelTol' (Relative Error Tolerance) and 'AbsTol' (Absolute Error Tolerance) properties using the 'odeset' function. Since 'ode45' automatically chooses the value of Δt for each time step it is very accurate.

We are now testing the accuracy of our method on the following initial-boundary value problem:

$$\frac{\partial u}{\partial t} = \frac{\partial^2 u}{\partial x^2} + \frac{\partial^2 u}{\partial y^2} + \frac{\partial^2 u}{\partial z^2} + 7, 0 < x, y, z < 1, t \geq 0 \tag{50}$$

$$u(x, y, z, 0) = x(1 - x) + y(1 - y) + z(1 - z), 0 < x, y, z < 1 \tag{51}$$

$$u_x(0, y, z, t) = u_y(x, 0, z, t) = u_z(x, y, 0, t) = 1, 0 < x, y, z < 1 \tag{52}$$

$$u_x(1, y, z, t) = u_y(x, 1, z, t) = u_z(x, y, 1, t) = -1, 0 < x, y, z < 1 \tag{53}$$

It is easy to see that the exact solution of the above problem is

$$u(x, y, z, t) = x(1 - x) + y(1 - y) + z(1 - z) + t \tag{54}$$

Figures 4 and **5** show the comparisons of numerical and exact solutions of Equations (50)–(54) at $t = 0.5$ and $t = 1$ (with $M = N = K = 21$), respectively. And, the accuracy result with respect to the MOL solution provided by 'ode45' is obtained with the maximum relative error tolerance of 2.0×10^{-10} for the solution at $t = 0.5$, while it is obtained with the maximum relative error tolerance of 1.0×10^{-12} for the solution at $t = 1$. Of course, the length of the integration interval also matters. Longer intervals may accumulate errors despite high local accuracy per step due to numerical instability or propagation of round-off errors. Since we obtained numerical instability after $t = 1.2$, we quit the solver. One could without a doubt continue solving the problem after this time by increasing the relative error tolerance. But doing this can result in impaired performance.

3.2. Error analysis of MOL

In this subsection we provide a $L2$ norm error analysis by comparing the exact and MOL solutions of the problem defined in Equations (50)–(53). As it is well known the $L2$ norm error is defined by the formula

$$L2 = \sqrt{\Delta x \sum_{j=1}^{N} \left(u_j^{MOL} - u_j^{exact}\right)^2}$$

where N is the number of grid points and $\Delta x = \frac{1}{N}$.

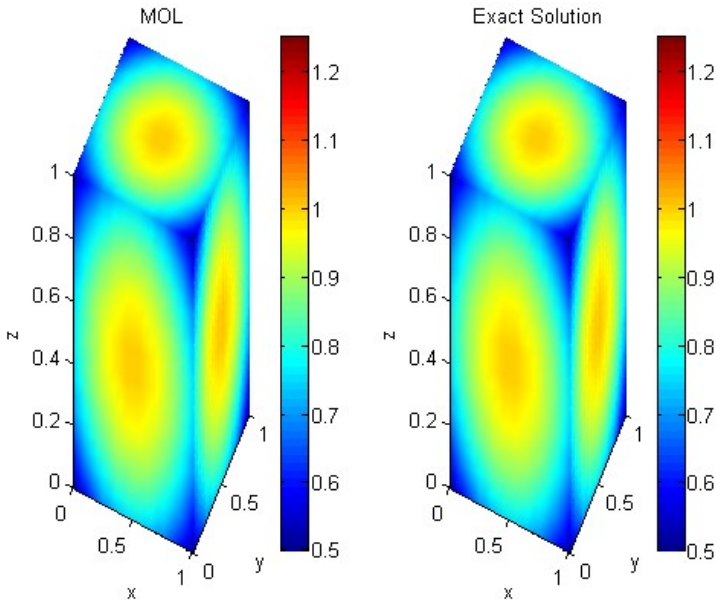

Figure 4. Comparison of MOL and exact solutions of Equations (50)–(54) at $t = 0.5$ with $M = N = K = 21$.

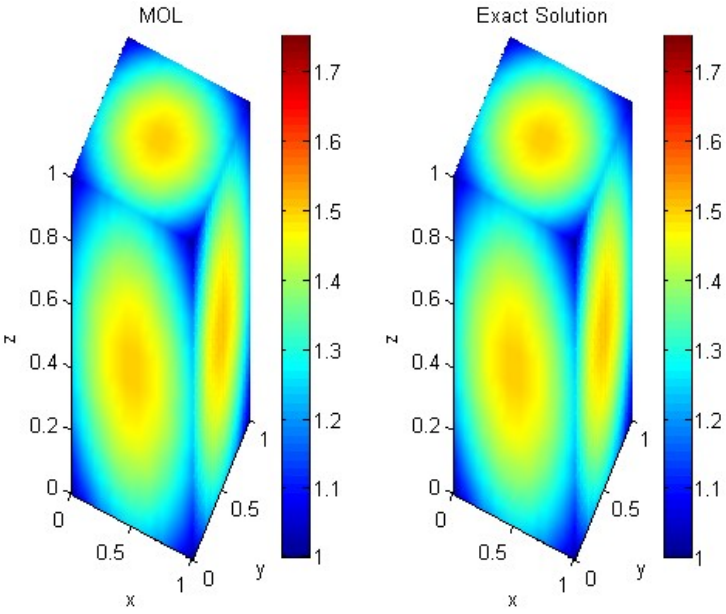

Figure 5. Comparison of MOL and exact solutions of Equations (50)–(54) at $t = 1$ with $M = N = K = 21$.

In our computations, we take $0 \leq x,\ y, z \leq 1$ and $M = N = K = 21$. We now use different values of *x, y* and z in the MOL and exact solutions of the problem, and obtain the $L2$ norm errors in **Table 1** below. Of course, these errors can be made smaller by choosing N large.

As seen from **Table 1** the $L2$ norm errors are pretty small for various values of *x, y* and z. These results are in good agreement with the pictures we have obtained in **Figures 4** and **5**.

Table 1. $L2$ norm errors.

t	x	y	z	u_{exact}	u_{MOL}	$L2$ errors
0.5	0	0	0	0.5000	0.499999999668361	$7.236963428151917 \times 10^{-11}$
0.5	0.1	0.1	0.1	0.7700	0.769999999668376	$7.236620615357449 \times 10^{-11}$
0.5	0.2	0.2	0.2	0.9800	0.979999999668422	$7.235632151610860 \times 10^{-11}$
0.5	0.3	0.3	0.3	1.1300	1.129999999668492	$7.234091311064704 \times 10^{-11}$
0.5	0.4	0.4	0.4	1.2200	1.219999999668581	$7.232157992266225 \times 10^{-11}$
0.5	0.5	0.5	0.5	1.2500	1.249999999668679	$7.230026011636324 \times 10^{-11}$
0.5	0.6	0.6	0.6	1.2200	1.219999999668776	$7.227903721827468 \times 10^{-11}$
0.5	0.7	0.7	0.7	1.1300	1.129999999668864	$7.225984939260558 \times 10^{-11}$
0.5	0.8	0.8	0.8	0.9800	0.979999999668933	$7.224473171177536 \times 10^{-11}$
0.5	0.9	0.9	0.9	0.7700	0.769999999668977	$7.223506511778297 \times 10^{-11}$
0.5	1	1	1	0.5000	0.499999999668992	$7.223177023862767 \times 10^{-11}$
1	0	0	0	1	0.999999999421016	$1.263446608235148 \times 10^{-10}$
1	0.1	0.1	0.1	1.2700	1.269999999421016	$1.263447092776200 \times 10^{-11}$
1	0.2	0.2	0.2	1.4800	1.479999999421016	$1.263445639153044 \times 10^{-11}$
1	0.3	0.3	0.3	1.6300	1.629999999421017	$1.263444185529887 \times 10^{-11}$
1	0.4	0.4	0.4	1.7200	1.719999999421018	$1.263443216447782 \times 10^{-11}$
1	0.5	0.5	0.5	1.7500	1.749999999421018	$1.263442731906730 \times 10^{-11}$
1	0.6	0.6	0.6	1.7200	1.719999999421017	$1.263443700988834 \times 10^{-11}$
1	0.7	0.7	0.7	1.6300	1.629999999421017	$1.263444670070939 \times 10^{-11}$
1	0.8	0.8	0.8	1.4800	1.479999999421016	$1.263445639153044 \times 10^{-11}$
1	0.9	0.9	0.9	1.2700	1.269999999421016	$1.263447092776200 \times 10^{-11}$
1	1	1	1	1	0.999999999421016	$1.263447335046726 \times 10^{-10}$

4. Discussion

In this work we have performed the MOL for the numerical solution of a mathematical model for the progression of TAF in 3D. **Figure 2** represents the source function u_r , the growth factor that is being supplied to the tissue throughout the domain. This function may also allow for the situation in which TAF may be generated at certain sites in the ECM. This is needed to initiate angiogenesis by enzymatic degradation of capillary basement lamina (BL). **Figures 6** and **7** show the TAF contours at different cross-sections of the cube at $t = 20$ for $0 \leq y \leq 1$ for $n = 1$ and $n = 2$, respectively. **Figure 8**, which is generated from **Figure 6a**, shows the TAF concentrations for $y = 0.3,0.4,0.5,0.6$ at $t = 20$ with $n = 1$, and **Figure 9**, which is generated from **Figure 7a**, shows the TAF concentrations for $y = 0.3, 0.4, 0.5, 0.6$ at $t = 20$ with $n = 2$. From these two figures we obtain that the maximum values of TAF on the cube at $t = 20$ are 630.5965 for $n = 1$, and 35.5193 for $n = 2$. Both of these values are reached when $y = 0.5$.

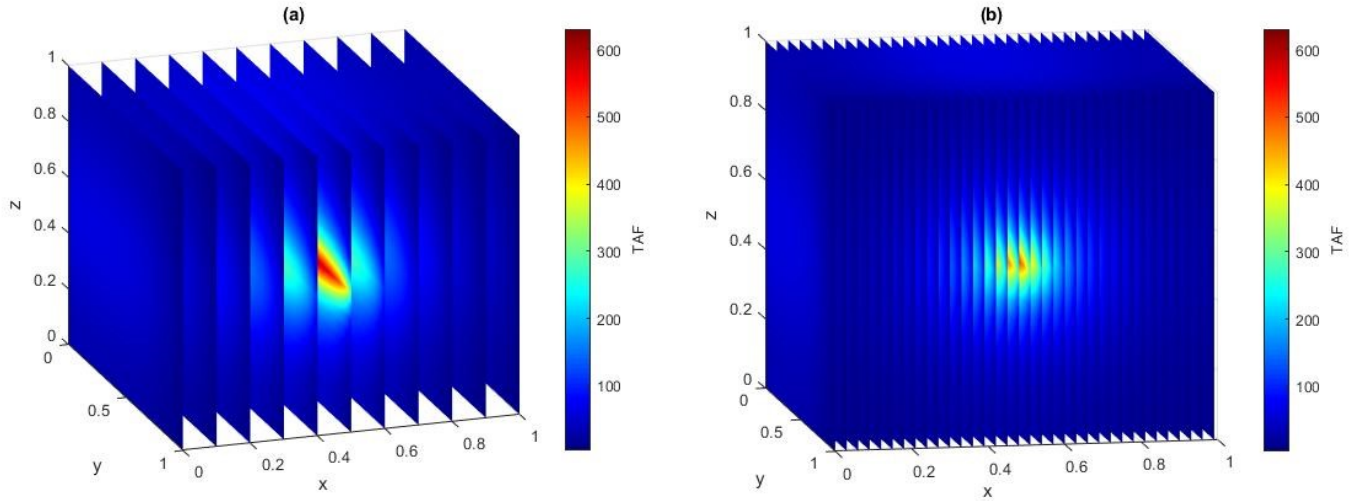

Figure 6. TAF contours at $t = 20$ for $0 \leq y \leq 1$ with **(a)** $h_y = 0.1$ and **(b)** $h_y = 0.03$ for $n = 1$.

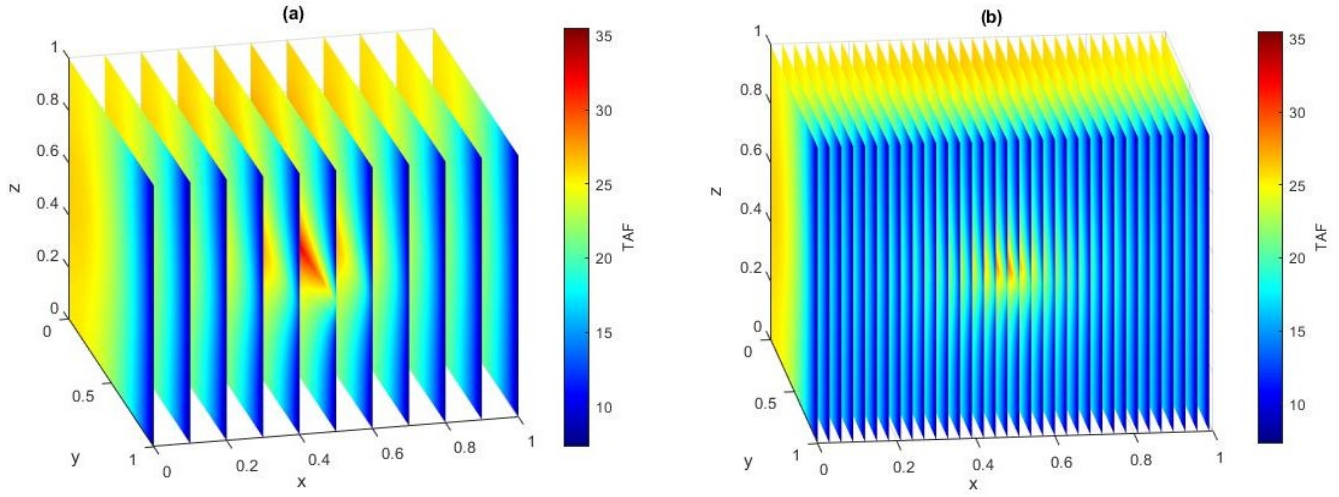

Figure 7. TAF contours at $t = 20$ for $0 \leq y \leq 1$ with **(a)** $h_y = 0.1$ and **(b)** $h_y = 0.03$ for $n = 2$.

It is worth saying a few words about the steady-state solutions of the model for both linear and non-linear cases. One sees from the comparison of **Figures 10** and **11** that in the non-linear case TAF reaches the steady state at about $t = 1.32$ while it reaches the steady state at about $t = 5$ in the linear case, which is the same result as in our 2D model presented in [19]. The reasons for this are as follows: In the linear case ($n = 1$), the diffusion rate is constant, so sharp peaks in u diffuse at a steady rate which can lead to slow equilibration, especially in regions with initially large ∇u, while in the nonlinear case ($n > 1$), diffusion is faster where u is small and slower where u is large which causes sharp peaks to spread out rapidly, accelerating the decay of large gradients and smoothing the solution much more efficiently. Hence, the nonlinearity enhances gradient-driven smoothing, leading to a faster transition to a steadystate.

Also, we have tested our method to verify it by taking

$$u_r(y, z, t) = 1 - \epsilon\cos(2\pi y)\cos(2\pi z)$$

And $z = 0$ in our code since the Authors of [19] did choose this source function in their model. Here ϵ is some small positive number. Once we run the code with these choices we get **Figures 12** and **13** which show the TAF concentrations for $n = 1$ and $n = 2$, respectively. These figures are the same as the ones obtained on pages 894 and 895 of [19]. In fact, one could test our method by letting $z = 1$ in u_r and get the same results.

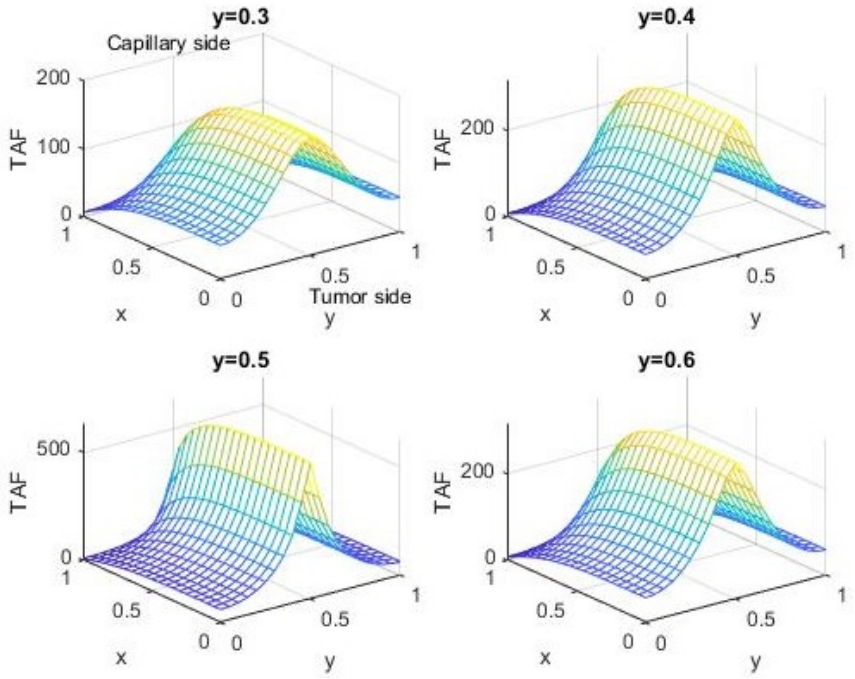

Figure 8. TAF concentration at $t = 20$ and $n = 1$ (linear case).

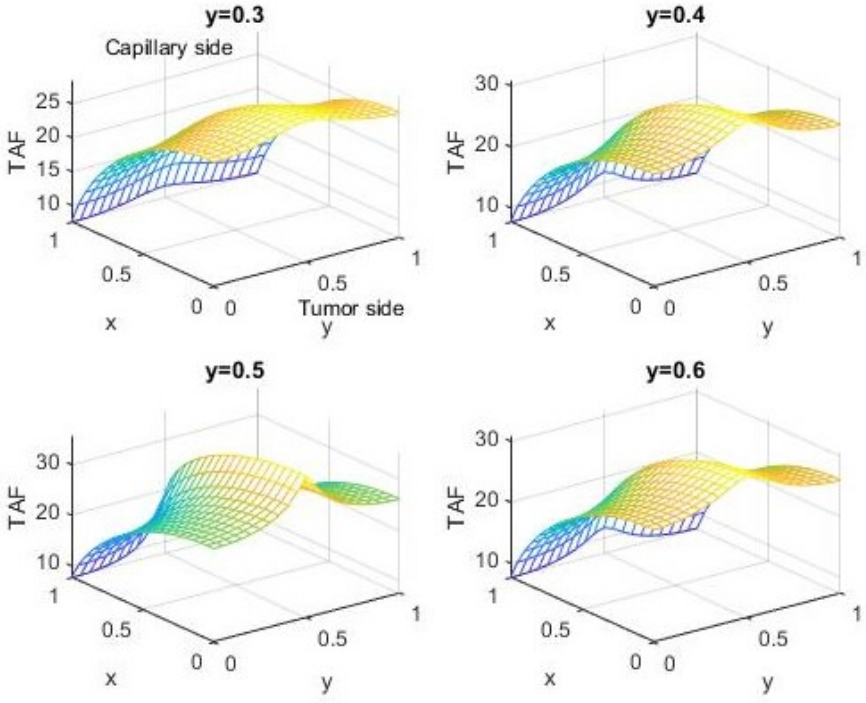

Figure 9. TAF concentration at $t = 20$ and $n = 2$ (nonlinear case).

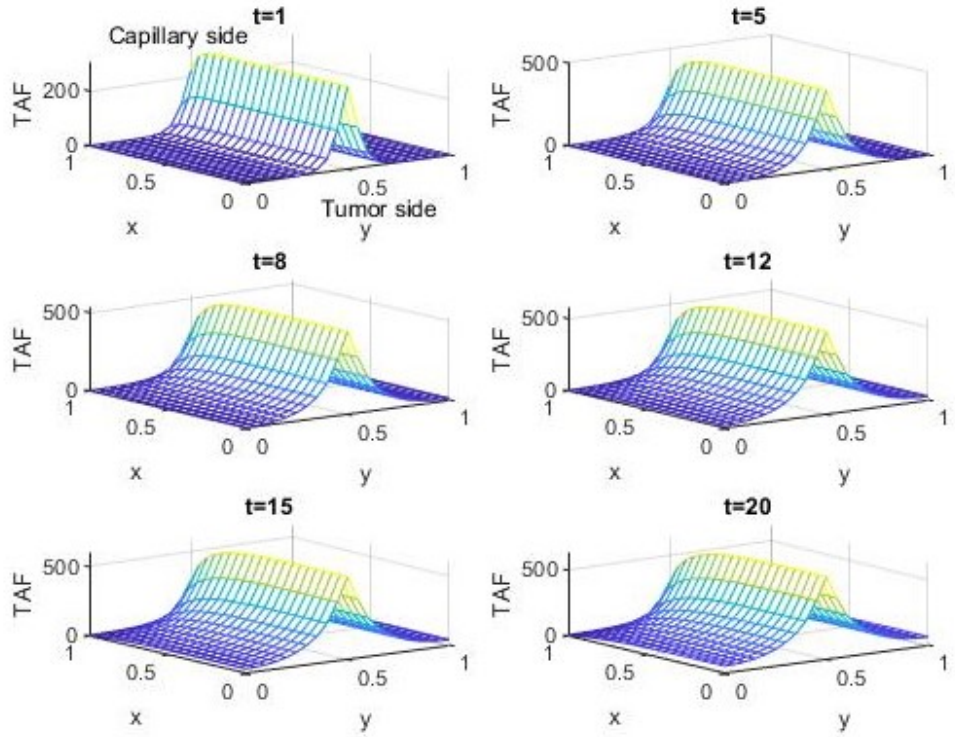

Figure 10. TAF concentration at $y = 0.5$ and $n = 1$ (linear case).

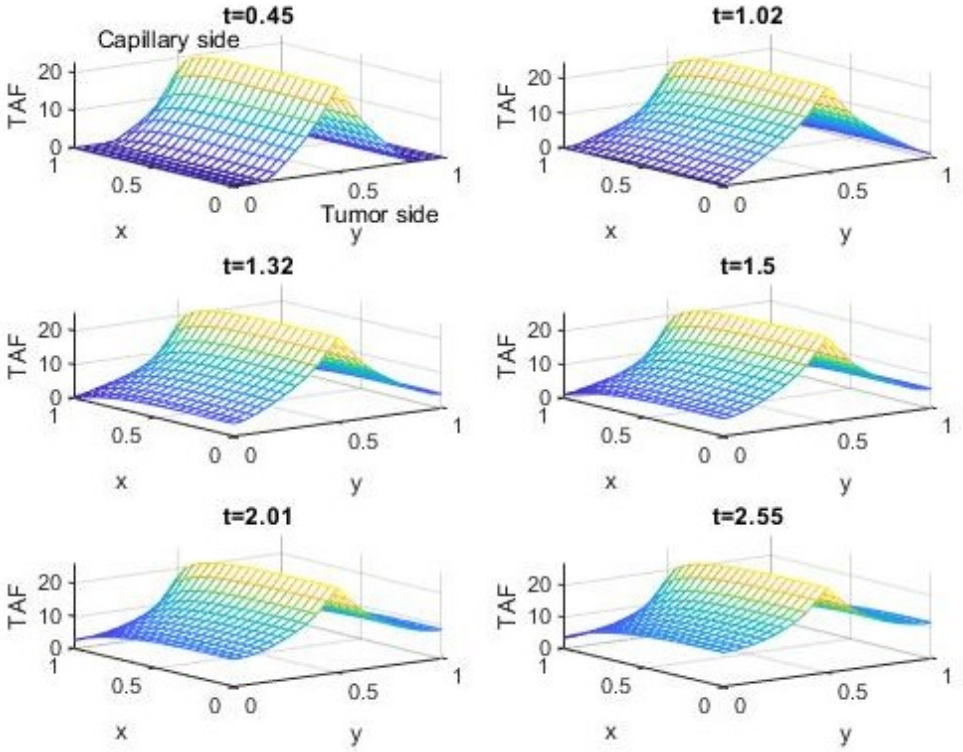

Figure 11. TAF concentration at $y = 0.5$ and $n = 2$ (nonlinear case).

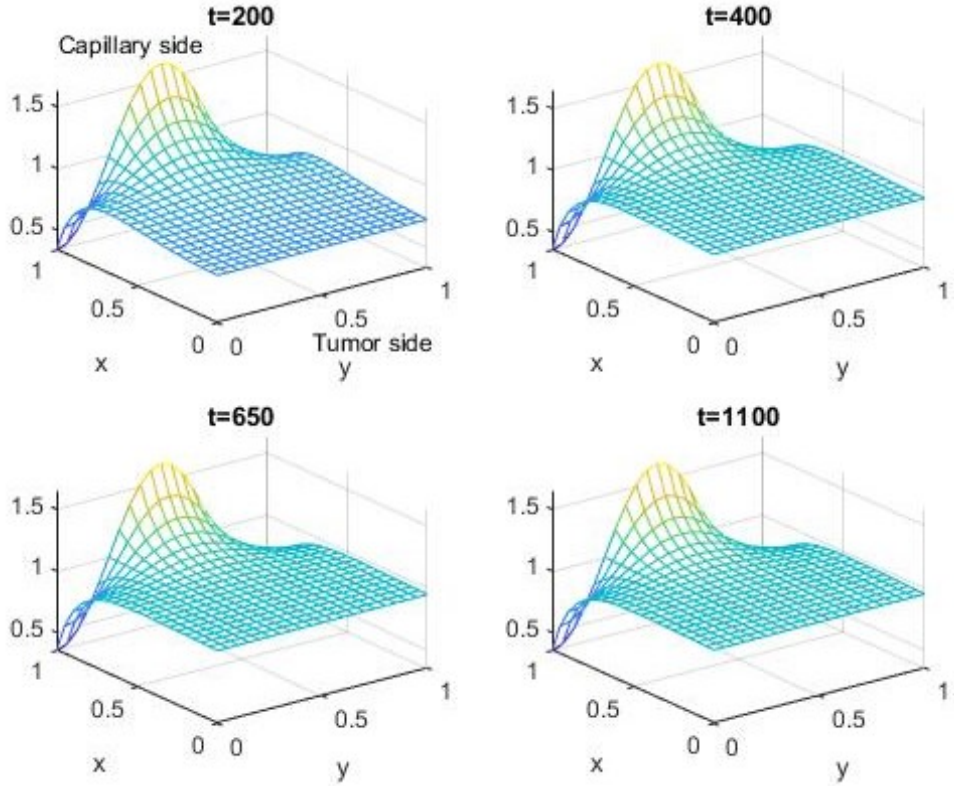

Figure 12. TAF concentration at $z = 0$ and $n = 1$ (linear case).

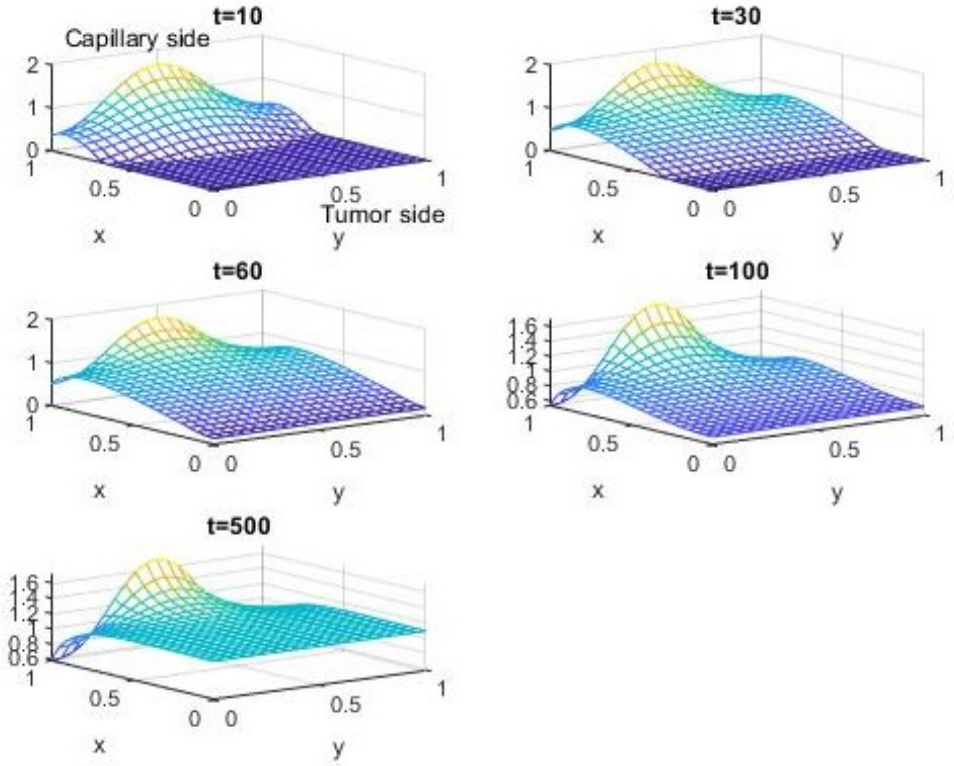

Figure 13. TAF concentration at $z = 0$ and $n = 2$ (nonlinear case).

5. Conclusion

In this study we have solved numerically a 3D mathematical model for the progression of TAF, a chemical that is needed to initiate angiogenesis. We did this using the MOL, a general way of converting a PDE to a system of ODE. When using the MOL one does not need large computer memory, linearization and physically unrealistic assumptions. Also, we have validated our large system of ODE by showing that it reduces to a relatively small system of ODE obtained by the 2D version of the model, and we have verified our method by showing a special case to match an already published paper. As a result, the MOL performs accurate and numerically stable solutions for nonlinear PDE appearing in science and engineering fields, as our outcomes support this fact.

Author contributions: Conceptualization, SP and MKD; methodology, SP; software, MKD; validation, SP and MKD; formal analysis, SP and MKD; investigation, SP and MKD; resources, SP; data curation, SP and MKD; writing—original draft preparation, MKD; writing—review and editing, SP and MKD; visualization, SP and MKD; supervision, SP; project administration, SP; funding acquisition, SP. All authors have read and agreed to the published version of the manuscript.

Conflict of interest: The authors declare no conflict of interest.

References

1. Emamjome M, Azarnavid B, Ghehsareh HR. A reproducing kernel Hilbert space pseudospectral method for numerical investigation of a two-dimensional capillary formation model in tumor angiogenesis problem. Neural Computing and Applications. 2049; 31: 2233–2241.
2. Pamuk S, Erdem A. The method of lines for the numerical solution of a mathematical model for capillary formation: The role of endothelial cells in the capillary. Applied Mathematics and Computation. 2007; 186(1): 831–835.
3. Shakeri F, Dehghan M. The method of lines for solution of the one-dimensional wave equation subject to an integral conservation condition. Computers and Mathematics with Applications. 2008; 56(9): 2175–2188.
4. Sharaf AA, Bakodah HO. A good spatial discretisation in the method of lines. Applied Mathematics and Computation. 2005; 171(2): 1253–1263.
5. Verwer JG, Sanz-Serna JM. Convergence of method of lines approximations to partial differential equations. Computing. 1984; 33: 297–313. doi: 10.1007/BF02242274.
6. Mousa MM. Efficient numerical scheme based on the method of lines for the shallow water equations. Journal of Ocean Engineering and Science. 2018; 3(4): 303–309.
7. Ali MR. The Method of Lines Analysis of Heat Transfer of Ostwald-de Waele Fluid Generated by a Non-uniform Rotating Disk with a Variable Thickness. Journal of Applied and Computational Mechanics. 2021;7(2): 432–441. doi: 10.22055/JACM.2020.30890.1787
8. Agud Albesa L, Boix García M, Pla Ferrando ML, Navarrete SCC. A study about the solution of convection–diffusion–reaction equation with Danckwerts boundary conditions by analytical, method of lines and Crank–Nicholson techniques. Mathematical Methods in the Applied Sciences. 2023; 46(2): 2133–2164. doi: 10.1002/mma.8633
9. Shi A, Persson PO, Zahr MJ. Implicit shock tracking for unsteady flows by the method of lines. Journal of Computational Physics. 2022; 454: 110906. doi: 10.1016/j.jcp.2021.110906
10. Spiller W. An enhancement of instruments for solution of general transmission line equations with method of lines, impedance-/admittance and field transformation in combination with finite differences. Optical and Quantum Electronics. 2022; 54: 591. doi: 10.1007/s11082-022-03894-3
11. Kazem S, Dehghan M. Semi-analytical solution for time-fractional diffusion equation based on finite difference method of lines (MOL). Engineering with Computers. 2019; 35: 229–241.

12. Salehi Y, Darvishi MT, Schiesser WE. Numerical solution of space fractional diffusion equation by the method of lines and splines. Applied Mathematics and Computation. 2018; 336: 465–480.
13. Soradi-Zeid S, Mesrizadeh M. The method of lines for parabolic integro-differential equations. Journal of Mathematical Modeling. 2020; 8(3): 291–308.
14. Bratsos AG. The solution of the two-dimensional sine-Gordon equation using the method of lines. Journal of Computational and Applied Mathematics. 2007; 206(1): 251–277.
15. Subramanian VR, White RE. Semianalytical method of lines for solving elliptic partial differential equations. Chemical Engineering Science. 2004; 59(4): 781–788.
16. Manshoor B, Salleh H, Khalid A, Abdelaal MAS. Method of Lines and Runge-Kutta Method in Solving Partial Differential Equation for Heat Equation. Journal of Complex Flow. 2021; 3(1): 21–25.
17. Ahmad I, Berzins M. MOL solvers for hyperbolic PDEs with source terms. Mathematics and Computers in Simulation. 2001; 56(2): 115–125.
18. Kazem S, Dehghan M. Application of finite difference method of lines on the heat equation. Numerical Methods Partial Differential Eq. 2018; 34(2): 626–660.
19. Erdem A, Pamuk S. The method of lines for the numerical solution of a mathematical model for capillary formation: The role of tumor angiogenic factor in the extra-cellular matrix. Applied Mathematics and Computation. 2007; 186(1): 891–897.
20. Eikenberry SE, Sankar T, Preul MC, et al. Virtual Glioblastoma: Growth, Migration and Treatment in a Three-Dimensional Mathematical Model. Cell Cell Proliferation. 2009; 42(4): 511–528.
21. Perfahl H, Byrne HM, Chen T, et al. Multiscale Modelling of Vascular Tumour Growth in 3D: The Roles of Domain Size and Boundary Conditions. PLoS One. 2011; 6(4): e14790.
22. Sakai K, Hayashi T, Sakai Y, et al. A three-dimensional model with two-body interactions for endothelial cells in angiogenesis. Scientific Reports. 2023; 13: 20549. doi: 10.1038/s41598-023-47911-1
23. Shirinifard A, Gens JS, Zaitlen BL, et al. 3D Multi-Cell Simulation of Tumor Growth and Angiogenesis. PLoS One. 2009; 4(10): e7190.
24. Stéphanou A, McDougall SR, Anderson ARA, Chaplain MAJ. Mathematical Modelling of Flow in 2D and 3D Vascular Networks: Applications to Anti-Angiogenic and Chemotherapeutic Drug Strategies. Mathematical and Computer Modelling. 2005; 41(10): 1137–1156.
25. Tang L, van de Ven AL, Guo D, et al. Computational Modeling of 3D Tumor Growth and Angiogenesis for Chemotherapy Evaluation. PLoS One. 2014; 9(1): e83962.
26. Xie H, Jiao Y, Fan Q, et al. Modeling Three-Dimensional Invasive Solid Tumor Growth in Heterogeneous Microenvironment under Chemotherapy. PLoS One. 2018; 13(10): e0206292.
27. Xu J, Vilanova G, Gomez H. Phase-Field Model of Vascular Tumor Growth: Three-Dimensional Geometry of the Vascular Network and Integration with Imaging Data. Computer Methods in Applied Mechanics and Engineering. 2020; 359: 112648.
28. Zhao G, Chen E, Yu X, et al. Three-Dimensional Model of Metastatic Tumor Angiogenesis in Response to Anti-Angiogenic Factor Angiostatin. Journal of Mechanics in Medicine and Biology. 2017; 17(10): 1750094.
29. Alias N, bin Masseri MIS, Islam MR, Khalid SN. The Visualization of Three Dimensional Brain Tumors' Growth on Distributed Parallel Computer Systems. Journal of Applied Sciences. 2009; 9(3): 505–512.
30. Karaa S, Zhang J, Yang F. A numerical study of a 3D bioheat transfer problem with different spatial heating. Mathematics and Computers in Simulation. 2005; 68(4): 375–388.
31. Al Qubeissi M. Proposing a Numerical Solution for the 3D Heat Conduction Equation. In: Proceedings of the 2012 Sixth Asia Modelling Symposium; 29–31 May 2012; Bali, Indonesia.
32. Tsega EG. Numerical Solution of Three-Dimensional Transient Heat Conduction Equation in Cylindrical Coordinates. Journal of Applied Mathematics. 2022; 1993151.
33. Tsega EG. A Numerical Solution of Three-Dimensional Unsteady State Heat Equation. International Journal of Mathematical Modelling & Computations. 2021; 11(01): 49–60.
34. Wang TY, Lee YM, Chen CP. 3D thermal-ADI—An efficient chip-level transient thermal simulator. In: Proceedings of the ISPD' 03: International Symposium on Physical Design; 6–9 April 2003; Monterey, CA, USA.
35. He CH, Liu HW, Liu C. A Fractal-Based Approach to the Mechanical Properties of Recycled Aggregate Concretes. Series: Mechanical Engineering. 2024; 22(2): 329–342. doi: 10.22190/FUME240605035H

Appendix A

Derivation of Equation (1)

Fick's Law of Diffusion: Fick's law describes the flux of a substance due to diffusion. In one dimension, it is given by

$$\boldsymbol{J} = -D\frac{\partial u}{\partial x}$$

where $\boldsymbol{J}$ is the flux (rate of flow of the substance), D is the diffusion coefficient (which can be a constant or a function of position), and u is the concentration.

In three dimensions, Fick's law becomes

$$J = -D(x, y, z)\nabla u$$

where ∇u is the gradient of the concentration field, and $D(x, y, z)$ is the diffusion coefficient, which may vary with spatial position (i.e., D can depend on x, y, and z).

Conservation of Mass (Continuity Equation): The change in concentration of the substance u at a point in space is governed by the conservation of mass. The rate of change of u at a point is related to the flux through the boundaries of an infinitesimal volume around that point. The general form of the continuity equation is:

$$\frac{\partial u}{\partial t} = -\nabla \cdot \boldsymbol{J}$$

where $\frac{\partial u}{\partial t}$ is the rate of change of concentration at a point in time, and $\nabla \cdot \boldsymbol{J}$ is the divergence of the flux, representing how the substance is spreading out in space.

Substituting Fick's Law: Now, substituting the expression for the flux $\boldsymbol{J} = -D(x, y, z)\nabla u$ into the continuity equation

$$\frac{\partial u}{\partial t} = -\nabla \cdot (-D(x, y, z)\nabla u)$$

This simplifies to

$$\frac{\partial u}{\partial t} = \nabla \cdot (D(x, y, z)\nabla u)$$

This is a standard diffusion equation, where $D(x, y, z)$ is the spatially varying diffusion coefficient.

Adding the Nonlinear Reaction Term: The equation we have provided includes a nonlinear term u^n which indicates that there is a reaction process occurring in the system that depends nonlinearly on u. In many physical and biological processes (such as in chemical reactions, population dynamics or progression of tumor cells in a nonlinear media), the rate of change of the concentration might depend on some power of the concentration u, leading to a reaction term of the form u^n where n is a constant that determines the nonlinear behavior.

The nonlinear term could represent, for instance, autocatalysis (where the rate of change of concentration increases as the concentration itself increases) or other forms of reaction kinetics. Hence, the equation becomes

$$u_t = \nabla \cdot (D(x, y, z)\nabla(u^n)).$$

This form of the equation suggests that the concentration of u changes over time due to a combination of:

- **Diffusion** is represented by $\nabla \cdot (D(x, y, z)\nabla(u^n))$,
- **Nonlinear reaction kinetics** is the term u^n that governs how the concentration itself evolves due to local interactions.

Adding the source term: We add a source function $u_r(y,z,t)$ to the above equation. It represents the TAF that is being supplied to the tissue throughout the domain.

$$u_t = \nabla \cdot \left(D(x,y,z)\nabla(u^n)\right) + u_r(y,z,t)$$

Appendix B

Algorithm 1 Matlab Code

```
%\%\%\%\%\%\%\%\%\%\%\%\%\%\%\%\%\%\%\%\%\%\%\%\%\%\%\%\%\%\%\%\%\%\%\%\%\%\%\%\%\%fparabolic3dsolver.m\\
clc; clear all; global D M N K hx hy hz alpha n tt
D=0.0036; alpha=0.05; M=21; N=21; K=21; hx=1./(M-1); hy=1./(N-1);hz=1./(K-1);
time=input('please enter the final time '); tt=input('the value of tt'); n=input('the value of porosity')
tspan=linspace(0,time,201); x=linspace(0,1,M); y=linspace(0,1,N); z=linspace(0,1,K); u0(1:(M*N*K))=0; u0=u0(:);
 option=odeset('reltol',10^-8,'abstol',10^-8);
 [t,U]=ode45('fparabolic3d',t,u0,option); u3=[];
 for i=1:length(t)
 u3=[u3 U(i,:)];
 end
 u3=u3(:);
 u_numeric = reshape(u3,M,N,K,length(t));
 u_numeric_1=pagetranspose(u_numeric); [X Y Z]=meshgrid(x,y,z);
 slice(X,Y,Z,u_numeric_1(:,:,:,find(tspan==tt)),[],[0:0.1:1],[]); xlabel('x'); ylabel('y');  zlabel('z'); view([45 50 55])
 colormap(jet) cb=colorbar; shading interp cb.Label.String='TAF';
 \%\%\%\%\%\%\%\%\%\%\%\%\%\%\%\%\%\%\%\%\%\%\%\%\%\%\%\%\%\%\%\%\%\%\%\%\%\%\%\%\%\%\bound.m\\
 function v=bound(y,z);
 delta=0.15; v0=1000; N=21; K=21; a=1/2; b=1/2; y=linspace(0,1,N); z=linspace(0,1,K);
 [Y ,Z]=meshgrid(y,z);
 f = @(y,z) sqrt(((y-a).^2 + (z-b).^2)); r=f(Y,Z); m=3; U_y= length(y); U_z= length(z);
 for i=1:U_y;
 for j=1:U_z;
  if r(i,j)<=delta;
  v(i,j)=v0*((1-exp(-(1-r(i,j)/delta).^2))/(1-exp(-1))).^m;
  else r(i,j)>$delta;
 v(i,j)=0;
  end
  end
  end
\%\%\%\%\%\%\%\%\%\%\%\%\%\%\%\%\%\%\%\%\%\%\%\%\%\%\%\%\%\%\%\%\%\%\%\%\%\%\%\%\%\%fparabolic3d.m\\
function u2=fparabolic3d(t,u);
global D alpha M N K hx hy hz n y z
u=reshape(u,M,N,K); A=bound(y,z);
D=0.0036; alpha=0.05; M=21; N=21; K=21; hx=1./(M-1); hy=1./(N-1); hz=1./(K-1); H_x=D./hx^2; H_y=D./hy^2;
 H_z=D./hz^2; H=1./hx^2+1./hy^2+1./hz^2;
u2(1,1,1)=(2*H_x).*u(2,1,1)^n-2*D.*(u(1,1,1^n).*(H+alpha/hx)+
(2*H_y).*u(1,2,1)^ n+(2*H_z).*u(1,1,2)^ n  +A(1,1);
u2(M,1,1)=(H_x).*(u(M-1,1,1)^n)+(2*H_y).*u(M,2,1)^n+
(2*H_z).*u(M,1,2)^n-2*D*u(M,1,1)^ n.*H +A(1,1);
u2(1,N,1)=(2*H_x).*u(2,N,1)^n+(2*H_y).*u(1,N-1,1)^n+
(2*H_z).*u(1,N,2)^n-2*D*u(1,N,1)^n.*(H+alpha/hx) +A(N,1);
u2(1,1,K)=(2*H_x).*u(2,1,K)^n+(2*H_y).*u(1,2,K)^n+
(2*H_z).*u(1,1,K-1)^n-2*D*u(1,1,K)^n.*(H+alpha/hx) +A(1,K);
u2(1,N,K)=(2*H_x).*u(2,N,K)^n+(2*H_y).*u(1,N-1,K)^n+
(2*H_z).*u(1,N,K-1)^n-2*D*u(1,N,K)^n.*(H+alpha/hx) +A(N,K);
u2(M,1,K)=(H_x).*(u(M-1,1,K)^n)+(2*H_y).*u(M,2,K)^n+...
(2*H_z).*u(M,1,K-1)^n-2*D*u(M,1,K)^n.*(H) +A(1,K);
u2(M,N,1)=(H_x).*( u(M-1,N,1)^n)+(2*H_y).*u(M,N-1,1)^n+...
(2*H_z).*u(M,N,2)^n-2*D*u(M,N,1)^n.*(H)+ A(N,1);
u2(M,N,K)=(H_x).*(u(M-1,N,K)^n)+(2*H_y).*u(M,N-1,K)^n+(2*H_z).*u(M,N,K-1)^n-2*D*u(M,N,K)^n.*(H) +A(N,K);
for i=2:M-1;
u2(i,1,1)= (H_x).*(u(i+1,1,1)^n+u(i-1,1,1)^n)+(2*H_y).*u(i,2,1)^n+...
(2*H_z).*u(i,1,2)^n-2*D.*u(i,1,1)^n.*(H) +A(1,1);
u2(i,1,K)=(H_x).*(u(i+1,1,K)^n+u(i-1,1,K)^n)+(2*H_y).*u(i,2,K)^n+...
(2*H_z).*u(i,1,K-1)^n-2*D.*u(i,1,K)^n.*(H) +A(1,K);
u2(i,N,1)=(H_x).*(u(i+1,N,1)^n+u(i-1,N,1)^n)+(2*H_y).*u(i,N-1,1)^n+...
```

Algorithm 1 (*Continue*)

```
(2*H_z).*u(i,N,2)^n-2*D.*u(i,N,1)^n.*(H) +A(N,1);
u2(i,N,K)=(H_x).*(u(i+1,N,K)^n+u(i-1,N,K)^n)+(2*H_y).*u(i,N-1,K)^n+...
(2*H_z).*u(i,N,K-1)^n-2*D.*u(i,N,K)^n.*(H) +A(N,K);
end
for j=2:N-1;
u2(1,j,1)=(2*H_x).*u(2,j,1)^ n+(2*H_z).*u(1,j,2)^n+
(H_y).*(u(1,j+1,1)^n+u(1,j-1,1)^n)-2*D.*u(1,j,1)^ n.*(H+alpha/hx) +A(j,1);
u2(1,j,K)=(2*H_x).*u(2,j,K)^n+(2*H_z).*u(1,j,K-1)^n-
2*D.*u(1,j,K)^n.*(H+alpha/hx)+(H_y).*(u(1,j+1,K)^n+u(1,j-1,K)^n) +A(j,K);
u2(M,j,1)=(H_x).*(u(M-1,j,1)^n)-2*D.*u(M,j,1)^n.*(H)+...
(H_y).*(u(M,j+1,1)^n+u(M,j-1,1)^n)+(2*H_z).*u(M,j,2)^n+A(j,1);
u2(M,j,K)=(H_x).*(u(M-1,j,K)^n)-2*D.*u(M,j,K)^n.*(H)+...
(H_y).*(u(M,j+1,K)^n+u(M,j-1,K)^n)+(2*H_z).*u(M,j,K-1)^n+A(j,K);
end
for k=2:K-1;
u2(1,1,k)= (2*H_x).*u(2,1,k)^n+(2*H_y).*u(1,2,k)^n+...
(H_z).*(u(1,1,k+1)^n+u(1,1,k-1)^n)-2*D.*u(1,1,k)^n.*(H+alpha/hx) +A(1,k);
u2(M,1,k)=(H_x).*(u(M-1,1,k)^n)+(2*H_y).*u(M,2,k)^n+...
(H_z).*(u(M,1,k+1)^n+u(M,1,k-1)^n)-2*D.*u(M,1,k)^n.*(H) +A(1,k);
u2(1,N,k)=(2*H_x).*u(2,N,k)^n+(2*H_y).*u(1,N-1,k)^n+...
(H_z).*(u(1,N,k+1)^n+u(1,N,k-1)^n)-2*D.*u(1,N,k)^n.*(H+alpha/hx) +A(N,k);
u2(M,N,k)=(H_x).*(u(M-1,N,k)^n)+(2*H_y).*u(M,N-1,k)^n+...
(H_z).*(u(M,N,k+1)^n+u(M,N,k-1)^n)-2*D.*u(M,N,k)^n.*(H) +A(N,k);
end
for j=2:N-1;
for k=2:K-1;
u2(1,j,k)= (2*H_x).*u(2,j,k)^n+(H_y).*(u(1,j+1,k)^n+u(1,j-1,k)^n)+...
(H_z).*(u(1,j,k+1)^n+u(1,j,k-1)^n)-2*D.*u(1,j,k)^n.*(H+alpha/hx) +A(j,k);
u2(M,j,k)=(H_x).*(u(M-1,j,k)^n)-2*D.*u(M,j,k)^n.*(H)+...
(H_y).*(u(M,j+1,k)^n+u(M,j-1,k)^n)+(H_z).*(u(M,j,k+1)^n+u(M,j,k-1)^n) +A(j,k);
end
end
for i=2:M-1;
for k=2:K-1;
u2(i,1,k)=(H_x).*(u(i+1,1,k)^n+u(i-1,1,k)^n)+(2*H_y).*u(i,2,k)^n+...
(H_z).*(u(i,1,k+1)^n+u(i,1,k-1)^n)-2*D.*u(i,1,k)^n.*(H) +A(1,k);
u2(i,N,k)=(H_x).*(u(i+1,N,k)^n+u(i-1,N,k)^n)+(2*H_y).*u(i,N-1,k)^n-
2*D.*u(i,N,k)^n.*(H)+(H_z).*(u(i,N,k+1)^n+u(i,N,k-1)^n) +A(N,k);
end
end
for i=2:M-1;
for j=2:N-1;
u2(i,j,1)= (H_x).*(u(i+1,j,1)^n+u(i-1,j,1)^n)+(2*H_z).*u(i,j,2)^n+...
(H_y).*(u(i,j+1,1)^n+u(i,j-1,1)^n)-2*D.*u(i,j,1)^n.*(H) +A(j,1);
u2(i,j,K)=(H_x).*(u(i+1,j,K)^n+u(i-1,j,K)^n)+(2*H_z).*u(i,j,K-1)^n-2*D.*u(i,j,K)^n.*(H)+(H_y).*(u(i,j+1,K)^n+u(i,j-
1,K)^n) +A(j,K);
end
end
for i=2:M-1;
for j=2:N-1;
for k= 2:K-1;
u2(i,j,k)=(H_x).*(u(i+1,j,k)^n+u(i-1,j,k)^n)-2*D.*u(i,j,k)^n.*(H)+...
(H_y).*(u(i,j+1,k)^n+u(i,j-1,k)^n)+(H_z).*(u(i,j,k+1)^n+u(i,j,k-1)^n) +A(j,k);
end
end
end
u2=u2(:);
```

Advances in Differential Equations and Control Processes 2025, 32(1), 2759.
https://doi.org/10.59400/adecp2759

Article

Herd immunity in a coronavirus disease 2019 epidemic model with consideration of vaccination and quarantine interventions

Moh Hasan*, Faizal Rifky Fahreza

Department of Mathematics, University of Jember, Jember 68121, Indonesia
*** Corresponding author:** Moh Hasan, hasan.fmipa@unej.ac.id

CITATION

Hasan M, Fahreza FR. Herd immunity in a coronavirus disease 2019 epidemic model with consideration of vaccination and quarantine interventions. Advances in Differential Equations and Control Processes. 2025; 32(1): 2759. https://doi.org/10.59400/adecp2759

ARTICLE INFO

Received: 10 February 2025
Accepted: 12 March 2025
Available online: 21 March 2025

Abstract: During the pandemic of COVID-19, people had reduced contact among each other. As a result of this behavior, several factors, such as economic conditions and the teaching and learning process, have been affected. Hence, it is important to identify whether the impact of COVID-19 is no longer as severe as when it was first observed. The study aimed to analyze herd immunity against COVID-19 in Indonesia according to the bifurcations and simulations of mathematical models of COVID-19 transmission. Based on the bifurcation of the disease system, whether the current pandemic was controlled with standard interventions was evaluated. The system behavior can be compared with herd immunity that should be achieved in a specific population. Thus, whether a system has resulted in the achievement of herd immunity can be evaluated. The behavior of this system can provide information on the achievement of group immunity during disease outbreaks.

Keywords: herd immunity threshold; infection rate, bifurcation diagram; basic reproduction number

1. Introduction

The mathematical compartment models of infectious disease transmission can provide an overview of disease dynamics [1]. The compartment model is built based on assumptions regarding the natural behavior of disease, which can simply be used to predict the peak point of disease transmission in a specific population [2–4]. The assumptions used in building disease distribution models are not limited to the natural behavior of diseases. Moreover, models can also be built by considering interventions or other factors such as migration [5], social restrictions or confinement [6], and implementation of vaccination and quarantine [7,8]. Using the mathematical models of infectious disease, we can exert efforts to control disease transmission [9,10], determine the efficacy of interventions [8,11], and view disease conditions based on models such as herd immunity conditions [12,13], where the condition of herd immunity in an outbreak can simply be demonstrated by simulating a model [12].

The compartment model of infectious disease transmission, which is built by several differential equations, is a continuous dynamical system. In a dynamical system, we can see how the system behaves. One of them is a change in system behavior if there is an alteration in the parameters of the system. Bifurcation is the instrument used to identify this change [14,15]. In a compartmental model of disease transmission, a bifurcation can appear as two types, namely, backward bifurcation and forward bifurcation, both of which can be explained graphically via a bifurcation diagram [1,16,17]. Via an analysis of this bifurcation, we can have an idea on whether the disease can disappear if standard interventions are carried out or how difficult it is

to control the disease during epidemic [18,19]. Further, bifurcation can be used to identify the efficacy of a parameter in making the disease system more controllable [20]. That is, it can assess vaccine efficacy and the appropriate vaccine timing, which can make the system more controlled [21].

Currently, we are experiencing the coronavirus disease 2019 (COVID-19) outbreak. COVID-19 has a unique transmission behavior. Hence, the disease outbreak, which is still experienced in Indonesia, has been interesting, and it can be assessed more deeply in terms of the mathematical models of disease transmission. Data have shown an increase in the number of COVID-19 cases in Indonesia during specific periods even after the implementation of vaccination. That is, the incidence of COVID-19 was high after school or year-end holidays [22]. In addition, the interventions carried out by the government, such as the implementation of health protocols in public spaces, vaccinations, and social restrictions, had an influence on the transmission process of COVID-19 in society [23,24]. Hence, the current status of the COVID-19 outbreak is interesting to assess when viewed from the epidemic model. Moreover, the interventions that can suppress the transmission of COVID-19 in society should be evaluated.

The use of mathematical modeling, particularly through bifurcation analysis, offers significant advantages in understanding the dynamics of COVID-19 spread. This approach facilitates the simulation of various scenarios related to virus transmission, enabling the prediction of infection wave peaks and troughs while identifying key factors that influence transmission. By employing bifurcation analysis, critical points can be pinpointed where minor changes in parameters may lead to substantial shifts in spread dynamics, including the attainment of herd immunity conditions. Consequently, mathematical modeling serves as a valuable tool in designing effective intervention strategies, appropriately allocating health resources, and ultimately controlling the pandemic.

This study aims to evaluate the achievement of herd immunity against COVID-19 in Indonesia through bifurcation analysis and the simulation of a mathematical model for the virus. Specifically, the objectives of this research are: (1) To determine whether Indonesia has attained herd immunity based on model analysis; (2) to estimate parameters, identify the type of basic reproduction number, and conduct a sensitivity analysis of parameters to reinforce the simulation results; (3) to predict future system behavior using bifurcation and compartment model simulations; and (4) to examine the unique distribution patterns of COVID-19 data in Indonesia. Ultimately, this study aims to provide a comprehensive understanding of the dynamics of COVID-19 spread and the status of herd immunity in Indonesia through a mathematical modeling approach.

To evaluate herd immunity against COVID-19 in Indonesia, we utilized bifurcations and simulations based on a mathematical model. The model will be analyzed in the final phase of data collection in this study. Other supporting processes such as parameter estimation, identification of the type of the basic reproduction number of the system, and sensitivity analysis of the parameters in the system will also be performed to support the results of the system simulation. Using data obtained at the final phase as the starting point for the simulation, the behavior of the system in the future when viewed from the bifurcations produced by the system and the

simulation of each compartment in the disease transmission system will be examined. Finally, the unique distribution pattern of data on COVID-19 in Indonesia was investigated.

2. Methods

A COVID-19 transmission model was examined with consideration of vaccination and quarantine interventions [25]. Since it was more pertinent to current intervention efforts against COVID-19, this model would have been updated by adding a booster vaccine compartment. The model was first fit to data that have been divided into several phases of the disease distribution period to obtain estimated results from the parameters of vaccination rate for doses 1, 2, and booster (φ_1, φ_2, and φ_3), recovery rate (γ), rate of movement from compartments $I(t)$ to $Q(t)$ (τ_1), and the COVID-19 mortality rate (ζ). Next, the equation of the basic reproduction number ($\mathcal{R}_0$) of the model was examined using the next-generation matrix. Then, by taking the force of infection parameter $\left(\beta^* = \frac{\lambda I^* + \lambda q Q^*}{N}\right)$, bifurcations in the system regarding the basic reproduction number ($\mathcal{R}_0$) were assessed. Next, a sensitivity analysis was performed to determine parameters with changes that can significantly affect the basic reproduction number. Finally, a simulation was run on the model to determine its behavior up to day 1800 (t). The numerical simulations are applied in PYTHON using the fourth-order Runge-Kutta method.

3. Results and discussion

Initially, the model presented in [25] is adjusted to include a booster vaccination compartment, resulting in the updated model depicted in Equation (1), with the used variables in Equation (1) described in **Table 1**. This modification aims to reflect the impact of booster vaccinations on the dynamics of the epidemiological model.

$$
\begin{aligned}
\frac{dS}{dt} &= \Lambda - \frac{\lambda SI}{N} - \frac{\lambda qSQ}{N} - \varphi_1 S + \rho R - \mu S,\\
\frac{dV_1}{dt} &= \varphi_1 S - \frac{\lambda pV_1 I}{N} - \frac{\lambda pqV_1 Q}{N} - \varphi_2 V_1 - \mu V_1,\\
\frac{dV_2}{dt} &= \varphi_2 V_1 - \frac{\lambda rV_2 I}{N} - \frac{\lambda rqV_2 Q}{N} - \varphi_3 V_2 - \mu V_2,\\
\frac{dV_3}{dt} &= \varphi_3 V_2 - \frac{\lambda sV_3 I}{N} - \frac{\lambda sqV_3 Q}{N} - \mu V_3,\\
\frac{dI}{dt} &= \frac{\lambda SI}{N} + \frac{\lambda pV_1 I}{N} + \frac{\lambda rV_2 I}{N} + \frac{\lambda sV_3 I}{N} + \frac{\lambda qSQ}{N} + \frac{\lambda pqV_1 Q}{N} + \frac{\lambda rqV_2 Q}{N} + \frac{\lambda sqV_3 Q}{N} - \tau_1 I + \tau_2 Q - \gamma I - \zeta I - \mu I,\\
\frac{dQ}{dt} &= \tau_1 I - \tau_2 Q - \gamma Q - \zeta dQ - \mu Q,\\
\frac{dR}{dt} &= \gamma I + \gamma Q - \rho R - \mu R,\\
\frac{dD}{dt} &= \zeta I + \zeta dQ.
\end{aligned}
\tag{1}
$$

Table 1. Variables in the model.

Variables	Description	Variables	Description
S	Susceptible compartment (individuals susceptible to COVID-19).	q	Reduced rate of infection due to quarantine.
V_1	Compartment of individuals who have received one dose of the vaccine.	p	Reduced rate of infection due to the first vaccine dose.
V_2	Compartment of individuals who have received two doses of the vaccine.	r	Reduced rate of infection due to the second vaccine dose.
V_3	Compartment of individuals who have received a vaccine booster dose.	s	Reduced rate of infection due to the vaccine booster dose.
I	Compartment of individuals exposed to COVID-19.	τ_1	The rate of movement from $I(t)$ to $Q(t)$.
Q	Compartment of individuals who were quarantined.	τ_2	The rate of movement from $Q(t)$ to $I(t)$.
R	Compartment of individuals who have recovered from COVID-19.	γ	Recovery rate.
D	Compartment of individuals who have died from COVID-19.	ζ	COVID-19 mortality rate.
λ	Infection rate.	ρ	Reinfection rate.
φ_1	First-dose vaccination rate.	d	Reduced mortality rate due to vaccination.
φ_2	Second-dose vaccination rate.	μ	Normal mortality rate.
φ_3	Booster-dose vaccination rate.	Λ	Normal birth rate.

The λ parameter is pivotal as it represents the infection rate in disease transmission dynamics. Specifically, λ indicates the speed at which a disease can be transmitted from an infected individual to a susceptible one. A high λ value suggests a greater potential for transmission, which can quickly accelerate the spread of the disease within a population. Conversely, a low λ value signifies a slower transmission rate, thereby allowing more time for interventions like quarantine and vaccination to mitigate spread. Understanding and managing λ is therefore critical in forecasting and addressing the impact of disease outbreaks. Given the significant influence of λ on disease dynamics, the next simulation will explore variations in its value. This exploration aims to thoroughly examine how alterations in the infection rate can affect the overall behavior of the system, ultimately providing deeper insights into transmission patterns and informing the development of more effective control strategies.

The data used in this study starts from the implementation of vaccination interventions in Indonesia, which are divided into six phases. The first phase was from 25 May 2021 to 8 August 2021. In this phase, the most significant increase in the number of cases was observed, and this period occurred after the holidays. Further, vaccination was implemented only in a small population of individuals in Indonesia. The second phase was from 9 August 2021 to 20 January 2022. The number of cases in this phase began to decrease until it entered the next phase. The third phase was from 21 January 2022 to 22 March 2022. The events in this phase were similar to those in the first phase. That is, there was a fairly high increase in cases. Moreover, this phase occurred after the holidays at the start of 2022. Booster dose vaccinations are also started at this phase. The fourth phase was from 23 March 2022 to 19 July 2022. In this phase, the number of cases began to decrease again until it entered the fifth phase. The fifth phase was from 20 July 2022 to 14 November 2022. In this phase, there was a fairly high increase in the number of cases. However, it was not as high as

the previous phase. Notably, this phase occurred after the school holidays, which have a high population mobilization. The final phase was from 15 November 2022 to 21 August 2023. During this phase, the number of cases began to decrease again. After dividing the data into several phases according to data behavior, parameter estimation and numerical simulations were then performed to identify the behavior of the system using data on the distribution of COVID-19 in Indonesia.

3.1. Parameter estimation

The values of the parameters in the model could be estimated using the Levenberg-Marquardt method. The estimation process was performed by fitting the model to COVID-19 data in Indonesia. The model was fitted to the six time periods described previously. Next, the parameter values were estimated as λ, φ_1, φ_2, φ_3, τ_1, γ, and ζ. Then, the other parameter values were assumed. **Table 2** shows the assumed parameter values.

Table 2. Assumed parameter values.

Parameters	Values	Description	Parameters	Values	Description
τ_2	0.002857	The rate of movement from $Q(t)$ to $I(t)$ [25].	q	0.05	Reduced rate of infection due to quarantine [25].
ρ	0.0065	Reinfection rate [26].	d	0.02	Reduced mortality rate due to vaccine [25].
p	0.590071	Reduced rate of infection due to one dose of the vaccine [25].	Λ	μN	Normal birth rate.
r	0.180143	Reduced rate of infection due to two-dose vaccine [25].	μ	0.1/100	Normal mortality rate.
s	0.05	Reduced rate of infection due to the vaccine booster dose.			

The parameter estimation process was carried out at each phase. The parameter estimates for each phase used different compartment initial values according to data on the distribution of COVID-19 at the beginning of each phase. Then, by estimating in the range $[0,1]$ with an initial guess of the estimated parameter of 1, the parameter estimation results were obtained, as presented in **Table 3**.

Table 3. Parameter estimation results.

Parameters	Phase 1	Phase 2	Phase 3	Phase 4	Phase 5	Phase 6
φ_1	2.6573×10^{-5}	2.2537×10^{-5}	1.1967×10^{-7}	2.0318×10^{-9}	2.1838×10^{-7}	4.0022×10^{-8}
φ_2	0.00404883	3.2261×10^{-8}	0.02138271	0.01665606	6.3478×10^{-4}	0.20056574
φ_3	9.2184×10^{-4}	0.01048115	0.00980319	0.04317824	2.4659×10^{-8}	1.2903×10^{-4}
λ	0.15726904	0.01516746	0.21959746	0.40082814	0.01847884	0.01675573
τ_1	0.21450170	0.23739794	0.10843339	0.40929794	0.01773789	0.03731990
γ	0.00325502	4.3557×10^{-4}	0.03614694	0.03712054	0.01526998	0.00596946
ζ	9.3787×10^{-4}	0.01578178	0.04053776	0.17200603	7.8497×10^{-5}	0.01750052

3.2. Basic reproduction number ($\mathcal{R}_0$)

The basic reproduction number (secondary infection) of the model was obtained using the next-generation matrix. Before finding the equation that defines $\mathcal{R}_0$, we first identified the disease-free equilibrium point. In disease-free conditions, disease transmission in the population was considered non-existent. Hence, the value for $I = Q = R = D = 0$ was obtained. Next, by applying $S'(t) = V_1'(t) = V_2'(t) = V_3'(t) = I'(t) = Q'(t) = R'(t) = D'(t) = 0$, we obtained:

$$E^0 = (S^0, V_1^0, V_2^0, V_3^0, I^0, Q^0, R^0, D^0) = \left(\frac{\Lambda}{k_1}, \frac{\varphi_1\Lambda}{k_1k_2}, \frac{\varphi_2\varphi_1\Lambda}{k_1k_2k_3}, \frac{\varphi_3\varphi_2\varphi_1\Lambda}{k_1k_2k_3\mu}, 0,0,0,0\right),$$

with $k_1 = \varphi_1 + \mu$, $k_2 = \varphi_2 + \mu$, $k_3 = \varphi_3 + \mu$.

When the disease-free equilibrium (DFE) state was observed, it was evident that the first vaccination dosage (φ_1) would cause the susceptible compartment, represented by $S(t)$, to continuously decrease. Similarly, it was observed that the transition rates between the first and second vaccination dose compartments caused them to decrease. On the other hand, the booster vaccination dose compartment was expected to grow as a result of the new people moving into that compartment from the previous one.

Then, by using the next generation matrix $\left(\mathbf{K} = \mathbf{FV^{-1}}\right)$ in the infected compartment in model (1), namely, compartments $I(t)$ and $Q(t)$, the matrix $\boldsymbol{\mathcal{F}}$, which is the rate of new infections, and $\boldsymbol{\mathcal{V}}$, which is the rate of movement of infected individuals, were obtained as follows:

$$\boldsymbol{\mathcal{F}} = \begin{bmatrix} \dfrac{\lambda SI + \lambda qSQ + \lambda pV_1I + \lambda pqV_1Q + \lambda rV_2I + \lambda rqV_2Q + \lambda sV_3I + \lambda sqV_3Q}{N} \\ 0 \end{bmatrix},$$

$$\boldsymbol{\mathcal{V}} = \begin{bmatrix} k_4I - \tau_2Q \\ k_5Q - \tau_1I \end{bmatrix},$$

with $k_4 = \tau_1 + \gamma + \zeta + \mu, k_5 = \tau_2 + \gamma + \zeta d + \mu$.

Then, the matrices **F** and **V** can be obtained as follows:

$$\mathbf{F} = \begin{bmatrix} \dfrac{\partial \mathcal{F}_1}{\partial I} & \dfrac{\partial \mathcal{F}_1}{\partial Q} \\ \dfrac{\partial \mathcal{F}_2}{\partial I} & \dfrac{\partial \mathcal{F}_2}{\partial Q} \end{bmatrix} = \begin{bmatrix} \dfrac{\lambda(S + pV_1 + rV_2 + sV_3)}{N} & \dfrac{\lambda q(S + pV_1 + rV_2 + sV_3)}{N} \\ 0 & 0 \end{bmatrix},$$

$$\mathbf{V} = \begin{bmatrix} \dfrac{\partial \mathcal{V}_1}{\partial I} & \dfrac{\partial \mathcal{V}_1}{\partial Q} \\ \dfrac{\partial \mathcal{V}_2}{\partial I} & \dfrac{\partial \mathcal{V}_2}{\partial Q} \end{bmatrix} = \begin{bmatrix} k_4 & -\tau_2 \\ -\tau_1 & k_5 \end{bmatrix}.$$

The next generation matrix is obtained as follows:

$$\mathbf{K} = \mathbf{FV^{-1}},$$
$$= \begin{bmatrix} \dfrac{\lambda(V_1p + V_2r + V_3s + S)(q\tau_1 + k_5)}{N(k_4k_5 - \tau_1\tau_2)} & \dfrac{\lambda(V_1p + V_2r + V_3s + S)(qk_4 + \tau_2)}{N(k_4k_5 - \tau_1\tau_2)} \\ 0 & 0 \end{bmatrix}.$$

Furthermore, the $\mathcal{R}_0$ equation from the model is the spectral radius of the **K** matrix. Hence, the $\mathcal{R}_0$ equation is obtained as follows:

$$\mathcal{R}_0 = \frac{\lambda(V_1 p + V_2 r + V_3 s + S)(q\tau_1 + k_5)}{N(k_4 k_5 - \tau_1 \tau_2)} \tag{2}$$

Next, by substituting E^0 into Equation (2), we obtain the basic reproduction number equation as follows:

$$\mathcal{R}_0 = \frac{(k_5 + q\tau_1)(\mu(p\varphi_1 + k_2)k_3 + \varphi_2(\mu r + s\varphi_3)\varphi_1)\lambda}{k_1 k_2 k_3\big(k_5(\gamma + \mu + \zeta) + \tau_1(d\zeta + \gamma + \mu)\big)} \tag{3}$$

According to the equation $\mathcal{R}_0$, the infection rate (λ), the reduction in infection rate due to quarantine (q), and the reduction in infection rate due to the first dose of vaccination to the booster (p, r, s) are important factors in determining the value of $\mathcal{R}_0$ in the system. As the rate of disease transmission (λ) increases, correspondingly increases the value of $\mathcal{R}_0$. In contrast, the reduction in infection rate due to vaccination (p, r, s), which is related to vaccine efficacy, tends to decrease $\mathcal{R}_0$ towards zero as efficacy approaches 100%. This demonstrates that higher vaccine efficacy leads to lower $\mathcal{R}_0$ values. Similarly, the parameter representing the reduction in disease transmission due to quarantine (q) shows that as compliance with the quarantine protocol increases, this value approaches zero, resulting in a decrease in the system's $\mathcal{R}_0$ value. After obtaining Equation (3), the corresponding $\mathcal{R}_0$ values for Model (1) are depicted in **Table 4**.

Table 4. Basic reproduction number in each phase.

	Phase 1	**Phase 2**	**Phase 3**	**Phase 4**	**Phase 5**	**Phase 6**
$\mathcal{R}_0$	2.8842	0.5003	1.3933	0.9872	0.615	0.3864

It can be seen from **Table 4**, phase 1 has the highest $\mathcal{R}_0$ value. This is consistent with the fact that vaccination attempts are still in their early stages and that this phase occurs after the holiday period, increasing the risk of COVID-19 transmission. In contrast, phase 2 shows a $\mathcal{R}_0$ value below 1, indicating a decrease in transmission rates. This matches the giving of up to two vaccine doses on a larger scale. However, in phase 3, the value of $\mathcal{R}_0$ increased and exceeded 1, but the secondary infection rate did not reach the same value as in phase 1. This increase in cases could be due to the post-year-end period, which is typically characterized by an increase in population movement, making individual interactions more frequent. During this phase, booster vaccine administration has also begun, and the impact on secondary infection rates will be observed later. Next, phases 4 to 6 are characterized by a consistent decrease in the value of $\mathcal{R}_0$. Notably, even after the school holidays in phase 5, the secondary infection rate remained below 1 and did not exceed the value in the previous phase. Overall, the data shows that vaccine implementation, particularly booster shots, has been effective in dealing with secondary infections in the system. Additionally, the continuous decrease in the value of $\mathcal{R}_0$ from phases 4 to 6 may also be an indication that the system is heading towards a herd immunity state, a hypothesis that will be further explored with additional simulation tools.

3.3. Bifurcation analysis

Bifurcation will be sought by finding the endemic equilibrium of model (1). Let $E^* = (S^*, V_1^*, V_2^*, V_3^*, I^*, Q^*, R^*, D^*)$ be the endemic equilibrium of model (1). Then, let the force of infection.

$$\beta^* = \frac{\lambda I^* + \lambda q Q^*}{N} \tag{4}$$

Next, by making model (1) equal to 0, it will be obtained as follows:

$$\begin{aligned}
S^* = {} & [(-k_4k_5 + \tau_1\tau_2)(\beta^* r + k_3)(\beta^* s + \mu)(\beta^* p + k_2)k_6\Lambda] \\
& / \Big[\big((-k_4k_5 + \tau_1\tau_2)k_6 + \rho\gamma(k_5 + \tau_1)\big)rsp\beta^{*4} \\
& + \Big(\big(\big((k_1 s + \mu)r + sk_3\big)p + rsk_2\big)(-k_4k_5 + \tau_1\tau_2)k_6 + \big(\big((s\varphi_1 + \mu)r + sk_3\big)p + rsk_2\big)\rho(k_5 + \tau_1)\gamma\Big)\beta^{*3} \\
& + \Big(\big(\big(k_1 r\mu + k_3(k_1 s + \mu)\big)p + \big((k_1 s + \mu)r + sk_3\big)k_2\big)(-k_4k_5 + \tau_1\tau_2)k_6 \\
& + \rho(k_5 + \tau_1)\gamma\big(\big(\mu\varphi_1 r + k_3(s\varphi_1 + \mu)\big)p + (s\varphi_1\varphi_2 + k_2\mu)r + sk_2k_3\big)\Big)\beta^{*2} \\
& + \Big(\big(p\mu k_1k_3 + \big(k_1 r\mu + k_3(k_1 s + \mu)\big)k_2\big)(-k_4k_5 + \tau_1\tau_2)k_6 \\
& + \rho\gamma(k_5 + \tau_1)(k_3\mu p\varphi_1 + \mu r\varphi_1\varphi_2 + s\varphi_1\varphi_2\varphi_3 + k_2k_3\mu)\Big)\beta^* + \mu k_1k_2k_3k_6(-k_4k_5 + \tau_1\tau_2)\Big] \\
V_1^* = {} & [\varphi_1\Lambda k_6(k_4k_5 - \tau_1\tau_2)(\beta^* r + k_3)(\beta^* s + \mu)] \\
& / \Big[-\Big(\big(\rho\gamma\varphi_1 + \tau_2k_6k_1 + \beta^*(\rho\gamma + k_6\tau_2)\big)\tau_1 + \big(\rho\gamma\varphi_1 - k_4k_6k_1 + \beta^*(\rho\gamma - k_4k_6)\big)k_5\Big)\beta^*(\beta^* s + \mu)(\beta^* r + k_3)p \\
& - (\beta^* s + \mu)\Big(\big(\tau_2k_6k_1 + \beta^*(\rho\gamma + k_6\tau_2)\big)\tau_1 + \big(-k_4k_6k_1 + \beta^*(\rho\gamma - k_4k_6)\big)k_5\Big)(\beta^* r + k_3)k_2 \\
& - \big(\mu r + s(\beta^* r + \varphi_3)\big)\varphi_2\rho\beta^*(k_5 + \tau_1)\gamma\varphi_1\Big] \\
V_2^* = {} & [(k_4k_5 - \tau_1\tau_2)(\beta^* s + \mu)k_6\Lambda\varphi_1\varphi_2] \\
& / \Big[-(\beta^* + k_1)(\beta^* r + k_3)(-k_4k_5 + \tau_1\tau_2)(\beta^* s + \mu)(\beta^* p + k_2)k_6 \\
& - \Big(\beta^{*3}prs + (prs\varphi_1 + (k_2 r + k_3 p)s + \mu pr)\beta^{*2} + \big(\big(rs\varphi_2 + p(sk_3 + \mu r)\big)\varphi_1 + sk_2k_3 + (k_2 r + k_3 p)\mu\Big)\beta^* \\
& + \big((\mu r + s\varphi_3)\varphi_2 + k_3 p\mu\big)\varphi_1 + k_2k_3\mu\Big)\rho\beta^*(k_5 + \tau_1)\gamma\Big] \\
V_3^* = {} & [\varphi_3\varphi_2\varphi_1\Lambda k_6(-k_4k_5 + \tau_1\tau_2)] \\
& / \Big[\big((-k_4k_5 + \tau_1\tau_2)k_6 + \rho\gamma(k_5 + \tau_1)\big)rsp\beta^4 \\
& + \Big(\big(\big((k_1 s + \mu)r + sk_3\big)p + rsk_2\big)(-k_4k_5 + \tau_1\tau_2)k_6 + \big(\big((s\varphi_1 + \mu)r + sk_3\big)p + rsk_2\big)\rho(k_5 + \tau_1)\gamma\Big)\beta^3 \\
& + \Big(\big(\big(k_1 r\mu + k_3(k_1 s + \mu)\big)p + \big((k_1 s + \mu)r + sk_3\big)k_2\big)(-k_4k_5 + \tau_1\tau_2)k_6 \\
& + \rho(k_5 + \tau_1)\gamma\big(\big(\mu\varphi_1 r + k_3(s\varphi_1 + \mu)\big)p + (s\varphi_1\varphi_2 + k_2\mu)r + sk_2k_3\big)\Big)\beta^2 \\
& + \Big(\big(p\mu k_1k_3 + \big(k_1 r\mu + k_3(k_1 s + \mu)\big)k_2\big)(-k_4k_5 + \tau_1\tau_2)k_6 \\
& + \rho\gamma(k_5 + \tau_1)(k_3\mu p\varphi_1 + \mu r\varphi_1\varphi_2 + s\varphi_1\varphi_2\varphi_3 + k_2k_3\mu)\Big)\beta + \mu k_1k_2k_3k_6(-k_4k_5 + \tau_1\tau_2)\Big] \\
I^* = {} & \Big[\Big(\big((p\beta^* k_3 + \beta^*(\beta^* p + \varphi_2)r + \varphi_2\varphi_3)\varphi_1 + \beta^*(\beta^* r + k_3)(\beta^* p + k_2)\big)s \\
& + \Big(\big(k_3 p + r(\beta^* p + \varphi_2)\big)\varphi_1 + (\beta^* r + k_3)(\beta^* p + k_2)\Big)\mu\Big)k_6\beta^* k_5\Lambda\Big] \\
& / \Big[-\Big(\tau_2(\beta^* + k_1)(\beta^* r + k_3)(\beta^* s + \mu)(\beta^* p + k_2)k_6 \\
& + \Big(\big((p\beta^* k_3 + \beta^*(\beta^* p + \varphi_2)r + \varphi_2\varphi_3)\varphi_1 + \beta^*(\beta^* r + k_3)(\beta^* p + k_2)\big)s \\
& + \Big(\big(k_3 p + r(\beta^* p + \varphi_2)\big)\varphi_1 + (\beta^* r + k_3)(\beta^* p + k_2)\Big)\mu\Big)\rho\beta^*\gamma\Big)\tau_1 \\
& - k_5\Big(-k_4(\beta^* + k_1)(\beta^* r + k_3)(\beta^* s + \mu)(\beta^* p + k_2)k_6 \\
& + \Big(\big((p\beta^* k_3 + \beta^*(\beta^* p + \varphi_2)r + \varphi_2\varphi_3)\varphi_1 + \beta^*(\beta^* r + k_3)(\beta^* p + k_2)\big)s \\
& + \Big(\big(k_3 p + r(\beta^* p + \varphi_2)\big)\varphi_1 + (\beta^* r + k_3)(\beta^* p + k_2)\Big)\mu\Big)\rho\beta^*\gamma\Big)\Big]
\end{aligned} \tag{5}$$

$$
\begin{aligned}
Q^* = &\Big[\Big(\big((p\beta^* k_3 + \beta^*(\beta^* p + \varphi_2)r + \varphi_2\varphi_3)\varphi_1 + \beta^*(\beta^* r + k_3)(\beta^* p + k_2)\big)s \\
&+ \Big(\big(k_3 p + r(\beta^* p + \varphi_2)\big)\varphi_1 + (\beta^* r + k_3)(\beta^* p + k_2)\Big)\mu\Big) k_6 \beta^* \tau_1 \Lambda\Big] \\
&/\Big[-\Big(\tau_2(\beta^* + k_1)(\beta^* r + k_3)(\beta^* s + \mu)(\beta^* p + k_2)k_6 \\
&+ \Big(\big((p\beta^* k_3 + \beta^*(\beta^* p + \varphi_2)r + \varphi_2\varphi_3)\varphi_1 + \beta^*(\beta^* r + k_3)(\beta^* p + k_2)\big)s \\
&+ \Big(\big(k_3 p + r(\beta^* p + \varphi_2)\big)\varphi_1 + (\beta^* r + k_3)(\beta^* p + k_2)\Big)\mu\Big)\rho\beta^*\gamma\Big)\tau_1 \\
&- k_5\Big(-k_4(\beta^* + k_1)(\beta^* r + k_3)(\beta^* s + \mu)(\beta^* p + k_2)k_6 \\
&+ \Big(\big((p\beta^* k_3 + \beta^*(\beta^* p + \varphi_2)r + \varphi_2\varphi_3)\varphi_1 + \beta^*(\beta^* r + k_3)(\beta^* p + k_2)\big)s \\
&+ \Big(\big(k_3 p + r(\beta^* p + \varphi_2)\big)\varphi_1 + (\beta^* r + k_3)(\beta^* p + k_2)\Big)\mu\Big)\rho\beta^*\gamma\Big)\Big] \\
R^* = &\Big[\Big(\Big(\big((p\beta^* k_3 + \beta^*(\beta^* p + \varphi_2)r + \varphi_2\varphi_3)s + \mu\big(k_3 p + r(\beta^* p + \varphi_2)\big)\big)\Big)\varphi_1 + (\beta^* r + k_3)(\beta^* s + \mu)(\beta^* p + k_2)\Big)\beta^*(k_5 + \tau_1)\Lambda\gamma\Big] \\
&/\Big[-(\beta^* + k_1)(\beta^* r + k_3)(-k_4 k_5 + \tau_1\tau_2)(\beta^* s + \mu)(\beta^* p + k_2)k_6 \\
&- \Big(\Big(\big((p\beta^* k_3 + \beta^*(\beta^* p + \varphi_2)r + \varphi_2\varphi_3)s + \mu\big(k_3 p + r(\beta^* p + \varphi_2)\big)\big)\Big)\varphi_1 + (\beta^* r + k_3)(\beta^* s + \mu)(\beta^* p + k_2)\Big)\rho\beta^*(k_5 \\
&+ \tau_1)\gamma\Big] \\
D^* = &\Big[(\tau_1 d + k_5)\beta^*\Lambda k_6\Big(\big((p\beta^* k_3 + \beta^*(\beta^* p + \varphi_2)r + \varphi_2\varphi_3)\varphi_1 + \beta^*(\beta^* r + k_3)(\beta^* p + k_2)\big)s \\
&+ \Big(\big(k_3 p + r(\beta^* p + \varphi_2)\big)\varphi_1 + (\beta^* r + k_3)(\beta^* p + k_2)\Big)\mu\Big)\zeta\Big] \\
&/\Big[-\Big(\tau_2(\beta^* + k_1)(\beta^* r + k_3)(\beta^* s + \mu)(\beta^* p + k_2)k_6 \\
&+ \Big(\big((p\beta^* k_3 + \beta^*(\beta^* p + \varphi_2)r + \varphi_2\varphi_3)\varphi_1 + \beta^*(\beta^* r + k_3)(\beta^* p + k_2)\big)s \\
&+ \Big(\big(k_3 p + r(\beta^* p + \varphi_2)\big)\varphi_1 + (\beta^* r + k_3)(\beta^* p + k_2)\Big)\mu\Big)\rho\beta^*\gamma\Big)\tau_1 \\
&+ k_5\Big(k_4(\beta^* + k_1)(\beta^* r + k_3)(\beta^* s + \mu)(\beta^* p + k_2)k_6 \\
&- \Big(\big((p\beta^* k_3 + \beta^*(\beta^* p + \varphi_2)r + \varphi_2\varphi_3)\varphi_1 + \beta^*(\beta^* r + k_3)(\beta^* p + k_2)\big)s \\
&+ \Big(\big(k_3 p + r(\beta^* p + \varphi_2)\big)\varphi_1 + (\beta^* r + k_3)(\beta^* p + k_2)\Big)\mu\Big)\rho\beta^*\gamma\Big)\Big]
\end{aligned}
$$

with $k_5 = \mu + \rho$. Furthermore, by substituting Equation (5) for Equation (4), we can obtain a non-zero equilibrium from model (1) with the equation form β^* as follows:

$$A{\beta^*}^4 + B{\beta^*}^3 + C{\beta^*}^2 + D\beta^* + E = 0, \tag{6}$$

with

$$
\begin{aligned}
A &= -prs\Big(k_6\big(k_5(\mu + \zeta) + \tau_1(d\zeta + \mu)\big) + \mu\gamma(k_5 + \tau_1)\Big), \\
B &= \Big(\Big(\Big(\big((\lambda\mu q + k_1\tau_2)\tau_1 + k_5(-k_1 k_4 + \lambda\mu)\big)k_6 + \rho\gamma\varphi_1(k_5 + \tau_1)\Big)s \\
&\quad + \big((-k_4 k_5 + \tau_1\tau_2)k_6 + \rho\gamma(k_5 + \tau_1)\big)\mu\Big)r \\
&\quad + \big((-k_4 k_5 + \tau_1\tau_2)k_6 + \rho\gamma(k_5 + \tau_1)\big)sk_3\Big)p \\
&\quad + \big((-k_4 k_5 + \tau_1\tau_2)k_6 + \rho\gamma(k_5 + \tau_1)\big)rk_2 s,
\end{aligned}
$$

$$
\begin{aligned}
C = \Big(& p\lambda r(\tau_1 q + k_5)\mu^2 \\
& + \Big(\big((\lambda\varphi_1(\tau_1 q + k_5)s + k_1(-k_4k_5 + \tau_1\tau_2)\big)r \\
& + k_3(\lambda(\tau_1 q + k_5)s + \tau_1\tau_2 - k_4k_5)\Big)p \\
& + (\lambda(\tau_1 q + k_5)s + \tau_1\tau_2 - k_4k_5)rk_2\Big)\mu \\
& + \big(pk_1k_3 + k_2(k_1 r + k_3)\big)s(-k_4k_5 + \tau_1\tau_2)\Big)k_6 \\
& + \rho\Big((k_3p\varphi_1 + r\varphi_1\varphi_2 + k_2k_3)s + \big((\varphi_1 r + k_3)p + k_2 r\big)\mu\Big)(k_5 \\
& + \tau_1)\gamma, \\
D = & \big(k_3p + r(p\varphi_1 + k_2)\big)k_6(\tau_1 q + k_5)\lambda\mu^2 \\
& + \Big(\Big(\big((p\lambda\varphi_1 qs + \lambda qsk_2 + \tau_2(k_1p + k_2)\big)\tau_1 \\
& + k_5\big(p\lambda\varphi_1 s + sk_2\lambda - k_4(k_1p + k_2)\big)\big)k_3 \\
& + \big((\lambda qs\varphi_1\varphi_2 + k_1k_2\tau_2)\tau_1 + k_5(\lambda\varphi_1\varphi_2 s - k_1k_2k_4)\big)r\Big)k_6 \\
& + \rho\gamma(k_5 + \tau_1)\big((p\varphi_1 + k_2)k_3 + r\varphi_1\varphi_2\big)\Big)\mu \\
& + \big(k_1k_2(-k_4k_5 + \tau_1\tau_2)k_6k_3 + \rho\gamma\varphi_1\varphi_2\varphi_3(k_5 + \tau_1)\big)s, \\
E = & \hat{E}(1 - \mathcal{R}_0),
\end{aligned}
$$

with $\hat{E} = -\mu k_1k_2k_3k_6\big(k_5(\gamma + \mu + \zeta) + \tau_1(d\zeta + \gamma + \mu)\big)$.

The polynomial Equation (6) can be analyzed to determine the chance of endemic equilibrium in the model. Remember that the values of A and $\hat{E}$ are always negative. The following theorems are obtained when the values B, C, and D are positive or negative and $\mathcal{R}_0$ is less than or greater than one:

Theorem 1. *The Model (1) has*

(i) a unique endemic equilibrium if $E > 0$, which occurs iff $\mathcal{R}_0 > 1$, provided that one of the following conditions is met:
   - *a) the coefficients B, C, and D are either all positive or all negative,*
   - *b) B is negative, D is positive, and C may be either positive or negative.*

(ii) two endemic equilibria when $E < 0$, a condition that holds true iff $\mathcal{R}_0 < 1$, provided that one of the following conditions is met:
   - *a) both B and C are positive, whereas D may be either positive or negative,*
   - *b) coefficients C and D may both be positive or negative, whereas variable B is always the inverse sign,*
   - *c) B with either C or D being negative, and the other coefficient is positive.*

(iii) three endemic equilibria when $E > 0$ iff $\mathcal{R}_0 > 1$, provided that one of the following conditions is met:
   - *a) B, with either C or D being positive and the other coefficient being negative,*
   - *b) D with B or C negative and the other coefficient positive.*

(iv) four endemic equilibria when $E < 0$ iff $\mathcal{R}_0 < 1$, and the coefficients B and D are positive, whereas C is negative.

(v) no endemic equilibrium otherwise.

Furthermore, we will explore the behavior of bifurcation on the model. First, let $\mathbf{x} = (x_1, x_2, x_3, x_4, x_5, x_6, x_7, x_8)^T = (S, V_1, V_2, V_3, I, Q, R, D)^T$. Therefore, the model can be rewritten in the form $\frac{dx}{dt} = f(x)$, with $f(x) = \big(f_1(x), \ldots, f_8(x)\big)$, as follows:

$$
\begin{aligned}
x_1' &= \Lambda - \frac{\lambda x_1 x_5}{N} - \frac{\lambda q x_1 x_6}{N} - \varphi_1 x_1 + \rho x_7 - \mu x_1 = f_1,\\
x_2' &= \varphi_1 x_1 - \frac{\lambda p x_2 x_5}{N} - \frac{\lambda p q x_2 x_6}{N} - \varphi_2 x_2 - \mu x_2 = f_2,\\
x_3' &= \varphi_2 x_2 - \frac{\lambda r x_3 x_5}{N} - \frac{\lambda r q x_3 x_6}{N} - \varphi_3 x_3 - \mu x_3 = f_3,\\
x_4' &= \varphi_3 x_3 - \frac{\lambda s x_4 x_5}{N} - \frac{\lambda s q x_4 x_6}{N} - \mu x_4 = f_4,\\
x_5' &= \frac{\lambda x_1 x_5}{N} + \frac{\lambda p x_2 x_5}{N} + \frac{\lambda r x_3 x_5}{N} + \frac{\lambda s x_4 x_5}{N} + \frac{\lambda q x_1 x_6}{N} + \frac{\lambda p q x_2 x_6}{N} + \frac{\lambda r q x_3 x_6}{N}\\
&\qquad + \frac{\lambda s q x_4 x_6}{N} - \tau_1 x_5 + \tau_2 x_6 - \gamma x_5 - \zeta x_5 - \mu x_5 = f_5,\\
x_6' &= \tau_1 x_5 - \tau_2 x_6 - \gamma x_6 - \zeta d x_6 - \mu x_6 = f_6,\\
x_7' &= \gamma x_5 + \gamma x_6 - \rho x_7 - \mu x_7 = f_7,\\
x_8' &= \zeta x_5 + \zeta d x_6 = f_8,\\
N &= x_1 + x_2 + x_3 + x_4 + x_5 + x_6 + x_7 + x_8.
\end{aligned}
\tag{7}
$$

Then choose λ as the bifurcation parameter with E^0 as the disease-free equilibrium point. After that the model (1) can undergo bifurcation at $\mathcal{R}_0 = 1$, then $\lambda^* = \lambda = \frac{k_1\big((\tau_1+k_5)\mu+(d\zeta+\gamma)\tau_1+k_5(\gamma+\zeta)\big)k_3k_2}{(q\tau_1+k_5)\Big(\big((k_3p+r\varphi_2)\varphi_1+k_2k_3\big)\mu+s\varphi_1\varphi_2\varphi_3\Big)}$. The Jacobian Matrix of the system (7) at E^0 and evaluated for $\lambda = \lambda^*$ is given as,

$$
\mathbf{J}(E^0, \lambda^*) = \begin{bmatrix}
-k_1 & 0 & 0 & 0 & -\frac{\lambda\mu}{k_1} & -\frac{\lambda q\mu}{k_1} & \rho & 0\\
\varphi_1 & -k_2 & 0 & 0 & -\frac{\mu\varphi_1 p\lambda}{k_1k_2} & -\frac{\mu\varphi_1 qp\lambda}{k_1k_2} & 0 & 0\\
0 & \varphi_2 & -k_3 & 0 & -\frac{\lambda\varphi_2\mu r\varphi_1}{k_1k_2k_3} & -\frac{\mu\varphi_1\varphi_2 qr\lambda}{k_1k_2k_3} & 0 & 0\\
0 & 0 & \varphi_3 & -\mu & -\frac{\varphi_1\varphi_2\varphi_3 s\lambda}{k_1k_2k_3} & -\frac{\lambda sq\varphi_3\varphi_2\varphi_1}{k_1k_2k_3} & 0 & 0\\
0 & 0 & 0 & 0 & \frac{K_1}{\big((\varphi_2+k_3)\mu+\varphi_2\varphi_3\big)\varphi_1+k_2k_3\mu} & \frac{K_2}{\big((\varphi_2+k_3)\mu+\varphi_2\varphi_3\big)\varphi_1+k_2k_3\mu} & 0 & 0\\
0 & 0 & 0 & 0 & \tau_1 & -k_5 & 0 & 0\\
0 & 0 & 0 & 0 & \gamma & \gamma & -k_6 & 0\\
0 & 0 & 0 & 0 & \zeta & d\zeta & 0 & 0
\end{bmatrix}
$$

with $K_1 = \Big(\big((\lambda r - k_4)\varphi_2 + k_3(\lambda p - k_4)\big)\mu + \varphi_2\varphi_3(\lambda s - k_4)\Big)\varphi_1 + k_2k_3\mu(\lambda - k_4)$ and $K_2 = \Big(\big((\lambda qr + \tau_2)\varphi_2 + k_3(\lambda pq + \tau_2)\big)\mu + \varphi_2\varphi_3(\lambda qs + \tau_2)\Big)\varphi_1 + k_2k_3\mu(\lambda q + \tau_2)$.

The Jacobian Matrix of system (7) has a zero-part eigenvalue and has all negative parts of the other eigenvalues. As a result, we applied the center manifold theorem to analyze behavior near $\lambda = \lambda^*$.

Furthermore, let $\mathbf{v} = (v_1, v_2, v_3, v_4, v_5, v_6, v_7, v_8)$ be the left eigenvector of the Jacobian Matrix $\mathbf{J}(E^0, \lambda^*)$ corresponding to the zero real part eigenvalue. Then we get $\mathbf{v}$ as follows:

$$\begin{aligned} &v_1 = 0, v_2 = 0, v_3 = 0, v_4 = 0, \\ &v_5 = -\frac{\zeta(d\tau_1 + k_5)(k_2k_3\mu + k_3\varphi_1\mu + \varphi_1\varphi_2\mu + \varphi_1\varphi_2\varphi_3)}{K_1k_5 + K_2\tau_1}v_8, \\ &v_6 = \frac{\zeta(K_1d - K_2)}{K_1k_5 + K_2\tau_1}v_8, v_7 = 0, v_8 = v_8 \end{aligned} \tag{8}$$

From the Jacobian Matrix $\mathbf{J}(E^0, \lambda^*)$, we obtained the right eigenvector corresponding to $\mathbf{v} \cdot \mathbf{w} = 1$. Let $\mathbf{w} = (w_1, w_2, w_3, w_4, w_5, w_6, w_7, w_8)$, then

$$\begin{aligned} &w_1 = 0, w_2 = 0, w_3 = 0, w_4 = 0, \\ &w_5 = -\frac{K_1k_5 + K_2\tau_1}{2\zeta(k_5 + d\tau_1)\left(\left((k_3 + \varphi_2)\mu + \varphi_2\varphi_3\right)\varphi_1 + k_2k_3\mu\right)}, \\ &w_6 = \frac{K_1k_5 + K_2\tau_1}{2\zeta(K_1d - K_2)}, w_7 = 0, w_8 = 0 \end{aligned} \tag{9}$$

Furthermore, we defined coefficients $\hat{a}$ and $\hat{b}$ using the Theorem of Castillo-Chavez and Song [16] as follows:

$$\hat{a} = \sum_{k,i,j=1}^{8} v_k w_i w_j \frac{\partial^2 f_k}{\partial x_i \partial x_j}(E_0, \lambda^*),$$
$$\hat{b} = \sum_{k,i=1}^{8} v_k w_i \frac{\partial^2 f_k}{\partial x_i \partial \lambda}(E_0, \lambda^*).$$

Considering the values of Equations (8) and (9), we get

$$\hat{a} = \frac{\psi_1\psi_2\lambda k_2(K_1k_5 + K_2\tau_1)\left(\left((k_3p + r\varphi_2)\varphi_1 + k_2k_3\right)\mu + s\varphi_3\varphi_2\varphi_1\right)k_1k_3\mu}{2\left(\left((\varphi_2 + k_3)\varphi_1 + k_2k_3\right)\mu + \varphi_1\varphi_2\varphi_3\right)^3(K_1d - K_2)^2\Lambda\zeta(d\tau_1 + k_5)} \tag{10}$$

$$\hat{b} = \frac{\psi_1\left(\left((k_3p + r\varphi_2)\mu + s\varphi_2\varphi_3\right)\varphi_1 + k_2k_3\mu\right)}{2(K_1d - K_2)\left(\left((\varphi_2 + k_3)\mu + \varphi_2\varphi_3\right)\varphi_1 + k_2k_3\mu\right)} \tag{11}$$

with

$$\psi_1 = \left(-\left((\varphi_2 + k_3)\varphi_1 + k_2k_3\right)q(d\tau_1 + k_5)\mu - \varphi_2\varphi_3q(d\tau_1 + k_5)\varphi_1 + K_1d - K_2\right)$$
$$\psi_2 = \left(-\left((\varphi_2 + k_3)\varphi_1 + k_2k_3\right)(d\tau_1 + k_5)\mu - \varphi_2\varphi_3(d\tau_1 + k_5)\varphi_1 + K_1d - K_2\right).$$

According to the Castillo-Chavez and Song theorem [16], backward bifurcation takes place when both coefficients $\hat{a}$ and $\hat{b}$ are positive. Therefore, our next step will be to identify the conditions under which these coefficients can be positive. We will focus on the components of coefficients $\hat{a}$ and $\hat{b}$ that may influence their sign, specifically $K_1d - K_2$, $K_1k_5 + K_2\tau_1$, ψ_1, and ψ_2. First, consider the value $K_1d - K_2$, which can be positive or negative.

$$\lambda < \frac{\left(((\varphi_2 + k_3)\mu + \varphi_2\varphi_3)\varphi_1 + k_2k_3\mu\right)(dk_4 + \tau_2)}{\left(((k_3p + r\varphi_2)\mu + s\varphi_2\varphi_3)\varphi_1 + k_2k_3\mu\right)(d - q)} \tag{12}$$

If the inequality (12) holds, $K_1d - K_2$ will be negative. This ensures that the denominator, $\hat{b}$, is negative. After checking the numerator of $\hat{b}$, there is ψ_1, which will be negative in this case, resulting in a negative numerator for $\hat{b}$. As a result, the coefficient for $\hat{b}$ is positive. The coefficient $\hat{a}$ in the negative $K_1d - K_2$ scenario is squared in the denominator $\hat{a}$, ensuring a positive denominator. Next, for the numerator $\hat{a}$ involving ψ_1 and ψ_2, negative values $K_1d - K_2$ imply that ψ_1 and ψ_2 are negative, so we only need to check $K_1k_5 + K_2\tau_1$, which can be positive or negative. If the inequality (13), which comes from $K_1k_5 + K_2\tau_1$, is satisfied, the numerator $\hat{a}$ is positive, and thus the coefficient $\hat{a}$ is positive. As a result, the system will undergo backward bifurcation.

$$\lambda > \frac{\left(((\varphi_2 + k_3)\mu + \varphi_2\varphi_3)\varphi_1 + k_2k_3\mu\right)\left(k_5(\gamma + \mu + \zeta) + \tau_1(d\zeta + \gamma + \mu)\right)}{(q\tau_1 + k_5)\left(((k_3p + r\varphi_2)\mu + \varphi_2\varphi_3s)\varphi_1 + k_2k_3\mu\right)} \tag{13}$$

In the case where the inequality (12) is not met or the value $K_1d - K_2$ is positive, it is easier to ensure that the denominators of these two coefficients are positive.

$$\lambda > \frac{((q\tau_1 + k_4)d + qk_5 + \tau_2)\left(((\varphi_2 + k_3)\mu + \varphi_2\varphi_3)\varphi_1 + k_2k_3\mu\right)}{\left(((k_3p + r\varphi_2)\mu + \varphi_2\varphi_3s)\varphi_1 + k_2k_3\mu\right)(d - q)} \tag{14}$$

The inequalities (14) and (15) derive from ψ_1 and ψ_2, respectively. First, we will look at the coefficient $\hat{b}$. If the inequality (14) is not satisfied, the numerator $\hat{b}$ becomes negative, which leads to forward bifurcation. However, if the inequality (14) is true, the coefficient $\hat{b}$ must be positive. This allows us to proceed to the coefficients $\hat{a}$. When evaluating the numerator of the coefficient $\hat{a}$, consider the value ψ_2 and the form $K_1k_5 + K_2\tau_1$.

$$\lambda > \frac{((\tau_1 + k_4)d + \tau_2 + k_5)\left(((\varphi_2 + k_3)\mu + \varphi_2\varphi_3)\varphi_1 + k_2k_3\mu\right)}{\left(((k_3p + r\varphi_2)\mu + \varphi_2\varphi_3s)\varphi_1 + k_2k_3\mu\right)(d - q)} \tag{15}$$

It is important to consider the inequalities (13) and (15). If both inequalities are satisfied, the coefficient $\hat{a}$ will be positive, meaning a backward bifurcation of the system occurs.

Based on the previous discussion, we can obtain the following theorem:

Theorem 2. *Model* (1) *will undergo a backward bifurcation at* $\mathcal{R}_0 = 1$ *if either inequalities* (12) *and* (13) *are met, or inequalities* (13)–(15) *are concurrently satisfied.*

The endemic equilibrium of model (1) is obtained by solving the β^* equation. Next, using Equation (6), we can determine all positive solutions along the bifurcation parameter ($\mathcal{R}_0$). Hence, we can obtain the bifurcation diagram of system 1 in each phase. Theorems 1 and 2 will then be used to characterize system dynamics in the phase following the giving of booster vaccinations to the population.

Table 5 shows that the coefficients A, B, C, D, and $\hat{E}$ are all negative. After checking Theorem 1, it is clear that in the post-booster vaccination phase, the system exhibits a unique endemic equilibrium when $\mathcal{R}_0 > 1$ and no endemic equilibrium when $\mathcal{R}_0 < 1$. This trend indicates that the system is moving toward forward bifurcation. To confirm this, Theorem 2 can be used. From columns 8–11 in **Table 5**, it shows that none of the inequalities are met during the post-vaccine booster phase. As a result, Theorem 2 states that the system will bifurcate forward. The presence of forward bifurcation indicates that this system is easier to control than systems with backward bifurcation. This is because smooth changes in stable equilibrium conditions can occur without causing sudden stability changes. To be more precise, we will attempt to model the system bifurcation diagram for each phase. **Figure 1** depicts the simulation results for each phase of the bifurcation diagram.

Table 5. The values A, B, C, D, $\hat{E}$, and the right hand side of inequalities (12)–(15) in the phase after booster vaccination.

Phase	A	B	C	D	$\hat{E}$	λ	Right hand side of inequality			
							(12)	(13)	(14)	(15)
4	-4.7×10^{-7}	-1.4×10^{-7}	-6×10^{-9}	-6.9×10^{-11}	-1.5×10^{-13}	0.401	−0.5	0.406	−0.6	−2.3
5	-4.5×10^{-9}	-1.4×10^{-10}	-1.1×10^{-12}	-3.1×10^{-15}	-7.4×10^{-18}	0.018	−0.12	0.03	−0.15	−0.77
6	-1.1×10^{-8}	-4.1×10^{-9}	-1×10^{-10}	-5.9×10^{-13}	-8.9×10^{-16}	0.017	−0.13	0.04	−0.15	−0.5

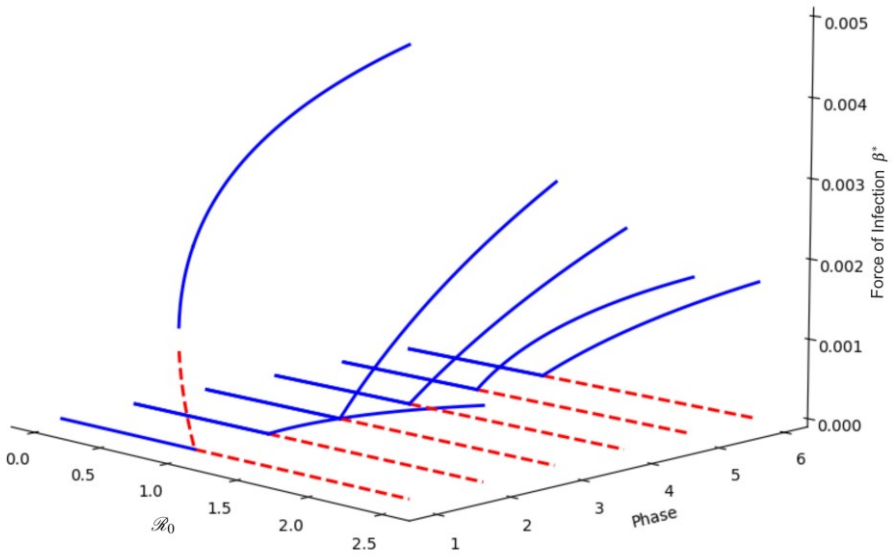

Figure 1. Bifurcation diagram.

Figure 1 shows simulation results of bifurcation diagrams for different phases, showing various bifurcation behaviors. The early phase is distinguished by a backward bifurcation pattern, indicating a more difficult disease control situation. This is due to a sudden increase in the stable equilibrium indicated by the force of infection values, particularly near the basic reproduction number ($\mathcal{R}_0$) of 1. In contrast, the next phase exhibits forward bifurcation, indicating a more controllable system. In this phase, changes in stability at the equilibrium point are predictable, and secondary infection rates greater than one do not result in an explosion of cases like in the first phase.

Next, we will look at the values obtained in each phase. When we examine the dynamics of total infection cases in a population, we can see that phases 1 and 3 saw an increase in cases, which was associated with increased population mobility. This is reflected in the bifurcation diagram, which shows higher values for these phases than other phases. The bifurcation diagram in phase 2 shows a shift from backward to forward and a significant decrease in the peak point $\mathcal{R}_0$ from phase 1. This indicates the impact of giving the two-dose vaccine. Finally, we observed conditions following the distribution of the booster vaccine to the public. The bifurcation diagrams for phases 4, 5, and 6 all show controlled conditions, as indicated by changes in the maximum value of $\mathcal{R}_0$ becoming lower. For instance, with $\mathcal{R}_0$ of 2.5, the value of β^* in phase 5 is 0.00193, and in phase 6, it is 0.00171. These changes suggest that giving additional vaccine doses can alter system dynamics, resulting in more controlled conditions. In practice, this means that any sudden increase in cases or secondary infections in a population will result in fewer severe cases than if no booster vaccine dose was given.

3.4. Sensitivity analysis

Sensitivity analysis of $\mathcal{R}_0$ was conducted to identify the parameters that could provide the most significant changes to $\mathcal{R}_0$. Sensitivity analysis of the parameter values in phase 6 was performed. Then, as shown in **Table 6**, the sensitivity index of each parameter was obtained.

Table 6. Parameter sensitivity index.

Parameters	Phase 6 Sensitivity Index	Parameters	Phase 6 Sensitivity Index
λ	1	φ_1	-3.349×10^{-5}
τ_1	−0.368	r	6.385×10^{-6}
ζ	−0.353	φ_3	-5.27×10^{-7}
γ	−0.327	s	2.287×10^{-7}
q	0.155	p	1.177×10^{-7}
τ_2	0.103	φ_2	-8.434×10^{-8}
μ	−0.055	ρ	-8.434×10^{-8}
d	−0.012		

Table 6 shows the sensitivity levels of the parameters, sorted from most sensitive to least sensitive. The parameters most sensitive to $\mathcal{R}_0$ include the rate of infection (λ), the rate of movement from $I(t)$ to $Q(t)$ (τ_1), the rate of COVID-19 mortality (ζ), and the rate of recovery (γ).

3.5. Numerical simulation

Numerical simulations were conducted to further explore the behavior of the system. The simulation was performed on a system with conditions such as those in phase 6. Hence, the estimated parameter values from phase 6 were used. First, we looked at the bifurcation diagram produced in the 6th phase. As shown in **Figure 1**, the system in phase 6 undergoes the forward bifurcation that was interpreted

previously. Now, we can further examine what happens when the system in this phase experiences backward bifurcation.

Based on the sensitivity analysis that was conducted previously, the parameter λ was the most sensitive to changes in $\mathcal{R}_0$. Next, variations in the λ value will be performed to obtain backward bifurcation in the system in phase 6. To accomplish this, we will use the conditions outlined in Theorem 2, which will guide modifications in λ to ensure the system transitions to the backward bifurcation state.

When selecting a parameter other than λ to explore backward bifurcation, it is essential to use a sufficiently large value. This necessity arises because λ is the parameter that significantly influences the development of backward bifurcation. A sensitivity value for λ approaching 1 suggests that even minor changes in this parameter can lead to substantial alterations in the system's dynamics. Conversely, the sensitivity values of other parameters in the model are generally below 0.5, with some being exceedingly low, nearing 0. This indicates that variations in these other parameters will have minimal impact on the system's behavior, particularly regarding the formation of backward bifurcation. Therefore, λ emerges as the pivotal parameter determining the occurrence of backward bifurcation in the model and thus becomes the primary focus of analysis and simulation aimed at understanding the dynamics of disease spread. We will begin by simulating the bifurcation of the system when λ equals 2.

If we looked at the backward bifurcation in **Figure 2**, the change in the equilibrium of the system from secondary infection from the left to the right, when the value $\mathcal{R}_0 = 1$ arrives, a backward bifurcation occurs. The equilibrium of the system, which previously had a value of 1, namely the disease-free equilibrium, in the range $0.839 < \mathcal{R}_0 < 1$ has three equilibria (two stable equilibria and one unstable equilibrium). Furthermore, if changes occur again when $\mathcal{R}_0 > 1$, the equilibrium of the system becomes two (an unstable disease-free equilibrium and a stable endemic equilibrium). We need to pay attention when the secondary infection value moves to > 0, at this point, there is a change in the endemic equilibrium value, which suddenly increases to a value of 0.00256. This is extremely different from forward bifurcation where endemic equilibrium changes occur gradually. Thus, during backward bifurcation, there could be a sudden increase in the number of cases if secondary infections in the system have exceeded number 1. As a result, standard medical interventions against COVID-19 will become more challenging due to the increase in the number of cases in the system.

To make it clearer, we looked at the bifurcation diagram between secondary infection parameters and compartment I^*. As depicted in **Figure 3**, we identified the change in the system's equilibrium when it passes secondary infection 1. The backward bifurcation produced by the system in phase 6 causes an endemic equilibrium, which immediately jumps to 5.3 million until the secondary infection value reaches the endemic equilibrium point for compartment I^* at 6.8 million. This was extremely different from forward bifurcation in a system where the endemic equilibrium point gradually increases. That is, at the endpoint, secondary infections in the diagram are only at 4.4 million. This difference could explain why a system with backward bifurcation experiences more difficulties in controlling disease transmission

with standard interventions because there was an extremely high increase in the number of cases compared with a system with forward bifurcation. On the other hand, forward bifurcation made it possible to implement efficient medical interventions that might lessen or even reverse the trend, possibly leading to the system's return to a state free of disease.

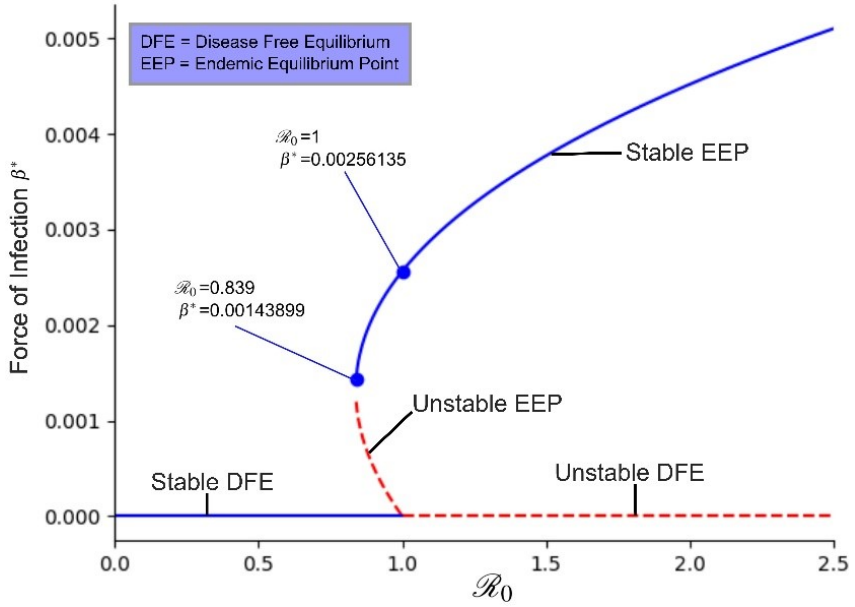

Figure 2. Backward bifurcation of the system in phase 6 with variation of λ.

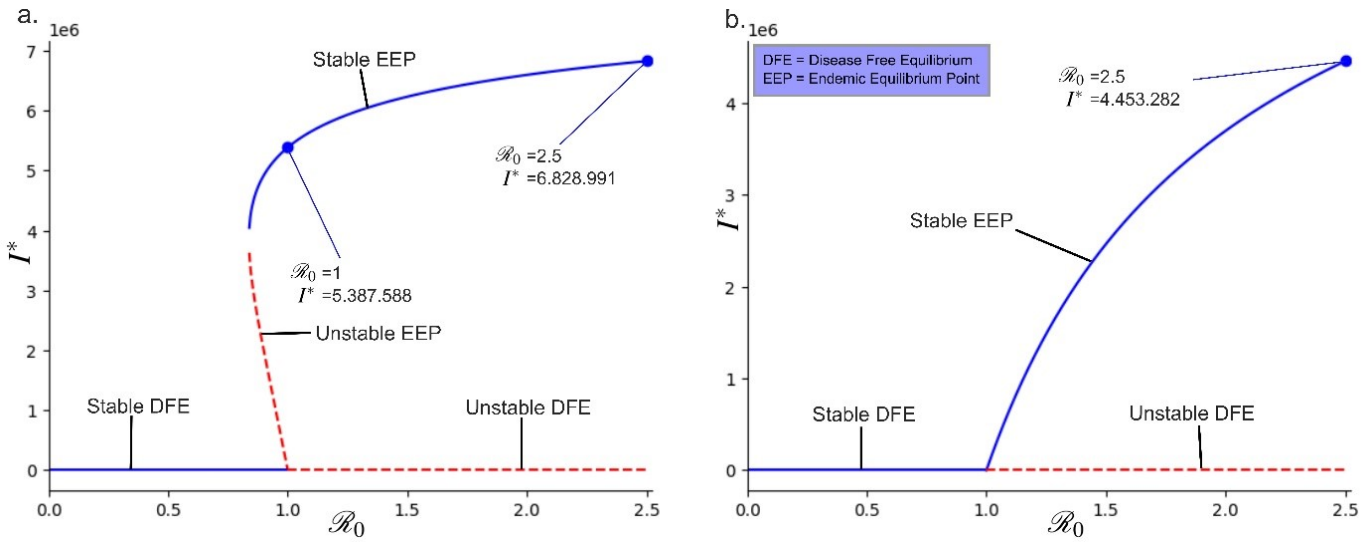

Figure 3. Backward bifurcation **(a)** and forward bifurcation **(b)** in a phase 6.

On the other hand, bifurcation simulations that varied the value of λ revealed that a progressive increase in λ leads to a shift in the system's behavior from forward bifurcation to backward bifurcation. This phenomenon suggests that a continuous rise in λ can exacerbate conditions for disease spread within the system. One significant drawback of backward bifurcation is the challenge it poses for implementing effective disease mitigation or management strategies. In this scenario, even if the basic reproduction number is reduced below one, the disease can still persist at a notable

endemic level. Consequently, control measures that are typically effective during forward bifurcation may prove insufficient, necessitating more intensive and sustained interventions to manage the disease spread. Therefore, the findings of this simulation underscore the critical need to monitor and regulate the value of λ in efforts to prevent and mitigate disease transmission.

Then, we could simulate several compartments in the system to identify the system's behavior. Previously, we could first look for the herd immunity threshold value in the system with $HIT = \left(1 - \frac{1}{\mathcal{R}_0}\right) \times \frac{1}{\text{VaccineEfficacy}}$ [27]. Vaccine efficacy with a value of 95% with the highest secondary infection value from the phase in the system can provide a threshold for herd immunity from the system of 68% or around 189 million people who must be, at least, immune to COVID-19 to achieve herd immunity. Next, we could look at the simulation of compartments $I(t)$ and $Q(t)$ in the system up to day 1800.

According to the simulation results in **Figure 4**, each compartment did not reach the predetermined HIT limit. However, based on the simulation results up to day 1800, the behavior of the system compartments was converging to one point.

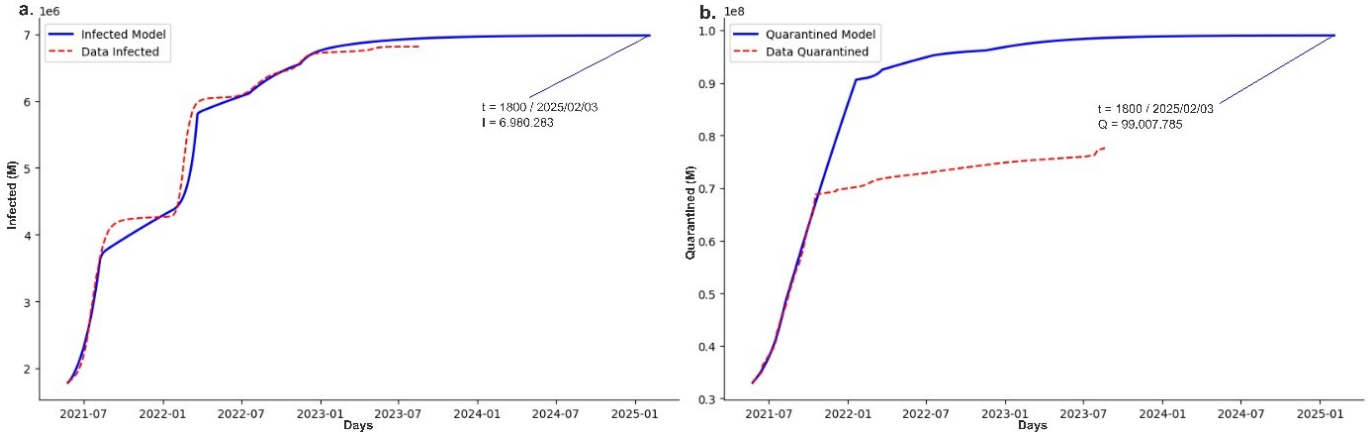

Figure 4. Simulation of the cumulative value of compartments $I(t)$ and $Q(t)$.

Next, we expanded the simulation to include more compartments, continuing until the desired herd immunity threshold was met. Our attention will shift to the First Dose Vaccine $\left(V_1(t)\right)$ compartment, recognizing that herd immunity can be achieved through both natural infection and medical interventions such as vaccination. This approach allows for the development of individual immunity within the population. The simulation will take place in the First Dose Vaccine $\left(V_1(t)\right)$ compartment until day 1800.

Figure 5 shows the state of the system after exceeding the herd immunity threshold (HIT). Following HIT, there was a convergence trend, with the administration of 246 million vaccine doses. This trend corresponds to expected outcomes in a real-world scenario in which herd immunity is achieved, as evidenced by low levels of infection while the disease persists, resulting in consistent case numbers and ongoing vaccination efforts. The infection and quarantine compartments show similar trends of stability and convergence. Based on the model simulation analysis, it was discovered that the system begins in phase 6, which leads to herd

immunity. This development is distinguished by the stabilization of infection cases and the achievement of values that exceed the herd immunity threshold, which has been established in the support compartment to achieve herd immunity.

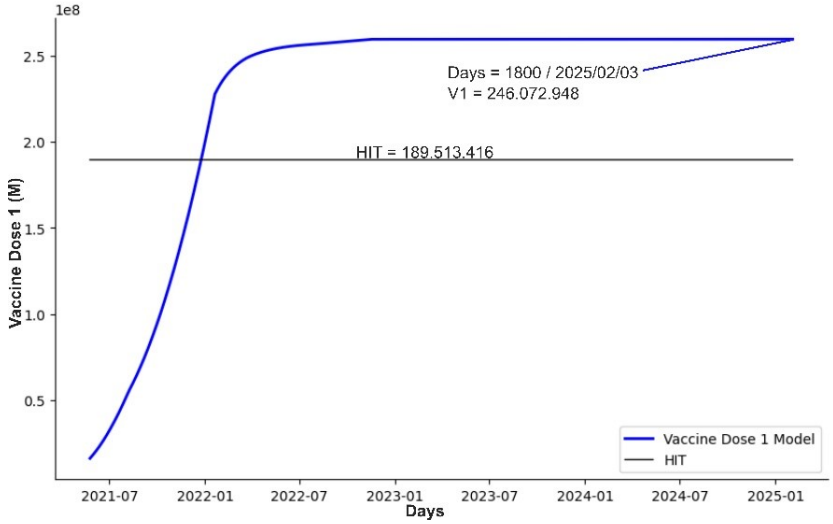

Figure 5. Simulation of the initial vaccination dose compartment $V_1(t)$ within a system.

Model simulations over time indicate that the system may have achieved herd immunity. To better understand how herd immunity works in the system under study, we will use additional tools at our disposal. Let us first consider the impact on a population once herd immunity is established. Herd immunity makes it difficult for disease-causing pathogens to infect susceptible individuals via contact within the population. When the majority of the population is immune to a pathogen, the number of susceptible individuals decreases, resulting in reduced or stopped transmission [28]. Next, focus on the secondary infection value ($\mathcal{R}_0$) and the bifurcation diagram in phase 6, as shown in **Figure 6**. We find that the secondary infection value ($\mathcal{R}_0$) is within the disease-free equilibrium zone. This indicates a stable situation without an epidemic. Secondary infection values ($\mathcal{R}_0$) below one indicates a gradual decline in the epidemic, potentially leading to its disappearance from the population. In contrast, a secondary infection ($\mathcal{R}_0$) value above zero but less than one indicates that, while the outbreak may subside, the disease, in this case COVID-19, may persist in the population indefinitely. Herd immunity dynamics are reflected in the secondary infection value ($\mathcal{R}_0$) and its bifurcation, which show characteristics consistent with this phenomenon. Thus, we conclude that the system, particularly in phase 6, has the potential to achieve herd immunity.

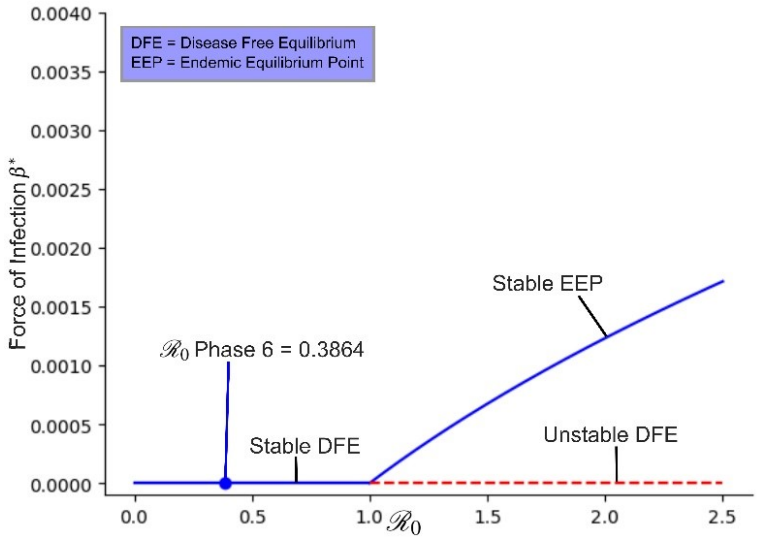

Figure 6. Bifurcation diagram and secondary infection value ($\mathcal{R}_0$) of the system in phase 6.

In addition to presenting numerical simulations of daily total cases, the upcoming simulation will concentrate on daily COVID-19 infection cases. This simulation aims to provide a more nuanced understanding of the day-to-day dynamics of disease transmission. By visualizing daily infection cases, we can closely observe the fluctuations and patterns of the spread, identify peaks and troughs, and assess the effectiveness of interventions such as quarantine measures and vaccination efforts. This information is vital for comprehending the speed of virus transmission, forecasting potential surges in cases, and developing more adaptable control strategies.

3.6. Discussion

The results from the numerical simulations reveal significant changes in the system's dynamics in response to variations in the parameter λ, which denotes the infection rate. At lower values of λ, the system demonstrates forward bifurcation characteristics typical of an epidemiological model, where the rise in cases occurs gradually and in a controlled manner. This indicates a scenario where the disease spreads slowly, allowing for effective interventions such as quarantine and vaccination to contain its spread.

However, as λ increases, the system transitions toward backward bifurcation. In this phase, the escalation in the infection rate leads to a sharp and rapid spike in cases, followed by a similarly steep decline. This change in bifurcation behavior highlights the model's sensitivity to the infection rate, underscoring the critical need to regulate λ to prevent uncontrolled surges in cases. These findings suggest that in environments with a high infection rate, intervention strategies must be more aggressive and prompter to avert entering the backward bifurcation phase, where control becomes significantly more challenging.

The results from the numerical simulations of total disease cases provide a complex understanding of herd immunity. Traditionally, herd immunity is defined by the percentage of the population that has immunity-either through natural infection or vaccination-needed to halt the spread of the disease. In this simulation, even though

the total cumulative cases of infection and quarantine have not yet reached the herd immunity threshold, the compartment for individuals who received the first dose of vaccination shows a significant level of immunity that exceeds the estimated required threshold. This suggests that vaccination may have established an effective immune barrier within the population.

Furthermore, the analysis of the system's $\mathcal{R}_0$ value, which is in the disease-free endemic area, provides additional support for the claim of herd immunity. A low $\mathcal{R}_0$ indicates that each infection case results in less than one new case, which is characteristic of herd immunity conditions. Additionally, it should be considered that herd immunity is not just about reaching a certain percentage, but also about the distribution of immunity within the population. In this simulation, widespread vaccination may have created a more even distribution of immunity, which is effective in protecting vulnerable groups and reducing the spread of the disease. Thus, although the herd immunity threshold metrics may not have been fully met, the combination of high vaccination rates, low $\mathcal{R}_0$ values, and effective immune distribution indicates that the system has achieved a functional level of herd immunity.

In **Figure 4**, we can observe a unique pattern in the system. In the first and third phases, there is a high increase in the number of cases. Then, in the remaining phase, the increase in the number of cases was not high. We first concentrate on the λ values in phases 1 and 3. The estimation results might not have been totally credible, as evidenced by the fact that phase 1, despite having the highest increase, had a lower infection rate than phase 3 when compared to the simulation shown in **Figure 4**. In addition, the infection rate (λ) in phase 4 was surprisingly higher than in phases 1 and 3. In order to go further, we would then look at the system's simulation of daily infection cases.

As shown in **Figure 7**, the highest spike was in phase 3. Furthermore, there was a low spike in the cumulative cases in phase 3 compared with that in phase 1. This finding could be attributed to the fact that the duration in phase 3 was shorter than that in phase 1. Then, we attempted to evaluate the reasons behind the high peak point of daily cases in phase 3 and why phase 3 was shorter than phase 1.

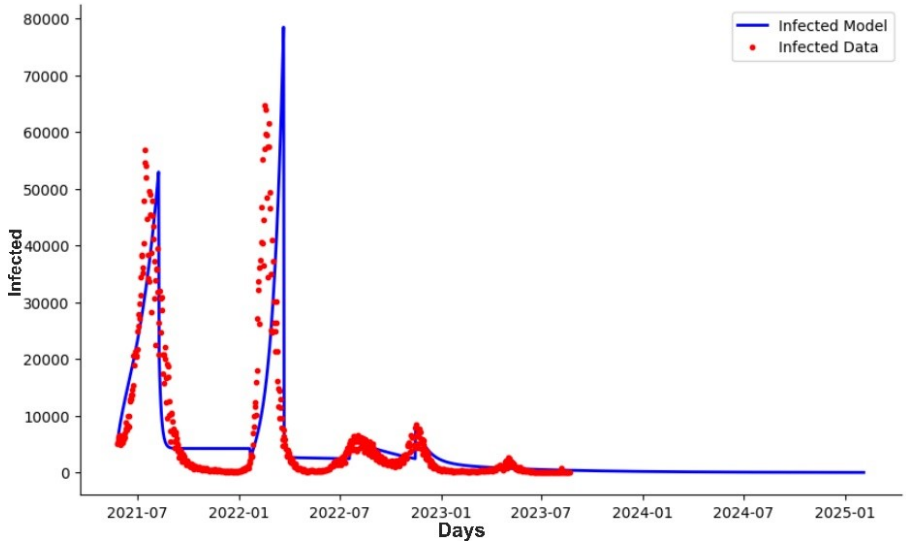

Figure 7. $I(t)$ distribution for daily cases.

According to the estimation results (**Table 3**), the value of τ_1, which was the rate of movement from compartment $I(t)$ to $Q(t)$ in phase 3, was smaller than the infection rate. This condition was reversed to the condition in phase 1. Therefore, the number of people who tested positive and who are quarantined in phase 3 was fewer compared with that in phase 1. If there were fewer individuals quarantined, then the number would be greater in other phases during an explosion of daily cases. Next, we paid attention to the estimation results of γ or recovery rate. γ in phase 3 is slightly greater than that in phase 1. This indicated that more people recovered quickly from the outbreak in phase 3 compared with phase 1. Therefore, this result indicated the achievement of group immunity. The conditions in phase 3, which included a high daily rate of infection cases and a faster recovery rate, provided reasons why this phase occurred more quickly than phase 1. That is, the cumulative cases in phase 3 were more likely to be lower than that in phase 1.

As we enter phase 4, we find that λ has the highest infection rate. The Phase 4 results show a significant λ, which correlates with a significant τ_1 value. This implies that strict quarantine regulations were implemented during this phase, effectively reducing the number of infection cases in the community. In contrast, a spike in cases occurs when τ_1 exceeds λ in phase 1. This difference could be attributed to the lower recovery rate in phase 1 compared to phase 4. The early phase of vaccination interventions, which has not yet had a significant impact on the population, adds to the explanation for the early phase peak. In contrast, Phase 4 includes intensive vaccination campaigns and booster vaccinations, which makes sense because it improves recovery rates and reduces the number of people at risk of infection following vaccination.

Finally, we conclude that the roles of λ, γ, and τ_1 are interrelated with the epidemic in the system. Balancing parameter values in the system, particularly the three parameters discussed previously, controlled the spread of the outbreak in the system. With a controlled system, forward bifurcation in the system can be achieved. Hence, it is easier to control secondary infections. Therefore, disease transmission in a controlled system also supports the achievement of herd immunity in a specific population.

Based on the numerical simulations obtained, we will compare them with an intriguing approach to disease spread modeling. Kyurkchiev [29] is developing a model that uses the infection rate and other parameters as polynomial functions, offering flexibility for complex disease dynamics. However, this complexity may complicate interpretation and analysis.

In contrast, the epidemiological model used in this study incorporates simpler parameters through vaccination and quarantine interventions. We effectively captured disease dynamics by partitioning the data according to its trends, demonstrating that flexibility does not require complex parameters. By understanding trends and partitioning accurately, we achieved reliable results with a simpler model.

Kyurkchiev's approach [29] may better suit diseases with complex dynamics and rapid parameter changes, while our model fits diseases with more stable trends where interventions significantly impact outcomes. It is crucial to balance flexibility and interpretability. Although complex models may provide more accurate results, they

can be harder to interpret. Simpler models, while potentially less accurate, are easier to understand and communicate to policymakers and the public, emphasizing the need to consider accuracy alongside usability in model selection.

The COVID-19 epidemic model developed in this study presents a distinct approach compared to the model proposed by Negi [7]. The primary difference lies in how the vaccination and infection compartments are represented, alongside the quarantine strategy employed. Our model breaks down the vaccination compartments into three doses, capturing the complexities of the vaccination program that includes both primary and booster doses. We placed an emphasis on quarantining individuals exhibiting mild symptoms, whereas those with moderate to severe symptoms were assigned to the infected compartment, highlighting differences in clinical management. Additionally, the bifurcation analysis we conducted offers insights into qualitative changes in epidemic dynamics as parameters shift, along with their biological implications.

Furthermore, we conducted model fitting on the daily COVID-19 case data in Indonesia. The results indicate that the model effectively represents disease spread trends, although it necessitates data partitioning to account for varying dynamics during specific periods. This demonstrates that our model can effectively capture the complexities of epidemiological data with the appropriate adjustments.

The Negi model [7], in contrast, consolidates the vaccination compartment into a single category while expanding the infection compartment to distinguish between symptomatic, asymptomatic, and hospitalized cases. This methodology facilitates a more profound understanding of transmission dynamics and the associated healthcare burden. Furthermore, Negi calibrated the model using disease distribution data from various countries, showcasing its capacity to effectively represent empirical data on a broad scale. Together, both models enhance our comprehension of COVID-19 dynamics. Our model focuses on the intricacies of vaccination, the quarantine of mild cases, and the representation of local data from Indonesia, whereas Negi's model offers greater detail regarding infection compartments and validation through cross-country data.

4. Conclusions

The numerical simulations indicate that the dynamics of COVID-19 spread are significantly influenced by the lambda parameter. Changes in lambda result in shifts from forward to backward bifurcation, suggesting that higher values can worsen disease spread and hinder mitigation efforts. However, some simulations show the potential for convergence towards a single point, implying the achievement of herd immunity. Thus, while an increase in lambda can complicate the situation, effective interventions may still lead to herd immunity. The simulated model adapted data on COVID-19 transmission in Indonesia. Results revealed the achievement of herd immunity in the system. The behavior of the system showed that the increase in the number of COVID-19 cases had started to converge to one value, and disease transmission was extremely minimal. This was similar to current conditions, showing that the number of COVID-19 cases no longer exists.

Author contributions: Conceptualization, MH; methodology, MH and FRF; software, FRF; validation, MH and FRF; formal analysis, MH and FRF; investigation, MH and FRF; resources, FRF; data curation, FRF; writing—original draft preparation, MH and FRF; writing—review and editing, MH and FRF; visualization, FRF; supervision, MH; project administration, FRF; funding acquisition, MH. All authors have read and agreed to the published version of the manuscript.

Conflict of interest: The authors declare no conflict of interest.

References

1. Brauer F, Castillo-Chavez C, Feng Z. Mathematical Models in Epidemiology. Springer; 2019.
2. Cooper I, Mondal A, Antonopoulos CG. A SIR model assumption for the spread of COVID-19 in different communities. Chaos, Solitons & Fractals. 2020; 139: 110057. doi: 10.1016/j.chaos.2020.110057
3. Khalaf SL, Flayyih HS. Analysis, predicting, and controlling the COVID-19 pandemic in Iraq through SIR model. Results in Control and Optimization. 2023; 10: 100214. doi: 10.1016/j.rico.2023.100214
4. Neves AGM, Guerrero G. Predicting the evolution of the COVID-19 epidemic with the A-SIR model: Lombardy, Italy and São Paulo state, Brazil. Physica D: Nonlinear Phenomena. 2020; 413: 132693. doi: 10.1016/j.physd.2020.132693
5. Zou Y, Yang W, Lai J, et al. Vaccination and Quarantine Effect on COVID-19 Transmission Dynamics Incorporating Chinese-Spring-Festival Travel Rush: Modeling and Simulations. Bulletin of Mathematical Biology. 2022; 84(2). doi: 10.1007/s11538-021-00958-5
6. Auger P, Moussaoui A. On the Threshold of Release of Confinement in an Epidemic SEIR Model Taking into Account the Protective Effect of Mask. Bulletin of Mathematical Biology. 2021; 83(4). doi: 10.1007/s11538-021-00858-8
7. Negi SS, Rana PS, Sharma N, Khatri MS. A novel SEIAHR compartment model for accessing the impact of vaccination, intervention policies, and quarantine on the COVID-19 pandemic: A case study of most affected countries Brazil, India, Italy, and USA. Computational and Applied Mathematics. 2022; 41(7). doi: 10.1007/s40314-022-01993-1
8. Yang B, Yu Z, Cai Y. The impact of vaccination on the spread of COVID-19: Studying by a mathematical model. Physica A: Statistical Mechanics and its Applications. 2022; 590: 126717. doi: 10.1016/j.physa.2021.126717
9. Tyagi S, Martha SC, Abbas S, Debbouche A. Mathematical modeling and analysis for controlling the spread of infectious diseases. Chaos, Solitons & Fractals. 2021; 144: 110707. doi: 10.1016/j.chaos.2021.110707
10. Mohammadi H, Rezapour S, Jajarmi A. On the fractional SIRD mathematical model and control for the transmission of COVID-19: The first and the second waves of the disease in Iran and Japan. ISA Transactions. 2022; 124: 103–114. doi: 10.1016/j.isatra.2021.04.012
11. Caetano C, Morgado ML, Patrício P, et al. Measuring the impact of COVID-19 vaccination and immunity waning: A modelling study for Portugal. Vaccine. 2022; 40(49): 7115–7121. doi: 10.1016/j.vaccine.2022.10.007
12. Law KB, Peariasamy KM, Mohd Ibrahim H, Abdullah NH. Modelling infectious diseases with herd immunity in a randomly mixed population. Scientific Reports. 2021; 11(1). doi: 10.1038/s41598-021-00013-2
13. MacIntyre CR, Costantino V, Trent M. Modelling of COVID-19 vaccination strategies and herd immunity, in scenarios of limited and full vaccine supply in NSW, Australia. Vaccine. 2022; 40(17): 2506–2513. doi: 10.1016/j.vaccine.2021.04.042
14. Yuan R, Jiang W, Wang Y. Saddle-node-Hopf bifurcation in a modified Leslie–Gower predator-prey model with time-delay and prey harvesting. Journal of Mathematical Analysis and Applications. 2015; 422(2): 1072–1090. doi: 10.1016/j.jmaa.2014.09.037
15. Lynch S. Dynamical Systems with Applications using Python. Springer International Publishing; 2018.
16. Castillo-Chavez C, Song B. Dynamical Models of Tuberculosis and Their Applications. Mathematical Biosciences and Engineering. 2004; 1(2): 361–404. doi: 10.3934/mbe.2004.1.361
17. Wangari IM, Stone L. Backward bifurcation and hysteresis in models of recurrent tuberculosis. PLoS One. 2018; 13(3): e0194256. doi: 10.1371/journal.pone.0194256
18. Asamoah JKK, Nyabadza F, Jin Z, et al. Backward bifurcation and sensitivity analysis for bacterial meningitis transmission dynamics with a nonlinear recovery rate. Chaos, Solitons & Fractals. 2020; 140: 110237. doi: 10.1016/j.chaos.2020.110237

19. Nadim SS, Chattopadhyay J. Occurrence of backward bifurcation and prediction of disease transmission with imperfect lockdown: A case study on COVID-19. Chaos, Solitons & Fractals. 2020; 140: 110163. doi: 10.1016/j.chaos.2020.110163
20. Omame A, Abbas M, Onyenegecha CP. Backward bifurcation and optimal control in a co-infection model for SARS-CoV-2 and ZIKV. Results in Physics. 2022; 37: 105481. doi: 10.1016/j.rinp.2022.105481
21. Nudee K, Chinviriyasit S, Chinviriyasit W. The effect of backward bifurcation in controlling measles transmission by vaccination. Chaos, Solitons & Fractals. 2019; 123: 400–412. doi: 10.1016/j.chaos.2019.04.026
22. World Health Organization. Coronavirus disease (COVID-19) pandemic. Available online: https://covid19.who.int/region/searo/country/id (accessed on 5 February 2024).
23. Toharudin T, Pontoh RS, Caraka RE, et al. National Vaccination and Local Intervention Impacts on COVID-19 Cases. Sustainability. 2021; 13(15): 8282. doi: 10.3390/su13158282
24. Djalante R, Lassa J, Setiamarga D, et al. Review and analysis of current responses to COVID-19 in Indonesia: Period of January to March 2020. Progress in Disaster Science. 2020; 6: 100091. doi: 10.1016/j.pdisas.2020.100091
25. Fahreza FR, Hasan M, Kusbudiono K. Model and Simulation of COVID-19 Transmission with Vaccination and Quarantine Interventions in Jember. InPrime: Indonesian Journal of Pure and Applied Mathematics. 2023; 5(1): 1–21. doi: 10.15408/inprime.v5i1.27192
26. Mao Y, Wang W, Ma J, et al. Reinfection rates among patients previously infected by SARS-CoV-2: Systematic review and meta-analysis. Chinese Medical Journal. 2021; 135(2): 145–152. doi: 10.1097/cm9.0000000000001892
27. Siqueira PC, Cola JP, Comerio T, et al. Herd immunity threshold for SARS-CoV-2 and vaccination effectiveness in Brazil. Jornal Brasileiro de Pneumologia. 2022; 48(2): e20210401. doi: 10.36416/1806-3756/e20210401
28. Suryawanshi YN, Biswas DA. Biswas DA. Herd Immunity to Fight Against COVID-19: A Narrative Review. Cureus. 2023; 15(1): e33575. doi: 10.7759/cureus.33575
29. Kyurkchiev N, Kyurkchiev V, Iliev A, Rahnev A. A New Modifications of the sir/seir models with “intervention polynomial factor”. methodological aspects. International Journal of Differential Equations and Applications. 2021; 20(1): 15–30.

Advances in Differential Equations and Control Processes 2025, 32(1), 2589.
https://doi.org/10.59400/adecp2589

Editorial

Transforming frontiers: The next decade of differential equations and control processes

Ji-Huan He[1,2,3]

[1] School of Jia Yang, Zhejiang Shuren University, Hangzhou 215123, China; hejihuan@suda.edu.cn
[2] School of Mathematics and Big Data, Hohhot Minzu College, Hohhot 010051, China
[3] National Engineering Laboratory for Modern Silk, College of Textile and Clothing Engineering, Soochow University, Suzhou 215006, China

CITATION

He JH. Transforming frontiers: The next decade of differential equations and control processes. Advances in Differential Equations and Control Processes. 2025; 32(1): 2589. https://doi.org/10.59400/adecp2589

ARTICLE INFO

Received: 14 January 2025
Accepted: 16 January 2025
Available online: 22 January 2025

Abstract: Mathematics serves as the fundamental basis for innovation, propelling technological advancement. In the forthcoming decade, the convergence of differential equations and control processes is poised to redefine the frontiers of scientific exploration. The integration of artificial intelligence and machine learning with differential equations is set to inaugurate a new era of problem-solving, enabling the extraction of latent physical insights and accelerating solution discovery. Multi-scale modeling, with its capacity to span disparate physical domains, has the potential to resolve long-standing puzzles in fields such as fluid mechanics and nanoscience. Furthermore, the integration of fractal geometry with differential equations holds the promise of novel perspectives for understanding and optimizing complex systems, ranging from urban landscapes to turbulent flows. The integration of artificial intelligence (AI) with control innovations is poised to play a pivotal role in the development of next-generation technologies, with the potential to transform diverse sectors such as medicine, communication, and autonomous systems. This paper explores these developments, highlighting their potential impacts and emphasizing the necessity for interdisciplinary collaboration to leverage their full potential.

Keywords: AI; machine learning; multi-scale modeling; turbulence; fractal geometry; nanotechnology; control processes

1. Introduction

Mathematics has exerted a profound and often unacknowledged influence on the development of modern technology. It provides the fundamental framework for understanding the natural world and engineering solutions. The employment of differential equations, which elegantly describe the dynamic relationships between variables and their rates of change, has been instrumental in modeling a vast array of phenomena. Control processes, in contrast, represent the strategic mechanisms employed for the purpose of manipulating these systems to achieve specific outcomes.

As we stand at the threshold of a new technological era, the synergy between differential equations and control processes is emerging as a hotbed of innovation. The ensuing decade is poised to witness a quantum leap in these fields, with far-reaching implications across multiple disciplines. These advancements hold the potential to enhance our understanding of the fundamental laws of nature while concomitantly driving a paradigm shift in our modes of living and working.

2. AI-powered problem solving: Unleashing the potential of data and physics

The integration of artificial intelligence and machine learning with differential equations is affecting a paradigm shift in the manner in which complex problems are approached. By leveraging the power of deep learning architectures and vast datasets, we can now decode the intricate physical principles encoded within differential equations.

Within the domain of fluid dynamics, for instance, neural networks are trained on substantial data derived from flow simulations and experimental measurements. This enables them to predict turbulent flow patterns with unprecedented accuracy. The concept of "physics-informed AI" has been shown to expedite the solution process and to uncover new facets of the underlying physical phenomena. For instance, in [1], the concept of point solution was introduced, which enables highly accurate estimation of the solution at a specific point. When multiple points are involved, this concept can be integrated with AI networks to address complex problems, such as weather forecasting [2] or tsunami prediction [3].

Furthermore, the integration of ancient mathematical algorithms [4–7] with modern AI techniques underscores the enduring relevance of mathematical principles. The capacity of AI to process multimodal data underscores its potential for applications in clinical care and other domains, as evidenced by [8]. The continuous evolution of this synergy is expected to open new frontiers in human-AI interaction and other crucial areas, as discussed in [9].

3. Multi-scale modeling: Bridging the micro and macro worlds

The exploration of multi-scale architectures and multi-physical field couplings is on the brink of a major breakthrough. In the domain of fluid mechanics, the Navier-Stokes Equations have historically posed significant challenges in fully encapsulating the intricacies of turbulence. However, multi-scale models offer a glimmer of hope in this regard. Turbulence frequently originates at the nanoscale, where the fluid exhibits unique discontinuities.

These multi-scale models possess the remarkable capacity to integrate the deterministic domain of Newtonian mechanics with the uncertainties inherent in quantum mechanics. This capacity renders them a formidable instrument in nanoscience, with the potential to elucidate some of the most perplexing enigmas in thermodynamics and physics. For instance, research in multiscale habitat selection modeling [10] and multiscale materials modeling [11] has already made significant strides.

Triboinformatics [12], an emerging interdisciplinary field, combines tribology and informatics to study frictional phenomena. By analyzing large amounts of data related to friction processes, this field aims to optimize tribological systems and enhance the efficiency and durability of mechanical assemblies across various industries.

4. Fractal frontiers: Connecting mathematics and the real world

The fractal geometry paradigm has introduced a revolutionary way of perceiving complexity. Specifically, the two-scale fractal geometry [13,14] provides a novel perspective by observing the world at diverse scales. This approach has the potential to render mathematical concepts more accessible and applicable to real-world problems.

In the domain of urban planning, fractal models facilitate the visualization of urban growth and evolution, thereby capturing the intricate patterns of infrastructure expansion and population distribution. The integration of differential equations with two-scale fractal derivatives facilitates the prediction of traffic flows, in addition to the management of the complex data analytics of individual vehicles and resource allocation within urban systems. This enhancement of urban design and promotion of sustainability is a key benefit.

In the study of turbulent fluids, the traditional mass conservation equations must be adapted in fractal space. By incorporating two-scale fractal dimensions into the temporal and spatial domains, as outlined by the fractional spatio-temporal relation [15], significant advancements may be achieved in the near future in the field of turbulence modeling.

5. AI-driven control innovations: Pioneering the future of technology

The forthcoming decade will be characterized by the emergence of AI-driven control as a catalyst for technological transformation. At the molecular level, the employment of nano-robots will necessitate the implementation of highly precise and adaptable control strategies. Algorithms of a reinforcement learning nature will be utilized to facilitate the training of these diminutive machines for such tasks as targeted drug delivery within the human body. This technological advancement has the potential to transform the medical field, enabling minimally invasive treatments and early disease detection.

The advent of 6G technology [16,17] will see intelligent control systems playing a pivotal role in the management of ultra-dense networks and ultra-low latency applications. The propagation of millimeter-wave signals in complex urban environments will be modeled using differential equations, while artificial intelligence (AI)-based controllers will optimize network resource allocation in real time. This integration of technology will ensure seamless connectivity for various applications, including augmented reality, virtual reality, and the Internet of Things.

Unmanned systems, including self-driving cars and drones, will achieve higher levels of autonomy. Fuzzy neural network control, enhanced by deep learning, will handle the uncertainties and nonlinearities in real-world driving conditions. The capacity of autonomous vehicles to formulate swift yet secure resolutions in intricate traffic scenarios will be thoroughly exhibited, while unmanned aerial vehicles will possess the capability to traverse challenging terrains for tasks such as search and rescue, infrastructure inspection, and precision agriculture.

6. Conclusion

The forthcoming decade is poised to witness significant advancements at the nexus of differential equations and control processes. These advancements promise to not only deepen our understanding of the natural world but also to reshape the way we live, work, and interact with technology. Mathematics is for innovation, invention, and revolution. It is the silent catalyst that propels humanity's progress, unlocking doors to unimagined possibilities and, more importantly, it is the shortcut to realizing one's life ideals.

It is incumbent upon the research community to wholeheartedly embrace these frontiers and foster interdisciplinary collaboration. Through the integration of expertise from diverse fields, we can fully realize the potential of these powerful mathematical tools and propel the next wave of technological innovation. Mathematics, as the driving force behind innovation, invention, and revolution, is pivotal to unlocking a future filled with endless possibilities.

Conflict of interest: The author declares no conflict of interest.

References

1. Liu YP, He JH. A fast and accurate estimation of amperometric current response in reaction kinetics. Journal of Electroanalytical Chemistry. 2025; 978: 118884.
2. He JH. An Old Babylonian Algorithm and Its Modern Applications. Symmetry. 2024; 16(11): 1467. doi: 10.3390/sym16111467
3. Dee DP, Uppala SM, Simmons AJ, et al. The ERA-Interim reanalysis: Configuration and performance of the data assimilation system. Quarterly Journal of the Royal Meteorological Society. 2011; 137(656): 553–597.
4. Wang Y, Hou WF, Gepreel K, Li HJ. A fractal-fractional tsunami model considering near-shore fractal boundary. Fractals. 2024; 32(2): 2450040.
5. Khan WA, Arif M, Mohammed M, et al. Numerical and Theoretical Investigation to Estimate Darcy Friction Factor in Water Network Problem Based on Modified Chun-Hui He's Algorithm and Applications. Mathematical Problems in Engineering. 2022; 8116282. doi: 10.1155/2022/8116282
6. He CH. An introduction to an ancient Chinese algorithm and its modification. International Journal of Numerical Methods for Heat & Fluid Flow. 2016; 26(8): 2486–2491.
7. Li XJ, Zhao R. Physics-informed deep ai simulation for fractal integro-differential equation. Fractals. 2024; 32(1): 2450022.
8. Xiang JX, Wang XY, Zhang XM, et al. A vision-language foundation model for precision oncology. Nature. 2025; doi: 10.1038/s41586-024-08378-w
9. Thorp HH, Vinson V, Kmec L. Steady going in 2025. Science. 2025; 387(6729): 7.
10. McGarigal K, Wan HY, Zeller KA, et al. Multi-scale habitat selection modeling: A review and outlook. landscape Ecology. 2016; 31(6): 1161–1175.
11. Schmauder S, Schäfer I. Multiscale materials modeling. Materials Today. 2016; 19(3): 130–131.
12. Nosonovsky M, Aglikov AS. Triboinformatics: Machine learning methods for frictional instabilities. Facta Universitatis Series Mechanical Engineering. 2024; 22(3): 423–433.
13. Liu YP, He JH, Mahmud MH. Leveraging lotus seeds' distribution patterns for fractal super-rope optimization. Fractals. 2024. doi: 10.1142/S0218348X24501433
14. Zhang TR, Anjum N, Tian D, Alsolami AA. Fast and accurate population forecasting with two-scale fractal population dynamics and its application to population economics. Fractals. 2024; 32(5). doi:10.1142/S0218348X24500828
15. Wang KL, He CH. A remark on Wang's Fractal Variational Principle. Fractals. 2019; 27(8): 1950134.
16. Tian D, Huang ZX, Xiang JJ. A modeling and experimental analysis of fractal geometric potential mems in the context of the development of 6G and beyond. Fractals. 2024. doi: 10.1142/S0218348X2450124X

17. Zeng Y, Zhang R, Lim TJ. Wireless Communications with Unmanned Aerial Vehicles: Opportunities and Challenges. IEEE Communications Magazine. 2016; 54(5): 36–42.

Advances in Differential Equations and Control Processes 2025, 32(1), 2989.
https://doi.org/10.59400/adecp2989

Editorial

Differential equations: A bibliometric analysis

João Paulo Davim

Department of Mechanical Engineering, University of Aveiro, Campus Santiago, Aveiro 3810-193, Portugal; pdavim@ua.pt

CITATION

Davim JP. Differential equations: A bibliometric analysis. Advances in Differential Equations and Control Processes. 2025; 32(1): 2989. https://doi.org/10.59400/adecp2989

ARTICLE INFO

Received: 21 March 2025
Accepted: 24 March 2025
Available online: 28 March 2025

Differential equations have many practical applications in several branches of knowledge. In mathematics, a differential equation "is an equation whose unknown is a function that appears in the equation in the form of its derivatives". The study of differential equations is a broad field in applied mathematics widely used to construct mathematical models of physical phenomena with wide application in engineering [1–5].

The bibliometric analysis used the database Scopus/Elsevier to search for the documents. Using the term {differential equations}, TITLE-ABS-KEY ({differential equations}), 356,655 documents were identified (a search carried out on 19 March 2025).

The results obtained in documents can be seen in **Table 1**, for the first ten positions concerning year, source, author, affiliation, country, document type, scientific area, and funding support. The better results obtained show in function of the number of documents produced: year 2024 (17,272), followed by the years 2023 (16,846) and 2021 (16,118); source *Applied Mathematics and Computation*—Elsevier (4412) followed by *Journal of Mathematical Analysis and Applications*—Elsevier (3016) and *Journal of Computational and Applied Mathematics*—Elsevier (2961); author Pop, I.—Universitatea Babeș-Bolyai (663), followed by Baleanu, D.—Lebanese American University, (661) and Hayat, T—Quaid-i-Azam University (508); affiliation CNRS Centre National de la Recherche Scientifique (4278) followed by Russian Academy of Sciences (3848) and Chinese Academy of Sciences (2677); country USA (69,349) followed by China (61,950) and India (21,152); document type article (279,742) followed by Conference Paper (65,215) and Book Chapter (4842); scientific area Mathematics (178,067) followed by Engineering (147,229) and Physics and Astronomy (83,597) and funding support National Natural Science Foundation of China (23,663) followed by National Science Foundation (11,525) and Ministry of Science and Technology of China (7800).

Table 1. Documents (356,655) by (source Scopus/Elsevier, 19 March 2025).

	Year	Source	Author	Affiliation
1	2024 (17,271)	Applied Mathematics and Computation (4412)	Pop, I. (663)	CNRS Centre National de la Recherche Scientifique (4278)
2	2023 (16,846)	Journal of Mathematical Analys. and Applications (3016)	Baleanu, D. (661)	Russian Academy of Sciences (3848)
3	2021 (16,118)	Journal of Computational and Applied Mathematics (2961)	Hayat, T. (508)	Chinese Academy of Sciences (2677)
4	2022 (15,808)	Nonlinear Analysis Theory Meth. and Applications (2949)	Alsaedi, A. (461)	King Abdulaziz University (2299)

Table 1. (*Continued*).

	Year	Source	Author	Affiliation
5	2020 (14,593)	Computers and Mathematics with Applications (2817)	Agarwal, R.P. (390)	National Academy of Sciences of Ukraine (2261)
6	2019 (14,123)	Lecture Notes in Computer Science (2669)	Ahmad, B. (338)	Lomonosov Moscow State University (2056)
7	2018 (13,260)	AIP Conference Proceedings (2608)	Dehghan, M. (323)	Ministry of Education of China (2032)
8	2017 (12,861)	Mathematical Methods in The Applied Sciences (2407)	Nisar, K.S. (322)	Harbin Institute of Technology (1788)
9	2015 (11,703)	Journal of Computational Physics (2266)	Ishak, A. (308)	Tsinghua University (1695)
10	2016 (11,661)	Proceedings of The IEEE Conf. on Decision and Control (2263)	Ntouyas, S.K. (308)	Shanghai Jiao Tong University (1640)
	Country	**Type**	**Area**	**Funding Support**
1	USA (69,349)	Article (279,742)	Mathematics (178,067)	National Natural Science Foundation of China (23,663)
2	China (61,950)	Conference Paper (65,215)	Engineering (147,229)	National Science Foundation (11,525)
3	India (21,152)	Book Chapter (4842)	Physics and Astronomy (83,597)	Ministry of Science and Technology of China (7800)
4	Russian Fed. (20,518)	Review (2701)	Computer Science (72,715)	European Commission (4737)
5	Germany (19,511)	Book (1492)	Materials Science (29,731)	Russian Foundation for Basic Research (3566)
6	UK (16,435)	Conference Review (860)	Chemical Engineering (17,861)	Deutsche Forschungsgemeinschaft (3145)
7	France (15,468)	Editorial (418)	Chemistry (13,269)	Fundamental Research Funds for the Central Universities (2652)
8	Italy (13,498)	Note (387)	Earth and Planetary Sciences (11,749)	UK Research and Innovation (2596)
9	Canada (11,043)	Letter (282)	Energy (11,642)	U.S. Department of Energy (2536)
10	Iran (10,308)	Report (74)	Environmental Science (9427)	Engineering and Physical Sciences Research Council (2532)

Conflict of interest: The authors declare no conflict of interest.

References

1. Abell ML, Braselton JP. Introductory Differential Equations. Academic Press; 2023.
2. Alazard T. Analysis and Partial Differential Equations. Springer; 2024.
3. Chicone C. Ordinary Differential Equations with Applications. Springer; 2024.
4. Ram M, Davim JP. (editors) Advanced Mathematical Techniques in Engineering Sciences. CRC Press; 2018.
5. Ram M, Davim JP. (editors) Mathematics Applied to Engineering. Academic Press; 2017.

Advances in Differential Equations and Control Processes 2025, 32(1), 3096.
https://doi.org/10.59400/adecp3096

Editorial

Differential equation-driven intelligent control: Integrating AI, Quantum computing, and adaptive strategies for next-generation industrial automation

Yue Cheng[1], Cheng-Li Luo[1], Chen Zhong[1], Hong Lin[1], Dragan Marinkovic[2,3], Ji-Huan He[1,*]

[1] School of Information Engineering, Yango University, Fuzhou 350015, China
[2] Fakultät V—Institut für Mechanik, FG Strukturmechanik und Strukturberechnung, Department of Structural Mechanics, Berlin Institute of Technology, D-10623 Berlin, Germany
[3] Faculty of Mechanical Engineering, University of Nis, 18000 Nis, Serbia
*** Corresponding author:** Ji-Huan He, hejihuan@ygu.edu.cn; hejihuan@suda.edu.cn

CITATION

Cheng Y, Luo CL, Zhong C, et al. Differential equation-driven intelligent control: Integrating AI, Quantum computing, and adaptive strategies for next-generation industrial automation. Advances in Differential Equations and Control Processes. 2025; 1(32): 3096. https://doi.org/10.59400/adecp3096

ARTICLE INFO

Received: 14 April 2025
Accepted: 16 April 2025
Available online: 24 April 2025

Abstract: The increasing intricacy of industrial systems highlights the inadequacies of conventional control theories in the management of high-dimensional nonlinear dynamics, real-time coupling, and multi-scale modelling. This article introduces a transformative paradigm—differential equation-driven intelligent control—that synergizes artificial intelligence (AI), quantum computing, and adaptive strategies to redefine next-generation industrial automation. The following innovations are at the core of this paradigm: Physics-informed neural networks (PINNs) for solving partial differential equations (PDEs), Quantum-enhanced linear algebra for stochastic differential equation (SDE) optimization, and symbolic regression for automated discovery of fractional-order dynamic models. A case study on flexible robotic arm dynamics demonstrates the tunability of hybrid rigid-flexible systems via fractional-order parameters and adaptive Lyapunov-based control. The concept of Equations as a Service (EaaS) is proposed to democratize access to distributed computational solvers, enabling real-time optimization for applications such as drone swarm coordination and carbon-neutral manufacturing. A number of critical challenges are addressed in this text, including the interpretability of AI (for example, through the use of SHAP-based explainability tools), the reliability of hybrid quantum-classical solvers, and ethical governance frameworks. Through interdisciplinary collaboration, the vision for self-evolving factories by 2030 is outlined—where differential equations autonomously refine parameters using real-time sensor data. Examples include smart grids adapting to renewable energy fluctuations at millisecond scales and robotic assembly lines recalibrating dynamics to mitigate material defects. The overarching objective of this paradigm shift, termed EaaS, is to transition differential equations from their traditional role as static descriptors to that of self-optimizing assets. This transition is expected to lay the foundation for resilient, explainable, and sustainable ecosystems in the era of Industry 5.0.

Keywords: differential equation-driven control; physics-informed neural networks (PINNs); quantum variational algorithms; symbolic regression; Equations as a Service (EaaS); explainable AI (XAI); self-evolving algorithm

1. Introduction

The advent of Industry 5.0 necessitates a paradigm shift in industrial automation, driven by the need to manage increasingly complex systems characterized by high-dimensional nonlinear dynamics, real-time coupling, and multi-scale interactions. Conventional control methodologies, such as PID controllers, are inadequate in addressing these challenges due to their reliance on linear approximations and static

parameterization. To illustrate this point, consider the example of flexible robotic arms governed by hybrid rigid-flexible dynamics (see Equation (1)). In such cases, traditional models are unable to capture memory effects, fractal damping, or adaptive responses to disturbances such as payload variations or unmodeled vibrations.

At the core of this transition lies differential equation-driven intelligent control, a framework that integrates physics-informed machine learning, quantum computing, and adaptive strategies to bridge the gap between theoretical models and real-world applications. To illustrate this, consider the dynamics of a flexible robotic arm described by:

$$\begin{aligned} & m(u)\left\{a\frac{d^2u}{dt^2}+(1-a)\left[p\frac{d^{2\alpha}u}{dt^{2\alpha}}+(1-p)D_t^{2\alpha}u\right]\right\} \\ & +C(u,\frac{du}{dt},\frac{d^\alpha u}{dt^\alpha})\left\{b\frac{du}{dt}+(1-b)(q\frac{d^\alpha u}{dt^\alpha}+(1-q)D_t^\alpha u)\right\} \\ & +G(u)=\tau(t,t^\alpha)+\Delta(u,t,,t^\alpha) \end{aligned} \tag{1}$$

Here, $d^\alpha u/dt^\alpha$ is the two-scale fractal derivative [1,2] quantifying motion in the fractal space, while the fractional order D_t^α governs memory-dependent energy dissipation [3,4]. The fractional order α is relative to the two-scale fractal dimensions [5]. Parameters *a* and *b* balance rigidity and flexibility, enabling tunable control from precision welding ($a = 1$) to soft robotics ($a = 0$) [6]. Weighting factors *p* and *q* model motion property in a fractal space or metamaterials' viscoelasticity. The term $G(u)$ adapts gravitational forces to elastic deformations, Δaggregates uncertainties, which are critical in systems with high-dimensional nonlinearity, and τ is the control input applied to the joints and which can be expressed as:

$$\tau=-K_1[u(t)-u_d(t)]-K_2\frac{d^\alpha}{dt^\alpha}[u(t)-u_d(t)]-K_3D_t^\alpha[u(t)-u_d(t)] \tag{2}$$

where $u_d(t)$ is the desired state, K_i ($i = 1\sim3$) are constants.

The limitations of classical approaches are not confined to robotics. Industrial systems, including smart grids, drone swarms, and additive manufacturing, necessitate real-time optimization and self-calibration under dynamic conditions. This necessitates innovations such as physics-informed neural networks (PINNs) for solving partial differential equations (PDEs) [7], quantum-enhanced solvers for stochastic optimization [8], and the symbolic regression [9] for automated discovery of fractional-order models. To illustrate this point, we may consider the use of PINNs, which are able to embed PDE constraints directly into neural networks, thus enabling accurate thermal management in a complex system [10]. Similarly, hybrid quantum-classical algorithms have been shown to accelerate matrix inversions for real-time control [11].

This editorial article proposes a synergistic framework within which differential equations evolve from static descriptors to self-optimizing assets. The proposed framework unifies AI-driven modelling, quantum acceleration, and adaptive execution, thereby addressing three critical gaps in the field.

1. Interpretability: The utilization of explainable AI (XAI) tools, such as SHAP values, facilitates the reconstruction of control decisions back to their underlying governing equations.

2. Scalability: The combination of quantum solvers with dimensionality reduction techniques is employed for the purpose of dealing with high-dimensional partial differential equations (PDEs).

3. Ethical governance: The incorporation of fairness and sustainability constraints into automated workflows.

Recent studies have optimized maintenance strategies in industrial settings through differential equation approaches [12], while a cooperative control strategy integrating longitudinal and lateral dynamics for preview-enabled intelligent vehicles was proposed in Ref. [13], demonstrating the universality of differential equations in cross-domain control problems. A case study on flexible robotic arms (Section 3) demonstrates how fractional-order parameters and Lyapunov-based adaptive control enable stability in variable environments. Furthermore, the concept of Equations as a Service (EaaS) (Section 4) democratizes computational power, allowing real-time optimization for applications ranging from traffic flow management to carbon-neutral manufacturing.

This interdisciplinary approach will enable the envisioned self-evolving factories by 2030, where differential equations will autonomously refine parameters using sensor data, enabling millisecond-scale adaptations—from smart grids responding to renewable fluctuations to assembly lines mitigating material defects. This transition not only redefines industrial automation but also establishes the foundations for resilient, explainable, and sustainable ecosystems in the era of Industry 5.0.

2. Technological convergence: AI, quantum, and adaptive control

2.1. AI-driven modeling: From data to physics-informed equations

Physics-informed neural networks (PINNs) are a machine learning framework that embeds partial differential equation (PDE) constraints, thus enabling solutions for complex thermal management and smart manufacturing. Symbolic regression is a process that automates the discovery of equations from sensor data, identifying fractional-order terms and weighting factors that model viscoelasticity in flexible materials.

2.2. Quantum acceleration

Quantum algorithms such as Harrow-Hassidim-Lloyd (HHL) [14] have been shown to accelerate matrix inversions for PDE discretization, thereby enabling real-time control of smart grids and robot swarms. Hybrid quantum-classical solvers combine quantum annealing for global exploration with classical feedback for precision, enhancing robustness in dynamic environments.

2.3. Adaptive execution

Reinforcement learning (RL) [15,16] is a process by which control policies are dynamically aligned with system evolution. To illustrate this, consider the example of self-calibrating 3D printers, which leverage RL to minimize warping defects through real-time thermal adjustments [17]. Edge devices are capable of solving ordinary differential equations (ODEs) in a localized manner, thereby facilitating millisecond

responses for high-speed assembly lines. The application of RL in the context of thermal adjustment within MEMS systems has also been demonstrated [18,19].

3. Case study: Adaptive control of flexible robotic arms

It is hypothesized that the dynamics of flexible robotic arms are governed by Equation (1). The parameter a is employed to balance rigidity and flexibility (e.g., a = 1 for precision welding and a = 0 for soft robotics). The parameter b is a measure of fractal damping models in tendon-driven robots operating in variable friction environments. The fractional order has been demonstrated to quantify memory effects for slow energy dissipation in viscoelastic materials and fractal damping effect.

A layered optimization strategy combines metaheuristic algorithms (e.g., genetic algorithms) for global parameter search, physics-informed machine learning for real-time inference, and quantum annealing for rapid convergence under dynamic conditions. Lyapunov-based adaptive controllers ensure stability.

4. Equations as a Service (EaaS): Democratizing computational power

It is to be posited herewith that one might consider the following hypothetical scenario: one is a city planner charged with the optimization of traffic light timings with a view to reducing congestion. The problem involves the solution of complex differential equations that model traffic flow patterns. The team is faced with the challenge of limited computational capabilities, as supercomputers are financially unfeasible and standard laptops are incapable of handling the required calculations. The following is an exposition of how Equations as a Service (EaaS) addresses this challenge:

Firstly, traffic flow equations (e.g. fluid dynamics-inspired models) and parameters (e.g. current traffic volume and road layouts) are uploaded to a cloud-based EaaS platform via a simple interface. The platform then utilizes intelligent workload distribution to ensure optimal performance. Specifically, quantum solvers address large-scale optimization to identify optimal traffic light sequences, GPU clusters simulate real-time traffic scenarios across thousands of virtual vehicles, and classical servers compile results into actionable reports highlighting congestion hotspots and proposed light timings. Thirdly, within minutes, users receive optimized traffic light schedules, predicted to reduce rush-hour delays. A further advantage is that costs are only incurred for the resources used, extremely cheap for both quantum processing and GPU, thus eliminating the need for upfront investments in hardware.

Beyond efficiency, EaaS offers two key advantages. Data security is ensured through blockchain encryption, and collaboration is streamlined by inviting global transportation experts to review and refine models with controlled access. Furthermore, an algorithm marketplace enables users to integrate specialized tools, such as a researcher's novel AI model for predicting sudden traffic jams, for a nominal fee, thereby enhancing the accuracy of simulations.

Fundamentally, EaaS democratizes computational power by treating it like electricity: users no longer need to own a "power plant" (supercomputer) to solve equations. Instead, users can access the necessary resources on demand, and only pay

for the resources they use. This approach is not limited in its application; it can be used for diverse purposes, ranging from the design of eco-friendly buildings to the prediction of weather patterns. The future of EaaS is envisaged as one in which zero-latency control, self-evolving factories and carbon-neutral manufacturing are enabled, thereby transforming equations from static tools into dynamic, accessible assets that drive innovation.

The field of self-evolving learning, a recent development in the area of deep learning technology, has the potential to further enhance such systems by enabling models to adapt autonomously to dynamic environments [20].

5. Challenges and future directions

Notwithstanding the immense potential inherent in the utilization of differential equation-driven intelligent control, there are several challenges that must be addressed if this technology is to realize its full impact. Primarily, the issue of scalability remains a critical hurdle. The resolution of high-dimensional partial differential equations (PDEs) for systems such as drone swarms or multi-robot coordination necessitates AI-driven dimensionality reduction techniques and hybrid quantum-classical solvers to manage computational complexity. To illustrate this point, consider the example of simulating carbon-neutral manufacturing processes, a task that may require real-time optimization across thousands of variables, thereby pushing classical algorithms to their limits. The same applies to smart structures, whose structural behavior is actively controlled to achieve goals such as vibration attenuation, noise reduction, enhanced safety, and improved robustness. This task can be successfully achieved only upon significant model reduction in order to render the problem mathematically tractable [21].

Secondly, interpretability gaps hinder trust in AI-augmented control systems. Explainable AI (XAI) tools, such as SHAP values or attention maps, are required to elucidate the fractional-order terms present in adaptive policies. To illustrate this point, consider a scenario in which a factory's energy optimization model unexpectedly prioritizes renewable energy sources over cost efficiency. In such a case, XAI frameworks must transparently trace this decision back to the governing equations and sustainability constraints embedded in the system.

Thirdly, there is a lag between technological advancements and the development of ethical governance frameworks. It is imperative for EaaS platforms to adopt transparency certifications to audit algorithmic safety, bias, and environmental impact. To illustrate this point, consider a quantum-enhanced solver employed for supply chain optimization, which might unwittingly favor regions offering cheaper labor, thereby giving rise to ethical concerns. It is therefore vital for policymakers and engineers to collaborate in a proactive manner in order to embed fairness and accountability into equation-driven automation. In the forthcoming period up to 2030, our Yango differential equation-driven intelligent control group (**Figure 1**) predicts that the focus will be on the development of self-evolving factories, in which differential equations will autonomously refine their parameters using real-time sensor data. The concept of a smart grid that updates its power distribution model instantaneously based on renewable energy fluctuations is another example of this

technological advancement. Similarly, a robotic assembly line that recalibrates its fractional-order dynamics to adapt to material defects is another example of this technological advancement. Achieving this objective necessitates the integration of sustainability constraints, such as carbon-neutral operations, directly into equation-solving workflows. The unification of control theory, quantum computing, and AI ethics is expected to transform equations from static descriptors into adaptive, self-optimizing assets that will drive resilient and equitable industrial ecosystems.

Figure 1. Yango differential equation-driven intelligent control group.

6. Conclusion

The integration of differential equation-driven intelligent control represents a paradigm shift in the domain of industrial automation. The integration of artificial intelligence, quantum computing, and adaptive strategies within this framework facilitates the development of resilient, explainable, and sustainable systems. The democratization of advanced mathematics, a consequence of the aforementioned developments, is set to accelerate innovation across a range of fields, from precision manufacturing to climate modelling. The future of automation is therefore likely to be characterized by the evolution, learning and self-optimization of equations, which has the potential to usher in a new era of Industry 5.0.

Author contributions: Conceptualization, JHH, CLL and DM; methodology, YC, CLL, CZ, HL, DM, JHH; validation, JHH, CLL and DM; formal analysis, JHH; investigation, YC, CLL, CZ, HL, DM, JHH; writing—original draft preparation, JHH; writing—review and editing, YC, CLL, CZ, HL, DM, JHH; supervision, JHH; project

administration, JHH; funding acquisition, JHH. All authors have read and agreed to the published version of the manuscript.

Institutional review board statement: Not applicable.

Conflict of interest: The authors declare no conflict of interest.

References

1. Zhang YR, Anjum N, Tian D, Alsolami AA. Fast and accurate population forecasting with two-scale fractal population dynamics and its application to population economics. Fractals. 2024; 32(5). doi: 10.1142/S0218348X24500828
2. He CH, Liu HW, Liu C. A fractal-based approach to the mechanical properties of recycled aggregate concretes. Facta Universitatis Series: Mechanical Engineering. 2024; 22(2): 329–342.
3. Wang H, Zhao J, Ku J, Liu Y. Existence of mild solution for (k,Ψ)-Hilfer fractional Cauchy value problem of Sobolev type. Advances in Differential Equations and Control Processes. 2024; 31(4): 439–472. doi: 10.17654/0974324324024
4. Sayevand K, Rostami M. Fractional optimal control problems: Optimality conditions and numerical solution. IMA Journal of Mathematical Control and Information. 2018; 35(1): 123–148.
5. He CH, Liu C. Fractal dimensions of a porous concrete and its effect on the concrete's strength. Facta Universitatis Series: Mechanical Engineering. 2023; 21(1): 137–150.
6. De Luca A, Siciliano B. Closed-form dynamic model of planar multilink lightweight robots. IEEE Transactions on Systems, Man, and Cybernetics. 1991; 21(4): 826–839. doi: 10.1109/21.108300
7. Karniadakis GE, Kevrekidis IG. Lu L, et al. Physics-informed machine learning. Nature Reviews Physics. 2021; 3: 422–440. doi: 10.1038/s42254-021-00314-5
8. Harrigan MP, Sung KJ, Neeley M, et al. Quantum approximate optimization of non-planar graph problems on a planar superconducting processor. Nature Physics. 2021; 17: 332–336. doi: 10.1038/s41567-020-01105-y
9. Wang Y, Wagner N, Rondinelli JM. Symbolic regression in materials science. MRS Communications. 2019; 9: 793–805. doi: 10.1557/mrc.2019.85
10. Son H, Cho H, Hwang HJ. Physics-Informed Neural Networks for Microprocessor Thermal Management Model. IEEE Access. 2023; 11: 122974–122979. doi: 10.1109/ACCESS.2023.3329562
11. Chen CC, Shiau SY, Wu MF, Wu YR. Hybrid classical-quantum linear solver using Noisy Intermediate-Scale Quantum machines. Scientific Reports. 2019; 9. doi: 10.1038/s41598-019-52275-6
12. Garg S, Rani N. Optimizing maintenance strategies of coil shop: A differential equation approach. Advances in Differential Equations and Control Processes. 2024; 31(4): 487–509. doi: 10.17654/0974324324026
13. Tang M, Chen X, Tang K, et al. Longitudinal and Lateral Cooperative Control of Preview Intelligent Vehicles with Stabilization. Journal of Intelligent & Robotic Systems. 2024; 110. doi: 10.1007/s10846-024-02197-x
14. Morgan J, Ghysels E, Mohammadbagherpoor H. An enhanced hybrid HHL algorithm. Physics Letters A. 2025; 532: 130181.
15. Mnih V, Kavukcuoglu K, Silver D, et al. Human-level control through deep reinforcement learning. Nature. 2015; 518: 529–533. doi: 10.1038/nature14236
16. Zamfirache IA, Precup RE, Petriu EM. Q-learning, policy iteration and actor-critic reinforcement learning combined with metaheuristic algorithms in servo system control. Facta Universitatis Series: Mechanical Engineering. 2023; 21(4): 615–630.
17. Hong H, Kim S, Kim W, et al. Design optimization of 3D printed kirigami-inspired composite metamaterials for quasi-zero stiffness using deep reinforcement learning integrated with bayesian optimization. Composite Structures. 2025; 359: 119031.
18. Lei XH, He JH. Frontiers in thermal science driven by artificial intelligence. Thermal Science. 2025. doi: 10.2298/TSCI 250101059L
19. He JH, Bai Q, Luo YC, et al. Modeling and numerical analysis for MEMS graphene resonator. Frontiers in Physics. 2025; 13. doi: 10.3389/fphy.2025.1551969
20. He JH. Transforming frontiers: The next decade of differential equations and control processes. Advances in Differential Equations and Control Processes. 2025; 32(1): 2589. doi: 10.59400/adecp2589
21. Milić P, Marinković D, Klinge S, Ćojbašić Ž. Reissner-Mindlin Based Isogeometric Finite Element Formulation for Piezoelectric Active Laminated Shells. Tehnicki Vjesnik. 2023; 30(2): 416–425. doi: 10.17559/TV-20230128000280

Academic Publishing Pte. Ltd.

Add: 73 Upper Paya Lebar Road, #07-02B-01, Centro Bianco, Singapore 534818

Tel: +65 83184869

E-mail: editorial_office@acad-pub.com

Web: http://ojs.acad-pub.com/